AAT48

Proceeding & Abstract

The 48th International Conference of the Anatomy Association of Thailand

13-15 May 2026

TSIX5 Phenomenal Hotel, Chonburi, Thailand

THE 48th INTERNATIONAL CONFERENCE OF THE ANATOMY ASSOCIATION OF THAILAND (AAT48)

May 13th -15th , 2026
Venue: Tsix5 Phenomenal Hotel, Pattaya, Chon Buri, Thailand

Organized by
Department of Anatomy, Faculty of Medicine,
Srinakharinwirot University
and
The Anatomy Association of Thailand

THE 48th INTERNATIONAL CONFERENCE OF THE ANATOMY ASSOCIATION OF THAILAND (AAT48)

The proceeding of the Anatomy Association of Thailand is officially published annually by the Anatomy Association of Thailand, Bangkok 10700, Thailand

Organized by
Department of Anatomy, Faculty of Medicine, Srinakharinwirot University,
and the Anatomy Association of Thailand

May 2026 -50 copies

ISBN: 978-616-622-122-0

Message from the Chairman of the Opening Ceremony, AAT48

Pansiri Phansuwan
Emeritus Professor, PhD, PFHEA
Chairman of The Commission on Higher Education Standards (CHES), Ministry of Higher Education, Science, Research, and Innovation (MHESI), Thailand

Dear Colleagues, Distinguished Guests, and Honored Delegates,

Welcome to the 48th Annual Conference of the Anatomical Association of Thailand (AAT48), proudly co-hosted by the Department of Anatomy, Faculty of Medicine, Srinakharinwirot University.

I am thrilled to celebrate the remarkable success of this year's gathering. Welcoming over 200 delegates from across the globe marks a historic milestone for the AAT and highlights the internationalization of this conference. This event underscores the vital importance of international research exchange. Robust collaboration among anatomical societies worldwide yields highly fruitful outcomes, driving innovation and advancing medical science beyond borders.

As we look to the future, we must continuously strengthen the quality of research and anatomical teaching. This mission is perfectly captured by the profound motto of our Srinakharinwirot University: "Education is Growth." By elevating our educational standards and embracing global partnerships, we nurture the intellectual and professional growth of our entire scientific community.

I extend my deepest gratitude to the organizing committees from the Anatomical Association of Thailand and the Department of Anatomy, Faculty of Medicine, Srinakharinwirot University for their tireless dedication. To all participants and contributing authors, thank you for bringing your expertise to this forum.

I wish you a highly productive conference and continued growth in your professional endeavors.

Message from the Dean of the Faculty of Medicine, Srinakharinwirot University

Nantana Choomchuay, M.D.
Assistant Professor

Esteemed delegates, honored guests, and respected colleagues,

It is a great honor to warmly welcome you to the 48th Annual Conference of the Anatomy Association of Thailand (AAT48), held under the theme "Anatomy 360°".

On behalf of the Faculty of Medicine, Srinakharinwirot University, I wish to express my sincere appreciation for your presence and your steadfast commitment to advancing knowledge in our field. This conference serves as a testament to our collective dedication to pushing the boundaries of discovery—from classical anatomical research into innovative, emerging frontiers.

Throughout this event, we invite you to explore anatomy through a holistic lens, bridging tradition with innovation to gain a deeper understanding of the human body. We are proud to host a diverse community of scholars, researchers, and professionals united by a shared pursuit of excellence and the development of meaningful global partnerships.

In closing, I would like to extend my heartfelt gratitude to the organizing committee, our partners, and everyone whose hard work has made this event possible.

I wish you all a productive, inspiring, and memorable conference.

Message from the President of the Anatomy Association of Thailand

Sutisa Thanoi, Ph.D.
Professor

On behalf of the Anatomy Association of Thailand (AAT), it is my great honour and pleasure to warmly welcome all distinguished guests, esteemed speakers, and participants to the 48th International Conference of the AAT (AAT48). This year's conference is proudly co-hosted in collaboration with the Department of Anatomy, Faculty of Medicine, Srinakharinwirot University. I would like to express my sincere gratitude to our partner institution for its invaluable contributions in making this event possible.

Under the theme of "360°: Revolving Perspectives for Advancing Anatomy", the conference highlights recent advances and future directions in anatomical sciences, including gross and microscopic anatomy, clinical anatomy, neuroscience, cell and molecular biology, and anatomical education. Through plenary and special lectures, panel discussions, technical seminars, and oral and poster presentations, we aim to foster insightful discussion and promote knowledge exchange. We are confident that this distinguished gathering will inspire insightful discussions and facilitate the sharing of cutting-edge research in anatomy. Furthermore, we are also proud to present the Young Anatomical Researcher Awards and the Distinguished Anatomy Teaching Awards, which recognise excellence and contributions to the field.

As President of AAT, I would like to extend my deepest appreciation to distinguished speakers, dedicated participants, and delegates, whose presence is essential to the success of this conference. I would also like to express my sincere gratitude to all sponsors, both national and international, for their generous support. In addition, I warmly thank the organising committee for their tireless efforts and meticulous planning.

I am delighted to welcome you to Pattaya, Chonburi, one of Thailand's most beloved destinations. I hope you will have the opportunity to enjoy its unique charm and create memorable experiences during your stay.

Once again, thank you for being part of AAT48. May this conference be both intellectually rewarding and an enjoyable experience for all.

Message from the Chair of the Scientific Committee

Krai Meemon, Ph.D.
Associate Professor

Ladies and Gentlemen,

On behalf of the Scientific Committee of the 48th International Conference of the Anatomy Association of Thailand (AAT48), it is my great honor and pleasure to warmly welcome all participants to this year's conference. The AAT48 conference is held from May 13-15, 2026, in Chonburi Province, Thailand, under the theme "Anatomy 360°". This year's meeting offers a dynamic and comprehensive scientific program, featuring 9 distinguished invited speakers, 3 expert panelists in a panel discussion, and a total of 72 research presentations comprising 22 oral and 50 poster presentations. Together, these contributions highlight the breadth and vitality of current research in anatomical sciences.

The scientific program spans a wide spectrum of topics, including gross and clinical anatomy, histology and cell biology, neuroscience, developmental biology, and advances in anatomical education. We are delighted to provide a platform that fosters meaningful knowledge exchange, encourages interdisciplinary collaboration, and strengthens professional connections within our community.

In addition to the scientific sessions, participants will have the opportunity to visit exhibitions from leading companies, showcasing the latest technologies and innovations in anatomical and biomedical sciences.

As Chair of the Scientific Committee, I would like to express my sincere appreciation to all invited speakers, panelists, presenters, delegates, and supporting staff. Your valuable contributions are essential to the success of this conference and to the continued advancement of our field.

I hope that you will find the conference both enriching and inspiring, and that your stay in Chonburi, one of Thailand's most vibrant and welcoming destinations, will be both enjoyable and memorable.

Thank you for being part of AAT48.

Message from the Chair of the Organizing Committee

Sirinun Pongmayteegul, Ph.D.
Assistant Professor

Dear Colleagues and Participants,

On behalf of the organizing committee, it is my great pleasure to welcome you to the 48th Annual Conference of the Anatomy Association of Thailand (AAT48). This year, we are proud to host this gathering under the theme "Anatomy 360°."

The idea behind "Anatomy 360°" is simple: it is about looking at our field from every perspective. We want to honor our traditional foundations while embracing the new technologies and teaching methods that are shaping our future. This conference is a space for all of us to bridge that gap—sharing our knowledge and exploring what comes next together.

Our program covers a wide range of topics, from fundamental research to modern clinical applications. Beyond the academic sessions, I hope this event serves as a warm, friendly platform for us to reconnect, exchange ideas, and launch new collaborations that will benefit our students and the entire anatomy family.

I would like to express my sincere thanks to the organizing committee and the staff at the Department of Anatomy, Srinakharinwirot University, for their hard work. I also extend my deepest gratitude to our sponsors and all attendees for your support in making this conference a success.

I hope you find the sessions valuable and truly enjoy your time with us at AAT48.

Organizing Committee

Chair
Sirinun Pongmayteegul

Co-Chair
Wisuit Pradidarcheep

Commitee
Amornpun Sereemaspun
Cheng Nilbu-nga
Chittapon Jantararussamee
Chitraporn Kuanpradit
Gun Anantasomboon
Janyaruk Suriyut
Jirawat Saetan
Kanta Pranweerapaiboon
Krai Meemon
Manussabhorn Phatsara
Nopporn Jongkamonwiwat
Pattanapong Boonprom
Paweena Kaewman
Pariwat Wisetwongsa
Phetcharat Phanthong
Pongsak Khanpetch
Ratchadaporn Pramong
Raksawan Poonkhum
Ruttachuk Rungsiwiwut
Sani Baimai
Somjai Apisawetakan
Sutisa Thanoi
Thewarid Berkban
Worawit Suphamungmee
Yutthapong Tongpob

Scientific Committee

Chair
Krai Meemon

Co-Chair
Somjai Apisawetakan

International Scientific Committee
Gavin P. Reynolds (UK)
George W Yip (Singapore)
Keiichi Akita (Japan)
Michael Aschner (USA)
S. Eleonore Köhler (The Netherlands)
Tracey Wilkinson (UK)
Vincent Van Waes (France)
Wout H. Lamers (The Netherlands)

Local Scientific Committee
Amarin Narkwichean
Atthaboon Watthammawut
Chitraporn Kuanpradit
Jirawat Saetan
Luca Lo Piccolo
Pariwat Wisetwongsa
Phetcharat Phanthong
Ruttachuk Rungsiwiwut
Sani Baimai
Sutisa Thanoi
Thewarid Berkban
Wisuit Pradidarcheep

CONTENTS

ORAL PRESENTATION

POSTER PRESENTATION

PLENARY LECTURE

Plenary Lecture – I

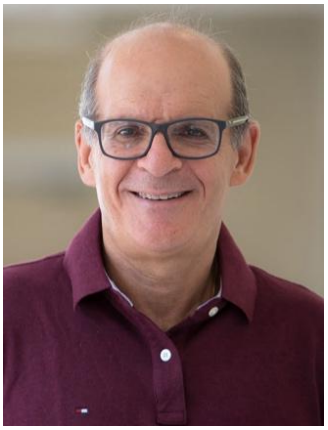

Professor Dr. Michael Aschner
Department of Molecular Pharmacology, Albert Einstein College of Medicine, Bronx, NY, USA
e-mail: michael.aschner@einsteinmed.edu

Modeling Metal Neurotoxicity Across Species: Insights from *Caenorhabditis elegans*

Exposure to neurotoxic metals remains a major environmental and occupational health concern, with strong links to neurodevelopmental and neurodegenerative disorders. A central challenge in the field is identifying conserved cellular and molecular mechanisms that underlie metal-induced nervous system dysfunction across species. Work from our laboratory has leveraged *Caenorhabditis elegans* as a genetically tractable and anatomically defined model to dissect fundamental pathways of metal neurotoxicity, with a particular focus on manganese, mercury, and other redox-active metals.

Using *C. elegans*, we have shown that metal exposure disrupts dopaminergic and glutamatergic signaling, induces oxidative stress, and alters mitochondrial and proteostatic homeostasis, pathways that are highly conserved in mammalian systems. Importantly, our studies highlight a pivotal role for glial cells in regulating metal uptake, sequestration, and neuronal vulnerability. Genetic manipulation of metal transporters, antioxidant defenses, and stress-response pathways in the worm has enabled the identification of modifiers that predict metal sensitivity in higher organisms.

Collectively, these findings demonstrate that *C. elegans* provides a powerful cross-species platform for linking environmental metal exposure to neuroanatomical and cellular outcomes relevant to human disease. By integrating insights from a simple nervous system with mammalian and human data, this work advances our understanding of conserved mechanisms of metal-induced neurotoxicity and supports the use of *C. elegans* for mechanistic discovery and translational risk assessment.

Dr. Aschner serves as the Harold and Muriel Block Chair in Molecular Pharmacology at Albert Einstein College of Medicine. He served on numerous toxicology panels (Institute of Medicine, US Environmental Protection Agency, Center for Disease Control, FDA, National Academy of Sciences, US Department of Defense) and was a member and chair of the Neurotoxicology and Alcohol study section (NIH). He served as President of the Society of Toxicology, President of the Academy of Toxicological Sciences, and President of the International Neurotoxicology Association. He is a recipient of an Honorary Doctorate from the University of Cordoba in Argentina. Research in his lab is designed to (1) shed novel mechanistic insight into metal-induced neurodegeneration; (2) identify targets for genetic or pharmacologic modulation of neurodegenerative disorders; (3) increase knowledge of the pathway involved in oxidative stress; (4) develop improved research models for human disease using knowledge of environmental sciences.

Plenary Lecture - II

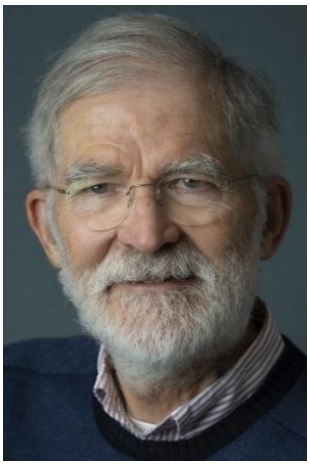

Professor Dr. Wouter H. Lamers
Department of Anatomy & Embryology, Maastricht University, Maastricht, The Netherlands
e-mail: wouterhlamers@gmail.com

The Developmental Appearance of Skeletal Muscles in the Human Arm and Back: A Developmental Analysis

LC Sprik[1], P Zhang[1], TJM Verlinden1, M Kressel[2], JPJM Hikspoors[1], GMC Mommen[1], G Moroşan-Puopolo[3], SE Köhler[1], Y Wu[4], WH Lamers[1*]
[1] Dept of Anatomy & Embryology, Maastricht University, Maastricht, The Netherlands
[2] Institute of Anatomy I, University of Erlangen-Nuremberg, Erlangen, Germany
[3] Dept of Anatomy and Molecular Embryology, Ruhr University Bochum, Bochum, Germany
[4] Dept of Digital Medicine, Biomedical Engineering College, Army Medical University, Chongqing, China

A comprehensive timeline of the morphogenesis and topography of human limb and back muscles is presently not available. In week 4.5-5.5 of development, myoblasts originating in somites C5-T1 migrate into the forelimb and start primary myogenesis. The ingrowth of a terminal nerve branch distinguishes the pre-muscle from other cell masses. We first observed the primary dorsal and ventral pre-muscle masses. From these, four secondary dorsal and two secondary ventral pre-muscle masses emerge. Each pre-muscle mass differentiates into a functionally related set of muscles (e.g., flexors or abductors). At ~6 weeks, the first individual muscles in the shoulder region appear. In the arm, individual muscles become distinguishable in the 8th week. Muscle splitting proceeds in a proximo-to-distal and superficial-to-deep sequence, but secondary myogenesis started simultaneously at 8 weeks in all muscle masses. Resolving the sequence and topographical location of the splitting events allowed the construction of a dendrogram of the lineages of the muscle masses of the arm. Too few or too many splitting events can account for the observed variations in limb muscle development. Apparently, most adult variations originate in the 8th week of development.

Undisputed features of the intrinsic back muscles are their epaxial origin and innervation by the dorsal rami of the spinal nerves. Our earlier reconstructions (Mekonen et al., 2016) had revealed that the intrinsic back muscles also develop by serial splitting. Two serial splits result in the development of three longitudinal muscle columns. Development is most advanced cranially and laterally. We now report that the lateral and intermediate columns each split once more, whereas the medial column is subject to two additional rounds of splitting. We could localize all intrinsic back muscles except the spinalis in 8-week-old embryos. The course of the proximal part of the dorsal root of the spinal nerve lies between the medial and intermediate columns. Next, we linked these developmental features to adult anatomy, using the “sectional anatomic” approach of the American and Chinese Visible Human series. The columns, as identified in the embryo, persist in the adult. Muscles of the medial and intermediate column follow, in addition to an interspinal or intertransverse course, a transversospinal course. If identifiable, the spinalis

muscle usually presents as a caudal extension of the semispinalis muscle. We will present a dendrogram of the adult intrinsic back muscles that is based on their development.

Primary myotubes extend from end to end of the muscle from the earliest times and attach directly to the tendon. In contrast, newly formed secondary myotubes are short cells that insert solely into the primary myotubes by a series of complex interdigitating folds along which adhering junctions occur.

Wouter H. Lamers obtained his MD degree from the University of Amsterdam in 1974 and his PhD degree from the same university in 1980 on a dissertation titled "Multihormonal control of enzyme clusters in liver ontogenesis". In 1981-1982, he was a visiting assistant professor at the Department of Biochemistry of Case Western Reserve University in Cleveland, OH. He returned to Amsterdam to study structure-function relations in developing and adult liver, with a focus on the regulation of zonation of gene expression in this organ. Ammonia-detoxifying enzymes served as a paradigm. He also took up human cardiac embryology as his scientific hobby. WHL's Hirsch index is 90. Since 1991, WHL has been a professor of Anatomy and Embryology in the Academic Medical Center of the University of Amsterdam and, since 2001, also a professor of Developmental Biology at Maastricht University. WHL was director/vice chairman of the Center for Liver and Gastrointestinal Research, director of the graduate school Metabolism and Nutrition, chairman of the Dutch Society of Anatomists, and served on several Dutch science committees. After retiring, WHL began to compose a pictorial atlas of human development, with an emphasis on three-dimensional modeling and corresponding accounts of the highlights observed in these models. Thus far, this project has produced 40 publications in peer-reviewed journals.

Plenary Lecture - III

Professor Dr. Keiichi Akita
Department of Clinical Anatomy, Graduate School of Medical and Dental Sciences, Institute of Science Tokyo
1-5-45 Yushima, Bunkyo-ku, Tokyo, Japan
e-mail: akita.fana@tmd.ac.jp

Morphological Continuity of Smooth and Skeletal Muscles from the Pelvic Floor to the Anal Canal: Revealing Unresolved Questions in Clinical Anatomy

A precise understanding of the muscular organization of the pelvic floor and anal canal is important for clarifying their anatomical relationships. We investigated the three-dimensional architecture of pelvic floor skeletal muscles and the histological organization of associated smooth muscle structures by combining macroscopic dissection, histology, and immunohistochemistry.

A major morphological feature of the pelvic floor is the continuity and bundle sharing among skeletal muscles. The levator ani and external anal sphincter (EAS) are not clearly separated but are continuous, and fine connecting bundles link the levator ani, EAS, bulbospongiosus, ischiocavernosus, superficial transverse perineal muscle, and external urethral sphincter. In parallel, smooth muscle components form a continuous morphological system. In males, smooth muscle structures extend from the rectal longitudinal muscle toward the central pelvic floor and the rectourethral region, with hypertrophic smooth muscle tissue contacting the levator ani anterolaterally. In females, smooth muscle fibers derived from the internal anal sphincter (IAS) and longitudinal muscle extend anteriorly into the vaginal vestibule and perineum and spread over the anterior surface of the EAS and levator ani.

Within the anal canal, in addition to the canonical layers of the IAS, longitudinal muscle, and EAS, an additional smooth muscle layer was identified on the luminal side of the IAS, corresponding to Treitz's muscle (M. submucosae ani). This structure appears to be formed by a localized directional change of the superficial-most IAS bundles, most frequently on the anterolateral wall, and is not uniformly distributed. Near the lower end of the anal canal, the longitudinal muscle becomes attenuated and disperses into the EAS, creating a distinct gap between the IAS and EAS. The spatial relationship between these layered muscular arrangements and the distribution of anal glands in the lower anal canal was also examined.

These findings indicate that the pelvic floor and anal canal constitute a continuous, layered sphincteric muscle complex, characterized by close structural continuity between skeletal and smooth muscle elements. Such continuity may provide an anatomical basis for coordinated anorectal function.

Dr. Keiichi Akita is Dean of the Faculty of Medicine at the Institute of Science Tokyo (Science Tokyo), where he also serves as Professor and Chair of the Department of Clinical Anatomy. He graduated from Sapporo Medical University in 1987 and received his PhD in Anatomy from Tokyo Medical and Dental University in 1991. Since joining Tokyo Medical and Dental University in 1991, he has held a series of academic and leadership positions in anatomy. His academic and professional career has been centered on clinical anatomy and medical education.

SPECIAL LECTURE

Special Lecture – I

Professor Dr. Gavin P Reynolds
Biomedical Sciences Research Centre,
Sheffield Hallam University, Sheffield, UK
e-mail: gavin.reynolds@shu.ac.uk

Uric Acid – Bad for the Body, Good for the Brain

Uric acid is well known as the cause of gout – a form of inflammatory arthritis due to deposits of sodium urate crystals in joints. It is also increasingly recognised as a risk factor in cardiovascular disease, in which it contributes to atherosclerotic plaques and vascular inflammation, and metabolic syndrome, as well as being an indicator of kidney disease. Uric acid is, for humans and some primates, the end product of purine metabolism, while for most animals it is metabolised further into the less toxic allantoin. What might be the evolutionary advantage of the higher concentrations of this toxic metabolite in humans? The answer remains unclear, but it may relate to its antioxidant action. The crystalline deposits of the sodium salt of uric acid are clearly toxic and pro-inflammatory, but the soluble form accounts for much of the circulating antioxidant capacity of the body, as well as having ion-chelating effects. These potentially protective properties of uric acid are particularly implicated in neurodegenerative diseases but may also be involved in psychiatric disorders.

The neuroprotective effects of uric acid have been most studied in relation to Parkinson's disease (Liu H, Reynolds GP. NPJ Parkinsons Dis. 2025;11:325). Originating in a deficit in uric acid observed in the substantia nigra in the PD brain, multiple studies have identified reductions in blood concentrations in PD patients. We observed that hospital admissions for PD were associated with an approximately 20% reduction in serum uric acid, compared to both vascular dementia and a healthy control group (Liu H et al. J Neural Transm. 2020;127:779-783).

Further studies have been undertaken in Alzheimer's disease (AD), another neurodegenerative disorder. Here too, there is evidence for deficits in uric acid; we found hospital admissions for AD were associated with similar reductions of approximately 20% vs vascular dementia (Liu H et al. J Alzheimers Dis. 2023;92:1283-1287). Interestingly, differentiating AD and PD was the influence of agricultural work, which was over-represented in PD but not AD by approximately 66%. This effect may reflect exposure to neurotoxic pesticides that target the dopaminergic neurons lost in PD.

More recently, evidence has accumulated pointing to uric acid having a role in psychiatric disorders such as depression. Here, the findings are not always consistent, with negative reports as well as observations of uric acid deficits in depression. We have undertaken a small study of adolescents hospitalized for depression and anxiety symptoms. Those showing a rapid recovery of symptoms appeared to have higher serum concentrations of uric acid than those who remained symptomatic.

What might be the underlying mechanisms relating low circulating uric acid to both neurodegenerative disease and recovery of depressive symptoms? Notably, both oxidative stress and neuroinflammation have been implicated in neurodegenerative disease and psychiatric disorders such as depression. Uric acid may have effects on both these processes, which are themselves closely linked–oxidative stress can be both a consequence of, and

a contributor to, inflammation. Thus, there is strong evidence for a neuroprotective action of uric acid in the human brain, for which its role in increasing the risk of peripheral disease is the price we pay.

Gavin Reynolds is Honorary Professor in the Biomolecular Sciences Research Centre at Sheffield Hallam University and Professor Emeritus, previously Chair of Neuroscience, at Queen's University Belfast. His main research interests are in the neurotransmitter pathology of schizophrenia, with a focus on the epigenetic effects of environmental risk factors and the relationship between psychiatric and physical illness, and the mechanisms underlying the effects of antipsychotics and other psychiatric drugs. Additional interests include neurodegenerative disease mechanisms and the biological effects of substance abuse. He has approximately 400 research publications, including papers in Nature and The Lancet, with an h-index of 87 and >28000 citations (Google Scholar).

Special Lecture – II

Professor Dr. Vincent Van Waes
Marie and Louis Pasteur University
INSERM, UMR 1322 LINC, Besançon, France
e-mail: vincent.van_waes@univ-fcomte.fr

Transcranial Direct Current Stimulation (tDCS) to Treat Psychiatric Disorders: Insights from Preclinical Studies

Non-invasive brain stimulation is opening new perspectives for the treatment of neuropsychiatric disorders, yet the neural mechanisms underlying its therapeutic effects remain poorly understood. Among these approaches, transcranial direct current stimulation (tDCS) has attracted attention for its capacity to modulate cortical excitability and influence large-scale brain networks involved in cognition and emotion. Understanding how tDCS alters brain function requires mechanistic investigations that cannot be fully achieved in humans alone. In this talk, I will present a series of preclinical studies conducted at the LINC (Laboratory for Integrative Research in Neuroscience and Cognitive Psychology, INSERM, Besançon, France) using rodent models to investigate the behavioral and neural consequences of repeated tDCS. These studies explore how stimulation modulates neural activation patterns and corticostriatal circuits associated with cognitive and affective processes relevant to neuropsychiatric disorders. I will also discuss the methodological challenges and translational limitations of current animal models of tDCS, and propose future directions aimed at strengthening the bridge between preclinical neuroscience and clinical applications. Together, these findings highlight the essential role of experimental models in advancing the mechanistic understanding and therapeutic development of non-invasive brain stimulation.

Vincent Van Waes is Professor of Neuroscience at Marie and Louis Pasteur University (France) and Director of the Integrative Research Laboratory in Neuroscience and Cognitive Psychology (LINC, INSERM UMR 1322). He obtained a Master's degree in Cognitive Science and a Ph.D. in Neuroscience from the University of Lille, with a European doctoral label in collaboration with Sapienza University of Rome (Italy). He completed postdoctoral training at the Chicago Medical School (North Chicago, USA) before joining Marie and Louis Pasteur University in 2010. Promoted to Full Professor in 2017, he served as Co-Director of LINC from 2018 to 2025 and has been Director of the unit since 2025.

Special Lecture – III

Dr. Amarin Narkwichean
Deputy Dean for Administration and Human Resources
Faculty of Medicine, Srinakharinwirot University
Honorary Associate Professor
School of Life Sciences, University of Nottingham
e-mail: amarin@g.swu.ac.th

Creating Life in the Lab: Clinical Embryology in the Era of Individualised Medicine

Assisted reproductive technology (ART), particularly in vitro fertilisation (IVF), has transformed the clinical landscape of human reproduction, translating fundamental embryological principles into real-world therapeutic interventions. Traditionally, embryology has been taught within a deterministic and generalised framework; however, contemporary IVF practice reveals a far more complex and dynamic reality, where each embryo, gamete, and patient represents a unique biological system requiring individualised management.

This presentation explores the evolving concept of clinical embryology within the IVF laboratory, emphasising the transition from standardised protocols to precision reproductive medicine. Key stages of the IVF process—including gamete handling, fertilisation techniques (e.g., intra-cytoplasmic sperm injection), embryo culture, and selection—will be discussed from both anatomical and clinical perspectives. Particular attention will be given to how emerging technologies have reshaped embryological practice beyond textbook paradigms.

Recent advances in artificial intelligence (AI), time-lapse imaging, and predictive analytics have enabled a more objective and data-driven approach to embryo assessment and treatment planning. AI-assisted models can integrate patient-specific variables, including ovarian reserve, hormonal profiles, and etiological factors, to optimise ovarian stimulation protocols and predict reproductive outcomes [1]. Furthermore, machine learning tools are increasingly used in embryo selection, where morphokinetic and morphological data are analysed to improve implantation prediction and reduce inter-observer variability [2]. These innovations signal a paradigm shift toward individualised IVF strategies, where treatment is tailored not only to the embryo but also to the patient's unique biological context.

Beyond embryo selection, personalisation extends to critical aspects such as endometrial receptivity and timing of embryo transfer. Emerging molecular and AI-driven approaches enable highly precise identification of the window of implantation, significantly improving clinical pregnancy rates in selected patient populations [3]. Collectively, these developments highlight the movement from probability-based treatment toward predictive and personalised reproductive care.

However, the integration of advanced technologies into embryology raises important ethical and societal considerations. The increasing capability to select embryos based on genetic and developmental potential challenges traditional concepts of human development, reproductive autonomy, and equity of access. Anatomists and medical educators play a crucial role in bridging foundational science with these evolving clinical and ethical dimensions.

In conclusion, clinical embryology is undergoing a transformative shift—from observational science to an actively engineered and individualised discipline. IVF laboratories are no longer merely sites of observation but are becoming hubs of precision medicine, where embryology, technology, and ethics converge to shape the future

of human reproduction. This presentation aims to provide anatomists with a contemporary perspective on embryology, highlighting its expanding role in modern medicine and its implications for education, research, and clinical practice.

References

1. Wen L, Wu D, Ruan J, Wang R, Long R, Chen R, et al. Artificial intelligence-driven precision treatment of reproductive medicine-related diseases: the optimal protocol choice for IVF-ET. Journal of Advanced Research. 2025.
2. Olawade DB, Teke J, Adeleye KK, Weerasinghe K, Maidoki M, Clement David-Olawade A. Artificial intelligence in in-vitro fertilization (IVF): A new era of precision and personalization in fertility treatments. Journal of Gynecology Obstetrics and Human Reproduction. 2025;54(3): 102903.
3. Xu Y, Du J, Zou Y, Lin X, Chen Y, Ma L, et al. Precise hourly personalized embryo transfer significantly improves clinical outcomes in patients with repeated implantation failure. Frontiers in Endocrinology. 2024; Volume 15 - 2024.

Amarin Narkwichean, MD, PhD, SFHEA, is a Clinical Lecturer, Consultant in Reproductive Medicine, and Clinical Embryologist at the Faculty of Medicine, Srinakharinwirot University, Thailand. He currently serves as Deputy Dean for Administration and Human Resources and holds an Honorary Associate Professorship at the University of Nottingham, UK. He earned his MD (First Class Honours) from Chulalongkorn University and completed specialty training in Obstetrics and Gynaecology, followed by a Master's degree and PhD in Human Development from the University of Nottingham. His clinical and research expertise focuses on assisted reproductive technology, ovarian aging, embryo implantation, and clinical embryology, alongside translational research in emerging fields such as extracellular vesicles. He is actively involved in international medical education through curriculum development, program leadership, and joint medical programs, with additional interests in patient safety, professionalism, and student well-being.

Special Lecture – IV

Dr. Luca Lo Piccolo
Center of Multidisciplinary Technology for Advanced Medicine,
Faculty of Medicine, Chiang Mai University, Thailand
e-mail: lopiccolo.l@cmu.ac.th

YEATS2-Dependent Regulation of Neuronal Metabolism Underlies Dopaminergic Neuron Vulnerability

Over the past several years, our work has focused on defining how YEATS family proteins shape neuronal physiology through metabolic regulation. In this talk, I will summarize our findings identifying YEATS2 as a key regulator of neuronal metabolic homeostasis required for dopaminergic neuron resilience. Using neuron-specific loss of YEATS2 in Drosophila, we show that disruption of YEATS2-dependent gene programs leads to metabolic imbalance, altered GPCR signaling, and pathological elevation of intracellular calcium. These defects preferentially compromise dopaminergic neurons, resulting in their functional impairment and degeneration, while other neuronal populations are largely spared. As dopaminergic neurons are lost, brain dopamine levels decline, destabilizing neural circuit activity and giving rise to seizure-like behavior, stress hypersensitivity, and locomotor dysfunction. Restoration of dopaminergic signaling with L-DOPA suppresses seizure-like activity, indicating that dopamine loss acts as a downstream mediator of circuit hyperexcitability rather than the primary lesion. Consistent with this model, direct correction of calcium imbalance through genetic or pharmacological modulation of ER calcium handling preserves dopaminergic neurons and rescues behavioral phenotypes. Together, these findings define a YEATS2-dependent metabolic pathway that links neuronal metabolic stress to selective dopaminergic vulnerability, with potential implications for understanding mechanisms of neuronal resilience in neurodegenerative disorders such as Parkinson's disease.

Keywords *Calcium homeostasis, Dopaminergic neuron vulnerability, Neuronal metabolism, Neuronal resilience, YEATS2*

Dr. Luca Lo Piccolo is a researcher at the Center of Multidisciplinary Technology for Advanced Medicine (CMUTEAM), Faculty of Medicine, Chiang Mai University, where he leads the Functional Genomics Unit (FGU). His work focuses on understanding how epigenetic regulation intersects with neuronal metabolism to shape brain function in both health and disease. By integrating functional genetics, epigenetics, and RNA biology, his research seeks to uncover the molecular mechanisms underlying neurodevelopmental and neurodegenerative disorders, with particular emphasis on motor neuron diseases and epilepsy. Using Drosophila and complementary cellular models, his laboratory investigates chromatin regulators, including YEATS domain–containing proteins, repeat expansion–associated toxicity, and stress pathways such as endoplasmic reticulum stress. Moreover, through scalable in vivo platforms combined with computational approaches, his group aims to identify and validate novel therapeutic strategies for neurological disorders.

Special Lecture – V

Professor Dr. S Eleonore Köhler
Maastricht University, FHML, The Netherlands
Anatomy & Embryology, UNS 50, 6229ER
e-mail: leo.koehler@maastrichtuniversity.nl

Human Gut Development: How to Teach a Complex Embryological Process

Human gut development is characterized by a so-called "physiological hernia" of part of the intestines into the umbilical cord during week 6 of development. At week 10, this hernia is resolved in all normally developing fetuses. The establishment of the adult configuration of the gut has been described in a 270-degree rotation model, which is mostly based on malformations and reverse engineering of normal development. Computer-based reconstructions of historical histological sections of human embryos and fetuses question the rotation model and instead explain the processes as a combination of differential growth and a slide-and-stack-type return of intestinal loops into the abdominal cavity.

For teachers, it is challenging to explain these complex processes, and they must decide where to simplify without losing the gist of the message. Nowadays, we are helped by interactive 3D models, but while these can be very instructive when used correctly (i.e., spending sufficient time on them to understand), they may still overwhelm students. Discussing models between teachers and researchers can result in creative solutions to teach complex processes and concepts that foster student engagement. One possible solution to explain gut herniation and return to the abdominal cavity will be presented.

S. Eleonore Köhler, PhD, is a biologist and Professor of Clinical Anatomy with extensive experience in anatomy, embryology, and health professions education. She earned her Biology degree from Göttingen, Germany (1986) and completed her PhD at the University of Basel, Switzerland (1990), focusing on site-directed mutagenesis of aspartate aminotransferase. After postdoctoral and senior research positions in Germany and Switzerland, she joined Maastricht University in 2002, where she has served as Head of the Department of Anatomy and Embryology since 2007 and was appointed Full Professor in 2017 within the School of Health Professions Education (SHE). Her research interests include human developmental anatomy, amino acid metabolism in inflammatory diseases, and self-determination in learning, alongside significant contributions to teaching, program management, and curriculum development in biomedical and health sciences education.

Special Lecture – VI

Associate Professor Dr. George W Yip
Department of Anatomy, Yong Loo Lin School of Medicine,
National University of Singapore,
4 Medical Drive, Block MD 10, Singapore 117594
e-mail: georgeyip@nus.edu.sg

Evolution of Anatomy Teaching in Medical Education

The study of anatomy is of fundamental importance in medical education. A good knowledge of human anatomy provides a strong foundation for clinical practice. The teaching of anatomy has evolved to meet the needs of the modern curriculum, which focuses on clinical relevance as well as horizontal and vertical integration. With advances in technology, medical students of today have access to a wide range of educational resources that can aid them in their learning of human anatomy. These include electronic books, pre-recorded lectures and videos, 3D-printed anatomical models, virtual reality, and other digital tools, amongst others. In this presentation, I will share the transformation of anatomy teaching at the National University of Singapore in recent years. Additionally, I will demonstrate how our Silent Mentor Programme has provided the opportunity to not only impart knowledge of human anatomy but also to inculcate humane values such as respect, gratitude, kindness, altruism, and professionalism in our medical students.

Dr George Yip is an Associate Professor and currently heads the Department of Anatomy in the Yong Loo Lin School of Medicine, National University of Singapore. He has taught Gross Anatomy, Embryology, and Histology through lectures, tutorials, and practical classes for more than 25 years. He is currently involved in developing new teaching materials and digital tools for anatomy education, including e-textbooks and an anatomy chatbot. He is also a member of the Undergraduate Steering Committee, the Curriculum Enhancement Taskforce, and the Curriculum Implementation Taskforce in the medical school. Over the years, he has received awards for teaching excellence and outstanding mentorship.

PANEL DISCUSSION

Panel Discussion – I

From Anatomical Research to Clinical Application: Bridging the Gap between Structure and Practice

Associate Professor Dr. Niyom Laoopugsin
Faculty of Medicine, Western University, Thailand
e-mail: niyomacupuncture@gmail.com

Abstract
Background: Anatomy has long been regarded as the cornerstone of medical education. However, a significant gap remains between anatomical knowledge acquired during preclinical training and its application in clinical practice. Bridging this gap is essential for improving diagnostic accuracy, procedural safety, and patient outcomes. **Objective:** To explore how anatomical research can be effectively translated into clinical practice and to highlight strategies for integrating anatomical knowledge into patient care and medical education. **Methods:** This presentation reviews current trends in anatomical research, including cadaveric studies, imaging-based anatomy, and emerging digital technologies such as three-dimensional visualization and artificial intelligence. Clinical case examples are used to demonstrate the application of anatomical principles in various specialties, including surgery, radiology, and orthopaedics. **Results:** Translational approaches in anatomy enhance clinical reasoning by linking structural knowledge with pathophysiology and clinical presentation. The integration of anatomy into clinical training through case-based and simulation-based learning improves learner engagement and competency. Additionally, anatomical research contributes to innovations in surgical techniques and diagnostic procedures, ultimately improving patient safety and outcomes. **Conclusion:** Anatomy should be viewed not merely as a foundational science but as a dynamic and clinically relevant discipline. Strengthening the integration between anatomical research and clinical application is crucial for advancing medical education and healthcare delivery in the modern era.

Keywords *Anatomy, Clinical application, Translational medicine, Medical education, Patient safety*

Panel Discussion – II

MD-KKU Skeletal Collection: A Documented Northeastern Thai Reference for Clinical Application and Anthropological Research

Professor Dr. Sitthichai Iamsaard
Department of Anatomy, Unit of Human Bone Warehouse for Research, Faculty of Medicine, Khon Kaen University, Khon Kaen 40002, Thailand
e-mail: sittia@kku.ac.th

Abstract

The MD KKU skeletal repository (known as UHBWR: unit of human bone warehouse for research, housed on the 7th floor, department of anatomy, faculty of medicine, Khon Kaen University), represents a documented reference collection of human skeletons from Northeastern Thailand donors, confirmed by official ID cards, governmental death certificates, and hospital records for precise biological profiles, including chronological age at death. UHBWR expanding resource now comprises 2018 complete skeletons (1371 males, 647 females), with an average age of 65.57 ± 13.91 years (range: 15-106 years)—males at 66.13 ± 13.59 years (18-103 years) and females at 64.41 ± 14.50 years (15-106 years). The average stature is 161.80 ± 8.16 cm (range: 140–190 cm), with males at 165.24 ± 6.95 cm (147–190 cm) and females at 155.76 ± 6.46 cm (140–180 cm). This provides unparalleled data on regional skeletal variation, pathology, trauma, and osteological markers

Building on its foundational role through the body donation program, the UHBWR has supported groundbreaking research in clinical research, forensic anthropology, and osteology, including age, sex, and stature estimation standards tailored to Southeast Asians, skeletal morphology, and pathology. This work has yielded numerous publications, conference presentations, and method validations that highlight population-specific differences from global standards. As the largest collection in Northeastern Thailand, the focused archive addresses the critical gaps in regionally representative samples for bioarchaeology, clinical research, forensic applications, and comparative studies across other ancestries.

We warmly invite national and international collaborators to leverage this unique, accessible resource for innovative projects on human skeletal biology. Access requests and partnerships are facilitated via our website: https://www.anatomymdkku.com/executive-committee-of-unit-of-huma. Join us in advancing global skeletal research, forensic sciences, and clinical applications through UHBWR.

Keywords *UHBWR, Documented skeletal collection, Forensic anthropology, Osteological analysis, Clinical applications*

Panel Discussion – III

Statistical Approaches in Forensic Anthropology Research: Principles, Applications, and Practical Considerations

Assistant Professor Suthat Duangchit
Department of Physiology, Faculty of Medical Science, Naresuan University, Phitsanulok, 65000, Thailand
e-mail: suthatd@nu.ac.th

Abstract

The construction of a biological profile from skeletal remains is a fundamental objective in forensic anthropology, and methodological validity depends upon the appropriate application of statistical procedures at each analytical stage. Before proceeding to inferential analysis, measurement reliability must be quantified using the Technical Error of Measurement (TEM), relative TEM (rTEM), Intraclass Correlation Coefficient (ICC), and Cohen's Kappa (κ), which collectively assess intra- and inter-observer consistency across continuous and categorical data. Osteometric variables are subsequently characterised through descriptive statistics, comprising means, standard deviations, and 95% confidence intervals, stratified by sex and age cohort. Intergroup differences are evaluated using independent samples t-tests for sexual dimorphism, paired t-tests for bilateral asymmetry, and one-way ANOVA with post-hoc correction for multi-group comparisons, with effect size indices reported to convey practical significance. For age estimation, cluster analysis is applied to classify individuals into empirically defined age groups based on skeletal indicators, after which intergroup differences are examined using appropriate comparative tests. Sex estimation is performed using Discriminant Function Analysis (DFA) and Binary Logistic Regression (BLR), both yielding classification equations for applied casework, with diagnostic performance reported as accuracy, sensitivity, specificity, and area under the receiver operating characteristic curve (AUC). Stature estimation utilises linear regression, with model adequacy assessed by the coefficient of determination (R^2) and Standard Error of Estimate (SEE). Emerging machine learning algorithms, including Random Forest, Support Vector Machine, and Artificial Neural Networks, extend analytical capacity for high-dimensional pattern recognition. Regardless of approach, method selection must be guided by data structure, sample size, and population specificity, with full disclosure of underlying assumptions and limitations.

Keywords *Forensic anthropology, Biological profile, Age estimation, Sex estimation, Stature estimation*

ORAL PRESENTATION

O-01

From Dental Waste to Neural Identity: Revealing the Intrinsic Transcriptomic Priming Underlying Neuronal Differentiation of Human Stem Cells from Apical Papilla

Anupong Thongklam Songsaad[1*], Surachet Benjathummarak[2], Tarinee Chodchavanchai[3], Tatcha Balit[4], Amarin Thongsuk[3], Nisarat Ruangsawasdi[5], Charoensri Thonabulsombat[3]
[1] Department of Anatomy, Faculty of Dentistry, Mahidol University, Bangkok, Thailand
[2] Center of Excellence for Antibody Research, Faculty of Tropical Medicine, Mahidol University, Bangkok, Thailand
[3] Department of Anatomy, Faculty of Science, Mahidol University, Bangkok, Thailand
[4] School of Medicine, Walailak University, Nakhon Si Thammarat, Thailand
[5] Department of Pharmacology, Faculty of Dentistry, Mahidol University, Bangkok, Thailand
*Corresponding author, e-mail: Anupong.son@mahidol.ac.th

Abstract

Human stem cells from apical papilla (hSCAPs) are isolated from the apical papilla of impacted third molars, typically discarded during routine tooth extraction. These stem cells are derived from an ectomesenchymal origin and are physiologically associated with odontogenic differentiation during tooth development. Interestingly, previous studies demonstrated that hSCAPs can acquire neuronal-like phenotypes under defined experimental conditions. However, whether this plasticity represents forced lineage conversion or instead reflects an intrinsic developmental predisposition remains unclear. Therefore, the present study hypothesized that neuronal differentiation of hSCAPs represents the unmasking of a pre-existing neural gene profile embedded within their developmental lineage, rather than an artificially induced fate transition. hSCAPs were subjected to neuronal induction using both 2D (monolayer culture) and 3D (neurosphere formation, followed by neurogenic maturation) procedures. Across neuronal differentiation paradigms, cells developed characteristic neuronal-like morphologies with elongated processes and prominent Nissl substance. Immunofluorescence analyses confirmed the expression of neuronal markers, while depolarization-evoked intracellular Ca^{2+} responses indicated coordinated neuronal-like physiological properties. To investigate the molecular basis of this differentiation capacity, whole-transcriptome sequencing was performed on undifferentiated hSCAPs. Baseline transcriptomic profiling revealed a dual developmental signature. In addition to odontogenic-associated regulators (*DSPP* and *DMP1*), consistent with their dental identity, hSCAPs exhibited an endogenous neural gene profile with enrichment of pathways related to axon guidance, synaptic organization, and cortical development. Transcriptional regulators involved in neuronal specification (*PRDM8* and *NFIB*) were constitutively expressed before neuronal induction, suggesting intrinsic neurodevelopmental potential. Synaptic modulators (*RGS4*), together with plasticity-associated regulators (*MALAT1* and *AHNAK*), further support the presence of a neural regulatory network. Persistent expression of neural stemness-associated genes (*NES* and *SOX2*) also indicates a latent neural priming state consistent with their ectomesenchymal origin. Together, these findings suggest that neuronal differentiation of hSCAPs reveals a developmentally encoded neural potential and highlight hSCAPs as promising cell sources for neural regeneration research.

Keywords *Human stem cells from apical papilla, Neural crest-derived stem cells, Neuronal differentiation, Neural priming, Transcriptome*

O-02

Sections of Brain Plastinated with P40: An Instructional Resource for Sectional Anatomy

Jessy JP[1*], Jayashri Pandey[2], Renu Dhingra[1]
[1] Department of Anatomy, All India Institute of Medical Sciences, New Delhi, India
[2] Department of Pediatrics, Sushila Tiwari Hospital, Haldwani, Uttarakhand, India
[3] Department of Anatomy, All India Institute of Medical Sciences, New Delhi, India
*Corresponding author, e-mail: jesjp07@gmail.com

Abstract
Background: Plastination preserves biological tissues while maintaining near-natural morphology and is widely used in anatomical teaching and research. Polyester resin, particularly P40, is well-suited for neural tissue because it enhances differentiation between gray and white matter. P40 sheet plastination produces thin, transparent sections that facilitate detailed anatomical visualization and radiological correlation. **Objective:** To standardize the P40 sheet plastination technique for brain slices and to compare its effectiveness with S10 plastination in terms of tissue preservation, shrinkage, and gray–white matter differentiation. **Methods:** Human brain slices were plastinated using the P40 sheet plastination technique under two impregnation conditions: room temperature and cold temperature (–25°C). The outcomes were evaluated based on (i) percentage tissue shrinkage, (ii) clarity of gray–white matter differentiation, (iii) visibility of vascular structures, and (iv) delineation of key anatomical landmarks. Gray–white differentiation and structural clarity were assessed using predefined qualitative criteria based on visual contrast and anatomical distinguishability. The results were compared with sections prepared using the S10 silicone plastination technique. Descriptive statistical analysis was performed to compare shrinkage between the two temperature conditions. **Results:** Room temperature impregnation resulted in faster processing but showed a higher mean percentage shrinkage compared to cold impregnation at –25°C. P40 plastinated sections demonstrated clearer visual contrast between gray and white matter based on qualitative assessment criteria, allowing improved identification of anatomical landmarks such as the anterior commissure, external capsule, and claustrum. Vascular structures were also more distinctly visualized. In comparison, S10/Silicon plastinated sections showed lower transparency and reduced gray–white contrast, limiting their effectiveness for detailed sectional anatomy. **Conclusion:** P40 sheet plastination provides thin, transparent brain sections with improved gray–white matter differentiation and anatomical clarity compared to S10 plastination. Cold temperature impregnation reduces tissue shrinkage and enhances specimen quality. These findings support the use of P40 plastinated brain slices as durable and effective teaching tools for sectional and radiological anatomy.

Keywords *Brain, Plastination, P40, S10, Gray–white matter differentiation, Sectional anatomy*

O-03

Efficacy of *Sida cordifolia* Root Extract against Pentylenetetrazole-Induced Kindling in Swiss Albino Mice: A Histomorphometric and Neurobehavioral Study

Naveen Kumar BD[1*], Tejaswi HL[1], Ravi M[2]
[1] Department of Anatomy, Adichunchanagiri Institute of Medical Sciences, Adichunchanagiri University, BG Nagara, Nagamangala, Mandya, Karnataka 574118
[2] Department of Pharmacology, Adichunchanagiri Institute of Medical Sciences, Adichunchanagiri University, BG Nagara, Nagamangala, Mandya, Karnataka 574118
*Corresponding author, e-mail: drnaveenanatomy@gmail.com

Abstract

Epilepsy is a chronic neurological disorder characterised by recurrent, unprovoked seizures arising from abnormal electrical activity in the brain and is often associated with oxidative stress and neuronal damage. *Sida cordifolia* L. has been traditionally used in the management of epilepsy and other neurological disorders; however, its antiepileptic potential lacks adequate scientific validation. Hence, the current study was undertaken to evaluate the therapeutic efficacy of a hydroalcoholic root extract of *Sida cardifolia* (HASC) in a Pentylenetetrazol (PTZ)-induced kindling model in Swiss albino mice, to assess its antiepileptic and neuroprotective effects. Kindling was induced by intraperitoneal administration of Pentylenetetrazole (40mg/kg) on alternative days for 11 days. Animals received group-specific treatments throughout the experimental period. Racine's scale score assessed seizure severity. Neuroprotective effects were evaluated through histopathological examination of the hippocampus (CA1 & CA3 regions). Antioxidant status was determined by measuring catalase, glutathione peroxidase, and lipid peroxidation levels. The data were statistically analysed using one-way ANOVA followed by Tukey's test as a post hoc test. p-value<0.05 was considered statistically significant. Repeated PTZ administration significantly increased seizure activities, reflected by elevated cumulative Racine's scale score ($p < 0.01$), and induced marked pyramidal neuronal necrosis in the hippocampus compared to the normal control group. Co-administration of HASC significantly reduced seizure score ($p < 0.05$) and preserved neuronal architecture in the CA1 and CA3 regions of the hippocampus. Furthermore, HASC restored antioxidant enzyme levels and significantly reduced lipid peroxidation ($p < 0.05$), indicating potent antioxidant activity. The selected dose, ranging from 200-400mg/kg of *Sida cardifolia* extract in the present experiment, corresponds to a human equivalent dose of approximately 65mg/kg (3.9g/day) based on surface area conversion. HASC demonstrated significant antiepileptic, antioxidant, and neuroprotective effects in the PTZ-induced kindling model. These findings suggest that *Sida cordifolia* root extract may be a promising adjunct or alternative therapeutic strategy for managing epilepsy.

Keywords *Antioxidant, Epilepsy, CA1, CA3, Hippocampus, Hydro alcoholic root extract of Sida cardifolia, Pentylenetetrazole, Kindling*

O-04

Investigating the Neuroprotective and Anxiolytic Effects of Cannabidiol (CBD) and Brahmi Combinations in A Chronic Unpredictable Mild Stress (CUMS) Model: A Behavioral and Proteomic Analysis

Plaiyfah Janthueng[1,7], Wanfrutkon Waehama[1,7], Sawanya Charoenlappanit[2], Sittiruk Roytrakul[2], Prapapan Temkitthawon[3,4], Paweena Kaewman[5,7], Jureeporn Roboon[5,7], Samur Thanoi[6], Sutisa Nudmamud-Thanoi[2,7*]
[1] Medical Science Graduate Program, Faculty of Medical Science, Naresuan University, Phitsanulok, Thailand
[2] National Center for Genetic Engineering and Biotechnology (BIOTEC), National Science and Technology Development Agency, Pathum Thani, Thailand
[3] Faculty of Pharmaceutical Sciences, Naresuan University, Phitsanulok, Thailand
[4] Center of Excellence in Cannabis Research, Faculty of Pharmaceutical Sciences and Center of Excellence for Innovation in Chemistry, Naresuan University, Phitsanulok
[5] Department of Anatomy, Faculty of Medical Science, Naresuan University, Phitsanulok, Thailand
[6] School of Medical Sciences, University of Phayao, Phayao, Thailand
[7] Centre of Excellence in Medical Biotechnology, Naresuan University, Phitsanulok, Thailand
*Corresponding author, e-mail: sutisat@nu.ac.th

Abstract
Background: Anxiety disorders are among the most prevalent mental disturbances, often triggered by chronic stress. Prolonged stress exerts a profound lead to neuroinflammation and subsequent alterations in the brain. Previous studies provided evidence that Cannabidiol (CBD) and Brahmi have neuroprotective effects and reduce anxiety-like behaviour in rodents. **Aim(s):** This study aimed to investigate the neuroprotective and anxiolytic effects of combined Brahmi and CBD treatments in chronic unpredictable mild stress (CUMS)-exposed rats. **Methods:** Six-week-old male Sprague Dawley rats were initially categorized into control and CUMS groups. Each main group was further subdivided into six cohorts to receive either a vehicle or extract, including 20 mg/kg of Brahmi extract, combinations of Brahmi with low (2.5 mg/kg) or high (5 mg/kg) doses of CBD-enriched extract (CBDE), and Brahmi combined with low or high doses of CBD isolate (CBDI). All rats were measured for locomotor, anxiety-like behaviours, and cognitive function on the last day of the protocol, using an open field test (OFT), elevated plus maze test (EPM), and novel object recognition, respectively. Hippocampal histological changes were evaluated using haematoxylin and eosin (H&E) staining. The differential proteomes in the hippocampus were analyzed using LC-MS/MS. After that, MS/MS data were identified and quantified using Mascot MS/MS ions search and searched against the NCBI protein database. **Results:** Combination treatment of CBD and Brahmi partially restored locomotor activity and anxiety-like behaviour compared with CUMS rats, while cognitive function was maintained or slightly elevated. Histological analysis revealed that extract treatment mitigated neuronal cell loss. Proteomic analysis identified 1,376 proteins shared across all CUMS groups. Functional enrichment analysis revealed that these proteins were primarily involved in the synaptic vesicle cycle, the AMPK signaling pathway, autophagy-animal, and the IL-17 signaling pathway. **Conclusion:** The combination of CBD and Brahmi extract effectively mitigates chronic stress-induced behavioural deficits and hippocampal neuronal damage, suggesting that the treatment exerts neuroprotective and anxiolytic effects.

Keywords *Anxiety, CUMS, Hippocampus, CBD, Brahmi*

O-05

Repeated Anodal tDCS Drives Temporal Reorganization of Corticostriatal Circuits

Siripaporn Kesyou[1,2], Bahrie Ramadan[2], Stephanie Dumontoy[2], Sutisa Nudmamud-Thanoi[3,4*], Vincent Van Waes[2*]
[1] Faculty of Medical Science, Medical Science graduate program, Naresuan University, Phitsanulok, Thailand
[2] Marie and Louis Pasteur University, INSERM, UMR 1322 LINC, Besançon, France
[3] Department of Anatomy, Faculty of Medical Science, Naresuan University, Phitsanulok, Thailand
[4] Centre of Excellence in Medical Biotechnology, Faculty of Medical Science, Naresuan University, Phitsanulok, Thailand
*Corresponding author, e-mail: vincent.van_waes@univ-fcomte.fr, sutisat@nu.ac.th

Abstract

Transcranial direct current stimulation (tDCS) is a non-invasive neuromodulation technique that delivers a weak, constant electrical current across the scalp to modulate cortical excitability. Although tDCS has demonstrated therapeutic potential in affective and addictive disorders, its circuit-level neural mechanisms remain incompletely understood. In the present study, we examined the spatiotemporal dynamics of neuronal activation induced by repeated anodal tDCS in mice, using a stimulation protocol closely aligned with those applied in clinical settings. Female Swiss mice were randomly assigned to a tDCS group, in which a stimulation electrode was surgically affixed to the skull (1 mm lateral and 1 mm anterior to bregma) for current delivery, or to a SHAM group that underwent the same procedure without electrical stimulation. Animals received 1, 4, 8, or 10 sessions of anodal stimulation (0.2 mA, 20 min per session, twice daily with sessions spaced approximately 4 h apart). Neuronal activation was quantified bilaterally using c-Fos immunohistochemistry across four rostrocaudal levels, encompassing 26 cortical regions and 23 striatal sectors. A single stimulation session induced robust, lateralized cortical activation beneath the anode, particularly within primary sensory and motor cortices, while striatal regions remained unresponsive. With repeated stimulation, cortical c-Fos induction progressively attenuated despite unchanged stimulation parameters, with residual activity primarily confined to associative and motor cortices. Notably, striatal recruitment emerged only after 10 repeated sessions, at which point activation became bilateral and spatially distributed across both dorsal and ventral subdivisions of the caudate–putamen and nucleus accumbens. Furthermore, striatal activation correlated with activity in anatomically corresponding cortical regions, indicating coordinated engagement of corticostriatal circuits after repeated stimulation. Together, these findings reveal a temporally staged transition from focal cortical activation to distributed corticostriatal circuit recruitment following repeated tDCS, providing a mechanistic framework for the cumulative therapeutic effects of neuromodulation.

Keywords *Transcranial direct current stimulation, Psychiatric disorders, Animal model, Mice, C-Fos, Neuronal activation, Corticostriatal circuits*

O-06

Genetic Association of the *COMT rs4680* Polymorphism with Suicidal Behavior in Major Depressive Disorder: A Systematic Review and Meta-Analysis

Sulaifan Waehama[1], Nathorn Chaiyakunapruk[2], Ratree Sawangjit[3], Nisalwa Japakeeya[4], Samur Thanoi[5], Paweena Kaewman[6,7,9], Jureepon Roboon[6,7,9], Gavin P Reynolds[6,8], Sutisa Nudmamud-Thanoi[6,7,9*]
[1] Medical Science Graduate Program, Faculty of Medical Science, Naresuan University, Phitsanulok, Thailand
[2] Department of Pharmacotherapy, University of Utah College of Pharmacy, South 2000 East, Salt Lake City, USA
[3] Clinical Trials and Evidence-Based Syntheses Research Unit, Mahasarakham University, Maha Sarakham, Thailand
[4] Faculty of Nursing, Thammasat University, Rangsit Campus, Pathumthani, Thailand
[5] School of Medical Sciences, University of Phayao, Phayao, Thailand
[6] Centre of Excellence in Medical Biotechnology, Faculty of Medical Science, Naresuan University, Phitsanulok, Thailand
[7] Department of Anatomy, Faculty of Medical Science, Naresuan University, Phitsanulok, Thailand
[8] Biomolecular Sciences Research Centre, Sheffield Hallam University, Howard Road, Sheffield, UK
[9] Frontier Research Cluster in Brain Health, Naresuan University, Phitsanulok, Thailand
*Corresponding author, e-mail: Sutisat@nu.ac.th

Abstract

The Catechol-O-methyltransferase (*COMT*) *rs4680* polymorphism has been extensively investigated in the pathophysiology of major depressive disorder (MDD). This variant involves a guanine (G) to adenine (A) substitution, resulting in a Val158Met amino acid change. However, its specific influence on susceptibility to suicidal behavior (SB), particularly suicide attempts (SA), among patients with MDD remains inconsistent. This study aimed to evaluate the association between *COMT rs4680* polymorphism and SB risk in MDD through a systematic review and meta-analysis. A systematic search of PubMed, ScienceDirect, and Scopus was conducted through February 2026. Eligible studies examined the relationship between *COMT rs4680* polymorphism and SB in MDD using standard diagnostic criteria and reported Hardy-Weinberg equilibrium assessments. Two independent reviewers screened studies, extracted data, and assessed methodological quality using the Newcastle-Ottawa Scale. Pooled odds ratios (ORs) with 95% confidence intervals (CIs) were calculated using fixed- or random-effects models according to heterogeneity (I^2) across different genetic models. From 1,750 screened records, four case-control studies met the inclusion criteria, comprising 243 MDD patients with SB and 685 controls. All studies showed a low overall risk of bias. The meta-analysis demonstrated a significant association under the recessive model (AA vs. AG+GG), indicating an increased risk of SB (OR = 1.56, 95% CI: 1.12–2.18, p = 0.009, I^2 = 37.30%). This association was stronger when specifically comparing patients with SA to controls without SA (OR = 1.70, 95% CI: 1.18–2.46, p = 0.004, I^2 = 44.20%). While other genetic models showed no significant associations, subgroup analysis of the Caucasian populations demonstrated a similar but non-significant trend. The *COMT rs4680* AA genotype is associated with an increased risk of SB, particularly SA, in patients with MDD. However, these findings should be interpreted with caution, given the limited evidence base. Further large-scale studies are required to confirm this association.

Keywords *rs4680, Major depressive disorder, Suicidal behavior, Genetic polymorphism, Meta-analysis*

O-07

CBD-Enriched Hemp Extract and CBD Isolate Improve Anxiety-Related Outcomes in Stress-Induced Anxiety Rats

Wanfrutkon Waehama[1,2], Jureepon Roboon[2,3], Prapapan Temkitthawon[4,5], Samur Thanoi[6], Sawanya Charoenlappanit[7], Sittiruk Roytrakul[7], Sutisa Nudmamud-Thanoi[2,3*]

[1] Department of Medical Science, Faculty of Medical Science, Naresuan University, Phitsanulok, Thailand
[2] Center of Excellence in Medical Biotechnology, Naresuan University, Phitsanulok, Thailand
[3] Department of Anatomy, Faculty of Medical Science, Naresuan University, Phitsanulok, Thailand
[4] Department of Pharmaceutical Chemistry and Pharmacognosy, Faculty of Pharmaceutical Sciences, Naresuan University, Phitsanulok, Thailand
[5] Center of Excellence in Cannabis Research, Faculty of Pharmaceutical Sciences and Center of Excellence for Innovation in Chemistry, Naresuan University, Phitsanulok, Thailand
[6] School of Medical Sciences, University of Phayao, Phayao, Thailand
[7] National Centre for Genetic Engineering and Biotechnology, National Science and Technology Development Agency, Pathum Thani, Thailand
*Corresponding author, e-mail: sutisat@nu.ac.th

Abstract

Anxiety disorders are common psychiatric conditions frequently associated with prolonged stress. Prolonged stress promotes inflammatory responses and glutamatergic excitotoxicity in the hippocampus. The endocannabinoid system (ECS) plays a critical role in regulating inflammatory signaling and glutamatergic transmission. Previous studies have demonstrated that cannabidiol (CBD) can reduce anxiety-like behaviors through modulation of the ECS. This study aimed to investigate the effects of CBD-enriched hemp extract (CBD-E) and CBD isolate (CBD-I) on behavioral and molecular alterations in rats with chronic unpredictable mild stress (CUMS)-induced anxiety. Male Sprague–Dawley rats were divided into six groups (n = 12/group): control, CUMS, CUMS administered with CBD-E (2.5 and 5 mg/kg), and CBD-I (2.5 and 5 mg/kg). Rats received oral administration of CBD-E or CBD-I while anxiety-like behaviors were induced by CUMS for 14 consecutive days. Behavioral assessments, including the open field test (OFT), elevated plus maze (EPM), and novel object recognition test (NOR), were performed on the last day of the stress induction period. Following behavioral testing, rats were sacrificed for hippocampal histological examination and proteomic analysis focusing on ECS-related, inflammatory-related, and excitotoxicity-related proteins. CUMS induced anxiety-like behaviors, as indicated by an increased closed arms entry in the EPM and a decreased percentage of normal hippocampal neurons compared with the control group. In contrast, CUMS rats treated with CBD-E and CBD-I showed a decreased number of closed-arm entries and a trend toward increased percentage of normal neurons compared with the CUMS group. Proteomic analysis revealed that CUMS increased TNF-α–related inflammatory proteins and disrupted ECS-related and excitotoxicity-related proteins, including decreased CB1 receptor expression and increased voltage-gated calcium channel and NMDA receptor subunits, as well as TNF-α. Conversely, CBD administration partially reversed these protein alterations. These findings suggest that CBD-E and CBD-I attenuate anxiety-like behaviors, improve hippocampal neuronal abnormalities, and partially restore stress-induced protein alterations.

Keywords *Anxiety, Cannabidiol, Hemp, Endocannabinoid, Excitotoxicity*

O-08

Comparison of Conventional Dissection Hall Teaching Versus Conventional Teaching Supplemented with Pirogov Virtual Dissection Table Sessions Among First-Year MBBS Students: A Comparative Study

Praveen K[1]*, Muralidhar Reddy Sangam[1], Roonmoni Deka[1]
[1] Department of Anatomy, All India Institute of Medical Sciences, Guwahati, Assam, India
*Corresponding author, e-mail: praveenk@aiimsguwahati.ac.in

Abstract
Background: Cadaveric dissection is the cornerstone of anatomy education, but students often face difficulty in three-dimensional spatial understanding. Virtual dissection tables offer interactive visualization and may enhance learning when integrated with traditional teaching. **Objective:** To compare learning outcomes between conventional dissection hall teaching and conventional teaching supplemented with Pirogov virtual dissection table sessions among first-year MBBS students. **Methods:** A comparative interventional educational study was conducted among 100 first-year MBBS students. Participants were randomly assigned to two groups of 50 each. Group A received conventional dissection teaching, while Group B received conventional teaching supplemented with Pirogov virtual dissection table sessions. The assessment was conducted over a duration of 2 hours, covering selected topics in each anatomical region, like the upper limb, thorax, abdomen, head, and neck. Learning outcome was assessed using pre and post-tests of 20 MCQs. The assessment method between the two groups was the same to have a meaningful comparison. Mean scores, standard deviations, and mean change in scores were calculated. Within-group improvement was analysed using a paired t-test, and between-group comparison of mean change scores was performed using an independent t-test. **Results:** Both groups showed significant improvement after teaching ($p<0.001$). There was no statistically significant difference in pre-test scores. Student performance means the overall score, which is the difference in post-test scores between the two groups. Mean change score in Group A was 3.5 ± 1.8, whereas Group B showed a significantly higher mean change score of 6.8 ± 2.0. The difference in mean change in score between groups was statistically significant ($t = 8.67$, $p < 0.001$). **Conclusion:** Blended learning, incorporating both conventional dissection hall teaching and Pirogov virtual dissection table sessions, results in significantly greater improvement in student learning compared to conventional teaching alone. However, further studies employing diverse assessment strategies are recommended to comprehensively evaluate the relative effectiveness of these teaching modalities.

Keywords *Anatomy education, Virtual dissection table, Blended learning, MBBS, Educational intervention*

O-09

Advancing Sustainable Histopathology: Differential Performance of Zero Formalin Fixatives in Maintaining Vimentin and Ki-67 Immunoreactivity

Thanat Triangkul[1], Ornjira Khampila[1], Panya Riubon[1], Juthapron Pavinai[1], Rojrit Rojanathanes[2], Saritvich Panyaboriban[1], Sayamon Srisuwatanasagul[1], Kongkiat Srisuwatanasagul[1*]
[1] Department of Anatomy, Faculty of Veterinary Science, Chulalongkorn University, Bangkok, 10330, Thailand
[2] Department of Chemistry, Faculty of Science, Chulalongkorn University, Bangkok, 10330, Thailand
*Corresponding author, e-mail: Kongkiat.S@chula.ac.th

Abstract

Formalin, a ubiquitous fixative in immunohistochemistry (IHC), is a recognized carcinogen that frequently obscures antigenic sites through protein crosslinking. This study evaluated the comparative efficacy of immunohistochemical reactions using alcohol-based fixatives (Zero Formalin; ZF) and benzalkonium chloride-based fixatives, both formulated to be formalin- and phenol-free. The investigation revealed that alcohol-based ZF solutions effectively preserved the immunoreactivity of both vimentin and Antigen Kiel-67 (Ki-67). Conversely, benzalkonium chloride-based fixatives supported the expression of vimentin alone, failing to maintain Ki-67 integrity. Quantitative analysis demonstrated that the median H-score for vimentin protein in the jejunum and ileum showed no statistically significant deviation between tissues fixed with alcohol-based solutions and those fixed with conventional 10% formalin ($p > 0.05$). Furthermore, the median Ki-67 positivity index in the small intestine remained statistically comparable between alcohol-based fixatives and the formalin gold standard ($p > 0.05$). In conclusion, alcohol-based ZF formulations demonstrated superior effectiveness in IHC reactions relative to benzalkonium chloride-based alternatives. These novel solutions offer a high-fidelity, safer methodological alternative to conventional formalin, effectively mitigating occupational biohazard exposure while maintaining protein integrity.

Keywords *Immunohistochemistry, Ki-67, Vimentin, Zero Formalin*

Background

Immunohistochemistry (IHC) is a foundational diagnostic modality in clinical and veterinary pathology for classifying neoplasms, directly impacting patient prognosis and therapeutic interventions (1). The fixative is the most critical reagent in this process, as it must preserve tissue architecture while maintaining the integrity of antigenic epitopes (2). While 10% neutral buffered formalin is the current "gold standard" due to its cost-efficiency and rapid action, its use carries significant health risks, including carcinogenicity (3). Furthermore, formalin-induced crosslinking necessitates complex antigen retrieval (AR) protocols to unmask epitopes (4).

To address these concerns, researchers at Chulalongkorn University have developed "Zero Formalin" (ZF) preservatives. These solutions aim to provide a safer laboratory environment for students and technicians by reducing hazardous exposure while maintaining high-quality tissue preservation for gross and microscopic anatomy.

The small intestine, a long, convoluted organ, is composed of four distinct layers: the mucosa, submucosa, muscularis externa, and serosa/ adventitia (5). Ki-67, a nuclear antigen, detects proliferating cells, primarily those at the base of the intestinal crypts (6). Vimentin, a 57 kDa intermediate filament protein, is generally expressed in mesenchymal cells within the lamina propria, including fibroblasts, macrophages, and endothelial cells (7).

The objective of this research was to compare the IHC efficacy of these novel formalin-free and phenol-free fixatives against traditional methods.

Materials and Methods

Fixatives solution preparation

Four experimental fixative formulations were used: Zero Formalin Formula 1 (ZF1), Zero

Formalin for histology (ZF Histo) (alcohol-based), as well as BZCU and BZ+Ramanoir (benzalkonium chloride-based). The precise chemical compositions are currently protected under Petty Patent Application Number 2403004132.

Sample preparation

Intestinal tissues (duodenum, jejunum, and ileum) were harvested from three domestic pigs (*Sus domesticus*) via the Veterinary Diagnostic Laboratory at Chulalongkorn University. Samples were fixed for 24-36 hours in one of five solutions, which were 1) 10% Formalin, 2) ZF1, 3) ZF Histo, 4) BZCU, or 5) BZ+Ramanoir. Following fixation, tissues underwent standard dehydration and paraffin embedding. Sections were cut at 4 μm and mounted on gelatin-coated slides for further IHC procedure.

Immunohistochemistry staining

The sections were deparaffinized in xylene and rehydrated through graded ethanol dilutions. For vimentin, antigen retrieval was performed using a citric acid buffer, pH 6.0, microwave method at 500 watts for 5 minutes (2 times). While Ki-67, antigen retrieval was performed using a citric acid buffer, pH 6.0, microwave method at 800 watts for 5 minutes, defrost mode for 3 minutes, and 400 watts for 5 minutes (4 times). Endogenous peroxidase activity was inhibited by immersing the sections in 3% (v/v) H_2O_2 in methanol at room temperature. Non-specific background staining was reduced by incubation with 1.5% normal horse serum (Vector Laboratories, CA, USA) for 30 minutes. The sections were incubated overnight at 4°C with a 1:100 dilution of mouse monoclonal antibody to Vimentin (sc-6260, Santa Cruz Biotechnology, TX, USA) or Ki-67 (GA626, Agilent Dako, CA, USA). Subsequently, the sections were applied with the secondary biotinylated horse anti-mouse antibody (Vector Laboratories, CA, USA) at a dilution of 1:200. Then, both immunoreactive staining were performed using horseradish peroxidase avidin biotin complex (ABC kits, Vector Laboratories, CA, USA) and the 3,3' diaminobenzidine tetrahydrochloride (DAB Peroxidase substrate kit, Vector Laboratories, CA, USA) as the chromogenic substrate. The tissue slides were counterstained using Mayer's hematoxylin. Finally, the tissue slides were mounted using glycerol gelatin media. All tissue slides were visualized using Panoramic scan and software Slideviewer (3DHISTECH, Budapest, Hungary).

Evaluation of immunoreaction

Vimentin and Ki-67 expression were analyzed using CellQuant software (3DHISTECH, Budapest, Hungary). The results were presented as the H-score and positivity index of the staining, respectively. Moreover, a positive index of Ki-67 was calculated from the division of positive cells by all intestinal cells in the slide. Furthermore, the expression of vimentin was digitally categorized into three levels (high, moderate, and low) and calculated as H-score = (% high ×3)+(% moderate ×2)+(%low ×1), following previous immunohistochemical studies (8,9).

Statistical analysis

All statistical analyses and data visualizations were conducted using R software (version 4.5.1). All quantitative data, including H-score and Positive Index, were expressed as median and interquartile range (IQR). The normality of data distribution was assessed using the Shapiro-Wilk test. Due to the non-normal distribution of the data, non-parametric statistical methods were used for all comparisons to ensure consistency across the study. For each organ type (duodenum, jejunum, and ileum), statistical significance among the groups (Formalin, ZF, ZF Histo, BZCU, and BZ+Ramanoir) was determined using the Kruskal-Wallis H test. When significant differences were detected, a Dunn's post-hoc test with Benjamini-Hochberg (BH) adjustment for multiple comparisons was performed to identify specific differences between groups. A p-value of less than 0.05 was considered statistically significant.

Results and Discussion

Qualitative evaluation

Vimentin expression was identified mainly in the cytoplasm of mesenchymal cells, fibroblasts within the lamina propria, endothelial cells, muscularis externa, and lymphatic nodules in ileal Peyer's patches (10,11). On the other hand, Ki-67 immunoreactivity was localized mainly in the nuclei of proliferative epithelial stem cells in the crypts of Lieberkühn, lymphocytes, and duodenal submucosal fibroblasts. (12). The results of vimentin immunostaining were depicted in Figures 1-3, while the results of Ki-67 immunostaining were shown in Figures 4-6

Quantitative assessment

Quantitative analysis of vimentin, an intermediate filament cytoskeletal protein, was demonstrated in Table 1. Vimentin, the marker to identify mesenchymal cells such as fibroblasts, endothelial cells, and smooth muscle cells, was

evaluated using H-scores to measure color intensity as well as the proportion of positive cells. Statistical results indicated significant regional variance; in the duodenum, both alcohol-based (ZF1, ZF Histo) and benzalkonium chloride-based fixatives (BZCU, BZ+Ramanoir) showed H-scores that differed significantly from the 10% formalin control ($p < 0.05$). However, high-fidelity preservation was achieved in the jejunum using ZF1 and in the ileum using ZF Histo, as these alcohol-based formulations showed no significant statistical difference compared to conventional formalin ($p > 0.05$). This efficacy suggests a mechanistic superiority for alcohol-based fixatives, which function as protein precipitants to preserve antigenic sites more effectively than the crosslinking mechanism of formalin. Furthermore, the use of alcohol-based fixation may lower the requirement for traditional antigen retrieval (AR) steps, offering a potential reduction in overall tissue processing time while maintaining diagnostic integrity.

The quantitative evaluation of Antigen Kiel-67 (Ki-67) focused on its role as a nuclear marker for cellular proliferation. Efficacy was determined by the positivity index (Ki-67 index), which measures the percentage of immunoreactive cells within the tissue sections (Table 2). Statistical analysis demonstrated that alcohol-based fixatives (ZF1 and ZF Histo) maintained high-fidelity preservation, as their positivity indices showed no significant statistical deviation from conventional 10% formalin across the small intestine segments ($p > 0.05$). In stark contrast, benzalkonium chloride (BAC)-based fixatives (BZCU and BZ+Ramanoir) exhibited a complete failure to preserve the Ki-67 epitope, resulting in a statistically significant reduction in immunoreactivity compared to the formalin gold standard ($p < 0.05$). This disparity likely arises from the mechanistic limitations of BAC; as a quaternary ammonium compound (QAC), it functions by denaturing proteins and disrupting cell membranes, a process that appears to induce the total loss of specific antigenic sites like Ki-67. Furthermore, the use of alcohol-based fixatives presents a superior alternative due to their ability to precipitate proteins rather than denature them, while avoiding the environmental risks and potential carcinogenic byproduct formation associated with QACs.

The qualitative and quantitative results underscore the significant impact of fixative selection on antigenic integrity. Vimentin, a mesenchymal marker found in fibroblasts and endothelial cells, was successfully preserved across all tested solutions, though regional differences were noted; specifically, alcohol-based and benzalkonium chloride (BAC)-based H-scores in the duodenum differed from the formalin control. However, alcohol-based fixatives such as ZF1 and ZF Histo demonstrated high-fidelity preservation in the jejunum and ileum, showing no significant difference from the formalin gold standard.

In contrast, the Ki-67 proliferation index revealed a stark divergence: while alcohol-based fixatives yielded results comparable to formalin, BAC-based fixatives (BZCU and BZ+Ramanoir) resulted in a near-total loss of immunoreactivity. This failure is attributed to the mechanism of BAC as a quaternary ammonium compound (QAC), which denatures proteins and disrupts cell membranes, thereby eliminating specific epitopes like Ki-67. Alcohol-based fixatives, functioning as protein precipitants, preserve antigenic sites more effectively, rendering secondary antigen retrieval (AR) unnecessary and reducing processing time.

While formalin remains the benchmark, its carcinogenic nature and the necessity for unmasking cross-linked antigens present significant drawbacks. Although alcohol-based fixatives are substantially safer (13), they may occasionally induce tissue shrinkage or brittleness (14,15). Furthermore, BAC-based alternatives pose environmental risks to marine ecosystems and may facilitate the formation of the carcinogen N-nitrosodimethylamine (NDMA) at high levels (16).

Conclusion

In conclusion, alcohol-based fixatives (ZF1 and ZF Histo) provide a highly effective and viable alternative to conventional formalin-based solutions for tissue fixation in immunohistochemistry. They offer comparable diagnostic accuracy for mesenchymal and proliferation markers while ensuring a significantly safer working environment by eliminating exposure to carcinogenic formaldehyde and phenol. Furthermore, by avoiding the environmental toxicity and antigenic degradation associated with benzalkonium chloride-based alternatives, alcohol-based formulations emerge as the superior choice for modern, sustainable, and high-performance histological processing.

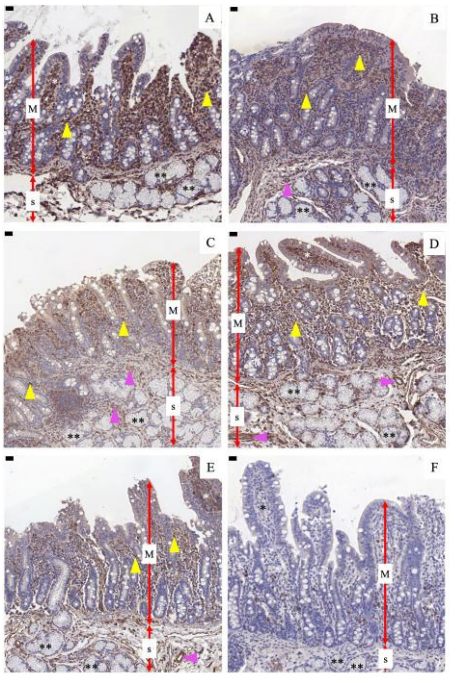

Fig. 1 Immunohistochemical expression of vimentin protein in swine duodenum with various fixative solutions. A: Fixed with 10% Formalin. B: Fixed with ZF1. C: Fixed with ZF Histo. D: Fixed with BZCU. E: Fixed with BZ+Ramanoir. F: Negative control. The red double-headed arrows show the boundary layers of tunica mucosa (M), and tunica submucosa (s). The asterisks show key structures of villi (*), and Brunner's (duodenal) glands (**). The colored arrowheads show positive staining of lamina propria (Yellow arrowheads), and endothelial cells (Pink arrowheads). Scale bar = 20 µm.

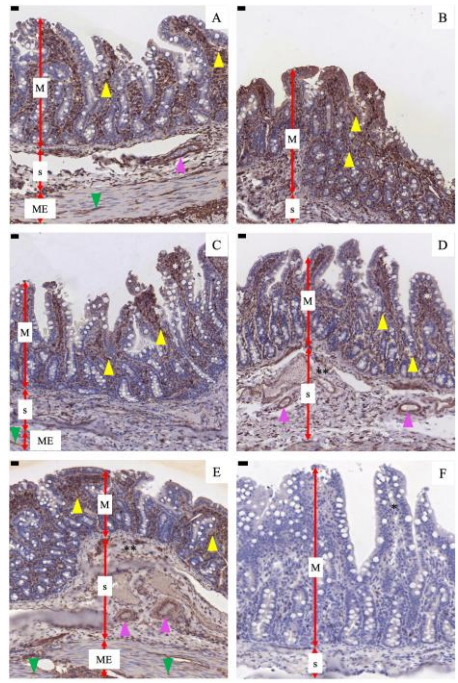

Fig. 2 Immunohistochemical expression of vimentin protein in swine jejunum with various fixative solutions. A: Fixed with 10% Formalin. B: Fixed with ZF1. C: Fixed with ZF Histo. D: Fixed with BZCU. E: Fixed with BZ+Ramanoir. F: Negative control. The red double-headed arrows show the boundary layers of tunica mucosa (M), tunica submucosa (s), and muscularis externa (ME). The asterisks show key structures of villi (*), and plicae circulares (**). The colored arrowheads show positive staining of lamina propria (Yellow arrowheads), endothelial cells (Pink arrowheads), and muscularis externa (Green arrowheads). Scale bar = 20 µm.

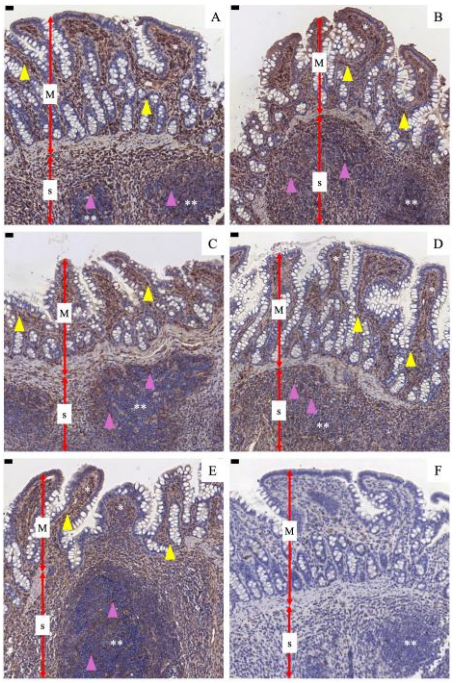

Fig. 3 Immunohistochemical expression of vimentin protein in swine ileum with various fixative solutions. A: Fixed with 10% Formalin. B: Fixed with ZF1. C: Fixed with ZF Histo. D: Fixed with BZCU. E: Fixed with BZ+Ramanoir. F: Negative control. The red double-headed arrows show the boundary layers of tunica mucosa (M), and tunica submucosa (s). The asterisks show key structures of villi (*), and Peyer's patches (**). The colored arrowheads show positive staining of lamina propria (Yellow arrowheads), and lymphatic nodules (Pink arrowheads) in Peyer's patches. Scale bar = 20 µm.

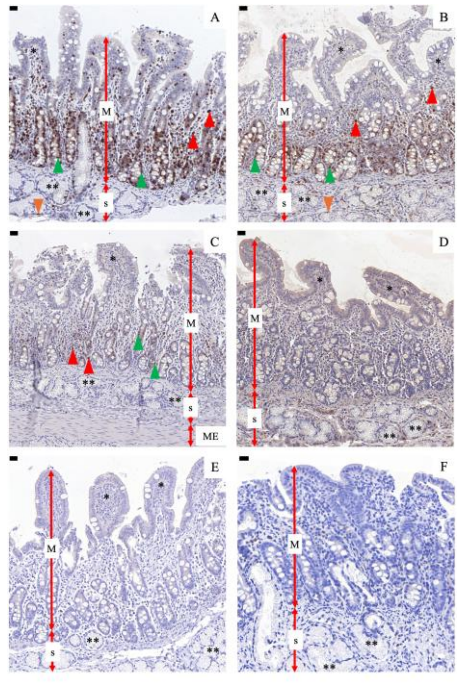

Fig. 4 Immunohistochemical expression of Ki-67 protein in swine duodenum with various fixative solutions. A: Fixed with 10% Formalin. B: Fixed with ZF1. C: Fixed with ZF Histo. D: Fixed with BZCU. E: Fixed with BZ+Ramanoir. F: Negative control. The red double-headed arrows show the boundary layers of tunica mucosa (M), and tunica submucosa (s). The asterisks show key structures of villi (*), and Brunner's (duodenal) glands (**). The colored arrowheads show positive staining of epithelial cells in crypts of Lieberkühn (Green arrowheads), lymphocytes in lamina propria (Red arrowheads), Brunner's (duodenal) glands (Orange arrowheads). Scale bar = 20 µm.

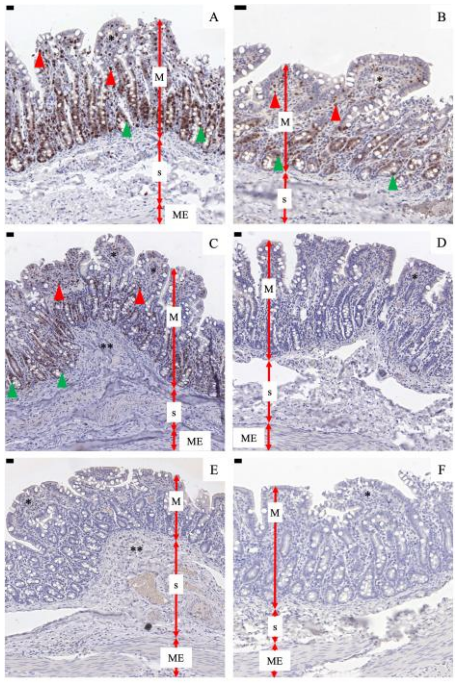

Fig. 5 Immunohistochemical expression of Ki-67 protein in swine jejunum with various fixative solutions. A: Fixed with 10% Formalin. B: Fixed with ZF1. C: Fixed with ZF Histo. D: Fixed with BZCU. E: Fixed with BZ+Ramanoir. F: Negative control. The red double-headed arrows show the boundary layers of tunica mucosa (M), tunica submucosa (s), and muscularis externa (ME). The asterisks show key structures of villi (*), and plicae circulares (**). The colored arrowheads show positive staining of epithelial cells in crypts of Lieberkühn (Green arrowheads), and lymphocytes in lamina propria (Red arrowheads). Scale bar = 20 µm.

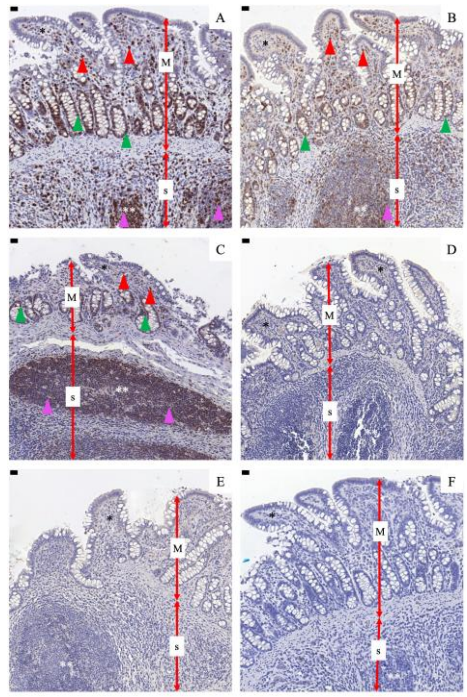

Fig. 6 Immunohistochemical expression of Ki-67 protein in swine ileum with various fixative solutions. A: Fixed with 10% Formalin. B: Fixed with ZF1. C: Fixed with ZF Histo. D: Fixed with BZCU. E: Fixed with BZ+Ramanoir. F: Negative control. The red double-headed arrows show the boundary layers of tunica mucosa (M), and tunica submucosa (s). The asterisks show key structures of villi (*), and Peyer's patches (**). The colored arrowheads show positive staining of epithelial cells in crypts of Lieberkühn (Green arrowheads), lymphocytes in lamina propria (Red arrowheads), and lymphatic nodules (Pink arrowheads) in Peyer's patches. Scale bar = 20 µm.

Table 1 The H score of vimentin protein in swine small intestine tissues with various fixative solutions (median ± IQR). Different superscript letters within a column indicate statistical significance ($p < 0.05$)

Group of fixatives	Duodenum	Jejunum	Ileum
10% Formalin	107.17 ± 2.08[a]	110.34 ± 2.09[a]	82.62 ± 2.21[a]
ZF1	96.59 ± 2.57[b]	112.76 ± 3.52[a]	101.67 ± 3.17[b]
ZF Histo	93.99 ± 1.97[b]	88.09 ± 2.75[b]	81.65 ± 1.73[a]
BZCU	87.39 ± 2.35[bc]	86.79 ± 2.02[b]	83.27 ± 2.42[a]
BZ+ Ramanoir	82.08 ± 3.90[c]	77.48 ± 3.07[b]	84.75 ± 2.70[a]

Table 2 The positivity index of Ki-67 protein in swine small intestine tissues with various fixative solutions (median ± IQR). Different superscript letters within a column indicate statistical significance ($p < 0.05$)

Group of fixatives	Duodenum	Jejunum	Ileum
10% Formalin	92.86 ± 10.40[a]	88.02 ± 15.88[a]	94.44 ± 15.09[a]
ZF1	83.31 ± 11.16[a]	75.88 ± 19.66[a]	81.28 ± 18.00[a]
ZF Histo	88.12 ± 24.02[a]	87.55 ± 19.92[a]	78.16 ± 37.87[a]
BZCU	6.06 ± 18.10[b]	2.88 ± 9.95[b]	3.21 ± 10.80[b]
BZ+ Ramanoir	0.38 ± 1.55[b]	0.41 ± 0.55[b]	8.56 ± 9.76[b]

Acknowledgements

We would like to thank Veterinary Diagnostic Laboratory Large Animal Teaching Hospital, Faculty of Veterinary Science, Chulalongkorn University, for tissue samples. This study was supported by Faculty of Veterinary Science Research grant 2026 (RI 6/2026) and Innovation and Invention grant, Ratchadaphiseksomphot Endowment Fund (CU_GI_68_004_3100_001).

References

1. Painter JT, Clayton NP, Herbert RA. Useful immunohistochemical markers of tumor differentiation. Toxicol Pathol 2010;38(1):131-41.
2. Lenz J, Macháčová D, Konečná P, Fiala L, Kyllar M, Tichý F. Effects of different fixatives over different fixation times, including Antigenfix, on immunohistochemical studies. Acta Veterinaria Brno 2022;91:179-88.
3. Sinha N, Nayak MT, Sunitha JD, Dawar G, Rallan N, Gupta S. Comparative efficacies of a natural fixative with a conventional fixative. J Oral Maxillofac Pathol 2017;21(3):458.
4. van Essen HF, Verdaasdonk MAM, Elshof SM, de Weger RA, van Diest PJ. Alcohol based tissue fixation as an alternative for formaldehyde: influence on immunohistochemistry. Journal of Clinical Pathology 2010;63(12): 1090.
5. Eyhab R, Al-Samawy E, Hussein D, Kadhim, Taher I, Alhmadi H, et al. Histo-Morphometric Compression Finding of the Small Intestine in Rats and Rabbit According to Different Foods. 2021; 9:433-7.
6. Saxena R, Darnell AJ. Proliferation in the normal gastrointestinal tract: an immunohistochemical study with Ki-67. Journal of Histotechnology. 2012;35(1):22-6.
7. Yin S, Chen F-f, Yang G-f. Vimentin immunohistochemical expression as a prognostic factor in gastric cancer: A meta-analysis. Pathology-Research and Practice. 2018;214(9):1376-80.
8. Prapaiwan N, Manee-In S, Thanawongnuwech R, Srisuwatanasagul S. Anti-Müllerian hormone levels in serum and testes of male dogs: relations with neuter status and bilateral abdominal cryptorchidism. Theriogenology 2023;208:171-7.
9. Srisuwatanasagul K, Prapaiwan N, Srisuwatanasagul S, Kunavongkrit A, Roongsitthichai A. Immunohistochemical study of Ki-67 protein, androgen receptor, and estrogen receptor beta in testicular tissues of male pigs immunocastrated with different times of GnRH vaccination. Anat Histol Embryol 2018;47(5):475-80.
10. Lalioti V, González-Sanz S, Lois-Bermejo I, González-Jiménez P, Viedma-Poyatos Á, Merino A, et al. Immunolocalization studies of vimentin and ACE2 on the surface of cells exposed to SARS-CoV-2 Spike proteins. bioRxiv 2021:442648.
11. Brzozowa-Zasada M, Wyrobiec G, Piecuch A, Jasiński D. Vimentin immunoexpression and its prognostic activity in colon cancer among Caucasian patients. Prz Gastroenterol 2022; 17(2):123-9.
12. Nayak J, Mohanty P, Lenka A, Sahoo N, Agrawala S, Panigrahi SK. Histopathological and Immunohistochemical Evaluation of CDX2 and Ki67 in Colorectal Lesions with their Expression Pattern in Different Histologic Variants, Grade, and Stage of Colorectal Carcinomas. J Microsc Ultrastruct 2021;9(4): 183-9.

13. Rahman MA, Sultana N, Ayman U, Bhakta S, Afrose M, Afrin M, et al. Alcoholic fixation over formalin fixation: A new, safer option for morphologic and molecular analysis of tissues. Saudi Journal of Biological Sciences 2022; 29(1):175-82.
14. Mayur Ramabhai Chaudhari MP, Keyurkumar Gulabbhai Patel. Comparative Evaluation of Formalin and Alcohol-Based Fixatives on Tissue Morphology and Immunostaining in Routine Histopathology. Journal of Heart Valve Disease 2025;30(7):31-4.
15. Titford ME, Horenstein MG. Histomorphologic assessment of formalin substitute fixatives for diagnostic surgical pathology. Arch Pathol Lab Med 2005;129(4):502-6.
16. Mohapatra S, Yutao L, Goh SG, Ng C, Luhua Y, Tran NH, et al. Quaternary ammonium compounds of emerging concern: Classification, occurrence, fate, toxicity and antimicrobial resistance. Journal of Hazardous Materials 2023;445:130393.

O-10

Determining Accurate Sizing and Safe Trajectory of Lateral Mass Screws in the First Cervical Vertebra of the Emirati Population

Ivan James Prithishkumar[1*], Dineshwary Suresh[1], Nerissa Naidoo[1], Rashid AlSharhan[2], Usama AlBastaki[3], Jeyaseelan Lakshmanan[1], Baylis Vivek Joseph[4]
[1] Department of Basic Sciences, College of Medicine, Mohammed Bin Rashid University of Medicine and Health Sciences, Dubai Health, Dubai, UAE
[2] Department of Clinical Sciences, College of Medicine, Mohammed Bin Rashid University of Medicine and Health Sciences, Dubai Health, Dubai, UAE
[3] Department of Diagnostic Imaging, Rashid Hospital, Dubai Health, Dubai, UAE
[4] Department of Neurosciences, Christian Medical College, Vellore, India
*Corresponding author, e-mail: drivanjames@gmail.com

Abstract
Background: The first cervical vertebra (C1) consists of an anterior and posterior arch, and a lateral mass. Instrumental fixation of the lateral mass to stabilize the C1 vertebra is required in conditions of atlantoaxial instability, including fractures, dislocations, and congenital anomalies. C1 bears a complicated relationship with the vertebral artery and cervical spinal cord, which are at critical risk of injury in a misdirected screw. **Objective:** To identify safe screw trajectories and optimum screw dimensions of the C1 lateral mass screws in the Emirati population. **Methods:** Computed Tomography images of the Cervical Spine in 160 Emirati adults, >18 years (M=80; F=80) were reviewed in the Department of Radiology, Rashid Hospital, Dubai. We studied screw dimensions and trajectories at three entry points: A) Centre of lateral mass, B) Junction of posterior arch and lateral mass, C) Through posterior arch. **Results:** Screw entry at Point A and Point B allows screws of intraosseous lengths 18-20mm in Emiratis. Medial angulation of 15-20° allows for maximum bone purchase. We recommend cephalic angulations of 19° in males and 16° in females. Screw entry at Point C with zero inclination allows for an intraosseous screw length of 28.0mm from the posterior arch to the anterior cortex of the lateral mass. Mean height of posterior arch at the vertebral artery groove was 3.2±0.4mm in males and 3.0±0.4mm in females. **Conclusion:** We recommend lateral mass screws of 3.5-4.0 mm width at all points, with screw lengths depending on the entry-point and angulation. A notching technique is recommended if screw entry through point C is considered. This is the first study reporting on the feasibility of C1 screw placement in the Emirati population. Pre-operative knowledge of screw sizes minimizes the risk of inadvertent injury to neurovascular structures in the vicinity of the C1 lateral mass.

Keywords *C1, Lateral mass, Screw, Atlas*

O-11

A Simplified Single-Solution Modified Thiel Embalming Protocol: Enhancing Visceral Stability and Cost-Efficiency for Anatomical Education

Napawan Taradolpisut[1], Wattana Weerachatyanukul[1], Arada Chaiyamoon[2], Thewarid Berkban[2], Tracey Wilkinson[3], Athikhun Suwannakhan[1,3*]
[1] Department of Anatomy, Faculty of Science, Mahidol University, Ratchathewi, Bangkok 10400, Thailand
[2] Department of Anatomy, Faculty of Medicine, Khon Kaen University, Khon Kaen 40002, Thailand
[3] Human Anatomy Unit, Department of Biomedical Sciences, College of Medicine and Health, University of Birmingham, Edgbaston, Birmingham B15 2TT, UK
*Corresponding author, e-mail: a.suwannakhan@bham.ac.uk

Abstract

The original Thiel embalming method is renowned for producing cadavers with lifelike flexibility and color. However, the original protocol is hindered by its complex multi-step preparation and high chemical costs of around £3,000 per cadaver. Additionally, the occasionally over-softened visceral tissues can be suboptimal for foundational anatomical study in undergraduate programs. This study aimed to develop a promising single-solution modified Thiel protocol using accessible commercial-grade chemicals to reduce costs and preparation complexity while improving visceral tissue firmness. Twelve cadavers (7 males, 5 females; age range 62–93 years) were embalmed using a simplified, single-solution formula. The total material cost was reduced by approximately 90% (from ~£3,000 to ~£300 per cadaver). After a three-month immersion period, cadaver quality was evaluated using objective joint range-of-motion (ROM) measurements (n=12) and a structured questionnaire (4-point Likert scale) completed by a diverse group of stakeholders (n = 56). The modified protocol maintained realistic tissue properties with a significantly simplified workflow. Objective ROM testing demonstrated excellent joint mobility, including shoulder flexion (121.7° ± 24.3°) and knee flexion (123.7° ± 23.3°), which are comparable to values observed in live individuals. Quantitative evaluations showed high mean scores for tissue color (3.37 ± 0.62) and limb flexibility (3.35 ± 0.76). The increased visceral firmness prevented the "collapse" of hollow organs, facilitating clearer structural identification. Medical specialists provided a high validation score of 3.71 ± 0.49 for surgical training suitability. This single-solution protocol offers a cost-effective alternative, reducing expenses tenfold. By balancing lifelike flexibility with improved visceral stability, it provides a versatile educational tool. Future research will incorporate objective tissue stiffness testing and histological analysis to further validate long-term preservation quality.

Keywords *Thiel embalming, Body preservation, Education*

O-12

Sex Estimation from Human Skulls in Northeastern Thailand

Natthawadee Wongwad[1], Suthat Duangchit[2], Kitinat Rodthongdee[2], Sittichai Iamsaard[3], Chanasorn Poodendaen[4], Narawadee Chompoo[4], Poonikha Namvongsakool[4], Phongpitak Putiwat[4], Pruet Boonsing[4], Kaemisa Srisen[4*]

[1] Graduate student, Department of Anatomy, Faculty of Medical Science, Naresuan University, Phitsanulok, Thailand

[2] Department of Physiology, Faculty of Medical Science, Naresuan University, Phitsanulok, Thailand

[3] Department of Anatomy, Faculty of Medicine, Khon Kaen University, Khon Kaen, Thailand

[4] Department of Anatomy, Faculty of Medical Science, Naresuan University, Phitsanulok, Thailand

*Corresponding author, e-mail: kaemisas@nu.ac.th

Abstract

Sex estimation is the most fundamental step in establishing a biological profile for personal identification in forensic anthropology. Among all skeletal elements, the human skull is recognized as the second most reliable indicator for sex estimation, surpassed only by the pelvis, owing to its distinct sexual dimorphism in both structural size and muscle attachment robusticity. However, genetic and geographical variations render sex prediction equations population-specific, and applying equations derived from one population to another often results in a marked decrease in accuracy. Currently, no region-specific forensic anthropological database exists for the Northeastern Thai population, which possesses unique genetic characteristics that may differ from other Thai regions. Therefore, this study aimed to develop a sex estimation equation specifically for this population. A total of 100 dry skulls (50 males and 50 females) were examined from the Unit of Human Bone Warehouse for Research (UHBWR), Department of Anatomy, Faculty of Medicine, Khon Kaen University. All specimens were from individuals aged 20 years or older. Five craniometric parameters were measured: Bregma–Basion (P1), Bregma–Nasion (P2), Basion–Nasion (P3), Nasion–Prosthion (P4), and Lambda–Nasion (P5). Statistical analysis was performed using independent *t*-tests and stepwise discriminant function analysis. The results revealed that mean values of all five parameters were significantly higher in males than in females ($p < 0.001$), consistent with the known effects of sex hormones on skeletal development. Stepwise DFA identified P1 and P5 as the most significant predictors, yielding the equation: $D = 0.916(P1) + 1.654(P5) - 39.623$. This equation achieved an overall classification accuracy of 86.0%, with 88.0% accuracy for males and 84.0% for females. Cross-validation confirmed the model's stability at 84.0%, indicating robustness and generalizability. In conclusion, the derived equation provides a reliable and population-specific tool for sex estimation from cranial measurements, with potential application in forensic identification cases within the Northeastern Thai population.

Keywords *Forensic anthropology, Biological profile, Sex estimation, Human skulls, Northeastern Thailand*

Background

Identifying individuals from skeletal remains is a core mission in forensic anthropology, playing a vital role in the judicial process, criminal investigations, and the identification of unknown persons. The first and most fundamental step in establishing a biological profile is sex estimation, as it significantly narrows the scope of the investigation [1]. The skull is traditionally recognized as the second most reliable indicator for sex estimation after the pelvis, although some studies suggest that certain postcranial elements may provide comparable or higher accuracy. This high reliability is attributed to its distinct sexual dimorphism, which is evident in both structural size and the robusticity of muscle attachment sites [2]. Currently, Thailand has several established standards for sex estimation from various skeletal elements, such as the femur, in the Northern Thai population [3] or the mandible in the Central Thai population [4]. In addition, several studies have investigated sex estimation from cranial structures in Thai populations, including analyses of maxillary suture length and three-dimensional craniometric approaches, further emphasizing the importance of population-specific standards [5,6]. However, these

approaches may have limitations in accuracy compared to the use of a complete skull and may be insufficient for highly complex identification cases. A crucial factor affecting the precision of predictive equations is "population specificity", as the skull exhibits significant genetic and geographical variations. Consequently, applying an equation developed for one population to another often results in a marked decrease in accuracy [7]. For the Northeast (Isan) region, which has a large population and unique genetic characteristics that may differ from those in the Northern or Central regions, there is still a lack of region-specific forensic anthropological databases. Using equations derived from other populations may lead to errors in sex estimation. Therefore, this study aims to analyze the cranial morphology of this population to develop efficient and accurate equations for practical application in the field.

Materials and Methods

A total of 100 dry skulls were collected, consisting of 50 male and 50 female specimens in well-preserved condition. Each specimen included recorded information on age, sex, and ancestry, with all individuals being at least 20 years old. The samples were obtained from the Unit of Human Bone Warehouse for Research (UHBWR), Department of Anatomy, Faculty of Medicine, Khon Kaen University. This study was approved by the Center for Ethics in Human Research, Khon Kaen University (Approval No. HE681653). Inclusion criteria were well-preserved adult skulls (≥20 years) with complete anatomical landmarks and documented information on sex, age, and geographical origin, without pathological conditions or damage affecting cranial morphology. Exclusion criteria included incomplete or damaged skulls, the presence of pathological conditions affecting cranial structure, and missing or incomplete donor information. The skulls were measured according to five parameters (Fig. 1) using a digital caliper with an accuracy of 0.01 mm, including:

P1 = Distance between Bregma-Basion
P2 = Distance between Bregma–Nasion
P3 = Distance between Basion–Nasion
P4 = Distance between Nasion–Prosthio
P5 = Distance between Lambda–Nasion

All measurements were performed by two trained observers. Interobserver reliability was assessed using the intraclass correlation coefficient (ICC) based on a two-way random-effects model with absolute agreement. The data collected were analyzed using IBM SPSS Statistics version 26.0. All measurements are presented as mean ± standard deviation (SD). Descriptive statistics and independent *t*-tests were performed to assess mean differences between male and female populations. Discriminant function analysis was conducted to develop predictive equations and assess the classification accuracy for sex estimation.

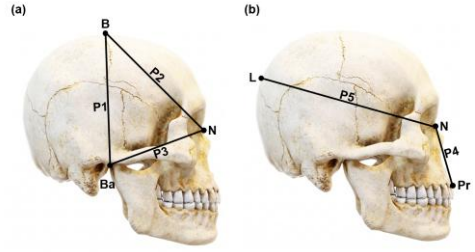

Fig. 1 Five measurements (P1–P5) used in this study: (a) distance between Bregma–Basion (P1), Bregma–Nasion (P2), and Basion–Nasion (P3); (b) distance between Nasion–Prosthion (P4) and Lambda–Nasion

Results

In this study, interobserver reliability for all parameters was excellent, with ICC values ranging from 0.992 to 0.998 (95% CI: 0.986–0.999).

The results of this study indicated that all parameters in males were significantly higher than those in females (Table 1), with statistically significant differences observed across all measurements ($p < 0.001$).

The discriminant function analysis developed for sex estimation demonstrated high performance, achieving an overall accuracy rate of 86%. The classification was determined using the following predictive equation (Table 2). The sectioning point for this model was set at 0; a calculated score (D) greater than 0 classified the individual as male, while a score less than 0 classified the individual as female.

According to the classification matrix (Table 2), the discriminant function equation demonstrated high predictive performance. The sensitivity (accuracy in identifying males) was 88.0% (44 out of 50), while the specificity (accuracy in identifying females) was 84.0% (42 out of 50). To further evaluate the reliability of the model, a cross-validation test was performed, yielding a sensitivity of 88.0%, a specificity of 80.0%, and a consistently high overall accuracy of 84.0%. The minimal disparity between the original and cross-validated results confirms the robustness and generalizability of the model for sex estimation within the Northeastern Thai population.

Table 1 Descriptive statistics and independent *t*-test statistics for sex differences in dry skull measurements

Parameter	Total (*n*=100) Mean ± SD (cm)	Male (*n*=50) Mean ± SD (cm)	Female (*n*=50) Mean ± SD (cm)	*t*-score	*p*-value
P1	13.33 ± 0.53	13.60 ± 0.44	13.06 ± 0.48	5.930	<0.001
P2	11.03 ± 0.51	11.23 ± 0.41	10.82 ± 0.53	4.318	<0.001
P3	9.72 ± 0.53	10.01 ± 0.46	9.43 ± 0.43	6.483	<0.001
P4	6.84 ± 0.55	7.11 ± 0.45	6.58 ± 0.51	5.464	<0.001
P5	16.56 ± 0.61	16.95 ± 0.45	16.18 ± 0.49	8.118	<0.001

Table 2 Discriminant function models and classification accuracy rates for sex estimation using the stepwise method

Discriminant function equation	Original analysis			Cross validation		
	Overall accuracy (%)	Sensitivity (%)	Specificity (%)	Overall accuracy (%)	Sensitivity (%)	Specificity (%)
D = 0.916(P1) + 1.654(P5) - 39.623	86.0	88.0	84.0	84.0	88.0	80.0

Discussion

In this study, interobserver reliability for all parameters was excellent, with ICC values ranging from 0.992 to 0.998 (95% CI: 0.986–0.999), indicating high consistency between observers. This strong agreement confirms that the measurements are reproducible and not influenced by individual variability between raters, thereby strengthening the validity and generalizability of the results.

The present study demonstrated significant sexual dimorphism in the cranial structures of the Northeastern Thai population. All measured parameters (P1–P5) were significantly larger in males than in females (Table 1), with *p*-values less than 0.001. This morphological divergence is primarily driven by the influence of sex hormones on skeletal development. Testosterone in males promotes prolonged periosteal apposition and the development of more prominent muscle attachment sites, such as the nuchal lines and mastoid processes [8-10]. In contrast, estrogen in females tends to limit bone lateral growth and leads to earlier fusion of cranial base synchondroses, resulting in a generally smaller and more gracile skull compared to males [11,12].

In this study, the discriminant function analysis yielded a classification equation with an overall accuracy of 86.0%. This accuracy rate is notably higher than previous studies in Thai populations using other skeletal elements, such as the mandible (79.3%) [4]. Although some international studies, such as research on Japanese populations using cranial measurements, reported a higher accuracy of 93.9% [7], our result of 86.0% classification accuracy for males (88.0%) compared to females (84.0%). This suggests that male crania in the Northeastern Thai population exhibit more pronounced "robust" features that the model can identify more easily. The cross-validation results demonstrated a slight reduction in accuracy, with a 4.0% shrinkage observed in females (from 84.0% to 80.0%). This level of reduction is considered acceptable and indicates good model stability, suggesting that the equation is not overfitted and can be generalized to similar populations.

The variation in results across different studies highlights the importance of population specificity. Factors such as genetics, environmental conditions, and lifestyle contribute to unique skeletal patterns [13,14]. Therefore, the sex estimation equation developed here is an appropriate tool for forensic use in Northeastern Thailand.

Conclusion

In conclusion, this research provides a vital regional database and a high-accuracy tool for sex estimation. By utilizing these specific human skull parameters, forensic anthropologists can develop a more precise biological profile, significantly improving the efficiency of human identification in the Thai justice system.

Acknowledgements

The authors would like to gratefully acknowledge the Unit of Human Bone Warehouse for Research (UHBWR), Department of Anatomy, Faculty of Medicine, Khon Kaen University, for

their support and for allowing the collection of skeletal data, which was essential for the success of this study.

References

1. Robinson MS, Bidmos MA. The skull and humerus in the determination of sex: reliability of discriminant function equations. Forensic Sci Int. 2009;186(1-3):86.e1-5.
2. Spradley MK, Jantz RL. Sex estimation in forensic anthropology: skull versus postcranial elements. J Forensic Sci. 2011;56(2):289-96.
3. Monum T, Prasitwattanseree S, Das S, Siriphimolwat P, Mahakkanukrauh P. Sex estimation by femur in modern Thai population. Clin Ter. 2017;168(3):e203-7.
4. Nanta K. Determination of sex in Thai people using metrical analysis of the mandible. Veridian E-Journal, Science and Technology, Silpakorn University. 2015;2(1).
5. Sinthubua A, Ruengdit S, Das S, Mahakkanukrauh P. A new method for sex estimation from maxillary suture length in a Thai population. Anat Cell Biol. 2017;50(4): 261–4.
6. Rooppakhun S, Piyasin S, Vatanapatimakul N, Kaewprom Y, Sitthiseripratip K. Craniometric Study of Thai Skull Based on Three-Dimensional Computed Tomography (CT) Data. J Med Assoc Thai. 2010;93(1):90-8.
7. Hoshioka Y, Torimitsu S, Makino Y, Yajima D, Chiba F, Yamaguchi R, et al. Sex estimation from skull measurements of a contemporary Japanese population using three-dimensional computed tomography images. Int J Legal Med. 2025;139(1):389-91.
8. Laurent M, Antonio L, Sinnesael M, Dubois V, Gielen E, Classens F, et al. Androgens and estrogens in skeletal sexual dimorphism. Asian J Androl. 2014;16(2):213-22.
9. Kirmani S, Atkinson EJ, Melton LJ 3rd, Riggs BL, Amin S, S. K. Relationship of testosterone and osteocalcin levels during growth. J Bone Miner Res. 2011;26(9):2212-6.
10. Del Bove A, Menéndez L, Manzi G, Moggi-Cecchi J, Lorenzo C, Profico A. Mapping sexual dimorphism signal in the human cranium. Sci Rep 2023;13(1):16847.
11. Börjesson AE, Lagerquist MK, Windahl SH, Ohlsson C. The role of estrogen receptor α in the regulation of bone and growth plate cartilage. Cell Mol Life Sci. 2013;70(21):4023-37.
12. Plotkin LI, Bruzzaniti A, R. P. Sexual Dimorphism in the Musculoskeletal System: Sex Hormones and Beyond. J Endocr Soc. 2024;8(10):bvae153.
13. Swift L, Obertova Z, Franklin D. Demonstrating the empirical effect of population specificity of anthropological standards in a contemporary Australian population. Int J Legal Med. 2024;138(2):537-45.
14. Reddy Y, Sreekanth C, Reddy B, Kumar B. The Effect of Genetic and Environmental Factors on Craniofacial Complex-A Twin-Study. J Indian Orthod Soc.2011 ;45(3):105-9.

O-13

An Anatomy-Based Surgical Risk Tier for Inferior Vena Cava Anomalies and Precaval Right Renal Artery: A Risk-Oriented Anatomical Framework

Pattaratida Pattanatanee[1], Arada Chaiyamoon[2], Ukrit Rompsaithong[3], Pattama Amarttayakong[4], Jaturat Kanpittaya[5], Areeya Madsusan[1], Sukrit Sangkhano[1,6*]

[1] Department of Occupational Health and Safety, School of Public Health, Walailak University, Thasala, Nakhon Si Thammarat, Thailand

[2] Department of Anatomy, Faculty of Medicine, Khon Kaen University, Khon Kaen, Thailand

[3] Department of Surgery, Faculty of Medicine, Khon Kaen University, Khon Kaen, Thailand

[4] Faculty of Medicine, Mahasarakham University, Mahasarakham, Thailand

[5] Department of Radiology, Faculty of Medicine, Khon Kaen University, Khon Kaen, Thailand

[6] Pre-clinical Science Unit, School of Public Health, Walailak University, Thasala, Nakhon Si Thammarat, Thailand

*Corresponding author, e-mail: sukrit.sa@mail.wu.ac.th

Abstract

Background: Retroperitoneal vascular variants involving the inferior vena cava (IVC) and renal vessels are frequently identified on multidetector computed tomography (MDCT), yet their influence on surgical exposure is often described only qualitatively. This study introduces the Anatomy-Based Surgical Risk Tier (ABSRT) framework, conceptually derived from hazard stratification principles in occupational health, to systematically classify vascular variants as structural hazards within the operative field. **Objective:** The framework evaluates variants based on their spatial relationship to the renal hilar aortocaval surgical corridor, specifically focusing on the operative window, defined as the anatomical space between the aorta, IVC, and renal hilum where vascular control is achieved. **Methods:** A retrospective review of 4,424 contrast-enhanced abdominal MDCT obtained from a university hospital in Northeastern Thailand database over a ten-year period was conducted to identify and categorize complex variants. Variants were classified into three tiers: Tier 1 (low risk), located posterior to or outside the operative field; Tier 2 (moderate risk), adjacent to the field but not crossing the operative window; and Tier 3 (high risk), traversing the operative window or crossing major vascular structures. **Results**: identified 12 patients (0.27%) with complex variants, including left-sided IVC (n=1), duplicated IVC (n=6), duplicated IVC with interiliac vein (n=1), duplicated IVC with circumaortic left renal vein (n=1), double right renal artery (RRA) (pre- and postcaval RRA) (n=2), and solitary precaval RRA (n=1). According to the ABSRT framework, seven cases (58.30%) were classified as Tier 1, two (16.70%) as Tier 2, and three (25.00%) as Tier 3. Left-sided and duplicated IVC variants were consistently classified as Tier 1, whereas precaval RRA variants were categorized as Tier 3. **Conclusion:** The proposed ABSRT framework provides a structured and clinically applicable anatomical approach for interpreting MDCT findings, translating anatomical variation into actionable surgical risk within the renal hilar aortocaval corridor. This systematic stratification may support preoperative planning and improve surgical safety in retroperitoneal procedures.

Keywords *Inferior vena cava anomalies, Precaval right renal artery, Renal vascular variants, Surgical risk, Multidetector computed tomography*

O-14

Comparison of Gastroscopy and Equine Weight Tape Methods for Estimating Esophageal Length in Cross-Breed Horses

Phinidda Cha-umphol[1*], Natnaree Kaewsiri[1], Chapkit Chansamorn[2]
[1] Faculty of Veterinary Medicine, Mahanakorn University of Technology, 140 Cheum-Sampan Road, Kathumrai, Nongchok, Bangkok 10530 Thailand
[2] Faculty of Science, Mahanakorn University of Technology, 140 Cheum-Sampan Road, Kathumrai, Nongchok, Bangkok 10530 Thailand
[*]Corresponding author, e-mail: phinidda@mut.ac.th

Abstract

This study evaluates the correlation between two esophageal measurement techniques in cross-breed horses: gastroscopic examination (internal) and equine weight tape (external). While gastroscopy is recognized as a precise method for determining actual esophageal length, its routine application requires specialized anatomical knowledge and equipment. Therefore, this study aims to determine if external measurement can serve as a reliable and practical alternative for clinical assessment. Therefore, this pilot study aims to assess the correlation between esophageal length measurements obtained through two methods. The measurements are based on three anatomical segments of the esophagus. The cervical esophagus, from the throat latch (pharyngeal region) to the thoracic inlet (the entrance to the chest cavity). The thoracic esophagus, from the thoracic inlet to the 12th rib (or the margin of the diaphragm). The abdominal esophagus, from the 12th rib to the left 15th rib. The means of the esophagoscopy technique and the measuring equine weight tape technique are 111.88 ±14.97 centimeters and 119.63 ± 14.83 centimeters, respectively. And the correlation was found to be $R = 0.922$ (p-value < 0.001). The external measurement of esophageal segments is clinically important for approximate lesion localization, guiding safe instrumentation such as nasogastric intubation and gastroscopy. It is reducing the risk of esophageal injury, particularly in the thoracic and abdominal regions. It serves as a reference for detecting abnormalities such as strictures or dilatation of the esophagus. Meanwhile, endoscopy offers distinct advantages in providing direct visualization of the mucosal lining and ensuring accurate overall length measurements.

Keywords *Esophagus, Anatomy, Endoscope, Esophageal length*

Background

The esophagus is a muscular tube that forms part of the gastrointestinal tract. In horses, the esophagus is relatively long compared to those of many other animals (dog, cat, buffalo, and cattle). The esophagus runs the entire length of the neck, connecting the pharynx in the throat to the stomach in the abdomen. This anatomical arrangement ensures that food and water can be transported efficiently from the mouth to the stomach, even when the horse is grazing with its head down. The anatomy of the esophagus is commonly divided into three parts based on its location and anatomical relationships: the cervical, thoracic, and abdominal esophagus. (König and Liebich, 2020; DeVito, 2020)

The cervical esophagus in a horse starts at the pharyngeal region. This area is located where the head meets the neck, just behind the mandible, referred to as the throat latch. The thoracic esophagus starts at the thoracic inlet and then extends down the chest cavity, passing behind the heart and the lungs, and through the diaphragm. The abdominal esophagus starts at the diaphragm and then extends to the esophageal hiatus into the abdominal cavity. It is short and connects to the stomach at the lower esophageal sphincter (LES) or cardiac sphincter. The length of the esophagus in horses, including light horses and ponies, generally ranges from approximately 125 to 200 centimeters. This length can vary based on the side and breed of the horses or ponies. (AL-Taai, 2022; Stick, 2012)

The cervical esophagus is superficially located and accessible for palpation; it is important for the detection and management of choke or esophageal obstruction. In contrast, the thoracic esophagus lies deep in the thoracic cavity, and it is closely associated with heart and lungs. Instrument insertion was performed under sedation technique. If they error, they may result in mediastinitis and pleuritis. The abdominal esophagus is functionally important for anti-reflux via the lower esophageal sphincter (LES).

In addition to pathological changes of the esophagus, such as stricture or dilatation, the functional length of the esophagus may be altered. It may result in an inaccurate estimation of insertion depth during gastroscope or nasogastric tube placement.

Although esophageal endoscopy (gastroscopy) is considered the gold standard for visualization and accurate measurement, it has limitations in distinguishing the boundary between the thoracic and abdominal esophagus, particularly at the esophageal hiatus, where anatomical landmarks cannot be clearly identified from endoscopic images alone. As a result, localization of lesions in the distal esophagus may remain uncertain. (Drozdzewska *et al.,* 2020; Loftin *et al*., 2017).

Other methods for measuring the esophagus in horses, like barium swallow studies and imaging techniques (such as ultrasound or radiography), may also be used. Using an equine weight tape measure is a non-invasive approach because it is a method to estimate the length of the esophagus from outside the horse's body. Measure from the throat (below the larynx) along the neck, across the chest cavity, and to the 12th rib. This technique can be particularly useful for a quick, rough estimate in field conditions where advanced diagnostic tools are unavailable.

This pilot study aimed to compare the accuracy and correlation between esophageal endoscopic measurement and external measurement by the equine weight tape method for determining the esophagus length in cross-breed horses.

Materials and Methods

Subjects

Eight cross-breed horses at faculty veterinary medicine of Mahanakorn University of technology are the sample will be selected for this pilot study.

Methods

A flexible gastroscope (Endoscope-Olympus CV-60; model OSF-V60) is inserted through the horse's nasopharynx and advanced down the esophagus (fasting 12-24 hours, sedation with xylazine hydrochloride 0.5 mg/kg IV). The gastroscope allows visualization of the esophageal lining and can also measure the length of the esophagus with a measurement scale.

External measurement by equine weight tape to identify anatomical landmarks. The throat latch is the area where the throat meets the base of the neck, where the esophagus starts. The thoracic inlet is the anatomical area where the neck transitions into the thoracic region, just above the withers. The diaphragm in a horse is a large, dome-shaped muscle located between the ribcage, and its upper border aligns roughly with the 12th Rib, which is a landmark for the diaphragm. The abdominal esophagus is short and connects to the stomach, and its upper left border aligns roughly with the 15th Rib. All procedures were approved by the Animal Care and Use Committee of Mahanakorn University of Technology (ACUC-MUT-2025-006.1).

Table 1 The physical appearance of cross-breed horses

Sample	Weight (kg)	Height (cm)	Chest size (cm)	Point of shoulder-buttock (cm)
H1	313	126	158	134
H2	466	150	172	152
H3	362	144	168	142
H4	295	154	155	138
H5	389	154	166	148
H6	290	146	165	148
H7	382	152	184	159
H8	180	136	138	142
Mean	334.65	145.52	163.25	145.38

Table 1 presents the physical appearance (weight, height, chest size, body length) and size of the eight samples. The sample population had an average weight of 334.65 kg, an average height of 145.52 cm, and an average chest circumference of 163.25 cm. The body length, measured from the highest point of the shoulder to the highest point of the buttocks, was 145.38 cm.

Data collection

Record the measurement from both methods for each horse. A veterinary anatomist team performed all procedures.

Statistical Analysis

The paired t-tests are used to compare the meaning of the two methods. The Pearson correlation analysis determines the strength and direction of the relationship between the two sets of measurements.

Results and Discussion

The results obtained from external measurement using an equine weight tape in eight horses are presented in Table 2.

Table 2 The length of each part of esophagus externally using a measuring equine weight tape

Sample	Cervical (cm)	Thoracic (cm)	Abdominal (cm)
H1	33	66	14
H2	56	66	16
H3	42	70	14
H4	38	62	17
H5	52	72	20
H6	56	80	14
H7	60	78	24
H8	52	74	20
Mean	48.63	71	17.38

Table 2 The eight sample horses had an approximate length of 48.63 cm from the throat to the entrance of the thoracic inlet refer cervical part, and 71 cm from the thoracic inlet to the 12th rib refer thoracic part. And the average length from the 12th rib to the 15th rib was 17.38 cm refer abdominal part.

The results of esophageal length measurement using gastroscopy, based on internal visualization (A-E) in Fig. 1 and scale markings on the endoscope, are presented in Table 3.

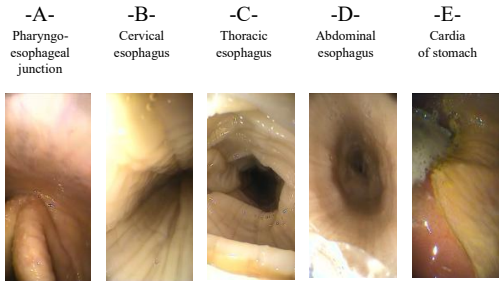

Fig. 1 The mucosal surface of esophagus

Fig 1A shows the location of the proximal end of the esophagus (pharyngoesophageal junction). Fig. 1B-C-D shows the mucosal surface of the cervical, the thoracic and the abdominal part of esophagus, respectively. Fig. 1E shows the terminal end of the esophagus at the cardiac sphincter. But the endoscopic technique cannot measure each esophageal portion.

Based on the results of both measurement methods, external measurements consistently produced greater esophageal length values compared to endoscopic measurements. This discrepancy may be attributed to the inclusion of overlying anatomical structures, including skin, muscle, and skeletal components, in the external approach. Correlation analysis revealed a variable relationship between the two methods, as illustrated in Fig. 2, from which the corresponding equation was derived.

The mean esophageal length measured by esophagoscopy was 111.88±14.97 cm, while the external measurement using equine weight tape was 119.63±14.83 cm (Table 4). A paired t-test revealed a statistically significant difference between the two methods ($t = -3.732$, $df = 7$, $p = 0.007$); the external method overestimates.

Table 3 Esophagus length measurements

Sample	Esophagoscopy scale (cm)	Equine weight tape (cm)
H1	94	99
H2	106	122
H3	95	112
H4	100	100
H5	120	124
H6	130	136
H7	130	138
H8	120	126
Mean	111.88	119.63

Table 4 The paired t-tests compare means of the two methods

	Mean	N	SD	Std. Error
Pair				
-esophagoscopy	111.88	8	14.97	5.29
-Equine weight tape	119.63	8	14.83	5.24

The systematic overestimation of esophageal length by external measurement (+ 17.4 cm) reflects the anatomical reality of measuring across muscular and skeletal structures. While the endoscope follows a relatively linear internal trajectory (Fig. 2).

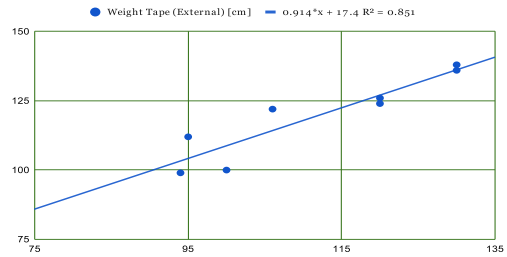

Fig. 2 The Linear regression of the relationship between the two measurement methods.

In addition, Pearson's correlation analysis (Table 5) was conducted to evaluate the strength and direction of the relationship between the two measurement methods. The result showed a strong positive correlation between esophagoscopy and measuring tape measurements (r=0.922, p=0.001).

Table 5 The Pearson correlation analysis between the two sets of measurements

	Esophagoscopy	Measuring tape
Esophagoscopy		
Pearson	1	0.922**
Correlation		.001
Sig (2-tailed)	8	8
N		
Measuring tape		
Pearson	0.922**	1
Correlation	.001	
Sig (2-tailed)	8	8
N		

Conclusion

The external measurement using anatomical landmarks remains essential, particularly in field practice, where physical palpation of the ribs provides a reliable reference. Meanwhile, endoscopy offers distinct advantages in providing direct visualization of the mucosal lining and ensuring accurate overall length measurements.

Acknowledgements

The authors especially thank Dr. Teerapol Chinkangsadarn and all cross-breed horses at the Faculty of Veterinary Medicine, Mahanakorn University of Technology.

References

1. AL-Taai, S.A.H. 2022. Esophagus. In: Pharynx-The Incredible Rendezvous Sites of Gas, Liquid and Solid. In Tech Open: EU. p.1-9.
2. DeVito, F.C. 2020. Horse Anatomy Coloring Book. Independently Published: USA. 154 pp.
3. Drozdzewska, K., Potocnik, E. and Schwarz, B. 2020. Nasogastric Intubation as Health and Safety Risk in Equine Practiced-A Questionnaire. *Journal of Equine Veterinary* Science. 88:102951.
4. Fubini, S.L. 2019. Esophagus. In: Equine Surgery. p.474-496.
5. König, H.E. and Liebich, H. 2020 .Veterinary Anatomy of Domestic Animals. 7th ed. Georg Thieme Verlag KG: Germany. 858pp.
6. Loftin, P., Cartmill, J. A. and Andrews, F.M. 2017.
7. Gastroscopy and Esophagoscopy. In: Manual of Clinical Procedures in the Horse. Wiley-Blackwell: USA. p.195–200.
8. Stick, J.A. 2012. Esophagus. In: Equine Surgery. 4th ed. Saunders Elsevier Inc.: USA. p.367-388.
9. Slovis, N.M. 2004. Atlas of Equine Endoscopy. Mosby Elsevier. USA. 254 pp.

O-15

Discrepancy Between Anatomical Renal Artery Length and Functional Surgical Space: A Preliminary Cadaveric Study

Tanathip Buadang[1], Pitcha Praprukdee[1], Chanoknan Pamorn[1], Pattarapon Suaygad[1], Panawich Jirachotthamrongkul[1], Supphawit Phanmekhakun[1], Sukrit Sangkhano[1,2*]
[1] Department of Occupational Health and Safety, School of Public Health, Walailak University, Thasala, Nakhon Si Thammarat, Thailand
[2] Pre-clinical Science Unit, School of Public Health, Walailak University, Thasala, Nakhon Si Thammarat, Thailand
*Corresponding author, e-mail: sukrit.sa@mail.wu.ac.th

Abstract
Background: Renal artery length is frequently reported in anatomical and surgical studies and is often considered during operative planning. However, in minimally invasive renal surgery, the arterial segment actually available for vascular clamping may be limited by the spatial relationships within the renal hilum, particularly by overlapping with the renal vein. **Objective:** This study aimed to evaluate the discrepancy between the anatomical renal artery length and the functional surgical space (FSS) relevant to arterial clamping. **Methods:** Ten cadavers (20 arteries) were examined. The anatomical renal artery length was measured from the aortic origin to the first branching point. The functional surgical space of the renal artery (FSS-RA) was measured and defined as the longest uninterrupted arterial segment visible from an anterior approach without venous retraction, with visibility defined as the absence of renal vein overlapping along the entire segment. Clamp feasibility was defined as FSS ≥15 mm. Median values were used to describe the measurements because of the skewed distribution of functional space. **Results:** The median anatomical renal artery length was 31.44 mm, whereas the median FSS-RA was only 7.01 mm. Clampable main renal arteries (FSS ≥15 mm) were observed in 5 kidneys (25%). Notably, 12 kidneys (60%) demonstrated anatomically adequate arterial length (≥20 mm) but insufficient functional surgical space (<15 mm). **Conclusion:** A substantial discrepancy exists between anatomical renal artery length and the FSS. In this study, FSS is presented as an applied anatomical parameter that may better represent the clampable arterial segment within the renal hilum than conventional morphometric measurements. This preliminary cadaveric study suggests that FSS-RA may better represent the clampable arterial segment within the renal hilum; however, further studies with larger samples and standardized assessment are warranted.

Keywords *Renal artery, Functional surgical space, Vascular clamping*

O-16

Early Histopathological Alterations in the Trachea of Streptozotocin-Induced Short-Term Diabetic Rats

Nitchanan Kitlertbanchong[1], Sani Baimai[1]*, Jirat Boonmameepool[2], Onsri Boonraksornpitak[1], Chutikan Kaensa[1]
[1] Department of Anatomy, Faculty of Medicine Siriraj Hospital, Mahidol University, Bangkok, Thailand, 10700
[2] Faculty of Allied Health Sciences, Burapha University, Chonburi, Thailand, 20131
*Corresponding author, e-mail: sani.bai@mahidol.ac.th

Abstract
Background: Diabetes mellitus (DM) induces systemic inflammation and oxidative stress that affect multiple organs, including the respiratory system. Although pulmonary and bronchial changes in DM are well documented, the trachea remains poorly studied. As a structurally distinct airway segment with pseudostratified ciliated epithelium and C-shaped hyaline cartilage rings, the trachea may be particularly susceptible to early metabolic insults. Identifying early tracheal structural changes could improve understanding of airway complications in DM. **Objective:** To determine whether short-term (4 weeks) streptozotocin (STZ)-induced hyperglycemia leads to early histopathological alterations in the rat trachea. **Methods:** Male Sprague–Dawley rats were randomly assigned to diabetic-short (DM-S) and control-short (C-S) groups (n = 12 per group). Diabetes was induced by a single intraperitoneal injection of streptozotocin (60 mg/kg) and confirmed by persistent hyperglycemia (>300 mg/dL). After 4 weeks, tracheal tissues were collected, processed as semithin sections (1.5 μm) for light microscopy, stained with hematoxylin and eosin and toluidine blue, and evaluated by blinded observers using qualitative and semi-quantitative assessment based on predefined histopathological criteria. **Results:** Compared with C-S rats, DM-S rats showed early tracheal epithelial changes, including focal desquamation, partial ciliary loss, and epithelial flattening, accompanied by mild lymphocytic infiltration. Occasional goblet cell metaplasia and slight submucosal gland hypertrophy were observed, while cartilage structure remained intact. Semi-quantitative assessment based on predefined criteria demonstrated increased epithelial injury and inflammatory changes in DM-S rats compared with C-S rats. **Conclusion:** Short-term DM induces early histopathological alterations in the trachea, suggesting that airway remodeling in diabetes may begin earlier than previously recognized. These findings highlight an underexplored aspect of diabetic airway involvement and provide preliminary evidence of early tracheal susceptibility to metabolic injury.

Keywords *Diabetes mellitus, Trachea, Histopathology, Streptozotocin, Airway remodeling*

O-17

Homogeneity of Mammary Epithelial Cells in Goat Milk-Derived *In Vitro* Culture

Shin Homsahwat[1#], Chanatpong Kankong[1#], Siwakorn Maiseaumsook[1#], Nawin Chanthra[2], Thanvarin Thitiphatphuvanon[3], Chomdao Sinthuvanich[4], Witchukorn Phuthong[5], Thao Phuong Trang[6], Prapatson Komsathorn[6], Sutthasinee Poonyachoti[6], Narongsak Chaiyabutr[6,7,8], Thomas A Lutz[9], Sapon Semsirmboon[10,11*], Sumpun Thammacharoen[6*]
[1] Faculty of Medicine, Kasetsart University.
[2] Department of Biochemistry and Genetic Engineering, Faculty of Medicine, Kasetsart University.
[3] Department of Anatomy, Faculty of Medicine, Kasetsart University.
[4] Department of Biochemistry, Faculty of Science, Kasetsart University
[5] Department of Physics, Faculty of Science, Kasetsart University.
[6] Department of Physiology, Faculty of Veterinary Science, Chulalongkorn University.
[7] The Academy of Science, The Royal Society of Thailand
[8] Queen Saovabha Memorial Institute, The Thai Red Cross Society.
[9] Institute of Veterinary Physiology, Vetsuisse-Faculty, University of Zurich
[10] Department of Physiology, Faculty of Medicine, Kasetsart University.
[11] Department of Anatomy, Faculty of Veterinary Science, Chulalongkorn University.
[#]These authors contributed equally.
*Corresponding author, e-mail: sapon.s@chula.ac.th, sumpun.p@chula.ac.th

Abstract

Mammary epithelial cells (MECs) are specialized cells essential for milk biosynthesis and secretion. As the global dairy sector faces increasing sustainability challenges related to greenhouse gas emissions, water consumption, and ethical concerns, cell-based milk production has emerged as a promising alternative. Goat milk provides a valuable biological model due to its high cellular content, comparable nutritional profile to cow milk, and superior digestibility in sensitive populations. Unlike tissue-based isolation, milk-derived MECs offer naturally purified sources with minimal contamination by non-milk-producing cells. MEC subtype composition and spatial distribution within culture are critical for scalable production. This study investigated whether distinct MEC subtypes exist in milk-derived cultures and validated a robust counting methodology. Mammary epithelial cells were characterized by cytokeratin-18 (CK-18) and DAPI: CK-positive cells (milk-producing luminal epithelium) and CK-negative cells (non-producing cell types). Since this population exploration was laborious, we established a standardized counting protocol by validating three critical parameters: inter-examiner reliability, counting methodology (manual vs. ImageJ-assisted), and sampling area coverage. The agreement of each examiner and two counting methods ensures our robust observation system. In fact, CK-negative cells represented <1% of total cells—substantially lower than in tissue-derived cultures (7–33%)—and proportions remained consistent across all sampling areas. Together with a good agreement of each area coverage counting, it suggested that producing MECs were a majority and were homogenously distributed within the culture. These findings demonstrate that this current isolation and culture offer a significant advantage in purification and a homogenously distributed culture.

Keywords *Breast, Capra milk, Cellular agriculture, Mammary epithelial cells, Myoepithelial cells*

Background

Goat milk has gained attention as an alternative to cow's milk, offering similar nutritional value and better tolerance in individuals with cow's milk allergy or digestive problems. Besides, milk plays a vital role in supporting infant development and elderly health, and it is widely used as a key ingredient in medical nutrition products for treating malnutrition, particularly in developing countries where access to protein and calcium is limited.

Despite its importance, the dairy industry faces sustainability challenges including greenhouse gas emissions, water use, and climate change. Laboratory-based milk production has therefore emerged as a promising alternative. Since some cell lines lose their ability to produce milk components over time, the continuous source of milk-producing cells, primary mammary epithelium cells (MECs), is one of the big challenges for industrial scale. Even though MECs can be isolated from both tissue and milk, the latter has the advantage of lower contamination from non-producing cells. With milk as a non-invasive source, MECs could be continuously harvested from live animals.

Within milk, MECs can be classified by their function into two types: milk-producing cells and non-producing cells. The proportion and distribution of these MECs within each culture directly affect the scalability of the production procedure. This current study aimed to investigate the composition of types of MECs and their distribution within the culture.

Materials and Methods

Isolation and culture of goat mammary epithelial cells

Fresh goat milk was collected and centrifuged at 300 × g for 10 min at 4°C. The pellet was washed four times with PBS and resuspended in DMEM/F12 supplemented with 10% FBS, 1% penicillin-streptomycin, and 10 ng/mL EGF. Cells were cultured in T25 flasks at 37°C with 5% CO_2. The media was changed every three days until reaching ~80% confluence.

Characterization of cells

To characterize milk-producing cells, isolated cells were seeded in 96-well plates and stained with a specific marker CK-18. After 80% confluence, cells were fixed with 4% paraformaldehyde and permeabilized with 0.1% Triton X-100. Then, they were incubated with rabbit anti-human CK-18 (1:200, Abcam) and donkey anti-rabbit IgG AlexaFluor 555 (1:200, Abcam). Nuclei were counterstained with DAPI (1:500). Images were acquired with a fluorescence microscope and analyzed using ImageJ. Cells that stained both CK-18 and DAPI were classified as CK-18 positive cells, while others were classified as CK-18 negative cells.

Cell homogeneity

Cell populations were randomly captured under 400x magnification for 30 areas from each goat at the 3rd, 5th, and 7th passage using Leica Application Suite X (LAS X). The number of positive and negative CK-18 cell of each area were independently counted by three examiners using ImageJ and averaged to calculate the proportion. The agreement of person, counting technique, and area coverage was validated. To validate both examiner and counting techniques, three examiners were trained with an example morphology image and assigned to do a preliminary count within the same picture for 50 pictures across all goat samples using manual counting and assisted software. Regarding the area coverage, three counting procedures under 400x magnification, including 30 random areas (R30), 60% coverage area of the well, and 100% coverage (whole well capture), were carried out on 5 goats at the 3rd, 5th, and 7th passage (Fig. 1).

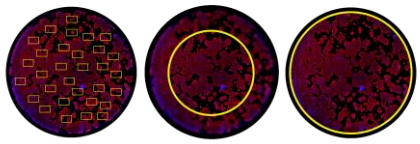

Fig. 1 The sampling area coverage methods: 30 random areas (a), 60% coverage (b), and 100% coverage (C).

Statistical analysis

Both positive and negative CK-18 cells were photographed with an Inverted Microscope DMi8 (Leica Microsystem, Wetzlar, Germany) equipped with a motorized stage. These cells were used to present as a proportion in each goat sample from three passages to represent the homogeneity of milk-MECs. The effect of one factor was investigated using Student's t-test, while the relationship between two factors was tested with the Chi-squared test. Additionally, the agreement between the two counting methods was examined by Pearson's correlation and Bland–Altman analysis.

Results and Discussion

In the mammary gland, luminal mammary epithelium forms a sphere surrounded by myoepithelium. This structure, called an acinus, stores secret milk. To secrete milk toward the nipple, myoepithelium contracts each acinus to pool milk within the gland cistern in preparation for sucking. Since these MECs are lining both the secretory (alveolar) portions and the conducting (ductal) portions, their desquamation is hypothesized to cause the presence of MECs in

milk. In addition to MECs, milk also contains many types of somatic cells, including red blood cells, lymphocytes, macrophages, and monocytes. Our isolation depends on the differences in cell attachment. Then, suspension cells such as lymphocytes and red blood cells were expected to be excluded by the washing step after 24 hours of culture. Regarding adherent cells, monocytes and macrophages within the organ are mostly considered terminally differentiated cells incapable of proliferation. These would be outnumbered by other proliferative cells such as MECs and fibroblasts. This fibroblast cell is a common adherent cell found in mammary gland tissue culture. However, our previous publication confirmed the absence of fibroblasts when using milk-cell isolation. This current isolation yielded only one type of morphology, which was a monolayer of cuboidal to polygonal cells. These are consistent with our previous publication, in which the isolation techniques did not yield fibroblast cells (Vimentin-positive cells). Therefore, this suggested that MECs could be solely isolated from milk, and their growth was enhanced by our culture procedure.

Mammary epithelial cells are classified by their function into two main types: luminal epithelium and myoepithelium. Since the luminal epithelium cell type is responsible for milk synthesis, its presence affects production. These cells are characterized by colocalization of cytokeratin-18 and nucleus staining (DAPI). Unlike luminal epithelium, CK-18-negative cells were recorded as a separate population, which may include basal or myoepithelial Cells (Fig. 2). Lack of this specific subtype of MECs identification is our limitation, and it should further be confirmed by the colocalization of cytokeratin 14 and alpha-smooth muscle actin. To further investigate their proportion and distribution, counting was required. Interestingly, nucleus size varies, and non-milk-producing cells were assumed to present a very small proportion. These factors could directly affect the counting accuracy, especially the software-assisted counting procedure. To validate the counting technique, we focused on inter-examiner reliability, counting methodology (manual vs. ImageJ-assisted), and sampling area coverage.

According to the result, there was no significant effect of three examiners on the number of counts in all three categories, including CK-18 positive cell, CK-18 negative cell, and Total cell (*p*-value = 0.984, 0.348, and 0.982) (Fig. 3). The cell counts from the two counting procedures showed no significant difference in all three categories (CK-18 positive, CK-18 negative, and total cell; *p*-values = 0.828, 0.812, and 0.381) (Fig. 4) and strongly correlated (Table 1). Interestingly, the mean bias (cell^2/mL) from Bland–Altman analysis was close to zero with a narrow limit of agreement. This suggested that counting MECs could be assisted by ImageJ with our settings.

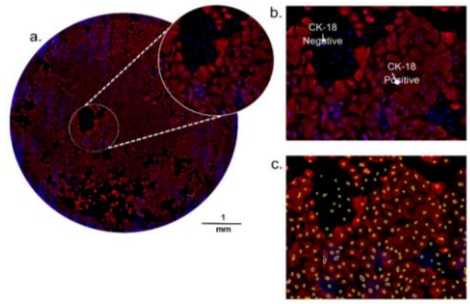

Fig. 2 Immunofluorescence staining of mammary epithelial cells isolated from goat milk, showing CK-18 (red) and nucleus (DAPI, blue). (a) Overall cell population under low magnification, (b) Representative field showing CK-18 positive and negative cells, and (c) Image analysis (ImageJ) highlighting identified nuclei for quantification.

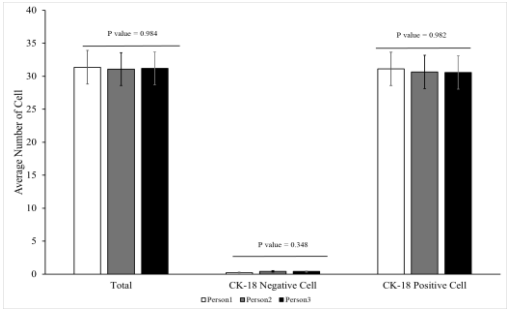

Fig. 3 Average cell counts of total cells, CK-18-positive cells, and CK-18-negative cells from three independent examiners.

Table 1 Bland Altman analysis of area 2 counting methods

Cell types	R^2	The mean difference between 2 counting methods		
		Means Bias (cell/cm^2)	Limits of Agreement	
			Lower	Upper
CK-18 Pos	0.99	-0.79	-4.75	3.17
CK-18 Neg	0.59	0.14	-0.76	1.04
Total Cell	0.99	-0.72	-3.76	2.31

Regarding population distribution within culture, heterogeneous distribution with a low number of MEC types could interfere with the study of the population. To validate this, the agreement between two different-sized sampling areas (area of coverage) was carried out through Bland-Altman analysis. Even though the mean bias of CK-18 positive and total cells is high, that of negative cells was close to zero with a narrow limit of agreement (Table 2). The high density of CK 18 - positive cells in the center (60% coverage) would be responsible for the high mean bias and the wide limit of agreement between R30 and 60% coverage. In contrast, there was no relationship between area coverage and cell proportion (p-value = 0.0877, Fig. 5). This suggested that each MEC type was homogenously distributed with culture area, validating the use of R30 for assessing the cell proportion in further research. This robust methodology could be scaled toward batch monitoring of Laboratory-based milk production.

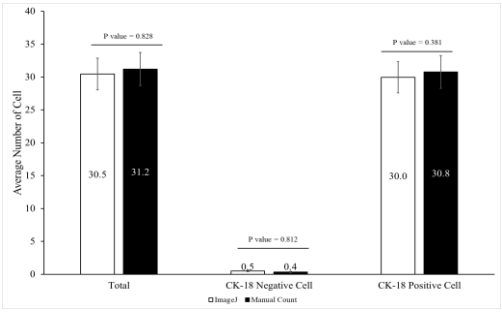

Fig. 4 Comparison of average cell counts (total, CK-18-positive, and CK-18-negative) between ImageJ-assisted (white bars) and manual counting (black bars).

Table 2 Bland Altman analysis of area coverage

Cell types	The mean difference between 2 counting areas		
	Means Bias (cell/cm^2)	Limits of Agreement	
		Lower	Upper
R30 and 60% coverage			
CK-18 Pos	83	-287.96	453.97
CK-18 Neg	0.76	-3.60	5.13
Total cell	83.50	-286.11	-293.38
R30 and 100% coverage			
CK-18 Pos	10.27	-236.36	256.91
CK-18 Neg	0.92	-4.05	5.89
Total cell	10.92	-239.38	161.38

Laboratory-based milk production requires cells that can continually produce. Although many MEC cell lines have been established, some have lost the capability to produce milk components. Then, sustainable harvesting from primary tissue could address these challenges. Invasive technique and batch variability limited the use of primary cells in a laboratory context. Using mammary gland tissue culture of dairy cow, the proportion of CK-18 positive cells ranged from 3 to 7 percent of the total cell population. The other types of cells accounted for less than 5 percent during early culture, but this increased to approximately 30 percent in the late culture. In contrast, the current culture showed consistently high proportions of CK-18 positive cells. The average proportion of CK-18 positive cells from three passages accounted for 99 percent of the population (Fig. 5).

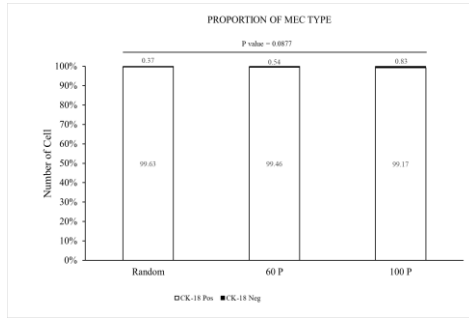

Fig. 5 Average proportions of CK-18-positive cells (white bars) and CK-18-negative cells (black bars) across three sampling areas.

Conclusion

This current technique could isolate MEC from milk and also promote the growth of CK-18 positive cells. Since CK-18 is a maker for luminal mammary epithelial cells, the majority type across three passages could be milk-producing cells. With these findings, we could establish a reproducible and ethically non-invasive method for isolating and maintaining goat MECs in vitro. Besides, their homogeneous distribution together with a robust counting system also benefits monitoring other aspects of cellular function.

Acknowledgements

This research was funded by Thailand Science Research and Innovation Fund, Chulalongkorn University (FOOD_FF 69 108_3100_009) and Research Development Program for Medical Students, Faculty of Medicine, Kasetsart University. We would also like to express

our gratitude to Dr. Nungnuch Saipin and Dr. Attapol Pornprapai for providing the commercial milk sample. Additionally, the culture procedure was collaboratively developed by Eva Bönzli at the Zentrum für Klinische Studien, Vetsuisse Faculty, University of Zurich.

References

1. Cravero D, Martignani E, Miretti S, Macchi E, Accornero P, Baratta M. Bovine mammary epithelial cells retain stem-like phenotype in long-term cultures. Res Vet Sci. 2014;97(2): 367–375.
2. Fu NY, Nolan E, Lindeman GJ, Visvader JE. Stem cells and the differentiation hierarchy in mammary gland development. Physiol Rev. 2020;100(2):489–523.
3. Kwon HC, Jung HS, Kim DH, Han JH, Han SG. Cellular characteristics and milk component productivity of primary bovine mammary cells for cell-cultured milk component production. J Anim Sci Technol. 2025;67(1):236–251.
4. Saipin N, Noophun J, Chumyim P, Rungsiwiwut R. Goat milk: Non-invasive source for mammary epithelial cell isolation and in vitro culture. Anat Histol Embryol. 2018;47(3):187–194.
5. Thammacharoen S, Semsirmboon S, Saipin N, Nguyen T, Kakhai C, Chaiyabutr N, et al. Mammary epithelial cells: Exploring the possibility of developing mammary organoids, artificial mammary glands, and mammary cell lines. Vet Integr Sci. 2025;24(2):1–1

O-18

Simvastatin Ameliorates Hypercholesterolemia and Sperm Quality but Fails to Restore Testicular Oxidative Defense in High-Fat Diet-Fed Rats

Siriporn Kreungnium[1,2], Kanyakorn Aitsarangkun Na Ayutthaya[1,2], Aubonwan Sitthikhankeao[1,2], Natthapong Khamaiam[1,2], Apichaya Niyomchan[3], Patcharada Amatyakul[4], Piyanee Sriya[5], Hiroki Nakata[6], Peter J Mark[7], Wai Chen[8], Kroekkiat Chinda[2,9,10], Kannika Adthapanyawanich[1,2,10], Yutthapong Tongpob[1,2,10*]

[1] Department of Anatomy, Faculty of Medical Science, Naresuan University, Phitsanulok, Thailand 65000

[2] Integrative Cardiovascular Research Unit (ICRU), Faculty of Medical Science, Naresuan University, Phitsanulok, Thailand 65000

[3] Department of Anatomy, Faculty of Medicine Siriraj Hospital, Mahidol University, Bangkok, Thailand 10700

[4] Department of Obstetrics and Gynecology, Faculty of Medicine, Naresuan University, Phitsanulok, Thailand 65000

[5] Department of Anatomy, Pramongkutklao College of Medicine, Bangkok, Thailand 10400

[6] Department of Clinical Engineering, Faculty of Health Sciences, Komatsu University, Ishikawa, Japan 923-0961

[7] School of Human Sciences, The University of Western Australia, Perth, Australia, 6009

[8] Curtin Medical School, and Curtin enAble Institute, Curtin University, Perth, Australia 6102

[9] Department of Physiology, Faculty of Medical Science, Naresuan University, Phitsanulok, Thailand 65000

[10] Centre of Excellence in Medical Biotechnology (CEMB), and AI CARE Research Cluster, Naresuan University, Phitsanulok, Thailand 65000

*Corresponding author, e-mail: yutthapongt@nu.ac.th

Abstract

Background: High-fat diet (HFD)-induced hypercholesterolemia impairs male reproductive function by promoting oxidative stress and suppressing testosterone synthesis. While statins possess antioxidant and anti-inflammatory properties beyond lipid-lowering, their effects on male reproductive dysfunction remain controversial. **Objective:** Therefore, we aimed to investigate the impact of simvastatin on sperm quality, testicular function, and oxidative stress in hypercholesterolemic rats. **Methods:** Male Wistar rats (n=18) were divided into normal diet (ND), HFD, and HFD plus simvastatin (40 mg/kg/day, oral gavage) groups. After 12 weeks of treatment, body weight, lipid profiles, sperm parameters, testicular histopathology, and testicular antioxidant enzyme activities were assessed. Data was analyzed using one-way ANOVA with Tukey's post-hoc test. **Results:** HFD increased body weight, serum cholesterol, and low-density lipoprotein levels (P<0.001 vs ND). Concurrently, sperm concentration and viability were markedly reduced (P<0.001, P<0.05 vs ND, respectively), accompanied by increased abnormality in testicular histopathology (P<0.05 vs ND) and decreased antioxidant enzymes, i.e., superoxide dismutase and catalase (P<0.05 vs ND), indicating oxidative stress. Simvastatin effectively reduced cholesterol and low-density lipoprotein levels (P<0.001 vs HFD) and increased sperm concentration (P<0.05 vs HFD). Simvastatin, however, failed to restore testicular histology and antioxidant enzyme activities of the testis. **Conclusion:** Despite simvastatin's effective lipid-lowering and improved sperm concentration, simvastatin showed limited protective effects on testicular oxidative stress and reproductive parameters in hypercholesterolemic rats. These findings revealed differential statin efficacy beyond cholesterol reduction, warranting comparative mechanistic studies to optimize therapeutic approaches for HFD-related male reproductive dysfunction.

Keywords *Hypercholesterolemia, Simvastatin, Male infertility, Oxidative stress, Spermatogenesis*

Background

Hypercholesterolemia induced by high-fat diet (HFD) consumption is associated with an increased incidence of metabolic disorders, characterized by elevated total cholesterol (TC), low-density lipoprotein cholesterol (LDL-C), and triglyceride (TG) levels, often accompanied by reduced high-density lipoprotein cholesterol (HDL-C) (1). In parallel, accumulating evidence indicates that HFD intake contributes to male infertility, which has become an increasingly significant global public health concern. This effect is mediated, in part, through reductions in testosterone levels, impaired spermatogenesis (2,3), and alterations in testicular morphology (4,5).

A HFD is also strongly associated with increased production of reactive oxygen species (ROS), which can overwhelm endogenous antioxidant defense systems. Excessive ROS generation leads to lipid peroxidation, mitochondrial dysfunction, and DNA damage (6,7). Such oxidative imbalance has been closely linked to reduced sperm concentration, decreased sperm motility, and compromised fertility outcomes (8). Furthermore, experimental studies demonstrate that HFD–induced metabolic disturbances elevate oxidative stress markers while concomitantly suppressing antioxidant enzyme activities in testicular tissue (6,7).

Statins are widely used lipid-lowering agents for the prevention and treatment of cardiovascular diseases. They exert their effects by inhibiting 3-hydroxy-3-methylglutaryl coenzyme A (HMG-CoA) reductase, the rate-limiting enzyme in cholesterol biosynthesis, thereby reducing endogenous cholesterol synthesis. As the most widely prescribed lipid-lowering agents, they are particularly valuable for obese patients, who often face additional risks such as hypertension and high cholesterol. These drugs improve lipid metabolism and reduce inflammation, thus enhancing cardiovascular health (9).

Simvastatin, a lipophilic HMG-CoA reductase inhibitor, is widely used in the management of hypercholesterolemia. Beyond its lipid-lowering effects, simvastatin has been reported to exert pleiotropic actions, including anti-inflammatory and antioxidant properties (10,11). Recent evidence suggests that statins may also protect against obesity-related organ damage through oxidative stress inhibition. Chen et al. (2025) recently demonstrated that atorvastatin, another HMG-CoA reductase inhibitor, protected against HFD-induced testicular dysfunction by reducing oxidative stress, enhancing testosterone synthesis, and preserving blood-testis barrier integrity in mice (7). However, the impact of statins on male reproductive function remains controversial. Clinical and experimental studies have demonstrated inconsistent effects of simvastatin on sperm parameters, testosterone levels, and oxidative stress markers (12,13). While some reports suggest potential adverse effects, others indicate neutral or minimal impacts on semen quality (14,15). The differential effects between various statins (e.g., lipophilic simvastatin versus atorvastatin) and across different experimental models warrant further investigation.

This study aimed to investigate the effects of simvastatin on male reproductive dysfunction induced by HFD–induced hypercholesterolemia in male rats.

Materials and Methods

Animals and treatment

Eighteen male Wistar rats (*Rattus norvegicus*), aged 7 weeks and weighing 250–350 g, were obtained from Nomura Siam International Co., Ltd., Bangkok, Thailand. The animals were housed under specific pathogen-free conditions with controlled environmental parameters, including a temperature of 22 ± 1 °C, relative humidity of 50 ± 5%, and a 12-h light/dark cycle, with ad libitum access to food and water. All experiments were approved by Naresuan University Animal Care and Use Committee (NUACUC), Phitsanulok, Thailand (ethical approval number: NUAE 660101), and were conducted in accordance with institutional guidelines for the care and use of laboratory animals. After a 7-day acclimatization period, the rats were randomly assigned into three groups: receiving a normal diet (ND), a high-fat diet group (HFD), receiving high fat diet (HFD), and receiving HFD + simvastatin 40 mg/kg/day (HFD+SIM) by oral gavage for 12 weeks. Body weight, food, and water intake were recorded daily throughout the experimental period. Behavioral observations were performed regularly to assess the general health and welfare status of the animals.

Lipid profile analysis

After 12 weeks of treatment, the rats were fasted for at least 12 hours and subsequently anesthetized with 100 mg/ml sodium thiopental by intraperitoneal injection. Then, serum was collected from thoracic inferior vena cava. Then, the serum was isolated by centrifugation at 3,000 rpm for 10 minutes at 4°C. The levels of TC, LDL-C, TG, and HDL-C were measured in the serum obtained from the blood samples. These assessments were performed using the enzyme-linked immunosorbent

assay (ELISA) method at the Biolab Medical Technology Clinic in Phitsanulok, Thailand.

Sperm collection and sperm quality evaluation

Rats were sacrificed, and the testes were collected and weighed. Semen was obtained from the cauda epididymis and diluted in 2 mL of prewarmed phosphate-buffered saline (PBS; pH 7.4, 38°C). A 10 µL sample was placed on a Makler counting chamber, where mature spermatozoa were observed and counted under 100X magnification using a light microscope. The counted sperm was used to calculate sperm concentration ($\times 10^6$ cells/mL) based on a previously described method (16). Sperm viability was assessed using eosin-nigrosin staining, where unstained sperm were classified as live and those stained pink or red as dead. The percentage of live sperm was calculated to determine sperm viability, as previously described (17). Sperm motility was assessed microscopically and expressed as the percentage of motile sperm. Observations were performed under a light microscope at a magnification of 100X. At least 200 spermatozoa were counted per sample, and the number of motile sperm was recorded to calculate the percentage of sperm motility.

Testicular histopathological analysis using hematoxylin and eosin (H&E) staining

The left side of the testicle was promptly preserved in 4% paraformaldehyde solution (pH 7.4). After fixation, the samples were dehydrated through a graded series of ethanol, cleared in xylene, and embedded in paraffin. Serial cross-sections of 3 µm thickness were obtained using a rotary microtome (Leica RM2235, Leica Biosystems, Germany). A minimum of two sections per animal were prepared for the staining method. The sections were deparaffinized and rehydrated. For H&E staining, sections were stained with hematoxylin for 8 min, rinsed under running tap water, and differentiated and blued in 1% lithium carbonate solution. After washing, the sections were counterstained with eosin for 30 sec, dehydrated through graded ethanol, cleared in xylene, and mounted with a coverslip using a synthetic resin. The slides were observed and photographed using a light microscope to assess the histopathological alterations. Two sections per rat were analyzed for seminiferous tubule abnormalities, including separation of the germinal epithelium, vacuolization, luminal sloughing of germ cells, irregularly shaped seminiferous tubules, and tubular atrophy. The degree of histopathological alteration was expressed as the percentage of affected seminiferous tubules relative to the total number of tubules examined.

Assessment of testicular antioxidant defense

Testicular antioxidant defense was evaluated by measuring the activities of superoxide dismutase (SOD), catalase (CAT), and glutathione peroxidase (GPx) using commercially available assay kits according to the manufacturer's instructions (Cayman Chemical, Ann Arbor, MI, USA; Item No. 706002 for SOD, 707002 for CAT, and 703102 for GPx).

Briefly, testicular tissues were homogenized in cold phosphate buffer (pH 7.4) and centrifuged at 10,000xg for 15 min at 4°C to obtain the supernatant. The resulting supernatants were used for the determination of antioxidant enzyme activities. Total protein concentration was determined using a standard protein assay, and enzyme activities were normalized to protein content.

SOD activity was determined based on its ability to inhibit the reduction of tetrazolium salt by superoxide radicals generated by xanthine oxidase and hypoxanthine. The absorbance was measured at 460 nm using a microplate reader, and SOD activity was expressed as units per milligram of protein (U/mg protein).

CAT activity was assessed by measuring the decomposition rate of hydrogen peroxide (H_2O_2). The reaction was terminated using a catalase inhibitor, followed by the addition of chromogenic substrate, and the absorbance was read at 540 nm. CAT activity was expressed as units per milligram of protein (U/mg protein).

GPx activity was determined using a coupled enzymatic reaction in which GPx reduces hydroperoxide while oxidizing reduced glutathione (GSH) to oxidized glutathione (GSSG). Glutathione reductase then converts GSSG back to GSH with the concomitant oxidation of NADPH to $NADP^+$. The decrease in absorbance due to NADPH consumption was monitored at 340 nm, and GPx activity was expressed as units per milligram of protein (U/mg protein).

Statistical analysis

Data analysis was conducted using Prism software (Version 9. 0, GraphPad Software, CA, USA). Experimental results are presented as mean ± standard deviation (SD). Statistical comparisons between groups were performed using one-way ANOVA followed by Tukey's post hoc test for multiple comparisons. Differences were defined as statistically significant if the *P*-value was less than 0.05.

Table 1 Metabolic parameters data

Parameters	ND	HFD	HFD+SIM
Food intake (g/day)	23.72 ± 1.74	18.72 ± 1.16***	19.44 ± 0.54***
Water intake (mL/day)	34.71 ± 2.96	21.46 ± 0.99***	20.75 ± 1.84***
Body weight gain (%)	92.71 ± 20.84	121.40 ± 9.10**	124.40 ± 20.68*
Absolute testicular weight (g)	2.07 ± 0.06	1.99 ± 0.21	1.93 ± 0.16
Relative testicular weight (%)	0.42 ± 0.03	0.33 ± 0.02***	0.33 ± 0.02***

The effects of simvastatin on metabolic parameters in HFD-induced hypercholesterolemic rats. Mean ± Standard deviation; *P<0.05 vs ND, **P<0.01 vs ND, ***P<0.001 vs ND; One-way ANOVA followed by Tukey's post hoc test. (n=5-6/groups).

Results

Simvastatin did not affect animal behavior, but reduced food and water intake in HFD-induced hypercholesterolemic rats

All animals remained clinically normal throughout the experimental period. No observable alterations were noted in the skin, fur, eyes, or mucous membranes. In addition, no signs of behavioral abnormalities or treatment-related adverse effects were observed in any group, including tremors, convulsions, salivation, diarrhea, lethargy, coma, or mortality. Moreover, both food and water intake were reduced in the HFD and simvastatin-treated groups compared with the ND group (P < 0.001, Table 1).

Simvastatin did not significantly affect body weight gain and testicular weights in HFD-induced hypercholesterolemic rats

After 12 weeks of HFD feeding, male Wistar rats in both the HFD and HFD+SIM groups showed increased body weight gain (P < 0.01, P < 0.05, Table 1) and relative testicular weights (P < 0.001, P < 0.001, Table 1) compared to the ND group. These findings suggested that weight gain was associated with reduced testicular weight. Moreover, simvastatin treatment did not result in significant weight loss throughout the experimental period.

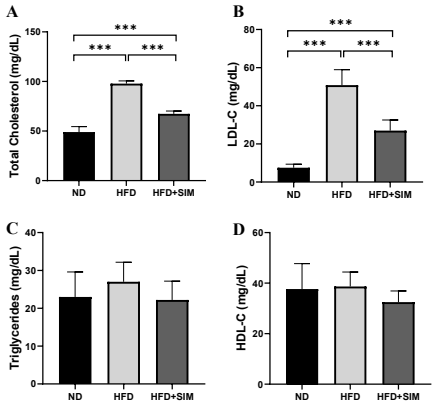

Fig. 1 Effects of simvastatin on (A) total cholesterol, (B) LDL-C, (C) triglycerides, and (D) HDL-C in HFD-induced hypercholesterolemic rats. Mean ± Standard deviation; ***P < 0.001; One-way ANOVA followed by Tukey's post hoc test. (n=5-6/groups).

Simvastatin lowered the lipid profile in HFD-induced hypercholesterolemic rats

Administration of a high-fat diet for 12 weeks, the HFD group markedly increased serum TC and LDL-C levels (P < 0.001 vs ND group, Fig. 1A and 1B). Treatment with simvastatin 40 mg/kg/day lowered serum TC and LDL-C (P < 0.001 vs the HFD group; Fig. 1A and 1B). However, no significant differences were observed in serum TG or HDL-C levels among the groups (Fig. 1C and 1D).

Simvastatin increased sperm concentration but did not improve sperm viability or motility in HFD-induced hypercholesterolemic rats

In this study, compared with the ND group, HFD-induced hypercholesterolemia reduced sperm concentration (P < 0.001, Fig. 2A) and viability (P < 0.05, Fig. 2B), but sperm motility remained unchanged (Fig. 2C).

Supplementation with simvastatin at a dose of 40 mg/kg/day significantly increased sperm concentration in HFD rats (P < 0.05). However, no significant improvement was observed in sperm viability or motility.

Simvastatin did not alter testicular histopathology in HFD-induced hypercholesterolemic rats

Structural abnormalities of the seminiferous tubules were evaluated according to predefined histopathological criteria (Fig. 3).

The percentage of normal seminiferous tubules decreased in the HFD group compared with the ND (P < 0.05, Table 2). Conversely, testicular abnormalities were increased in the HFD group (P

< 0.05, Table 2). Oral administration of simvastatin did not significantly restore testicular normality or reduce the percentage of abnormalities compared with the HFD group (Table 2).

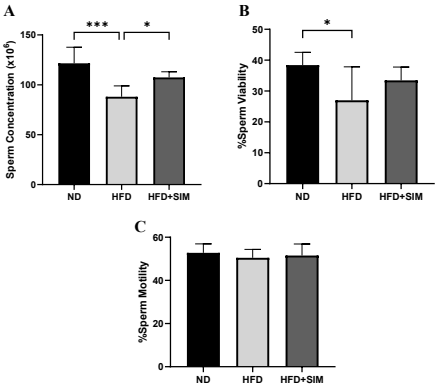

Fig. 2 Effects of simvastatin on sperm quality: (A) sperm concentration, (B) sperm viability, and (C) sperm motility in HFD-induced hypercholesterolemic rats. Mean ± Standard deviation; **P*<0.05, ****P*<0.001; One-way ANOVA followed by Tukey's post hoc test. (n=5-6/groups).

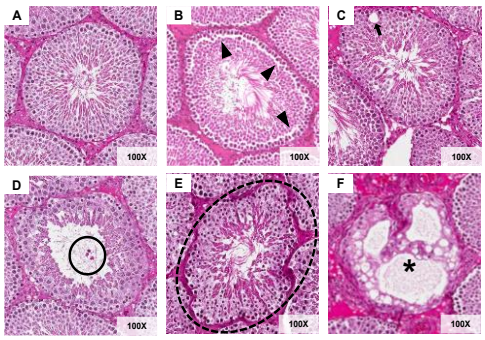

Fig. 3 Histopathological features of rat seminiferous tubules (H&E, 100X). (A) Normal seminiferous tubules with intact germinal epithelium. (B) Separation of the germinal epithelium (head arrows). (C) Vacuolization within the seminiferous epithelium (an arrow). (D) Luminal sloughing of germ cell (a circle). (E) Irregularities of a tubular wall (a circle dash). (F) Tubular atrophy (an asterisk).

Discussion

Lipid-lowering effects of simvastatin

As indicated by the results, hypercholesterolemia was successfully induced in rats by an HFD, as demonstrated by dramatic increases in body weight gain, serum total cholesterol, and LDL-C levels. Simvastatin is a second-generation lipophilic statin that is rapidly absorbed after oral administration, reaching peak plasma concentrations approximately 1–2 hours post-dose (18). The recommended adult dosage typically ranges from 10 to 40 mg per day, while the 80 mg dose is restricted to patients who have been receiving this regimen chronically without evidence of muscle toxicity (19).

In the present animal study, administration of simvastatin at a dose of 40 mg/kg/day significantly reduced serum total cholesterol and LDL-C levels. This lipid-lowering effect is consistent with the

Table 2 Histopathological alterations of seminiferous tubules

Parameters	ND	HFD	HFD+SIM
Normal seminiferous tubules (%)	74.34 ± 1.50	65.19 ± 6.31*	71.45 ± 5.93
Abnormal seminiferous tubules (%)	25.66 ± 1.50	34.81 ± 6.31*	28.55 ± 5.93
Vacuolization (%)	23.97 ± 1.63	26.80 ± 7.86	25.43 ± 5.19
Separation (%)	0.67 ± 0.68	6.68 ± 8.04	1.45 ± 1.09
Luminal sloughing (%)	0.33 ± 0.42	0.21 ± 0.21	0.42 ± 0.51
Irregular (%)	0.69 ± 0.33	1.12 ± 0.71	1.24 ± 1.56
Atrophy (%)	0.00 ± 0.00	0.00 ± 0.00	0.00 ± 0.00

The effects of simvastatin on histopathological alterations of seminiferous tubules in HFD-induced hypercholesterolemia rats. Mean ± Standard deviation; **P*<0.05 vs ND; One-way ANOVA followed by Tukey's post hoc test. (n=5/groups).

Simvastatin did not enhance testicular antioxidant defense in HFD-induced hypercholesterolemic rats

Our findings demonstrated a reduction in testicular antioxidant defense capacity (Fig. 4) in hypercholesterolemic male rats. Specifically, SOD and CAT activities (Fig. 4A, 4B) significantly decreased compared with the ND group (*P*<0.05), whereas GPx activity (Fig. 4C) showed no significant difference. Simvastatin treatment did not significantly alter SOD, CAT, or GPx activities compared with the HFD group.

known mechanism of simvastatin as an inhibitor of HMG-CoA reductase, which suppresses hepatic cholesterol synthesis and enhances LDL receptor expression, thereby increasing LDL clearance from the circulation (20). Similarly, Chen et al. (2025)

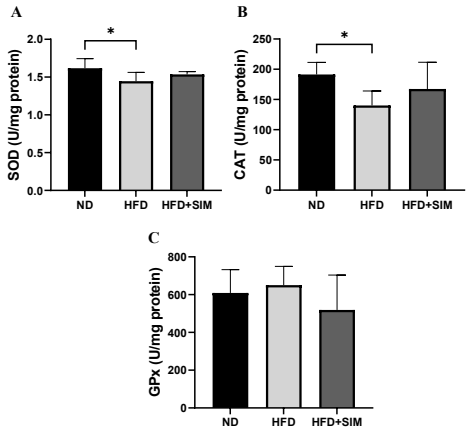

Fig. 4 Effects of simvastatin on antioxidants level; (A) SOD, (B) CAT, and (C) GPx in HFD-induced hypercholesterolemic rats. Mean ± Standard deviation; **P*<0.05; One-way ANOVA followed by Tukey's post hoc test. (n=5/groups).

demonstrated that atorvastatin treatment (3,6, and 12 mg/kg/day) produced dose-dependent reductions in serum cholesterol and triglycerides in HFD-fed mice (7), confirming the efficacy of HMG-CoA reductase inhibitors in managing diet-induced hyperlipidemia across different species and statin types.

In the present study, exposure to HFD-induced hypercholesterolemia resulted in a significant increase in body weight gain in rats, consistent with the obesogenic effects of HFD observed in rodent models of metabolic syndrome and diet-induced obesity (21). HFD feeding elevates overall energy intake and promotes adiposity, leading to progressive weight gain compared to animals fed a standard diet. Interestingly, despite the increased body weight, we observed reduced daily food and water intake in the HFD-induced hyper-cholesterolemic group. Although HFDs are energy dense, rats often consume less food by mass while maintaining or increasing total caloric intake, which reflects compensatory feeding behavior to satisfy energy requirements while reducing the volume of intake. Additionally, alterations in satiety hormones and central appetite regulation secondary to HFD feeding may suppress both food and fluid intake (22).

Effects on sperm parameters and testicular morphology

Consumption of an HFD contributes to the development of various metabolic disorders with high global prevalence and is associated with impaired male reproductive function, which includes reduced sperm quality, testicular dysfunction, and morphological changes (3,23,24). Previous studies demonstrated that HFD reduced sperm quality and impaired testicular morphology (3,25,26). These findings are consistent with the present study, further supporting the detrimental effects of HFD on semen parameters and testicular structures.

Notably, Chen et al. (2025) reported similar findings in mice fed a 60% HFD for 8 weeks, showing reduced sperm count and motility, increased sperm deformity rates, and abnormal testicular morphology with decreased Johnsen scores. Additionally, they also demonstrated that atorvastatin treatment at 6 and 12 mg/kg/day significantly improved these parameters in a dose-dependent manner (7). In contrast, our findings showed that while simvastatin (40 mg/kg/day) significantly increased sperm concentration, it did not improve sperm viability or motility. This discrepancy may reflect important differences between the two statins, the animal models employed (rats versus mice), or the duration of treatment (12 weeks versus 8 weeks).

A systematic review reported that statin therapy exerts variable effects on sperm concentration, motility, viability, and morphology, with several studies indicating that simvastatin administration does not significantly alter these parameters in individuals with hyper-cholesterolemia (14,15). Conversely, long-term treatment with pravastatin, another HMG-CoA reductase inhibitor, has been associated with reduced sperm motility after 6 and 12 months of therapy (13). These inconsistent findings across different statins suggest that individual pharmacological properties—such as lipophilicity, tissue penetration, and pleiotropic effects—may differentially influence reproductive outcomes (27).

Effects on testicular histopathology

The testicles can be damaged by metabolic disorders associated with hyperlipidemia; previous studies have also reported that high-fat and high-cholesterol diet–induced obesity can impair testicular morphology (3). In particular, experimental evidence from a 12-week HFD-induced obesity model showed marked structural changes in testicular tissue, characterized by reduced seminiferous tubular diameter and

epithelial height, reflecting impaired spermatogenic architecture (28). However, oral administration of simvastatin at a dose of 40 mg/kg did not ameliorate the histopathological alterations in spermatogenic cell integrity or restore the structural organization of the seminiferous tubules in hypercholesterolemic rats.

This finding contrasts with the results of Chen et al. (2025), who demonstrated that atorvastatin treatment significantly improved testicular histology, restored the thickness of the seminiferous epithelium, and increased Johnsen scores in HFD-fed mice (7). The protective effect of atorvastatin on testicular morphology was associated with enhanced expression of tight junction proteins (Occludin and ZO-1) at the blood-testis barrier and reduced apoptotic markers (decreased BAX/BCL2 ratio). These molecular changes were not observed with simvastatin in our study, suggesting potential mechanistic differences in how different statins interact with testicular tissue.

Testicular oxidative stress and antioxidant defense

Excessive production of reactive oxygen species (ROS) plays a crucial role in the histopathological alterations observed in the testicular structures. Elevated ROS levels can enhance lipid peroxidation and concurrently impair the endogenous antioxidant defense system (29), thereby contributing to oxidative imbalance and subsequent structural damage within the testicular tissue. This oxidative imbalance impairs membrane integrity, mitochondrial function, and DNA stability in germ cells. Consequently, elevated ROS levels can compromise sperm quality by reducing functional capacity, decreasing motility, and inducing DNA damage, ultimately leading to diminished fertility potential (29-31).

In our study, HFD-induced hyper-cholesterole-mia significantly reduced testicular antioxidant enzyme activities (SOD and CAT) while increasing oxidative stress, indicating the increase of oxidative stress within the testicular micro-environment. Notably, despite its lipid-lowering efficacy, simvastatin administration did not significantly increase SOD, CAT, or GPx activities in the testis of HFD-induced hypercholesterolemic rats.

This finding is particularly striking when compared to the results of Chen et al. (2025), who demonstrated that atorvastatin treatment significantly restored testicular SOD and GSH-px activities and reduced malondialdehyde (MDA) levels (a lipid peroxidation marker) in HFD-fed mice (7). Moreover, Chen et al. (2025) provided mechanistic evidence that atorvastatin's protective effects were mediated through the inhibition of oxidative stress and mitochondrial dysfunction, with concomitant downregulation of inflammatory markers (COX2 and iNOS) and restoration of antioxidant-related gene expression (SOD1, SOD2, GPX1, GPX2) (7). The inability of simvastatin to restore antioxidant capacity in our study suggests that the beneficial effects observed may not be mediated through restoration of the endogenous antioxidant defense system, at least under the present experimental conditions.

Previous reports have indicated that the antioxidant effects of different statins are variable and appear to be dose-, tissue-, and model-dependent, with significant changes observed in oxidative stress biomarkers. (32). The lipophilic properties of simvastatin may result in different tissue distribution and cellular uptake compared to atorvastatin, potentially explaining the differential effects on testicular oxidative stress markers. Additionally, the duration of treatment (12 weeks in our study versus 8 weeks in Chen et al.) and species differences (rats versus mice) may contribute to the observed variations in antioxidant response.

Comparison of simvastatin and atorvastatin effects

The divergent outcomes between our study and that of Chen et al. (2025) highlight important considerations regarding statin selection for managing obesity-related reproductive dysfunction. While both simvastatin and atorvastatin are lipophilic HMG-CoA reductase inhibitors, they differ in their pharmacokinetic profiles, tissue penetration, and pleiotropic effects. Atorvastatin demonstrated robust protective effects across multiple endpoints—including oxidative stress reduction, testosterone synthesis enhancement, blood-testis barrier preservation, and apoptosis inhibition (7). In contrast, simvastatin in our study showed more limited benefits, primarily affecting sperm concentration without restoring oxidative balance or histological integrity.

These differences may be attributed to several factors: (1) differential bioavailability and tissue distribution between the two statins; (2) variations in their antioxidant potencies independent of cholesterol-lowering effects; (3) species-specific responses (rats versus mice); (4) differences in dosing regimens and treatment durations; or (5) distinct mechanisms of mitochondrial protection. Chen et al. (2025) proposed that atorvastatin's protective effects were primarily mediated through mitochondrial oxidative stress inhibition (7), a mechanism that warrants investigation for simvastatin in future studies.

Study limitations and future directions

This study has several limitations that should be acknowledged. First, the study involved administering simvastatin at the start of an HFD, representing a preventive rather than a therapeutic model. Consequently, pathological alterations in the male reproductive system, including oxidative stress and testicular dysfunction, may not have been sufficiently established, which could explain the absence of significant differences observed among groups. Although statins inhibit HMG-CoA reductase and reduce circulating cholesterol levels—a key precursor for testosterone biosynthesis—compensatory mechanisms within Leydig cells may preserve androgen homeostasis under normal physiological conditions. Furthermore, the pleiotropic antioxidant and anti-inflammatory effects of statins are more pronounced in the presence of elevated oxidative stress, which may not have been fully developed in this preventive model. In addition, the relatively small sample size (n=6 per group) may limit the statistical power and generalizability of the findings. Second, important molecular markers associated with oxidative stress were not evaluated. Specifically, direct indicators of lipid peroxidation, such as malondialdehyde (MDA) (7), as well as markers of inflammatory responses and apoptosis signaling pathways (7,33), were not assessed. In addition, circulating testosterone levels were not measured, which limits the interpretation of the endocrine contribution to the observed alterations in spermatogenesis and testicular structure. The measurement of testosterone would have been particularly valuable given Chen et al.'s (2025) demonstration that atorvastatin significantly increased serum testosterone levels and upregulated key steroidogenic enzymes (StAR and P450scc) in HFD-fed mice (7).

Future studies should address these limitations by including a larger sample size and performing comprehensive biochemical and molecular analyses. Measurement of oxidative stress biomarkers (e.g., MDA and antioxidant enzyme activities), inflammatory cytokines (e.g., TNF-α, IL-6), apoptosis-related signaling markers (e.g., BAX/BCL2 ratio, caspase activation), and serum testosterone levels would provide deeper mechanistic insight. Additionally, direct comparison studies between different statins (simvastatin, atorvastatin, and other HMG-CoA reductase inhibitors) under identical experimental conditions would help elucidate the specific mechanisms underlying their differential effects on testicular function. Investigation of mitochondrial function markers, blood-testis barrier integrity proteins (Occludin, ZO-1), and dose-response relationships would further clarify the therapeutic potential of statins in preventing obesity-related male reproductive dysfunction. Integrating endocrine, histological, and molecular evaluations will allow for a more complete understanding of the pathways underlying testicular dysfunction and impaired spermatogenesis in HFD-induced hypercholesterolemic rats.

Conclusion

Simvastatin (40 mg/kg/day) effectively reduced serum lipid levels and increased sperm concentration in hypercholesterolemic rats but failed to restore testicular antioxidant defenses, sperm viability, motility, or histological integrity. In contrast to atorvastatin, which comprehensively protects testicular function through oxidative stress inhibition (7). These findings revealed that simvastatin appears to provide limited reproductive protection, even though it effectively lowers lipid levels. Critical differences in efficacy among these statins underscore the need for direct comparative studies to guide statin selection in hyper-cholesterolemic and dyslipidemic patients concerned about male fertility.

Acknowledgements

This research was partially supported by the Global and Frontier Research University Fund, Naresuan University (Grant Nos. R2566C053 and R2567C003); the Frontier Research and Innovation Cluster Fund, Naresuan University (Grant No. R2569C005); the Agricultural Research Development Agency (Public Organization) (Grant Nos. PRP6605031550 and R2566A091); and the Reinventing University Program 2023–2026, Ministry of Higher Education, Science, Research and Innovation (MHESI), Thailand (Grant Nos. R2567A147, R2568A037 and R2569A017). This work was supported by Naresuan University, and National Science, Research and Innovation Fund (NSRF) (Grant No. R2569B090).

The authors gratefully acknowledge the Faculty of Medical Sciences, Naresuan University, and the members of the ICRU for their continuous support throughout this research.

References

1. Maulana H, Ridwan A. High-Fat Diets-Induced Metabolic Disorders to Study Molecular Mechanism of Hyperlipidemia in Rats. 3BIO: Journal of Biological Science, Technology and Management. 2021.
2. Barbagallo F, Condorelli RA, Mongioì LM, Cannarella R, Cimino L, Magagnini MC, et al.

Molecular Mechanisms Underlying the Relationship between Obesity and Male Infertility. Metabolites. 2021;11(12):840.
3. Liu CY, Chang TC, Lin SH, Wu ST, Cha TL, Tsao CW. Metformin Ameliorates Testicular Function and Spermatogenesis in Male Mice with High-Fat and High-Cholesterol Diet-Induced Obesity. Nutrients. 2020;12(7).
4. Liu L, Zhang M, Jiang F, Luo D, Liu S, Su Y, et al. High cholesterol diet-induced testicular dysfunction in rats. Hormones (Athens). 2023; 22(4):685-94.
5. Liu CY, Chang TC, Lin SH, Tsao CW. Is a Ketogenic Diet Superior to a High-Fat, High-Cholesterol Diet Regarding Testicular Function and Spermatogenesis? Front Nutr. 2022;9: 805794.
6. Billah MM, Khatiwada S, Lecomte V, Morris MJ, Maloney CA. Ameliorating high-fat diet-induced sperm and testicular oxidative damage by micronutrient-based antioxidant intervention in rats. European Journal of Nutrition. 2022; 61(7):3741-53.
7. Chen Y, Gu L, Xiong Y, Liu Y. Protective effects of atorvastatin on testicular dysfunction and reduced sperm quality induced by high-fat diet in mice: The inhibitory mechanism of oxidative stress. European Journal of Pharmacology. 2025;992:177357.
8. Walczak-Jedrzejowska R, Wolski JK, Slowikowska-Hilczer J. The role of oxidative stress and antioxidants in male fertility. Cent European J Urol. 2013;66(1):60-7.
9. Haines BE, Wiest O, Stauffacher CV. The Increasingly Complex Mechanism of HMG-CoA Reductase. Accounts of Chemical Research. 2013;46(11):2416-26.
10. Bruder-Nascimento T, Callera GE, Montezano AC, Belin de Chantemele EJ, Tostes RC, Touyz RM. Atorvastatin inhibits pro-inflammatory actions of aldosterone in vascular smooth muscle cells by reducing oxidative stress. Life Sci. 2019;221:29-34.
11. Verma K, Makwana S, Paliwal S, Paliwal V, Jain S, Paliwal S, et al. Simvastatin ameliorates oxidative stress levels in HepG2 cells and hyperlipidemic rats. Curr Res Pharmacol Drug Discov. 2022;3:100088.
12. Azzarito C, Boiardi L, Vergoni W, Zini M, Portioli I. Testicular function in hypercholesterolemic male patients during prolonged simvastatin treatment. Horm Metab Res. 1996; 28(4):193-8.
13. Dobs AS, Schrott H, Davidson MH, Bays H, Stein EA, Kush D, et al. Effects of high-dose simvastatin on adrenal and gonadal steroidogenesis in men with hypercholesterolemia. Metabolism. 2000;49(9):1234-8.
14. Purvis K, Tollefsrud A, Rui H, Haug E, Norseth J, Viksmoen L, et al. Short-term effects of treatment with simvastatin on testicular function in patients with heterozygous familial hypercholesterolaemia. Eur J Clin Pharmacol. 1992; 42(1):61-4.
15. Dobs AS, Sarma PS, Schteingart D. Long-term endocrine function in hypercholesterolemic patients treated with pravastatin, a new 3-hydroxy-3-methylglutaryl coenzyme A reductase inhibitor. Metabolism. 1993;42(9): 1146-52.
16. Ferramosca A, Conte A, Moscatelli N, Zara V. A high-fat diet negatively affects rat sperm mitochondrial respiration. Andrology. 2016;4(3):520-5.
17. Akarca-Dizakar SÖ, Erdoğan D, Peker T, Coşkun Akçay N, Türkoğlu İ, Eşmekaya MA, et al. Effects of co-administered melatonin, fructose and bisphenol A (BPA) on rat epididymis and sperm characteristics. Biotechnic & Histochemistry. 2020;95(1):18-26.
18. Kane M. Simvastatin Therapy and SLCO1B1 Genotype. In: Pratt VM, Scott SA, Pirmohamed M, Esquivel B, Kattman BL, Malheiro AJ, editors. Medical Genetics Summaries. Bethesda (MD): National Center for Biotechnology Information (US); 2012.
19. Lolekha P, Khovidhunkit W, Deerochanawong C, Thongtang N, Boonyasirinant T, Rattarasarn C, et al. 2024 The Royal College of Physicians of Thailand (RCPT) clinical practice guidelines on management of dyslipidemia for atherosclerotic cardiovascular disease prevention. Asian Biomed (Res Rev News). 2024;18(6):246-67.
20. Bansal AB, Cassagnol M. HMG-CoA Reductase Inhibitors. StatPearls. Treasure Island (FL) ineligible companies. Disclosure: Manouchkathe Cassagnol declares no relevant financial relationships with ineligible companies.: StatPearls Publishing Copyright © 2025, StatPearls Publishing LLC.; 2025.
21. Delle C, Cankar N, Digebjerg Holgersson C, Hvorup Knudsen H, Schiøler Nielsen E, Kjaerby C, et al. Long-term high-fat diet increases glymphatic activity in the hypothalamus in mice. Scientific Reports. 2023;13(1):4137.
22. Volcko KL, Carroll QE, Brakey DJ, Daniels D. High-fat diet alters fluid intake without reducing sensitivity to glucagon-like peptide-1 receptor agonist effects. Physiol Behav. 2020;221: 112910.

23. Hafez MH, Gad SB, El-Sayed YS. Quercetin-mediated restoration of high-fat diet-induced male reproductive dysfunction through modifying spermatogenesis and unraveling 3β-HSD, 17β-HSD, and StAR pathways. BMC Pharmacology and Toxicology. 2025;26(1):90.
24. Mu Y, Yan W-j, Yin T-l, Zhang Y, Li J, Yang J. Diet-induced obesity impairs spermatogenesis: a potential role for autophagy. Scientific Reports. 2017;7(1):43475.
25. Hao Y, Feng Y, Yan X, Chen L, Ma X, Tang X, et al. Gut Microbiota-Testis Axis: FMT Mitigates High-Fat Diet-Diminished Male Fertility via Improving Systemic and Testicular Metabolome. Microbiology Spectrum. 2022; 10(3):e00028-22.
26. Liu CY, Chen CC, Chiang LH, Yang BH, Chang TC, Tsao CW. Hirsutella sinensis intensifies testicular function and spermatogenesis in male mice with high-fat diet-induced obesity. J Chin Med Assoc. 2024;87(8):765-73.
27. Climent E, Benaiges D, Pedro-Botet J. Hydrophilic or Lipophilic Statins? Front Cardiovasc Med. 2021;8:687585.
28. Suleiman JB, Nna VU, Zakaria Z, Othman ZA, Eleazu CO, Abu Bakar AB, et al. Protective effects of bee bread on testicular oxidative stress, NF-κB-mediated inflammation, apoptosis and lactate transport decline in obese male rats. Biomed Pharmacother. 2020;131: 110781.
29. Billah MM, Khatiwada S, Lecomte V, Morris MJ, Maloney CA. Ameliorating high-fat diet-induced sperm and testicular oxidative damage by micronutrient-based antioxidant intervention in rats. Eur J Nutr. 2022;61(7):3741-53.
30. Jing J, Peng Y, Fan W, Han S, Peng Q, Xue C, et al. Obesity-induced oxidative stress and mitochondrial dysfunction negatively affect sperm quality. FEBS Open Bio. 2023;13(4): 763-78.
31. O'Flaherty C. Reactive Oxygen Species and Male Fertility. Antioxidants. 2020;9(4):287.
32. Al-Shalchi RF, Mohammad FK. Oxidative Stress-Induced Adverse Effects of Three Statins Following Single or Repetitive Treatments in Mice. Cureus. 2024;16(1):e51433.
33. Zhang Z, Chen H, Li Q. High-fat diet led to testicular inflammation and ferroptosis via dysbiosis of gut microbes. International Immunoharmacology. 2024;142:113235.

O-19

Histological and Proteomic Alterations of the Human Placenta Associated with Maternal Exposure to High and Low Seasonal Particulate Matter (PM) Levels

Keerakarn Somsuan[1,2*], Wariya Mongkolwat[2], Tanapon Makkid[1], Iwaya Wongpia[1,2,3], Panida Navasumrit[4,5], Krittinee Chaisatra[4], Siripat Aluksanasuwan[1,2], Arunothai Wanta[1,2], Sangkae Chamnanvanakij[1], Supakorn Rojananin[1,7], Phateep Hankittichai[1,2], Atthapan Morchang[1,2], Artitaya Rongjumnong[1,2], Papawarin Karamart[1,2]
[1] School of Medicine, Mae Fah Luang University, Chiang Rai, 57100, Thailand
[2] Cancer and Immunology Research Center (CIRC), Mae Fah Luang University, Chiang Rai, 57100, Thailand
[3] Mae Fah Luang University Medical Center Hospital, Mae Fah Luang University, Chiang Rai, 57100, Thailand
[4] Laboratory of Environmental Toxicology, Chulabhorn Research Institute, Laksi, Bangkok 10210, Thailand
[5] Graduate Program in Environmental Toxicology, Chulabhorn Graduate Institute, Laksi, Bangkok 10210, Thailand
[6] Bangkok Hospital, Bangkok Dusit Medical Services (BDMS), Soi Soon Vijai, Bangkok, Thailand
*Corresponding author, e-mail: keerakarn.som@mfu.ac.th

Abstract

Exposure to fine particulate matter (PM) is associated with adverse pregnancy outcomes, yet the underlying placental mechanisms remain unclear. In this study, pregnant women who delivered during the low PM season (January to February 2023) were classified as the control group, whereas those who delivered during the high PM2.5 season (March to April 2023) were classified as the PM2.5-exposed group. The mean PM2.5 concentration at the Mae Sai, Chiang Rai province monitoring station during January–February 2023 was 45.60 µg/m³, whereas it increased to 172.77 µg/m³ during March–April 2023. All participants were healthy pregnant women with no history of smoking or alcohol consumption, and provided written informed consent at Mai Jun Hospital, Chiang Rai province. Placental tissues were collected at delivery from both the control and PM2.5-exposed groups (n = 10 per group) and subsequently analyzed to assess structural, molecular, and oxidative alterations. The histological analyses using hematoxylin and eosin, Masson's trichrome, and Periodic Acid–Schiff staining revealed pronounced villous and placental membrane abnormalities, along with increased collagen deposition in PM2.5-exposed placentas. Proteomic profiling identified significant alterations (unpaired t-test, $p < 0.05$) in proteins involved in antioxidant activity, superoxide metabolic process, and iron ion homeostasis, with pathway enrichment highlighting ferroptosis-related processes. The expression of key proteins was validated by Western blot analysis. Consistently, the ferroptosis driver transferrin receptor was upregulated, while the antioxidant and ferroptosis-suppressive proteins GPX4 and SOD1 were dysregulated (unpaired t-test, $p < 0.05$). MDA levels were significantly elevated in the PM2.5-exposed group (unpaired t-test, $p < 0.05$). Finally, no significant differences were observed in infant clinical outcomes, including birth weight and head circumference, between the groups (unpaired t-test, $p > 0.05$). Together, these findings demonstrate that PM2.5 exposure induces placental structural changes and activates ferroptosis-associated oxidative stress pathways, providing mechanistic insight into how air pollution may impair placental function and contribute to adverse pregnancy outcomes.

Keywords *Air pollution, Ferroptosis, Histopathology, Oxidative stress, Placenta*

O-20

Sildenafil Attenuates Venous Congestion-induced Hepatic Mitochondrial Injury and Fibrosis in A Rat Model of Pulmonary Arterial Hypertension

Phithiwat Tunlimsoon[1,2], Phonthipha Siadkham[1,2], Natthapong Khamaiam[1,2], Aubonwan Sitthikhankaeo[1,2], Siriporn Kreungnium[1,2], Ratchanon Meenapa[2,3], Benyapha Phunsee[2,3], Usana Chatturong[3], Tipparat Meebangsua[3], Kannika Adthapanyawanich[1,2,4], Kroekkiat Chinda[2,3,4], Soontaree Petchdee[5], Krongkarn Chootip[3*], Yutthapong Tongpob[1,2,4*]

[1] Department of Anatomy, Faculty of Medical Science, Naresuan University, Phitsanulok, Thailand 65000
[2] Integrative Cardiovascular Research Unit, Faculty of Medical Science, Naresuan University, Phitsanulok, Thailand 65000
[3] Department of Physiology, Faculty of Medical Science, Naresuan University, Phitsanulok, Thailand 65000
[4] Centre of Excellence in Medical Biotechnology, and AI CARE Research Cluster, Naresuan University, Phitsanulok, Thailand 65000
[5] Department of Large Animal and Wild Animal Clinical Sciences, Faculty of Veterinary Medicine, Kasetsart University (Bangkhen Campus), Bangkok, Thailand 10900
*Corresponding authors, e-mail: yutthapongt@nu.ac.th, krongkarnc@gmail.com

Abstract

Background: Pulmonary arterial hypertension (PAH) causes sustained venous outflow obstruction that extends to the liver, resulting in congestive hepatopathy, mitochondrial dysfunction, and fibrotic remodeling. Although sildenafil, a phosphodiesterase type 5 (PDE5) inhibitor, is widely used in PAH treatment, its effects on mitochondrial integrity in congestive hepatopathy remain unclear. **Objective:** This study investigated whether sildenafil attenuates hepatic mitochondrial dysfunction and fibrotic remodeling in a monocrotaline (MCT)-induced rat model of pulmonary arterial hypertension. **Methods:** Male Sprague–Dawley rats (n=6/group) were assigned to three groups: control, MCT (60 mg/kg, single subcutaneous injection), and MCT plus sildenafil (30 mg/kg/day, oral gavage for 21 days). Liver tissues were collected for relative weight measurement and histopathological analysis. Hepatic congestion and fibrosis were evaluated using hematoxylin and eosin and Masson's trichrome staining. Liver mitochondrial function was assessed in isolated liver mitochondria by measuring reactive oxygen species (ROS) production using DCFH-DA fluorescence, mitochondrial swelling under basal and $CaCl_2$-stimulated conditions by monitoring absorbance at 540 nm, and mitochondrial membrane potential ($\Delta\Psi m$) using JC-1 fluorescence with red-to-green ratio analysis. Statistical analysis was performed using one-way ANOVA followed by Tukey's post-hoc test. **Results:** MCT increased relative liver weight ($p<0.01$), induced sinusoidal dilation and central venous congestion, and enhanced perisinusoidal collagen deposition. These structural alterations were accompanied by marked mitochondrial dysfunction, including increased ROS production ($p<0.0001$), exaggerated mitochondrial swelling ($p<0.01$), increased susceptibility to Ca^{2+}-induced permeability transition ($p<0.01$), and reduced $\Delta\Psi m$ ($p<0.05$) compared with control. When compared to MCT, sildenafil treatment significantly attenuated collagen accumulation ($p<0.01$), reduced mitochondrial ROS ($p<0.0001$), stabilized mitochondrial swelling responses ($p<0.05$), and restored $\Delta\Psi m$ toward control levels ($p<0.05$). **Conclusion:** Congestive hepatopathy in PAH is closely linked to mitochondrial injury driven by anatomically mediated venous congestion. Sildenafil mitigates liver injury likely by preserving mitochondrial structural and functional integrity, thereby limiting progression from passive congestion to fibrotic remodeling.

Keywords *Pulmonary arterial hypertension, Congestive hepatopathy, Hepatic mitochondria, Sildenafil, Monocrotaline*

O-21

Targeting Piezo1-Regulated Mitophagy Immunometabolic Pathway in An Organoid Model of Osteoarthritis

Kavitha Raja[1*], Dineshwary Suresh[1,2], Surendra Rawat Singh[1], Ivan James Prithishkumar[1], Thomas Nau[3], Nerissa Naidoo[1]
[1] Mohammed Bin Rashid University of Medicine and Health Sciences, Dubai Health, Dubai, United Arab Emirates
[2] Faculty of Medicine, Health and Life Science, Swansea University, Wales, United Kingdom
[3] King's College Hospital London Dubai, Dubai, United Arab Emirates
*Corresponding author, e-mail: kavitha.raja@dubaihealth.ae

Abstract
Background: Osteoarthritis (OA) is a progressive degenerative joint disease characterized by cartilage degradation, subchondral bone remodelling, and chronic inflammation. Mechanosensitive ion channels, particularly Piezo1, play a critical role in maintaining cartilage homeostasis under physiological conditions by regulating calcium signalling; however, under inflammatory conditions, aberrant Piezo1 activation leads to calcium overload, metabolic dysregulation, and mitochondrial dysfunction, thereby promoting osteochondral degeneration. **Objective:** This study investigated the Piezo1–HIF-1α–mitophagy immunometabolic axis using a three-dimensional (3D) osteochondral organoid model. **Methods:** Human mesenchymal stem cell-derived chondrocytes and RAW 264.7-derived osteoclasts were co-cultured to generate scaffold-free 3D organoids. Osteoarthritic-like conditions were induced using lipopolysaccharide (LPS). **Results:** A well-characterized bioactive nutraceutical compound with antioxidant and anti-inflammatory properties was applied to modulate mechanotransduction and mitochondrial homeostasis. Piezo1 pathway activation and mitophagy regulation were evaluated using calcium influx assays, along with gene and protein expression analyses of HIF-1α, GLUT1, and LDHA, and mitophagy markers including PINK1, Parkin, LC3B, and p62. Organoid maturation was confirmed by histological staining and extracellular matrix markers (COL2A1, ACAN), while inflammatory and catabolic responses were assessed via IL-1β, TNF-α, MMP-13, and ADAMTS-5. LPS stimulation resulted in increased Piezo1 activation, intracellular calcium influx, glycolytic reprogramming, impaired mitophagy, and elevated inflammatory mediator expression. Nutraceutical treatment restored calcium homeostasis, enhanced mitophagic flux, reduced inflammation, and preserved extracellular matrix integrity. **Conclusion:** These findings demonstrate that Piezo1 dysregulation drives OA progression via mitophagy-dependent immunometabolic pathways, highlighting this axis as a potential disease-modifying therapeutic target.

Keywords *Osteoarthritis, Organoid, Piezo1-mediated pathway, Inflammation, Mitophagy*

O-22

Phenylallylpentane-2,4-Dione Derivatives Ameliorated LPS-Induced Inflammation Independent of NF-κB Signaling Pathway in BV-2 Cell Culture

Nantaphat Paelaong[1], Thanyaphat Sahaya[1], Supitcha Nilrat[1], Kittisak Sripha[2], Yingrak Boondam[3*]
[1] Faculty of Pharmacy, Mahidol University, Si Ayutthaya Rd, Bangkok, Thailand
[2] Department of Pharmaceutical Chemistry, Faculty of Pharmacy, Mahidol University, Si Ayutthaya Rd, Bangkok, Thailand
[3] Department of Physiology, Faculty of Pharmacy, Mahidol University, Si Ayutthaya Rd, Bangkok, Thailand
*Corresponding author, e-mail: yingrak.boo@mahidol.ac.th

Abstract

Alzheimer's disease (AD) is a neurodegenerative disease that is the most common cause of dementia. Nowadays, it is widely recognized that neuroinflammation plays an important role in the progression of the disease. Several harmful substances, including amyloid beta (Aβ) and lipopolysaccharide (LPS), could trigger the activation of microglia and subsequent inflammation through the activation of the nuclear factor-κB (NF-κB) signaling pathway. β-diketone is a pharmaceutical scaffold reported to have a wide range of biological activities, including anti-inflammation and anti-oxidation. Recently, a series of phenylallylpentane-2,4-dione derivatives (the CINNAs), which contain the β-diketone scaffold, has been synthesized as a part of an ongoing project. Due to previously reported activities of this scaffold, this work aimed to preliminarily assess the biological activities of three CINNA compounds (CINNA4, CINNA5, and CINNA6). The anti-oxidation activity was initially investigated using the DPPH radical scavenging assay, while the LPS-induced BV-2 cell culture model was used to investigate the anti-inflammatory activity. Specifically, MTT cytotoxicity assay and western blot analysis were used to investigate the effects of the CINNAs on LPS-induced cytotoxicity and inflammatory responses, respectively. From the results of the DPPH assay, none of the CINNAs possess any significant radical scavenging activity compared to the known antioxidant L-ascorbic acid. In contrast, CINNA5 and CINNA6 appeared to have protective effects against LPS-induced cytotoxicity in the MTT assay. Following this, both compounds at 40 μM concentration were investigated for their anti-inflammatory activity. From western blot analysis, both compounds could decrease the production of tumor necrosis factor (TNF)-α, a pro-inflammatory cytokine, compared to the LPS group. Despite this, they did not affect the activation of NF-κB, in a statistically significant way. In conclusion, CINNA5 and CINNA6 could ameliorate LPS-induced inflammation in BV-2 cell culture independent of NF-κB signaling pathway, and so investigation of their effects on other signaling pathways should be further conducted to elucidate their molecular mechanisms.

Keywords *Alzheimer's disease, Microglia, BV-2 cell line, Neuroinflammation, Drug discovery*

Background

Alzheimer's disease (AD) is one of the neurodegenerative diseases characterized by progressive memory loss and cognitive decline. Previously, the aggregation of its characteristic abnormal proteins, beta amyloid (Aβ) plaques and neurofibrillary tangles (NFTs), in the brain were thought to be the main perpetrators that drive neurodegeneration, however, recently, more evidence pointed to the activation of microglia, the resident immune cells in the central nervous system (CNS), and subsequent neuroinflammation in response to Aβ as the major player in the development of AD (1,2). Therefore, the current trend in drug discovery of AD is to find compounds that could modulate various steps of the neuroinflammation process, for example, the activation of pro-inflammatory signaling pathways and the production of reactive oxygen species (ROS) and reactive nitrogen species (RNS) (3). Besides Aβ itself, researchers have also employed lipopolysaccharide (LPS), a bacterial endotoxin, as

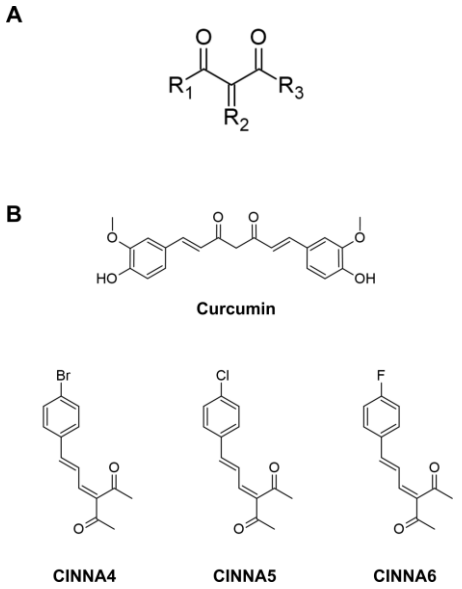

Fig. 1 The general structure of β-diketone scaffold (A) and compounds containing the scaffold mentioned in this work (B).

an inducer of microglial activation in a cell culture model. This is due to the ability of LPS that could bind to toll-like receptor (TLR) 4, whose resultant dimerization triggers the activation of the nuclear factor-κB (NF-κB) signaling pathway. As the name implies, NF-κB is the transcription factor that is able to translocate into the nucleus and induce the production of pro-inflammatory mediators, ranging from cytokines such as tumor necrosis factor (TNF)-α and interleukin (IL)-6, to enzymes such as cyclooxygenase (COX)-2 and inducible nitric oxide synthase (iNOS) (4,5).

β-diketone (Fig. 1A) is a pharmaceutical scaffold reported to have a wide range of biological activities, including anti-oxidation and anti-inflammation (6). In particular, curcumin (Fig. 1B), a pleiotropic natural compound that contains the scaffold in its structure, was found to have significant potency in both regards. In terms of anti-inflammatory activity, curcumin was reported to ameliorate neuroinflammation in BV-2 microglial cell culture through the inhibition of NF-κB, among other possible pathways (7,8). Moreover, subsequent molecular docking studies revealed that curcumin exerts its effect via the interactions with pro-inflammatory molecules such as TNF-α, the aforementioned cytokine, and myeloid differentiation protein 2 (MD-2), which is an LPS-binding component of TLR4 (9). There is evidence that curcumin owes its diverse activity to the β-diketone scaffold that could tautomerize into the enol form, which is optimal for target binding (9). In a similar vein, the enol form of curcumin was also found to be important for its antioxidant activity, along with the hydroxyl and methoxy substituents (10). Therefore, β-diketone proves to be an attractive scaffold for the discovery of anti-neuroinflammatory compounds.

Recently, a team of researchers led by Sripha had synthesized a series of phenylallylpentane-2,4-dione derivatives as a part of an attempt to discover anti-neuroinflammatory compounds for the treatment of AD (11). Because of their β-diketone scaffold, preliminary investigations have been conducted to assess their protective effects against LPS-induced cytotoxicity in BV-2 cell culture, from which several candidates have been identified. This work aimed to further investigate a group of selected candidates: CINNA4, CINNA5, and CINNA6 (Fig. 1B) for their protective effects against LPS-induced inflammation through NF-κB signaling pathway.

Materials and methods

In vitro DPPH radical scavenging assay

2,2-diphenyl-1-picrylhydrazyl (DPPH), a stable free radical compound, was used to biochemically investigate the antioxidant activity of the CINNAs. Firstly, DPPH (Sigma-Aldrich, MA, USA) was dissolved in methanol to obtain the working solution at a concentration of 0.2 mM. After that, 100 µL of CINNA compounds and ascorbic acid (positive control) at various concentrations were combined with 100 µL of DPPH working solution in a 96-well plate. After incubating in the dark for 30 min, the absorbance was measured at 517 nm using the multimode microplate reader (BioTek, VT, USA).

Cell culture and treatments

BV-2 microglial cells (Cytion GmbH, Heidelberg, Germany) were cultured in Dulbecco's Modified Eagle's Medium (DMEM) with 10% fetal bovine serum (FBS), 1% penicillin/streptomycin, and 1% HEPES buffer (Thermo Fischer Scientific, MA, USA) in a T75 flask. The cells were maintained in the CO_2 incubator at 37°C with 5% CO_2. The medium was changed every 48 hours, and the passaging/subculture was conducted once the cells reached 80% confluency.

For the experiments, the cells were subcultured into protocol-appropriate well plates and incubated for 24 hr. After that, the cells were treated according to their designated groups. The Control group received no treatment. The LPS group was treated only with 10 ng/mL LPS (Thermo Fischer Scientific, MA, USA). Lastly, the CINNA

groups were co-treated with LPS and CINNAs at selected concentrations. All groups were then incubated for another 24 hr before the cells were collected or the assay continued.

Table 1 The IC_{50} obtained from DPPH Radical Scavenging Assay for CINNA4, CINNA5, CINNA6, and L-ascorbic acid

Compounds	IC_{50} (μM)
CINNA4	<500
CINNA5	<500
CINNA6	<500
L-ascorbic acid	15.118

MTT cytotoxicity assay

The MTT assay was used to assess the protective effects of CINNAs against LPS-induced cytotoxicity in the cell line model. Briefly, the BV-2 cells were subcultured into a 96-well plate with the initial seeding density of 1.8×10^4/well and treated according to the general protocol. After 24-hour incubation, the medium was replaced with 0.5 mg/mL MTT solution (Thermo Fischer Scientific, MA, USA). The plate was further incubated in the dark for 2 hr before the remaining MTT solution was replaced with dimethyl sulfoxide (DMSO) to dissolve the crystallized formazans. The absorbance was measured at 570 nm using the multimode microplate reader.

Western blot analysis

To investigate the effects of CINNAs on the expression of TNF-α (a pro-inflammatory cytokine) and the activation of NF-κB, BV-2 cells were subcultured into a 12-well plate with an initial seeding density of 1.2×10^5/well and treated according to the general protocol. After a 24-hour incubation period, the cell pellets were collected and lysed to obtain their proteins. Following the preparation of protein samples, the proteins were separated by size using SDS-PAGE electrophoresis, then transferred to a polyvinylidene difluoride (PVDF) membrane (Bio-Rad, CA, USA). The membrane was incubated with primary antibodies (p-NF-κB and NF-κB from Cell Signaling Technology (MA, USA). TNF-α and β-actin (internal control) from Abcam (Cambridge, UK)) overnight at 4°C. Following that, it was further incubated with horseradish peroxidase (HRP)-conjugated secondary antibodies (Abcam, Cambridge, UK) for 1 hr at room temperature. The signals for proteins of interest were visualized using SuperSignal™ West Pico PLUS Chemiluminescent Substrate (Thermo Fischer Scientific, MA, USA). Lastly, the blot image analysis was performed using ImageJ software (National Institutes of Health, MD, USA).

Statistical analysis

The values of results are presented as mean ± SEM of biologically independent experiments. The statistical analysis was performed using IBM SPSS Statistics 22 program. The comparison between groups was analyzed by ANOVA followed by LSD post-hoc test. p-value < 0.05 was considered significant.

Results and discussion

CINNAs did not exhibit antioxidant activity in DPPH radical scavenging assay

Before the experiments in the cell culture model, the CINNAs were preliminarily assessed for their radical scavenging capabilities, as ROS production is another important mechanism in the event of microglial activation besides the release of pro-inflammatory modulators. Here, the DPPH radical scavenging assay was employed for such a purpose, and L-ascorbic acid, a known antioxidant, was used as a positive control. As seen in Table 1, the IC_{50} of L-ascorbic acid was found to be approximately 15.118 μM. This is in line with the results obtained from previous literature (12,13), confirming the validity of the assay. On the other hand, it was found that none of the CINNAs possess any significant free radical scavenging activity; all are estimated to have IC_{50} over 500 μM.

Despite these results, it is important to consider that the neutralization of DPPH radicals mainly relies on the donation of hydrogen atoms from the antioxidants: the so-called 'hydrogen atom transfer (HAT)' mechanism. Particularly, compounds with hydroxyl or phenolic substituents, which possess mobile hydrogen atoms, tend to be very effective at scavenging DPPH radicals (10,13). Therefore, the three CINNAs, which lack such functional groups, might not be able to demonstrate their antioxidant activity via this assay. As such, further investigations, for example, in the cell culture model, might be needed to confirm their antioxidant activity via other mechanisms, e.g., direct inhibition of ROS- or RNS-producing enzymes.

CINNA5 and CINNA6 exerted protective effects against LPS-induced cytotoxicity in BV-2 cell culture

MTT cytotoxicity assay was used to investigate the protective effects of CINNAs against LPS-induced cytotoxicity. As shown in Fig. 2A, for the LPS-treated group, exposure to LPS for 24 hr

resulted in a significant decrease in cell viability compared to the control group (*: $p < 0.05$). When comparing the cell morphology between both groups, it could be observed that there are noticeable clumps of cell debris in the LPS-treated group compared to the control. In addition, the cells also appear more circular and less branched, signifying their activated state (Fig. 2B (upper-left and upper-right)). In contrast, co-treatment of LPS with CINNAs could mitigate such negative effects to a varying degree. Out of the three compounds at three different concentrations, CINNA5 at the concentrations of 20 and 40 μM, and CINNA6 at the concentrations of 20, 40, and 60 μM were found to significantly increase cell viability of the BV-2 cells compared to the group that was treated with LPS alone (#: $p < 0.05$). Therefore, CINNA5 and CINNA6 at the same concentration: 40 μM, which exhibited similar levels of protective effects (Fig. 2B (lower-left and lower-right)), were selected to be

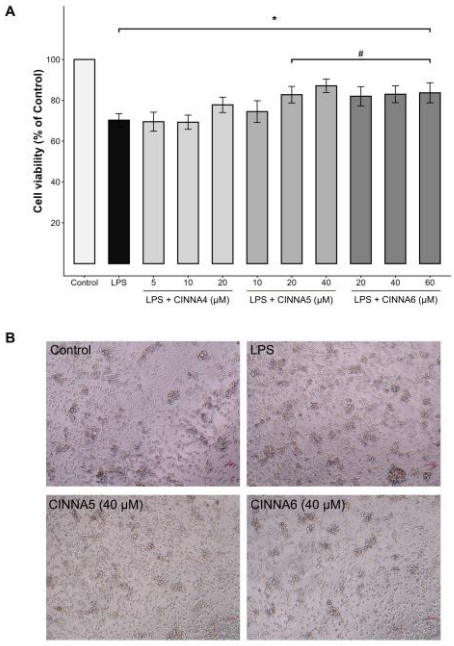

Fig. 2 The protective effects of CINNAs against LPS-induced cytotoxicity in BV-2 microglial cells. (A) The bar plot represents the cell viability of BV-2 microglial cells in each group after 24 hr exposure to LPS with or without the CINNAs compared to the control group. The results are expressed as mean ± SEM (n = 6 with at least 3 technical replicates; *: $p < 0.05$ compared to the control group and #: $p < 0.05$ compared to the LPS-treated group) (B) The morphology of BV-2 cells in selected groups (from upper-left, clockwise: the control group, the LPS-treated group, the LPS + CINNA6 (40 μM) group, and the LPS + CINNA5 (40 μM) group).

further investigated for their anti-inflammatory effects in the next steps of experiments.

CINNA5 and CINNA6 attenuated LPS-induced pro-inflammatory cytokine release independent of NF-κB signaling pathway

In the event of microglial activation, several pro-inflammatory modulators are released to eliminate the harmful substances and recruit more immune cells to the site of inflammation. While this is initially beneficial, a prolonged inflammatory environment could result in cellular damage and death. In this experiment, the western blot analysis was used to investigate the protective effects of the CINNAs against LPS-induced release of the cytokine TNF-α. It was observed that treatment with LPS dramatically increased the relative protein expression of TNF-α compared to the control group (not shown). However, co-treatment with both CINNA5 and CINNA6 resulted in a significant reduction of its expression compared to the group receiving LPS alone (#: $p < 0.05$, Fig. 3). For this reason, it could be concluded that CINNA5 and CINNA6 could attenuate LPS-induced pro-inflammatory cytokine release.

As previously mentioned, it has been established that LPS could trigger microglial activation mainly via TLR4/NF-κB signaling

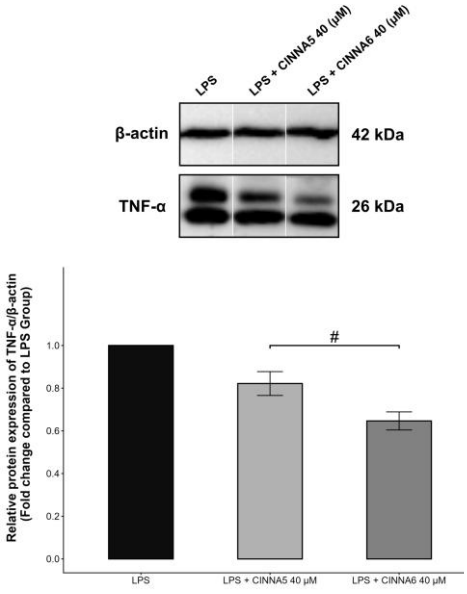

Fig. 3 The protective effects of CINNA5 and CINNA6 (40 μM) against LPS-induced expression of TNF-α in BV-2 microglial cells. The results are expressed as mean ± SEM (n = 3; #: $p < 0.05$ compared to the LPS-treated group).

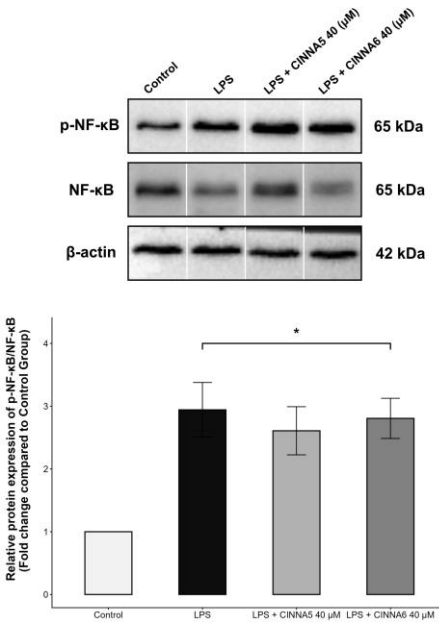

Fig. 4 CINNA5 and CINNA6 did not appear to affect the activation of NF-κB signaling pathway. The results are expressed as mean ± SEM (n = 3; *: $p < 0.05$ compared to the control group).

pathway, and that curcumin could inhibit the activation of NF-κB through binding with the LPS-binding component of TLR4, MD-2. To investigate whether the anti-inflammatory activity of CINNA5 and CINNA6 was also mediated through the inhibition of NF-κB. The activation of NF-κB, signified by the increased phosphorylated form in relation to the protein total form, was also monitored using western blot analysis. As seen in Fig. 4, treatment with LPS resulted in a significant increase in NF-κB activation compared to the control group. Despite this, both CINNA5 and CINNA6 seemed to affect the LPS-induced NF-κB activation in statistically significant ways.

Even though NF-κB is the major signaling pathway involved in LPS-induced inflammation, microglial activation could also trigger the activation of other signaling pathways, both dependent and independent of TLR4. In particular, the activation of TLR4 also leads to the activation of mitogen-activated protein kinases (MAPKs), which, in turn, activate activator protein-1 (AP-1), a transcription factor that could induce pro-inflammatory mediator expression in a similar manner to NF-κB. Moreover, the initial release of pro-inflammatory cytokines through NF-κB could also induce the activation of MAPKs in a positive feedback loop (5,14). Therefore, more research is needed to determine the molecular mechanisms of CINNA5 and CINNA6 in alleviating LPS-induced cytokine production.

Conclusion

In summary, the phenylallylpentane-2,4-dione derivatives, here dubbed the CINNAs, were investigated to determine their antioxidant and anti-inflammatory activities due to their reportedly biologically active β-diketone scaffold. From the results of the DPPH assay, it could be concluded that none of the compounds possess any appreciable free radical scavenging activity. In contrast, the results in the MTT assay implied the protective effect of CINNA 5 and CINNA6 against LPS-induced cytotoxicity in BV-2 cell culture model. Further western blot analysis confirmed the ability of both compounds to ameliorate the LPS-induced expression of the cytokine TNF-α. In spite of that, CINNA5 and CINNA6 did not appear to mediate such activity through the major pro-inflammatory signaling pathway, NF-κB. Thus, the molecular mechanisms by which both compounds could inhibit TNF-α remain determined.

Acknowledgements

The authors would like to express gratitude to the Faculty of Pharmacy, Mahidol University, for providing laboratory equipment, facilities, as well as supporting grants for the conduct of this research.

References

1. Zhang J, Zhang Y, Wang J, Xia Y, Zhang J, Chen L. Recent advances in Alzheimer's disease: mechanisms, clinical trials and new drug development strategies. Sig Transduct Target Ther. 2024;9(1):1–35. doi:10.1038/s 41392-024-01911-3
2. Morris GP, Clark IA, Vissel B. Questions concerning the role of amyloid-β in the definition, aetiology and diagnosis of Alzheimer's disease. Acta Neuropathol. 2018;136(5):663–89. doi:10.1007/s00401-018-1918-8
3. Leng F, Edison P. Neuroinflammation and microglial activation in Alzheimer disease: where do we go from here? Nat Rev Neurol. 2021;17(3):157–72. doi:10.1038/s41582-020-00435-y
4. Boondam Y, Cheepsunthorn P. Patterns of microglial innate immune responses elicited by amyloid β1–42 and lipopolysaccharide: the similarities of the differences. Asian Biomed (Res Rev News). 2017 Feb 4;8(3):353–9.
5. Skrzypczak-Wiercioch A, Sałat K. Lipopoly-saccharide-induced model of neuro-

inflammation: Mechanisms of action, research application and future directions for its use. Molecules. 2022;27(17):5481. doi:10.3390/molecules 27175481
6. Hansen PE. Structural Studies of β-Diketones and Their Implications on Biological Effects. Pharmaceuticals (Basel). 2021 Nov 20;14(11): 1189. doi:10.3390/ph14111189
7. Jin C yun, Lee J dong, Park C, Choi Y hyun, Kim G young. Curcumin attenuates the release of pro-inflammatory cytokines in lipopoly-saccharide-stimulated BV2 microglia. Acta Pharmacol Sin. 2007 Oct;28(10):1645–51. doi:10.1111/j.1745-7254.2007.00651.x
8. Kang G, Kong PJ, Yuh YJ, Lim SY, Yim SV, Chun W, et al. Curcumin suppresses lipopolysaccharide-induced cyclooxygenase-2 expression by inhibiting activator protein 1 and nuclear factor κB bindings in BV2 microglial cells. J Pharmaco Sci. 2004;94(3):325–8. doi:10.1254/jphs.94.325
9. Gupta SC, Prasad S, Kim JH, Patchva S, Webb LJ, Priyadarsini IK, et al. Multitargeting by curcumin as revealed by molecular interaction studies. Nat Prod Rep. 2011;28(12):1937–55. doi:10.1039/C1NP00051A
10. Charlton NC, Mastyugin M, Török B, Török M. Structural features of small molecule antioxidants and strategic modifications to improve potential bioactivity. Molecules. 2023; 28(3):1057. doi:10.3390/molecules28031057
11. Nimwongcharoensuk P, Chitcharoenwarakit W. Synthesis and biological evaluation of 3,4-dihydropyrimidin-2-(1h)-one derivative as anti-oxidative agents. Faculty of Pharmacy, Mahidol University; 2024.
12. Sharma OP, Bhat TK. DPPH antioxidant assay revisited. Food Chem. 2009;113(4):1202–5. doi:10.1016/j.foodchem.2008.08.008
13. Mishra K, Ojha H, Chaudhury NK. Estimation of antiradical properties of antioxidants using DPPH assay: critical review and results. Food Chem. 2012;130:1036–43. doi:10.1016/j.food chem.2011.07.127
14. Kaminska B. MAPK signaling pathways as molecular targets for anti-inflammatory therapy—from molecular mechanisms to therapeutic benefits. Biochim Biophys Acta. 2005;1754(1):253–62. doi:10.1016/j.bbapap. 2005.08.017

POSTER PRESENTATION

P-01

Maternal and Prenatal Safety Evaluation of *Zingiber officinale* Extract in A Rat Developmental Toxicity Model: Preliminary Investigation

Natthapong Khamaiam[1,2], Nitchanan Piyatrakullert[2,3], Siriporn Kreungnium[1,2], Jirawan In-sutha[3], Wiyada Khangkhachit[4], Phonthipha Siadkham[1,2], Girana Bunsung[2], Kornkanok Ingkaninan[5], Kalyarut Phumlek[6], Hiroki Nakata[7], Peter J Mark[8], Wai Chen[9], Kroekkiat Chinda[2,3,10], Kannika Adthapanyawanich[1,2,10], Yutthapong Tongpob[1,2,10*]

[1] Department of Anatomy, Faculty of Medical Science, Naresuan University, Phitsanulok, Thailand 65000
[2] Integrative Cardiovascular Research Unit (ICRU), Faculty of Medical Science, Naresuan University, Phitsanulok, Thailand 65000
[3] Department of Physiology, Faculty of Medical Science, Naresuan University, Phitsanulok, Thailand 65000
[4] Medical and Health Food Technology, Faculty of Science, Chulabhorn Royal Academy, Bangkok, Thailand 10210
[5] Department of Pharmaceutical Chemistry and Pharmacognosy, Faculty of Pharmaceutical Sciences, and Center of Excellence for Innovation in Chemistry, Naresuan University, Phitsanulok, Thailand 65000
[6] Research and Innovation Cluster for Natural Health Products, Faculty of Pharmaceutical Sciences, Naresuan University, Phitsanulok, Thailand 65000
[7] Department of Clinical Engineering, Faculty of Health Sciences, Komatsu University, Ishikawa, Japan 923-0961
[8] School of Human Sciences, The University of Western Australia, Perth, Australia, 6009
[9] Curtin Medical School, Curtin University, Perth, Australia, 6102
[10] Centre of Excellence in Medical Biotechnology (CEMB), and AI-CARE Research Cluster, Naresuan University, Phitsanulok, Thailand 65000
*Corresponding author, e-mail: yutthapongt@nu.ac.th

Abstract

Ginger (*Zingiber officinale* Roscoe) is among the most commonly used herbal remedies during pregnancy, primarily for the management of nausea and vomiting. Its major bioactive constituents — gingerols and shogaols — confer antioxidant and anti-inflammatory activities, suggesting potential relevance to fetoplacental physiology. Despite its widespread use, dose-dependent safety data in the context of maternal and prenatal development remain insufficient. This study aimed to assess the maternal and prenatal safety profile of ginger extract across a range of clinically relevant doses using a rat prenatal developmental toxicity model. Time-mated female Wistar rats were randomly allocated to four groups (n = 5/group): a vehicle control (10% propylene glycol, 1 mL/kg/day) and three ginger extract-treated groups receiving 250, 500, or 1000 mg/kg/day by oral gavage from gestational day (GD) 1 through GD 21, representing a range of clinically relevant exposures. At GD 21, maternal body weight and weight gain were recorded. Fetoplacental outcomes — including the number of viable fetuses, fetal and placental weights, sex-specific fetal weights, fetal linear dimensions (nose–vertex, vertex–rump, shoulder–rump, and vertex–shoulder distances), placental diameter, and umbilical cord length — were systematically evaluated. Data were analyzed using one-way ANOVA with Tukey's post hoc test. No statistically significant differences were observed between any ginger extract-treated group and the vehicle control in maternal body weight gain, fetal body weight, placental weight, number of viable fetuses, or sex-specific fetal weights ($p > 0.05$). All fetoplacental morphometric parameters remained comparable across all groups. Oral administration of ginger extract at doses up to 1000 mg/kg/day throughout gestation did not induce maternal toxicity or adverse fetoplacental outcomes. However, these findings should be considered preliminary given the small sample size per group, and further investigation encompassing internal fetal visceral and skeletal examination, as well as histopathological analyses, is required.

Keywords *Zingiber officinale, Ginger extract, Prenatal toxicity, Fetoplacental development, Developmental safety*

P-02

Hepatoprotective Role of Resveratrol in Acute Restraint Stress-Induced Wistar Albino Rats

BV Murlimanju[1], Anusha Anandu Naik[1], Pooja K Suresh[2], Y Lakshmisha Rao[1], Prasad Alathady Maloor[3]
[1] Department of Anatomy, Kasturba Medical College Mangalore, Manipal Academy of Higher Education, Manipal, India
[2] Department of Pathology, Kasturba Medical College Mangalore, Manipal Academy of Higher Education, Manipal, India
[3] Department of Anatomy, Manipal University College Malaysia, Melaka, Malaysia

Abstract
Background: Acute stress is known to induce significant hepatic injury through oxidative and inflammatory mechanisms. Resveratrol (RSV), a natural polyphenolic compound, possesses antioxidant and anti-stress properties that may confer hepatoprotection. However, its role in stress-induced hepatic microstructural alterations remains inadequately explored. The goal was to document the histomorphology of the liver in an acute restraint stress-induced rat model, and the objective was to observe the microanatomical changes after the administration of resveratrol (RSV). **Methods:** Eighteen pathogen-free male Wistar albino rats (n=6 per group) were divided into three groups: control (vehicle), stress (restraint stress for 6 hours/day for 14 days), and treatment (restraint stress for 14 days followed by RSV administration at 10 mg/kg body weight orally for another 14 days). Restraint stress was induced using well-ventilated restrainers without causing pain. Liver tissues were processed for histopathological evaluation using hematoxylin and eosin staining, and injury was assessed using standard scoring systems. **Results:** The present study observed that there was a loss of lobular architecture in the liver of the stress-induced group. The hepatic cords were disorganised along with the sinusoidal dilation. Granular and hydropic degeneration of hepatocytes was marked in these groups, and there were focal areas of necrosis, particularly in the perivenular region. The central veins of the hepatic lobules were grossly dilated, suggesting hepatic injury. In the post-treatment group, the hepatic lobular architecture was restored. The hepatic cords looked organized, and sinusoids were not dilated. **Conclusion:** There were no focal areas of necrosis, and there was reversal of dilatation of the central vein, which is suggestive of hepatoprotective activity of RSV in the acute restraint stress-induced animal model. However, the limitation of this study design is that RSV was administered after the cessation of stress, and a better interpretation can be drawn if both are given in parallel.

Keywords *Antioxidant activity, Hepatoprotective, Liver injury, Resveratrol, Stress*

P-03

Brahmi and Thai Mixed Berry Extracts Attenuate Chronic Stress-Induced Testicular Dysfunction in Rats

Pornpimon Chuaypen[1,4], Darunrat Onla-or[1,4], Jureepon Roboon[1,4], Kornkanok Ingkaninan[2], Samur Thanoi[3], Sutisa Nudmamud-Thanoi[1,4], Paweena Kaewman[1,4*]
[1] Department of Anatomy, Faculty of Medical Science, Naresuan University, Phitsanulok, Thailand
[2] Department of Pharmaceutical Chemistry and Pharmacognosy, Faculty of Pharmaceutical Sciences, Naresuan University, Phitsanulok, Thailand
[3] Department of Anatomy, School of Medical Science, University of Phayao, Phayao, Thailand
[4] Centre of Excellence in Medical Biotechnology, Naresuan University, Phitsanulok, Thailand
*Corresponding author, e-mail: paweenakae@nu.ac.th

Abstract

Chronic stress impairs male reproductive function by disrupting spermatogenesis and sperm quality. *Bacopa monnieri* (Brahmi) reduces stress, while Thai mixed berries exhibit protective effects against stress-induced testicular damage. This study aimed to investigate the protective effects of Brahmi and Thai mixed berries against chronic stress-induced reproductive damage in rats. Male Sprague-Dawley rats (7 weeks old) were randomly assigned to four groups (n = 5-6 rats per group): Control, Chronic Unpredictable Mild Stress (CUMS), CUMS-Berries, and CUMS-Brahmi+Berries. Chronic stress was induced in all CUMS groups via a 14-day CUMS protocol. The Control and CUMS groups received reverse osmosis by oral gavage once daily during the same period. Rats in CUMS-Berries group received Thai mixed berry extract containing total anthocyanins (0.043 mg/g extract/kg BW), while rats in CUMS-Brahmi+Berries group received Brahmi (20 mg/kg BW) and the Thai mixed berries. Post-treatment, reproductive parameters, including testicular weight, sperm concentration, and histological evaluation of seminiferous tubule stages, were assessed. The results showed a significant decrease in testicular weight and sperm concentration in the CUMS group compared with the Control group. Testicular weight was significantly improved in the CUMS-Berries group, while sperm concentration was significantly improved in the CUMS-Brahmi+Berries group compared with the CUMS group. CUMS group showed altered seminiferous epithelial stage distribution, with increased early stages and reduced middle and late stages, indicating disrupted spermatogenesis and meiotic arrest. Notably, treatment with the combination of Brahmi and Thai mixed berries restored these parameters to levels comparable to the Control group. In conclusion, chronic stress impairs male reproductive function, whereas Thai mixed berries, particularly in combination with Brahmi, attenuate these effects.

Keywords *Chronic stress, Thai mixed berry, Brahmi, Testicular function, Sperm quality*

P-04

Combined Gamma-Oryzanol and Curcumin Attenuate Testicular Damage in Dexamethasone-Induced Depressive Rats

Darunrat Onla-or[1,4], Pornpimon Chuaypen[1,4], Jureepon Roboon[1,4], Waree Tiyaboonchai[2], Samur Thanoi[3], Sutisa Nudmamud-Thanoi[1,4], Paweena Kaewman[1,4*]
[1] Department of Anatomy, Faculty of Medical Science, Naresuan University, Phitsanulok, Thailand
[2] Department of Pharmaceutical Technology, Faculty of Pharmaceutical Sciences, Naresuan University, Phitsanulok, Thailand
[3] Department of Anatomy, School of Medical Science, University of Phayao, Phayao, Thailand
[4] Centre of Excellence in Medical Biotechnology, Naresuan University, Phitsanulok, Thailand
*Corresponding author, e-mail: paweenakae@nu.ac.th

Abstract

Depression has been associated with dysfunction in various organ systems, including the male reproductive system. Dexamethasone (DEX), a corticosteroid, induces depression through elevated cortisol levels, which can impair testicular function. Changes in testicular morphology and sperm quality can serve as indicators of testicular dysfunction. This study aimed to investigate the protective effects of combined Gamma-oryzanol (GO) and Curcumin (Cur), natural compounds with antioxidant and anti-inflammatory properties, on DEX-induced depression. Male Sprague–Dawley rats (6 weeks old) were divided into five groups (n = 4–5 rats per group). Rats in the DEX and treatment groups were induced into depression by DEX (1.5 mg/kg daily for 28 days). The Control and DEX groups received reverse osmosis water. The treatment groups received GO+Cur at low dose (5+25 mg/kg), GO+Cur at high dose (10+50 mg/kg), and fluoxetine (Flx,10 mg/kg). At the end of the experiment, testis weight, sperm concentration, and testicular morphology were evaluated. Testis weight and sperm concentration were significantly decreased in the DEX and DEX+Flx groups compared with the Control group. GO+Cur administration at both doses significantly improved testis weight compared with the DEX+Flx group. Notably, high-dose GO+Cur restored sperm concentration compared with all other depressive groups. Histological analysis revealed that DEX induced seminiferous tubules abnormalities, including germinal epithelium separation, vacuolization, luminal sloughing of germ cells, tubular irregularity, and atrophy. Compared with the DEX group, the DEX+high-dose GO+Cur group exhibited fewer histological abnormalities and a higher number of normal seminiferous tubules. In conclusion, co-administration of GO and Cur, particularly at a high dose, attenuates DEX-induced testicular damage by improving sperm concentration and preserving the normal structure of seminiferous tubules. These findings suggest that combined GO and Cur may better support reproductive function under DEX-induced depressive conditions compared to standard antidepressants like Flx.

Keywords *Depression, Sperm concentration, Seminiferous tubule, Gamma-oryzanol, Curcumin*

P-05

Neutrophil-Associated Extracellular Matrix Remodeling of the Aortic Wall in Sweet Syndrome: An Anatomical and Histopathological Study

Nichapha Chandee[1*], Kulwadee Kanjana[3], Itsares Muikham[1], Boottoh Nambunruang[1], Dusit Kongnawakun[2], Ratirat Golaga[4]
[1] Department of Medical Education, School of Medicine, Suranaree University of Technology, University Avenue, Nakhon Ratchasima, Thailand
[2] School of Pathology, School of Medicine, Suranaree University of Technology, University Avenue, Nakhon Ratchasima, Thailand
[3] Division of Medical Sciences, School of Medicine, Walailak University, Nakhon Si Thammarat, Thailand
[4] Division of Sports Science and Health Promotion, Faculty of Public Health, Valaya Alongkorn Rajabhat University under the Royal Patronage, Pathum Thani, Thailand
*Corresponding author, e-mail: Nichapha.ch@sut.ac.th

Abstract
Background: Sweet syndrome is a neutrophil-mediated inflammatory disorder that primarily affects the skin, while its involvement in large vessels such as the aorta remains insufficiently characterized. **Objective:** This case-based vascular pathology study aimed to examine whether neutrophil-associated inflammation is associated with structural remodeling of the aortic wall through integrated anatomical, histological, and ultrastructural analyses. **Methods:** Aortic specimens (n = 4), including one case with clinically confirmed Sweet syndrome and three normal controls, were obtained from a limited number of cadaveric specimens and comparatively analyzed. Control specimens were selected to be comparable in age and sex. Where available, underlying conditions and tissue preservation conditions were also considered to minimize potential confounding effects. Histological evaluation was performed using hematoxylin–eosin and Masson's trichrome staining to assess tissue architecture and collagen distribution. Ultrastructural alterations were further investigated using scanning electron microscopy. **Results:** Affected aorta exhibited a pronounced expansion of the tunica adventitia and disorganization of smooth muscle fibers within the tunica media. Masson's trichrome staining demonstrated increased collagen deposition and extracellular matrix accumulation, consistent with active fibrotic remodeling. Ultrastructural examination revealed fragmented smooth muscle fibers, irregularly arranged collagen bundles, and the presence of activated fibroblasts, indicating disruption of extracellular matrix organization and compromised structural integrity of the vascular wall. These features were not observed in normal cadaveric aortas. Collectively, the findings provide anatomical and histopathological evidence that neutrophil-associated inflammation is closely linked to extracellular matrix remodeling and collagen reorganization within the aortic wall. Such structural alterations may reduce vascular integrity and suggest a potential, yet underrecognized, involvement of large vessels in Sweet syndrome. **Conclusion:** This study underscores the value of integrating histological and ultrastructural approaches to elucidate inflammation-driven vascular remodeling and to broaden current understanding of systemic manifestations associated with neutrophilic inflammatory disorders.

Keywords *Sweet syndrome, Aorta, Extracellular matrix remodeling, Collagen deposition, Histopathology*

P-06

The Effects of Probiotics on Small Intestinal Histopathology in Rats Exposed to Chronic Unpredictable Mild Stress

Jariya Samo-on[1], Suwapat Pakansit[1], Chadaporn Santawong[1], Pensiree Klinhom[1], Manwika Singsuwan[1], Maythanil Kantavaree[1], Siripaporn Kesyu[2,4], Porntipha Vitheejongjaroen[5], Jureepon Roboon[1,4], Paweena Kaewman[1,4], Samur Thanoi[3], Sutisa Nudmamud-Thanoi[1,4], Ittipon Phoungpetchara[1,4*]
[1] Department of Anatomy, Faculty of Medical Science, Naresuan University, Phitsanulok, Thailand
[2] Medical Science Graduate Program, Faculty of Medical Science, Naresuan University, Phitsanulok, Thailand
[3] School of Medical Sciences, University of Phayao, Phayao, Thailand
[4] Center of Excellence in Medical Biotechnology (CEMB), Naresuan University, Phitsanulok, Thailand
[5] Charoen Pokphand Foods Public Company Limited, Ayutthaya,13170, Thailand
*Corresponding author, e-mail: ittiponp@nu.ac.th

Abstract
Background: Chronic stress has become increasingly prevalent in modern society, negatively impacting both physical and mental health, including the digestive system. Prolonged stress can disrupt intestinal function and alter gut microbiota balance, leading to gastrointestinal dysfunction. Probiotics, particularly *Lactobacillus* species, have been reported to restore microbial balance and enhance intestinal health, offering a promising approach to mitigating stress-related gastrointestinal disorders. **Objective:** To investigate the effects of probiotic supplementation on anxiety-related responses and histological changes in the small intestine of rats subjected to chronic unpredictable mild stress (CUMS). **Methods:** Twenty male Sprague–Dawley rats were randomly assigned to experimental groups: control, probiotic-treated, stress-induced (CUMS), CUMS with probiotics, and CUMS with fluoxetine. The probiotic used was *Lactobacillus rhamnosus* (CPF01), administered orally at a dose of 1 mL/day (10^9 CFU/day) for 28 days after CUMS induction. A CUMS protocol was employed to induce chronic stress. **Results:** Stress exposure was associated with significant body weight loss in the CUMS group compared to the control group. Notably, probiotic supplementation during CUMS induction showed a tendency toward higher body weight gain compared to both the CPF01-control (non-CUMS) and control groups. By histopathological examination, CUMS stress exposure resulted in marked alterations in the small intestine, including reduced villus height, epithelial disorganization, shortened intestinal glands, increased epithelial degeneration, and a decreased goblet cell count. In contrast, both the CUMS with probiotics and non-CUMS with probiotics receiving groups showed improved intestinal morphology, characterized by increased villus height, restored epithelial organization, elongated intestinal glands, regenerated epithelial cells, and an increased number of goblet cells. **Conclusion:** These findings suggested that chronic stress impairs intestinal structure and function. Probiotic supplementation may effectively improve intestinal morphology and support gut health under stressful conditions, highlighting its potential as a therapeutic intervention.

Keywords *Chronic unpredictable mild stress, Probiotics, Small intestine, Inflammation*

P-07

The Effect of Cannabidiol (CBD)-Brahmi Extract on the Histopathology of Liver Tissue in Rats Induced with Chronic Unpredictable Mild Stress (CUMS)

Chadaporn Santawong[1], Pensiree Klinhom[1], Jariya Samo-on[1], Manwika Singsuwan[1], Maythanil Kantavaree[1], Plaiyfah Janthueng[2,4], Wanfrutkon Waehama[2,4], Jureepon Roboon[1,4], Paweena Kaewman[1,4], Samur Thanoi[3], Sutisa Nudmamud-Thanoi[1,4], Ittipon Phoungpetchara[1,4*]
[1] Department of Anatomy, Faculty of Medical Science, Naresuan University, Phitsanulok, Thailand
[2] Medical Science Graduate Program, Faculty of Medical Science, Naresuan University, Phitsanulok, Thailand
[3] School of Medical Sciences, University of Phayao, Phayao, Thailand
[4] Center of Excellence in Medical Biotechnology (CEMB), Naresuan University, Phitsanulok, Thailand
*Corresponding author, e-mail: ittiponp@nu.ac.th

Abstract
Background: Nowadays, stress is a burgeoning health concern, particularly among adolescents and working adults. Beyond its psychological impact, chronic stress significantly impacts metabolic organs, especially the liver—a vital organ for detoxification and metabolism that is highly susceptible to stress-induced oxidative damage and inflammatory responses. Cannabidiol (CBD), derived from Hemp (*Cannabis sativa*), and Brahmi (*Bacopa monnieri*) are medicinal plants known for their potential anxiolytic, antioxidant, and anti-inflammatory properties, making them suitable candidates for development into preventive health products. **Objective:** To investigate the effects of CBD extract and Brahmi on histopathological changes in the liver tissue of rats subjected to chronic unpredictable mild stress (CUMS). **Methods:** Forty-two male Sprague-Dawley rats were divided into seven groups (n=6 per group): Control (CA), Stress-induced (UA), Stress-induced treated with Brahmi (UB), Stress-induced treated with CBD isolate (UD), Stress-induced treated with CBD-enriched hemp extract (UG), Stress-induced treated with a combination of Brahmi and CBD isolate (UJ), and Stress-induced treated with Brahmi and CBD-enriched hemp extract (UL). Brahmi extract (20 mg/kg) and CBD (isolate or enriched hemp extract at 5 mg/kg) were administered orally. The animals were subjected to a chronic unpredictable mild stress (CUMS) protocol for 14 days to induce physiological stress. **Results:** Compared to the control group, stress exposure resulted in marked histopathological alterations in the liver, including disorganized hepatocyte arrangement, increased sinusoidal width, cellular degeneration, white blood cell infiltration, and the presence of intracellular fat vacuoles. In contrast, treatment with CBD and Brahmi demonstrated notable hepatoprotective effects, evidenced by improved hepatocyte architecture, reduced sinusoidal dilation, and a more organized cellular arrangement. **Conclusion:** These findings indicate that chronic stress induces significant liver tissue damage. CBD and Brahmi exhibit potent hepatoprotective potential alongside their known anti-inflammatory, anxiolytic, and antidepressant properties. These botanical agents serve as promising therapeutic alternatives with significant potential for development into health products for disease prevention.

Keywords *Stress, Liver, Cannabidiol (CBD), Hemp, Brahmi*

P-08

The Effect of CBD-Brahmi Extract on the Histopathology of Gastric Tissue in Rats Induced by Chronic Unpredictable Mild Stress

Pensiree Klinhom[1], Chadaporn Santawong[1], Jariya Samo-on[1], Manwika Singsuwan[1], Maythanil Kantavaree[1], Plaifah Janthueng[2,4], Wanfrutkon Waehama[2,4], Jureepon Roboon[1,4], Paweena Kaewman[1,4], Samur Thanoi[2], Sutisa Nudmamud-Thanoi[1,4], Ittipon Phoungpetchara[1,4*]
[1] Department of Anatomy, Faculty of Medical Science, Naresuan University, Phitsanulok, Thailand
[2] Medical Science Graduate Program, Faculty of Medical Science, Naresuan University, Phitsanulok, Thailand
[3] School of Medical Science, University of Phayao, Thailand
[4] Center of Excellence in Medical Biotechnology (CEMB), Naresuan University
*Corresponding author, e-mail: ittiponp@nu.ac.th

Abstract
Background: Chronic stress contributes to gastrointestinal dysfunction via the brain–gut axis, leading to gastric mucosal irritation, inflammation, and structural damage. Proton pump inhibitors (PPIs) are widely used for treatment but may cause adverse effects. Therefore, alternative therapies from locally cultivated medicinal plants with fewer side effects are of interest. *Bacopa monnieri* (Brahmi) and cannabidiol (CBD) from hemp have demonstrated anti-stress and anti-inflammatory properties. **Objective:** To evaluate the effects of Brahmi extract and CBD extracts on gastric mucosal pathology in rats subjected to Chronic Unpredictable Mild Stress (CUMS). **Methods:** Forty-two male Sprague Dawley rats were assigned to seven groups (n = 6/group): control group receiving corn oil (1 ml/kg), stress group receiving corn oil (1 ml/kg), stress + Brahmi extract (20 mg/kg), stress + CBD isolate (5 mg/kg), stress + CBD-enriched hemp extract (5 mg/kg), stress + Brahmi extract (20 mg/kg) combined with CBD isolate (5 mg/kg), and stress + Brahmi extract (20 mg/kg) combined with CBD-enriched hemp extract (5 mg/kg). All treatments were administered via oral gavage once daily for 14 days. After CUMS induction, gastric tissues from the fundus were stained with hematoxylin and eosin (H&E). Mucosal and submucosal thickness, as well as parietal cell density per gastric area, were measured. Data were expressed as mean ± SD and analyzed using one-way ANOVA with GraphPad Prism, with statistical significance at $p \leq 0.05$. **Results:** Chronic stress was significantly reduced in mucosal thickness compared with controls. Treatment with Brahmi (20 mg/kg) alone and in combination with CBD-enriched hemp extract (5 mg/kg) significantly restored mucosal thickness. Changes in submucosal thickness and parietal cell density were observed but were not statistically significant. **Conclusion:** Brahmi extract, particularly when combined with CBD-enriched hemp extract, may protect against stress-induced gastric mucosal damage, suggesting its potential as an alternative therapeutic strategy for stress-related gastric inflammation.

Keywords *Cannabidiol, Bacopa monnieri, CUMS, Gastric histopathology, Gastric mucosal*

P-09

Standardized Extract of *Centella asiatica* (ECa 233) Ameliorates High-Fat Diet–Induced Steatohepatitis in Rats

Phonthipha Siadkham[1,2], Wittawat Tajai[1,2], Suthaphat Kongsak[2], Akkarawat Sathong[2], Aphinya Chaiklam[2], Saowalak Rungruang[2,3], Apichaya Niyomchan[4], Piyanee Sriya[5], Mayuree H Tantisira[6], Peter J Mark[7], Wai Chen[8,9], Kannika Adthapanyawanich[1,2,11], Kroekkiat Chinda[2,10,11*], Yutthapong Tongpob[1,2,11*]

[1] Department of Anatomy, Faculty of Medical Science, Naresuan University, Phitsanulok, Thailand, 65000
[2] Integrative Cardiovascular Research Unit, Faculty of Medical Science, Naresuan University, Phitsanulok, Thailand, 65000
[3] Department of Medical Sciences, Mahidol University, Amnatcharoen Campus, Amnatcharoen, Thailand, 37000
[4] Department of Anatomy, Faculty of Medicine Siriraj Hospital, Mahidol University, Bangkok, Thailand, 10700
[5] Department of Anatomy, Pramongkutklao College of Medicine, Rajvithi Road, Ratchathewi, Bangkok, 10400
[6] Faculty of Pharmaceutical Sciences, Burapha University, Chonburi, Thailand, 20131
[7] School of Human Sciences, The University of Western Australia, Crawley, Western Australia, Australia, 6009
[8] Curtin Medical School, Curtin University, Perth, Australia, 6102
[9] Service 5, Fiona Stanley Hospital, North Metro Health Services, Perth, Australia, 6150
[10] Department of Physiology, Faculty of Medical Science, Naresuan University, Phitsanulok, Thailand, 65000
[11] Centre of Excellence in Medical Biotechnology, and AI CARE Research Cluster, Naresuan University, Phitsanulok, Thailand, 65000
*Corresponding author, e-mail: yutthapongt@nu.ac.th, kroekkiatc@nu.ac.th

---

Abstract

Background: High-fat diet (HFD) consumption drives non-alcoholic fatty liver disease, leading to steatohepatitis characterized by hepatic steatosis, inflammation, and cellular injury. *Centella asiatica* standardized extract (ECa 233), containing 88.19% triterpenoid glycosides (madecassoside and asiaticoside), has shown metabolic benefits, but its hepatoprotective effects against HFD-induced steatohepatitis remain unrevealed. **Objective:** To investigate the hepatoprotective effects of ECa 233 on biochemical and histopathological changes in HFD-induced steatohepatitis. **Methods:** Male Wistar rats were divided into three groups (n = 5/group): normal diet (ND), HFD, HFD + ECa 233 (30 mg/kg/day). Rats were treated daily by oral gavage for 12 weeks. Body weight, liver index and serum biochemical parameters were investigated. Formalin-fixed liver sections were evaluated using hematoxylin-eosin (for hepatocellular degeneration) and Masson's trichrome staining (for collagen deposition), with blinded histopathological assessment. **Results:** HFD significantly increased body weight gain and liver index (p<0.001 vs ND). Serum triglycerides, total cholesterol, low-density lipoprotein cholesterol (LDL-cholesterol), aspartate aminotransferase (AST), and alanine aminotransferase (ALT) were also significantly increased (p<0.001 vs ND). Histology showed micro- and macro-vesicular steatosis, lobular inflammation, hepatocellular ballooning, megamitochondria formation, and increased collagen deposition in HFD-fed rats. Pronounced reductions in triglycerides, total cholesterol, LDL-cholesterol, AST, and ALT were observed ($p<0.001$ vs HFD). Histo-pathological evaluation also showed reduced micro- and macro-vesicular steatosis, lobular inflammation, hepatocellular ballooning, megamitochondria formation, and collagen deposition (p<0.01 vs HFD). **Conclusion:** ECa 233 attenuates HFD-induced steatohepatitis and improves biochemical and histopathological alterations in HFD-fed rats. These findings suggest that ECa 233 may have beneficial effects in HFD-associated liver injury. Further studies are required to elucidate the underlying mechanisms.

Keywords *Centella asiatica, ECa 233, High-fat diet, Steatohepatitis, Hepatoprotection*

P-10

Comparative Protective Effects of Dried Mulberry Fruit and Standardized Extract Against High-Fat Diet-Induced Male Reproductive Dysfunction in Rats

Kanyakorn Aitsarangkun Na Ayutthaya[1,2], Siriporn Kreungnium[1,2], Saowalak Rungruang[2,3], Wittawat Tajai[1,2], Apichaya Niyomchan[4], Patcharada Amatyakul[5], Hiroki Nakata[6], Wai Chen[7,8], Sutthinee Wisutthathum[9], Kannika Adthapanyawanich[1,2,10], Kroekkiat Chinda[2,10,11*], Yutthapong Tongpob[1,2,10*]

[1] Department of Anatomy, Faculty of Medical Science, Naresuan University, Phitsanulok, Thailand 65000
[2] Integrative Cardiovascular Research Unit (ICRU), Faculty of Medical Science, Naresuan University, Phitsanulok, Thailand 65000
[3] Department of Medical Sciences, Mahidol University, Amnatcharoen Campus, Amnatcharoen, Thailand 37000
[4] Department of Anatomy, Faculty of Medicine Siriraj Hospital, Mahidol University, Bangkok, Thailand 10700
[5] Department of Obstetrics and Gynecology, Faculty of Medicine, Naresuan University, Phitsanulok, Thailand 65000
[6] Department of Clinical Engineering, Faculty of Health Sciences, Komatsu University, Japan 9230961
[7] Curtin Medical School, Curtin University, Perth, Australia 6102
[8] Service 5, Fiona Stanley Hospital, North Metro Health Services, Perth, Australia 6150
[9] Department of Biochemistry, Faculty of Medical Science, Naresuan University, Phitsanulok, Thailand 65000
[10] Centre of Excellence in Medical Biotechnology (CEMB), and AI CARE Research Cluster, Naresuan University, Phitsanulok, Thailand 65000
[11] Department of Physiology, Faculty of Medical Science, Naresuan University, Phitsanulok, Thailand 65000
*Corresponding author, e-mail: yutthapongt@nu.ac.th, kroekkiatc@nu.ac.th

Abstract

Background: Long-term high-fat diets (HFD) consumption triggers oxidative stress and inflammation, contributing to testicular and sperm damage, and may lead to male infertility. Mulberry fruit is rich in anthocyanins with potent antioxidant properties that can mitigate these effects. However, research specifically comparing the efficacy of dried mulberry fruit (dMF) and standardized extract of mulberry fruit (SEM) remains limited. **Objective:** To evaluate comparative protective effects of dMF and SEM against HFD-induced male reproductive dysfunction in rats. **Methods:** Twenty-four male Wistar rats were divided into four groups (n=6/group): Normal diet (ND), HFD, HFD+dMF (100 mg/kg/day), and HFD+SEM (100 mg/kg/day). During the 90-day oral daily administration period, body weight and testicular weight were recorded. Sperm were collected from the caudal epididymis to evaluate sperm parameters. Testicular tissues were examined histopathologically for changes in seminiferous tubules using standardized scoring methods. **Results:** Compared to the ND group, the HFD group showed significantly increased testicular abnormalities: germ cell separation (p=0.0149) and vacuolization within seminiferous tubules (p=0.0002), along with reduced sperm concentration (p=0.0009), motility (p=0.0008), viability (p=0.0021), and normal morphology (p<0.0001). Both dMF and SEM interventions offered protection; however, SEM implied superior protective effects: with more comprehensive restoration of sperm concentration (p=0.0197), motility (p=0.0001), and morphology (p=0.0009) compared to the HFD group. Furthermore, SEM was especially effective in preserving testicular cell structure, with a significant reduction in vacuolization compared to both HFD (p=0.0006) and dMF-treated groups (p=0.0212). **Conclusion:** SEM demonstrates superior protective efficacy over dMF in mitigating HFD-induced male reproductive dysfunction while preserving sperm quality and testicular integrity, positioning SEM as a promising natural intervention for HFD-related male infertility. Further studies are required to elucidate the underlying molecular mechanisms of SEM.

Keywords: *Mulberry fruit extract, Sperm quality, Male reproductive dysfunction, High-fat diet*

Background

The global rise in long-term high-fat diet (HFD) consumption has led to a dramatic increase in the prevalence of metabolic syndrome, which has become a major public health concern worldwide (1,2). Prolonged HFD intake promotes excessive lipid accumulation (3), resulting in an imbalance between pro-inflammatory and anti-inflammatory cytokines (3,4,5). This state of chronic low-grade inflammation, coupled with enhanced oxidative stress, serves as a central driver for metabolic disturbances (6,7).

Besides cardiovascular consequences, emerging evidence indicates that HFD-induced metabolic dysfunction is a major contributor to male reproductive impairment (8,9,10). At the structural level, HFD-induced metabolic abnormalities lead to ectopic lipid deposition within the testicular parenchyma, triggering localized oxidative stress that disrupts the blood-testis barrier (BTB) (10,11,12). These pathological changes impair the function of Sertoli and Leydig cells, which are essential for supporting spermatogenesis and testosterone production (11,13,14). Consequently, HFD consumption is closely associated with testicular atrophy, impaired spermatogenesis, reduced sperm quality, and increased sperm DNA damage (8,10,15,16).

The overproduction of reactive oxygen species (ROS), notably through electron leakage in the mitochondrial electron transport chain within the testicular microenvironment, is a major cause of these effects (17,18). The high content of polyunsaturated fatty acids in the membranes of germ cells makes the testes highly susceptible to lipid peroxidation (19,20). In HFD models, this oxidative surge is frequently accompanied by a compromised cellular defense system, characterized by reduced activity of essential antioxidant enzymes such as superoxide dismutase (SOD), catalase (CAT), and glutathione peroxidase (GPx) (21,22). This exhaustion of the testicular antioxidant defense system creates a vicious cycle of oxidative damage that culminates in germ cell apoptosis (22).

Mulberry fruit (*Morus alba* L.), originally cultivated in the Himalayan foothills of southern China and now widely grown throughout Southeast Asia, including Thailand, has attracted considerable scientific interest due to its rich phytochemical composition (23). It is abundant in anthocyanins, flavonoids, and other polyphenolic compounds with potent antioxidant and anti-inflammatory properties (24,25,26). Previous studies have reported that mulberry supplementation improves lipid metabolism, attenuates oxidative stress, and enhances metabolic homeostasis in experimental models of diet-induced metabolic disorders (27,28, 29,30). Furthermore, both dMF and various mulberry extracts have demonstrated protective effects across multiple organ systems, including the cardiovascular system, the liver (31,32), and potentially the male reproductive system by mitigating oxidative damage to sperm (33).

While mulberry-derived compounds are hypothesized to protect testicular cytoarchitecture from oxidative insults, comparative evidence regarding whether dMF or standardized extract of mulberry fruit (SEM) provides superior protection against HFD-induced reproductive damage remains limited. The bioavailability and therapeutic efficacy of bioactive compounds can differ substantially between whole fruit preparations and standardized extracts due to differences in compound concentration, matrix effects, and intestinal absorption. Understanding these differences is critical for optimizing therapeutic interventions and informing evidence-based recommendations for managing HFD-induced reproductive dysfunction.

Therefore, the present study aimed to evaluate and compare the protective effects of dMF and SEM against HFD-induced male reproductive dysfunction in rats. By systematically assessing sperm parameters and testicular histopathology, this study is expected to provide further insight into the relationship between HFD-induced metabolic disturbances and male reproductive impairment, as well as to explore the comparative potential of different mulberry preparations as natural interventions for mitigating HFD-induced reproductive damage. It was hypothesized that SEM, which contains a higher concentration of bioactive compounds such as anthocyanins, may exert greater protective effects against HFD-induced reproductive alterations compared with dMF.

Materials and Methods

Plant sample preparation and anthocyanin content determination

dMF was prepared by the Department of Pharmacy and Natural Products, Thailand Institute of Scientific and Technological Research (TISTR), Bangkok, Thailand. Fresh mulberries (*Morus alba L.*) were collected, freeze-dried, and mechanically processed into dMF powder.

SEM was prepared using 70% ethanol extraction at room temperature for 72 hours. The extraction solvent was subsequently removed through controlled evaporation under reduced pressure at 40°C to ensure product purity. The resulting extract was stored at −20°C in the dark until use to maintain stability.

Total anthocyanin content was quantified using the pH differential method as previously described by Chaiwong et al. (2021) (31). The results were expressed as cyanidin-3-glucoside equivalents (mg/100 g of sample). The antioxidant activity of both formulations was evaluated using the DPPH radical scavenging assay, and the IC_{50} value was determined from the dose–response curve.

Animals and experimental design

Twenty-four male Wistar rats (8-week-old, weighing 250-300 g) were obtained from Nomura Siam International Co. Ltd., Bangkok, Thailand. All animal procedures were approved by Naresuan University Animal Care and Use Committee (NUACUC), Phitsanulok, Thailand, with an ethical protocol number of NU-AEE 670303.

The rats were housed in environmentally controlled conditions (22±1ºC, and 12 h light/dark cycle) with food and water provided *ad libitum*. After a 7-day acclimatization period on a standard laboratory diet, rats were randomly divided into four groups (n=6/group) and treated by oral gavage administration for 90 consecutive days as follows:

Group 1 Normal diet (ND): rats received vehicle (distilled water) and were fed a normal diet (protein 28.2%, carbohydrate 52%, total fat 19.8%, energy density 4.2 kcal/g).

Group 2 High-fat diet (HFD): rats received vehicle and were fed a HFD supplemented with sugar (protein 26.5%, carbohydrate 14.3%, total fat 59.28%, sodium chloride 0.1% w/w, propylene glycol, energy density 5.35 kcal/g).

Group 3 HFD+dMF: rats were fed HFD, and dried mulberry fruit (100 mg/kg/day) was administered by gastric gavage tube once daily as an aqueous suspension. The selected doses were based on previous studies (Chaiwong et al., 2021) (31).

Group 4 HFD+SEM: rats were fed with HFD and received standardized extract of mulberry fruit (100 mg/kg/day) administered by gastric gavage tube once daily as an aqueous suspension.

Throughout the experiment period, rats were weighed weekly and monitored daily for general health status, behavioral changes, and adverse effects. Food intake was recorded weekly. On the 91st day, rats were fasted for 6-8 hours before being euthanized under anesthesia. Immediately following euthanasia, testis and caudal epididymis were rapidly collected and weighed for evaluation.

Sperm quality analysis

After the rats were sacrificed, the caudal epididymis was rapidly removed and placed in pre-warmed 1x phosphate-buffered saline (PBS, 37°C) to obtain sperm suspension. All parameters were evaluated under a light microscope at 20x magnification, with a total of 200 spermatozoa analyzed per sample.

Sperm concentration and motility

A 20 µL aliquot of sperm suspension was loaded into a Makler counting chamber. Concentration was calculated by counting spermatozoa in rows 2, 5, and 8, with results expressed as 10^6 cells/mL. Concurrently, sperm motility was assessed via video recordings and categorized into progressive motility, non-progressive motility, or immotile.

Sperm viability

Sperm viability was evaluated using the Eosin-Nigrosin staining method. A 20 µL drop of sperm suspension was mixed with an equal volume of Eosin-Nigrosin (1:1 ratio) on a glass slide. The percentage of viable (unstained) spermatozoa cells was recorded.

Sperm morphology

A 20 µL aliquot of sperm suspension was smeared onto a glass slide and processed using the Diff-Quik staining assay. The proportion of morphologically normal and abnormal spermatozoa, including specific head, neck, and tail defects, was quantified.

Testicular histopathological assessment

Testicular tissues were cut and fixed in 10% Neutral Buffered Formalin immediately after collection. Following fixation, the tissues were processed using standard histology procedures: dehydration through graded alcohol series, clearing in xylene, and embedding in paraffin wax. Tissue blocks were sectioned at 3 µm thickness using a rotary microtome. The tissue sections were deparaffinized, rehydrated, and stained with hematoxylin and eosin.

Histopathological evaluation was performed under a light microscope at 10x magnification by two independent observers blinded to the treatment groups. For each animal, at least 100 seminiferous tubules were examined and scored according to the following criteria:

1. **Normal:** Intact seminiferous tubules with orderly arranged germ cells at different stages of spermatogenesis, complete spermatogenic epithelium, and no pathological changes.
2. **Vacuolization:** Presence of clear vacuoles within the seminiferous epithelium, indicating cytoplasmic damage or fluid accumulation.

3. **Germ cell separation:** Detachment of germ cells from the basement membrane and Sertoli cells, with loss of normal cellular adhesion.
4. **Luminal sloughing:** Presence of detached germ cells or cellular debris within the tubular lumen, indicating severe epithelial disruption.
5. **Irregularity:** Distortion of tubular shape, uneven thickness of the seminiferous epithelium, or disorganized cellular arrangement.
6. **Atrophy:** Reduced tubular diameter, thinning of the germinal epithelium, and decreased number of germ cells.

Results were expressed as the percentage of tubules exhibiting each pathological feature.

Statistical analysis

Data were expressed as means ± standard deviation (SD). Statistical analyses were performed using GraphPad Prism software version 10 (GraphPad Software, CA, USA). The differences between multiple groups were assessed using one-way analysis of variance (ANOVA) followed by Tukey's *post hoc* test for multiple comparisons. A p-value <0.05 was considered statistically significant. All measurements were conducted by investigators blinded to the treatment groups, where applicable.

Results

Anthocyanin contents of mulberry fruit extract

Anthocyanin was higher in SEM compared with dMF. SEM contained 1,608.88 mg/100 g of cyanidin-3-glucoside equivalents, whereas dMF contained 1,250 mg/100 g, representing approximately a 28.7% increase in anthocyanin concentration in the standardized extract. Despite differences in anthocyanin content, both preparations exhibited comparable antioxidant capacity in the DPPH radical-scavenging assay. The IC_{50} values were identical at 0.24 mg/mL, indicating similar in vitro free radical scavenging potency between SEM and dMF.

The relatively high anthocyanin content may provide a biochemical basis for the antioxidant properties of the preparations and could potentially be linked to their observed biological effects in this study (Table 1).

Animal welfare and general observations

Throughout the 90-day experimental period, all animals exhibited normal behaviors, with no visible alterations to their skin, fur, eyes, or mucous membranes. No adverse effects such as tremors, convulsions, salivation, diarrhea, lethargy, coma, or mortality were observed in any experimental group.

Table 1 Extraction yield and antioxidant properties of dMF and SEM

Sample	ATCN (mg/ 100 g)	DPPH IC_{50} (mg/mL)	Yield (g)	Storage
dMF powder	1,250.0 0	0.24	1	-20 ℃
SEM (70% Ethanol extract)	1,608.8 8	0.24	1.62	4 ℃

*ATCN: Total anthocyanin content expressed as cyanidin-3-glucoside equivalents.

Effects of dMF and SEM on body weight and relative testicular weight in HFD-treated rats

After 90 days of treatment, no significant differences in final body weight were observed among the experimental groups (Table 2). However, relative testicular weight (testis weight/body weight ratio) was significantly reduced in the HFD+SEM group compared to both the ND group (p = 0.0312) and the HFD group (p = 0.0287). Neither the HFD alone nor the HFD+dMF treatment significantly affected relative testicular weight compared to the ND group (Table. 2).

Effects of dMF and SEM on sperm parameters *in HFD-treated rats*

To determine whether HFD consumption and subsequent interventions affected spermatogenesis, comprehensive sperm quality parameters were evaluated (Table 2).

HFD-induced sperm damage

Rats fed an HFD exhibited marked deterioration in sperm quality across all parameters compared to the ND group (Table 2). Specifically, the HFD group showed: 39.6% reduction in sperm concentration (p = 0.0009); 40.1% reduction in sperm viability (p = 0.0021); 57.7% reduction in progressive motility (p = 0.0008); and 30.7% reduction in normal sperm morphology (p<0.0001). Correspondingly, the proportion of immotile spermatozoa was significantly elevated in the HFD group compared to the ND group (p = 0.0077). No statistically significant differences were observed in non-progressive motility across any experimental groups.

Table 2 Body weight, relative testicular weight and sperm quality parameters in HFD-fed rats at 90 days

Parameters	Group			
	ND	**HFD**	**HFD+dMF$_{100}$**	**HFD+SEM$_{100}$**
Initial weight (g)	224.94±47.26	183.41±50.98	215.94±62.43	216.04±69.58
Final weight (g)	529.17±52.48	534.46±58.19	544.22±35.29	573.50±59.51
Relative testicular weight (%)	0.39±0.03	0.41±0.05	0.36±0.03	0.32±0.04$^{*,\#}$
Sperm quality parameters	**ND**	**HFD**	**HFD+dMF$_{100}$**	**HFD+SEM$_{100}$**
Sperm concentration (10^6/ml)	31.17±4.79	18.83±5.53***	25.00±3.52	25.00±7.77$^{\#}$
Sperm viability (%)	38.08±10.13	22.83±4.42**	28.17±5.38	36.00±2.00$^{\#\#}$
Number of viable sperm (10^6/ml)	14.25±2.97	5.55±1.17***	7.39±1.54***	8.87±1.65$^{***,\#}$
Sperm progressive (%)	44.45±5.07	18.79±8.18***	36.89±11.16	49.07±12.17$^{\#\#\#}$
Sperm non progressive (%)	13.86±10.12	10.80±7.79	11.17±7.09	11.81±7.67
Sperm immotile (%)	41.70±12.29	70.40±14.94**	51.94±17.76	39.11±6.78$^{\#\#}$
Normal sperm morphology (%)	76.17±6.84	52.75±3.01***	64.67±2.40$^{**,\#\#}$	66.00±6.07$^{**,\#\#\#}$
Sperm head defect (%)	16.33±6.31	35.83±4.59***	27.17±2.54$^{**,\#}$	23.33±4.65$^{\#\#\#}$
Sperm neck defect (%)	7.50±1.52	11.42±2.85*	8.17±1.91	10.67±2.23

Values represent mean±SD of 6 rats in each group. Statistical significance was denoted as follows: *p≤0.05, ** p ≤0.01, *** p ≤0.001 vs ND group; $^{\#}$ p ≤0.05, and $^{\#\#}$ p ≤0.01, $^{\#\#\#}$ p ≤0.001 vs HFD group.

Table 3 Histopathological changes of seminiferous tubules in HFD-fed rats at 90 days

Parameters	Group			
	ND	**HFD**	**HFD+dMF$_{100}$**	**HFD+SEM$_{100}$**
Normal (%)	57.28±5.49	40.30±10.59**	45.07±6.33*	44.81±6.13*
Epithelial separation (%)	14.58±5.16	26.78±7.34*	22.45±6.96	19.40±5.35
Vacuolization (%)	24.89±2.82	37.42±5.18***	33.69±2.01**	25.97±5.53$^{\#\#\#,\$}$
Luminal sloughing (%)	0.70±0.45	0.56±0.44	0.35±0.27	1.29±0.44$^{\#,\$\$}$
Irregular (%)	3.15±2.98	2.15±1.59	1.75±1.41	4.62±3.55
Tubular atrophy (%)	0.00±0.00	0.18±0.22	0.07±0.10	0.07±0.11

Values represent mean±SD of 6 rats in each group. Statistical significance was denoted as follows: * p≤0.05, ** p≤0.01, *** p≤0.001vs ND group; # p≤0.05, $^{\#\#\#}$ p≤0.001 vs HFD group; and $^{\$}$ p≤0.05, $^{\$\$}$ p≤0.01 vs dMF group.

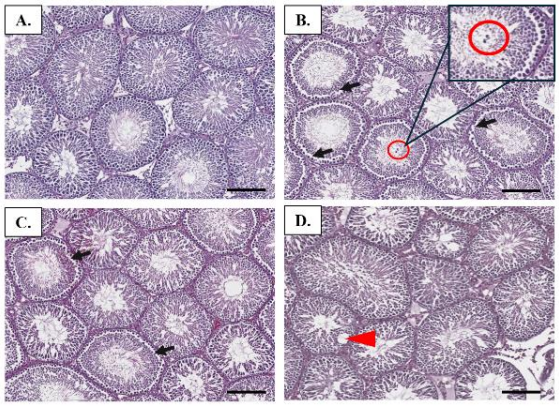

Fig. 1 Representative histopathological features of seminiferous tubules. (A) ND group showing normal seminiferous tubule architecture; (B) HFD group displaying separation of the germinal epithelium (black arrows) and luminal sloughing of germ cells (red circle); (C) HFD+dMF group; and (D) HFD+SEM group exhibiting vacuolization (red arrowhead). All images were captured at 10x magnification for analysis. Scale bars represent 100 µm.

Protective effects of SEM

Supplementation with SEM significantly ameliorated HFD-induced sperm damage across multiple parameters (Table 2). Compared to the HFD group, the HFD+SEM group demonstrated: significant restoration of sperm concentration (p = 0.0197); significant improvement in sperm viability (p= 0.0078); significant enhancement of progressive motility (p = 0.0001); and significant increase in normal sperm morphology (p = 0.0009). Furthermore, SEM treatment significantly reduced the proportion of immotile spermatozoa compared to the HFD group (p=0.0036).

Protective effects of dMF

The HFD+dMF group showed partial protective effects, with significant improvement only in normal sperm morphology compared to the HFD group (p = 0.0025). Other sperm parameters (concentration, viability, and motility) in the dMF-treated group did not reach statistical significance compared to the HFD group, although trends toward improvement were observed (Table 2).

Effects of dMF and SEM on testicular histopathology in HFD-treated rats

Histopathological examination revealed that the observed impairments in sperm quality were closely associated with structural damage within the seminiferous tubules (Fig. 1, Table 3).

HFD-induced testicular damage

The HFD group exhibited significant histopathological alterations compared to the ND group, characterized by decreased percentage of normal tubular structures (p = 0.0039), increased germ cell separation (p = 0.0149), and increased vacuolization within seminiferous tubules (p = 0.0002) (Figure 1, Table 3).

Protective effects of SEM

Treatment with SEM effectively preserved testicular histological integrity. Compared to the HFD group, the HFD+SEM group demonstrated a significant reduction in vacuolization (p = 0.0006) and a trend toward improved overall tubular histopathology. Notably, SEM treatment also showed superior protective effects compared to dMF treatment, with significantly reduced vacuolization in the HFD+SEM group versus the HFD+dMF group (p = 0.0212). However, the HFD+SEM group exhibited a modest but significant increase in luminal sloughing compared to both the HFD group (p=0.0266) and the HFD+dMF group (p = 0.0035). Despite this finding, the overall protective profile of SEM on testicular architecture was superior, as evidenced by the comprehensive improvements in sperm parameters (Fig. 1, Table 2).

Protective effects of dMF

The HFD+dMF group showed partial histological protection with trends toward reduced pathological changes, though these improvements were generally less pronounced than those observed with SEM treatment (Fig. 1, Table 3).

Summary of comparative efficacy

Taken together, these findings demonstrate that while both mulberry preparations offer protective effects against HFD-induced reproductive dysfunction, SEM provides superior and more comprehensive protection by preserving both testicular architecture and sperm functional parameters.

Discussion

The findings of the present study are consistent with the hypothesis that SEM may exert greater protective effects against HFD-induced male reproductive dysfunction than dMF. First, the SEM-treated rats exhibited the highest sperm quality across all measured parameters, which would be inconsistent with true testicular atrophy. Second, histopathological analysis revealed superior preservation of seminiferous tubule integrity in the SEM group, with a significant reduction in vacuolization: a pathological feature often associated with lipid accumulation and cellular edema (34). Third, the HFD group, despite having normal testicular weight, showed severe functional impairment, suggesting that maintenance of testicular mass under HFD conditions may reflect pathological lipid deposition rather than healthy tissue. In the present study, although HFD consumption did not significantly alter the gross testicular weight, it induced profound functional impairment, as evidenced by the marked decline in sperm concentration and motility. This suggests that biochemical and cellular changes occurred prior to any observable macroscopic alterations in organ mass. Thus, the “leaner” testicular phenotype observed with SEM treatment may represent a functionally superior state characterized by reduced lipid burden and inflammation, rather than tissue loss.

The superior protective efficacy of SEM compared to dMF observed across multiple reproductive parameters represents a key finding of this study. While dMF provided partial improvements (primarily in sperm morphology), only SEM-treated rats exhibited comprehensive restoration of sperm concentration, motility,

viability, and testicular histopathology approaching normal levels. This disparity in therapeutic efficacy can be attributed to several factors related to bioavailability and bioactive compound concentration (35). Our findings are consistent with previous reports indicating that ethanolic extraction can significantly enhance the concentration of bioactive polyphenols from mulberry fruit compared to unprocessed forms (Chaiwong et al., 2021) (31).

First, the standardization and concentration of bioactive compounds play a critical role. Our analysis confirmed that SEM contains approximately 28.7% higher total anthocyanin content (1,608.88 mg/100 g) compared to dMF (1,250 mg/100 g). The quantification of these compounds using the pH differential method aligns with established protocols for characterizing mulberry-derived antioxidants, which have been shown to correlate with systemic protective effects against metabolic stress (Chaiwong et al., 2021) (31). Anthocyanins have been extensively documented to possess potent antioxidant properties and exert protective effects on male reproductive function through multiple mechanisms (36, 37, 38). These compounds can scavenge ROS, activate endogenous antioxidant defense systems such as the Nrf2/ARE pathway, and suppress pro-inflammatory signaling cascades, including NF-κB activation (24, 26). Such mechanisms are particularly relevant in the context of HFD-induced reproductive dysfunction, where excessive ROS production and chronic inflammation are primary pathogenic drivers (17,18,21,22).

Second, bioavailability considerations are crucial. In dMF, anthocyanins and other polyphenolic compounds remain embedded within the complex plant matrix, including cell wall structures, and bound to proteins and carbohydrates. This structural encapsulation can significantly limit their liberation during gastrointestinal digestion and subsequent intestinal absorption (35). In contrast, the ethanol extraction process used to produce SEM effectively releases these bioactive compounds from the plant matrix, concentrating them into a more readily bioavailable form. This enhanced bioavailability likely enables SEM to deliver a more potent antioxidant surge within the testicular microenvironment, thereby more effectively counteracting HFD-induced oxidative stress and inflammatory damage.

Third, the standardization of SEM ensures consistent bioactive compound composition across batches, which may contribute to more reliable and reproducible therapeutic effects compared to whole fruit preparations that can vary based on growing conditions, harvest timing, and storage (23,35).

Beyond anthocyanins, mulberry extracts contain additional bioactive compounds, including flavonoids, resveratrol, and phenolic acids that may act synergistically to provide comprehensive metabolic protection (23,25,26). These compounds have been shown to improve lipid metabolism (27,28,39), reduce hepatic steatosis (29,30,31), attenuate systemic inflammation (24,31), and enhance endothelial function (27)—all processes that indirectly support male reproductive health by improving the overall metabolic milieu.

The observation of modest but significant increases in luminal sloughing in the SEM-treated group warrants discussion. Luminal sloughing, characterized by the presence of detached germ cells within the tubular lumen, can reflect either pathological epithelial damage or a physiological process of cellular turnover and renewal. In the context of our findings, several considerations suggest that this observation does not negate SEM's overall protective efficacy. First, the SEM group simultaneously exhibited the most significant improvements in all functional sperm parameters and a substantial reduction in other pathological features, particularly vacuolization. Second, the degree of luminal sloughing observed was modest and significantly lower than the severe epithelial disruption typically associated with testicular pathology. Third, some degree of germ cell shedding into the lumen is a normal component of spermatogenesis, particularly during the renewal of the spermatogenic epithelium. It is possible that SEM's enhancement of testicular metabolic activity and cellular turnover may transiently increase this physiological process. Nevertheless, further investigation is warranted to fully elucidate the significance of this finding.

The clinical implications of our findings are noteworthy. With the global increase in obesity and metabolic syndrome, male infertility associated with diet-induced metabolic dysfunction has become an increasingly prevalent concern (1,2,8,9). Our results suggest that SEM, as a concentrated and standardized natural product, holds promise as a therapeutic intervention for men with HFD-related reproductive impairment. The superior efficacy of standardized extracts over whole food preparations underscores the importance of bioavailability optimization and dose standardization in the development of nutraceutical interventions.

Study limitations and future directions

This study has several limitations that should be acknowledged. First, although sperm parameters

and testicular histopathology demonstrated clear improvements, the underlying mechanisms were not explored. In particular, oxidative stress biomarkers, antioxidant enzyme activities, inflammatory cytokines, and hormonal profiles were not assessed.

Second, this study employed a single dose (100 mg/kg/day) for both dMF and SEM. While this approach allowed direct comparison at equal doses, dose-response studies would be valuable to determine optimal therapeutic dosing for each preparation and to assess whether higher doses of dMF might achieve efficacy comparable to SEM.

Third, the study was conducted over 90 days with assessment at a single endpoint. Longer-term studies examining the durability of protective effects, as well as time-course studies to identify the earliest protective changes, would provide valuable information about treatment duration requirements and mechanisms of action.

Fourth, while histopathological assessment and sperm quality analysis are important endpoints, actual fertility outcomes were not evaluated. Future studies incorporating mating trials and assessing pregnancy rates, litter sizes, and offspring health would strengthen the translational relevance of these findings.

Fifth, the mechanisms by which SEM reduces relative testicular weight while improving sperm parameters and testicular architecture remain speculative. Direct measurement of testicular lipid content, inflammatory markers within testicular tissue, and assessment of blood-testis barrier integrity would help clarify whether this represents beneficial lipid clearance or other tissue remodeling processes.

Finally, although our current data highlights the benefits of SEM, directly measuring anthocyanin and flavonoid levels in plasma or testicular tissue would provide definitive evidence regarding the comparative bioavailability of both mulberry preparations.

Future research should further extend these findings by incorporating detailed molecular pathway analyses, including oxidative stress pathways (including Nrf2/ARE and Keap1 signaling), antioxidant enzyme activities (i.e., SOD, CAT, GPx), inflammatory pathways (i.e., NF-κB, MAPK, TNF-α, IL-1β, IL-6), and hormonal regulation to provide deeper insight into the protective effects of SEM. Additionally, dose-response studies, long-term follow-up assessments, fertility outcome measures, and pharmacokinetic evaluations would provide a more comprehensive understanding of the therapeutic potential and optimal application of SEM in HFD-related male reproductive dysfunction.

Conclusion

This study demonstrates that long-term HFD consumption significantly impairs male reproductive function, through deteriorated sperm quality and testicular damage. SEM exhibits superior protective efficacy compared to dMF, comprehensively restoring sperm parameters and preserving testicular integrity. The enhanced therapeutic profile of SEM is attributed to its 28.7% higher anthocyanin content and improved bioavailability through standardized extraction. These findings establish SEM as a promising evidence-based intervention for diet-induced male reproductive dysfunction. Future investigations should elucidate underlying molecular mechanisms, optimize therapeutic dosing, and evaluate long-term fertility outcomes to fully translate these findings into clinical practice.

Acknowledgements

This work was supported by Naresuan University (NU), and National Science, Research and Innovation Fund (NSRF) (Grant No. R2566B062), Agricultural Research Development Agency (Public Organization) (Grant No. CRP6205031380), and partially supported by Global and Frontier Research University Fund, Naresuan University (Grant Nos. R2566C053, R2567C003), and the Reinventing University Program 2023 and 2025, The Ministry of Higher Education, Science, Research and Innovation (MHESI), Thailand (Grant Nos. R2566A043, R2568A026, and R2568A037).

References

1. Tang C, Wang Y, Xu Z, Chen D, Xu J, Yang D, et al. The relationships between high-fat diet and metabolic syndrome: Potential mechanisms. Food Bioscience. 2024;59:104261.
2. Alberti KG, Zimmet P, Shaw J, Group IDFETFC. The metabolic syndrome: a new worldwide definition. Lancet. 2005;366(9491): 1059-62.
3. Ertunc ME, Hotamisligil GS. Lipid signaling and lipotoxicity in metaflammation: indications for metabolic disease pathogenesis and treatment. J Lipid Res. 2016;57(12):2099-114.
4. Wang Y, Wang H, Hegde V, Dubuisson O, Gao Z, Dhurandhar NV, et al. Interplay of pro- and anti-inflammatory cytokines to determine lipid accretion in adipocytes. Int J Obes (Lond). 2013;37(11):1490-8.
5. Kiran S, Rakib A, Kodidela S, Kumar S, Singh UP. High-Fat Diet-Induced Dysregulation of Immune Cells Correlates with Macrophage

Phenotypes and Chronic Inflammation in Adipose Tissue. Cells. 2022;11(8).
6. Fernandez-Garcia JC, Cardona F, Tinahones FJ. Inflammation, oxidative stress and metabolic syndrome: dietary modulation. Curr Vasc Pharmacol. 2013;11(6):906-19.
7. Tumurkhuu M, Bhat SA, Hossain MZ, Shafiq M, Hasnain MS, Nayak AK, et al. Editorial: Cellular and molecular mechanisms in metabolic disorders: role of inflammation and oxidative stress. Front Pharmacol. 2025;16: 1580553.
8. Martins AD, Majzoub A, Agawal A. Metabolic Syndrome and Male Fertility. World J Mens Health. 2019;37(2):113-27.
9. Leisegang K, Henkel R, Agarwal A. Obesity and metabolic syndrome associated with systemic inflammation and the impact on the male reproductive system. Am J Reprod Immunol. 2019;82(5):e13178.
10. Chen Y, Gu L, Xiong Y, Liu Y. Protective effects of atorvastatin on testicular dysfunction and reduced sperm quality induced by high-fat diet in mice: The inhibitory mechanism of oxidative stress. Eur J Pharmacol. 2025;992: 177357.
11. Chen ZF, Shen YF, Gao DW, Lin DF, Ma WZ, Chang DG. Metabolic pathways and male fertility: exploring the role of Sertoli cells in energy homeostasis and spermatogenesis. Am J Physiol Endocrinol Metab. 2025;329(1):E160-E78.
12. Morgan DH, Ghribi O, Hui L, Geiger JD, Chen X. Cholesterol-enriched diet disrupts the blood-testis barrier in rabbits. Am J Physiol Endocrinol Metab. 2014;307(12):E1125-30.
13. Luo D, Zhang M, Su X, Liu L, Zhou X, Zhang X, et al. High fat diet impairs spermatogenesis by regulating glucose and lipid metabolism in Sertoli cells. Life Sci. 2020;257:118028.
14. Monageng E, Offor U, Takalani NB, Mohlala K, Opuwari CS. A Review on the Impact of Oxidative Stress and Medicinal Plants on Leydig Cells. Antioxidants (Basel). 2023;12(8).
15. Crisostomo L, Videira RA, Jarak I, Starcevic K, Masek T, Rato L, et al. Diet during early life defines testicular lipid content and sperm quality in adulthood. Am J Physiol Endocrinol Metab. 2020;319(6):E1061-E73.
16. Ghosh S, Mukherjee S. Testicular germ cell apoptosis and sperm defects in mice upon long-term high fat diet feeding. J Cell Physiol. 2018;233(10):6896-909.
17. Valko M, Leibfritz D, Moncol J, Cronin MT, Mazur M, Telser J. Free radicals and anti-oxidants in normal physiological functions and human disease. Int J Biochem Cell Biol. 2007;39(1):44-84.
18. Feillet-Coudray C, Fouret G, Vigor C, Bonafos B, Jover B, Blachnio-Zabielska A, et al. Long-Term Measures of Dyslipidemia, Inflammation, and Oxidative Stress in Rats Fed a High-Fat/High-Fructose Diet. Lipids. 2019;54(1):81-97.
19. Lenzi A, Gandini L, Lombardo F, Picardo M, Maresca V, Panfili E, et al. Polyunsaturated fatty acids of germ cell membranes, glutathione and blutathione-dependent enzyme-PHGPx: from basic to clinic. Contraception. 2002;65(4):301-4.
20. Lenzi A, Gandini L, Picardo M, Tramer F, Sandri G, Panfili E. Lipoperoxidation damage of spermatozoa polyunsaturated fatty acids (PUFA): scavenger mechanisms and possible scavenger therapies. Front Biosci. 2000;5:E1-E15.
21. Fernandez-Sanchez A, Madrigal-Santillan E, Bautista M, Esquivel-Soto J, Morales-Gonzalez A, Esquivel-Chirino C, et al. Inflammation, oxidative stress, and obesity. Int J Mol Sci. 2011;12(5):3117-32.
22. Billah MM, Khatiwada S, Lecomte V, Morris MJ, Maloney CA. Ameliorating high-fat diet-induced sperm and testicular oxidative damage by micronutrient-based antioxidant intervention in rats. Eur J Nutr. 2022;61(7):3741-53.
23. Yuan Q, Zhao L. The Mulberry (Morus alba L.) Fruit-A Review of Characteristic Components and Health Benefits. J Agric Food Chem. 2017; 65(48):10383-94.
24. Santos ÉdFd, Sabino YNV, Montenegro EN, Faria CA, de Almeida TC, Gameiro J, et al. Antitumor, anti-inflammatory, and antioxidant activities of anthocyanins from food and isolated sources: Methodological insights and interactions with the intestinal microbiota. Journal of Functional Foods. 2025;134:107026.
25. He J, Giusti MM. Anthocyanins: natural colorants with health-promoting properties. Annu Rev Food Sci Technol. 2010;1:163-87.
26. Salehi B, Sharifi-Rad J, Cappellini F, Reiner Z, Zorzan D, Imran M, et al. The Therapeutic Potential of Anthocyanins: Current Approaches Based on Their Molecular Mechanism of Action. Front Pharmacol. 2020;11:1300.
27. Chan KC, Yang MY, Lin MC, Lee YJ, Chang WC, Wang CJ. Mulberry leaf extract inhibits the development of atherosclerosis in cholesterol-fed rabbits and in cultured aortic vascular smooth muscle cells. J Agric Food Chem. 2013; 61(11):2780-8.

28. Sun X, Yamasaki M, Katsube T, Shiwaku K. Effects of quercetin derivatives from mulberry leaves: Improved gene expression related hepatic lipid and glucose metabolism in short-term high-fat fed mice. Nutr Res Pract. 2015; 9(2):137-43.
29. Song H, Lai J, Tang Q, Zheng X. Mulberry ethanol extract attenuates hepatic steatosis and insulin resistance in high-fat diet-fed mice. Nutr Res. 2016;36(7):710-8.
30. Ann JY, Eo H, Lim Y. Mulberry leaves (Morus alba L.) ameliorate obesity-induced hepatic lipogenesis, fibrosis, and oxidative stress in high-fat diet-fed mice. Genes Nutr. 2015;10(6): 46.
31. Chaiwong S, Chatturong U, Chanasong R, Deetud W, To-On K, Puntheeranurak S, et al. Dried mulberry fruit ameliorates cardiovascular and liver histopathological changes in high-fat diet-induced hyperlipidemic mice. J Tradit Complement Med. 2021;11(4):356-68.
32. Huang HP, Ou TT, Wang CJ. Mulberry (sang shen zi) and its bioactive compounds, the chemoprevention effects and molecular mechanisms in vitro and in vivo. J Tradit Complement Med. 2013;3(1):7-15.
33. Inanc ME, Gungor S, Yeni D, Avdatek F, Ipek V, Turkmen R, et al. Protective role of the dried white mulberry extract on the reproductive damage and fertility in rats treated with carmustine. Food Chem Toxicol. 2022;163: 112979.
34. Hafez MH, Gad SB, El-Sayed YS. Quercetin-mediated restoration of high-fat diet-induced male reproductive dysfunction through modifying spermatogenesis and unraveling 3beta-HSD, 17beta-HSD, and StAR pathways. BMC Pharmacol Toxicol. 2025;26(1):90.
35. Bora S, k.A M, Priyadharshini P, PR, Shanmugam R. Mulberry (Morus spp.) Nature's Medicine for Modern Health and Industry2025.
36. Zhang J, Liu W, Cui F, Kolehmainen M, Chen J, Zhang L, et al. Exploring the potential protective role of anthocyanins in mitigating micro/nanoplastic-induced reproductive toxicity : A steroid receptor perspective. J Pharm Anal. 2025;15(2):101148.
37. Jiang X, Zhu C, Li X, Sun J, Tian L, Bai W. Cyanidin-3- O-glucoside at Low Doses Protected against 3-Chloro-1,2-propanediol Induced Testis Injury and Improved Spermatogenesis in Male Rats. J Agric Food Chem. 2018;66(48):12675-84.
38. Dong M, Lu J, Xue H, Lou Y, Li S, Liu T, et al. Anthocyanins from Lycium ruthenicum Murray Mitigate Cadmium-Induced Oxidative Stress and Testicular Toxicity by Activating the Keap1/Nrf2 Signaling Pathway. Pharmaceuticals (Basel). 2024;17(3).
39. Chang JJ, Hsu MJ, Huang HP, Chung DJ, Chang YC, Wang CJ. Mulberry anthocyanins inhibit oleic acid induced lipid accumulation by reduction of lipogenesis and promotion of hepatic lipid clearance. J Agric Food Chem. 2013;61(25):6069-76.

P-11

Evaluating the Combined Therapeutic Potential of β-Eudesmol and Gefitinib against EGFR-Driven Breast and Lung Cancers: A Preliminary Investigation

Warintorn Wongho[1], Akawan Changtong[2], Pattareeya Sereesantiwong[2], Sangkab Sudsaward[1]*, Sasiprapa Khunchai[1]*
[1] Department of Anatomy, Faculty of Medical Science, Naresuan University, Phitsanulok, Thailand
[2] Department of Doctor of Optometry, Faculty of Allied Health Sciences, Naresuan University, Phitsanulok, Thailand
*Corresponding authors, e-mail address: sangkabs@nu.ac.th, sasiprapak@nu.ac.th

Abstract
Background: Breast and lung malignancies are the most prevalent causes of cancer-related mortality worldwide, and they are frequently exacerbated by the development of resistance to targeted therapies. Although epidermal growth factor receptor (EGFR) tyrosine kinase inhibitors (TKIs) such as gefitinib demonstrate initial efficacy, long-term outcomes are often hindered by intrinsic resistance mechanisms, including wild-type EGFR overexpression in breast cancer and acquired mutations such as T790M in lung cancer. Therefore, the identification of novel chemosensitizers represents a pressing clinical requirement. β-eudesmol (BE), a naturally occurring sesquiterpene, demonstrates potential anticancer properties; however, its ability to resensitize resistant tumors to gefitinib has yet to be characterized. **Objective:** The objective is to examine the combined cytotoxic effects of BE and gefitinib, as well as their influence on surface EGFR expression in cancer cells exhibiting drug resistance. **Methods:** MDA-MB231 cells, characterized by triple-negative breast cancer (TNBC) and wild-type EGFR overexpression, along with NCI-H1975 cells, which exhibit EGFR T790M mutation in non-small cell lung cancer (NSCLC), were subjected to treatment with gefitinib, BE, or a combination of both agents for durations of 24 and 48 h. The MTT assay was employed to assess cell viability. The impact of BE (0–320 μM) on the localization of surface EGFR was evaluated through flow cytometry. **Results:** The BE single treatment exhibited moderate cytotoxicity, with CC_{50} values at 24 h of 448.6 μM for MDA-MB231 and 204.5 μM for NCI-H1975. Co-treatment with a sublethal concentration of gefitinib (30 μM) combined with BE (320 μM) showed a significant reduction in cell viability in MDA-MB231 cells, yielding values of 73.1 ± 3.43% and 59.4 ± 2.48% at 24 and 48 h., respectively. In contrast, gefitinib administered alone produced cell viability rates of 91.2 ± 2.35% and 79.6 ± 3.14% at the same time points *($p < 0.05$).* In NCI-H1975 cells, the combination treatment exhibited cell viability of 86.4 ± 8.5% at 24 h and 77.6 ± 7.7% at 48 h Notably, in NCI-H1975 cells, this combination showed a tendency toward enhanced cytotoxicity at the 48-h mark. Flow cytometric analysis revealed that surface EGFR levels in MDA-MB231 cells remained largely unaffected (relative MFI: 100% vs. 105.6% for control and 320 μM BE, respectively), whereas BE treatment reduced the mean fluorescence intensity (MFI) of surface EGFR in NCI-H1975 cells by approximately 26.3% compared to the control. **Conclusion:** BE effectively enhances the sensitivity of drug-resistant cancer cells to gefitinib, especially in the wild-type EGFR-overexpressing triple-negative breast cancer model. Moreover, the observed decrease in surface EGFR levels in NCI-H1975 suggests potential modulation of the receptor by BE. The precise underlying mechanisms warrant further investigation, underscoring BE as a potentially effective chemosensitizer for resistant EGFR-driven cancers.

Keywords *β-eudesmol, Gefitinib, Epidermal growth factor receptor (EGFR), Combination therapy*

Background

Breast and lung cancers remain the leading causes of cancer-related mortality worldwide. According to the American Cancer Society 2025, despite significant therapeutic advancements, clinical outcomes are often constrained. Triple-negative breast cancer (TNBC), lacking key hormonal and HER2 receptors, represents the most aggressive phenotype and is frequently hindered by drug resistance. Simultaneously, non-small cell lung cancer (NSCLC), accounting for approximately 85% of all lung cancer cases, is primarily driven by specific genetic alterations, particularly the aberrant activation of the epidermal growth factor receptor (EGFR). In the targeted treatment of these malignancies, gefitinib has been established as a standard EGFR tyrosine kinase inhibitor (EGFR-TKI). Although it demonstrates a robust initial objective response rate of 70–76% (1), its long-term clinical efficacy is inevitably compromised by the rapid emergence of drug resistance.

A substantial body of evidence establishes EGFR as a critical determinant driving disease progression and drug resistance (2-4). The clinical significance of EGFR-targeted therapy is particularly pronounced in Asian populations, where the prevalence of EGFR mutations reaches 40–60%. However, the therapeutic outcome of TKIs is strictly dictated by the EGFR mutational status. Gefitinib yields robust responses in tumors harboring classical sensitizing mutations, such as the L858R substitution, but fails against tumors that have acquired the secondary T790M mutation. This mutation alters the receptor's structure, causing steric hindrance that prevents gefitinib from binding, thereby driving acquired drug resistance. Conversely, tumors expressing wild-type (WT) EGFR, a characteristic frequently observed in TNBC, exhibit intrinsic resistance to gefitinib because the receptor lacks the structural alterations required for optimal drug sensitivity.

Given these limitations, single-agent EGFR inhibition consistently fails to yield satisfactory clinical outcomes. To overcome both intrinsic and acquired resistance mechanisms, combination therapy has been strongly advocated as a pivotal clinical strategy (3,4). Consequently, the discovery of novel bioactive compounds capable of acting as chemosensitizers is an urgent medical necessity. Such combination regimens can effectively bypass resistance networks and resensitize tumors to TKI therapy.

Natural products represent a cornerstone of anticancer drug discovery, with sesquiterpenes garnering significant attention for their anti-neoplastic properties (5-7). For instance, β-elemene, a representative sesquiterpene, has been shown to downregulate EGFR expression and induce programmed cell death in glioblastoma models (8). Previous studies have demonstrated that BE induces apoptosis via the Bcl-2 protein family (9) and suppresses cancer cell metastasis by blocking the epithelial-mesenchymal transition (EMT) (10). However, to the best of our knowledge, no prior research has investigated the direct modulatory effect of BE on EGFR signaling pathways or its potential to overcome EGFR-TKI resistance.

Building upon the structural and functional similarities within the terpene family, we hypothesized that BE could effectively sensitize drug-resistant cancer cells to gefitinib therapy. Therefore, the present study aimed to investigate the synergistic cytotoxic effects of combining BE with gefitinib in two distinct resistant models: MDA-MB231 cells (representing intrinsic resistance via WT EGFR) and NCI-H1975 cells (representing acquired resistance driven by the T790M mutation). Furthermore, we sought to elucidate the underlying molecular mechanisms of this combination strategy, specifically evaluating its impact on surface EGFR presentation and the induction of cellular apoptosis. Ultimately, this research endeavors to provide a novel preclinical rationale for utilizing BE as a chemosensitizer to improve clinical outcomes in refractory EGFR-driven malignancies.

Materials and Methods

Chemicals and reagents

Synthetic BE was purchased from ChemFaces Biochemical. A total of 100 mg of BE was dissolved in 95% ethanol to prepare an 80 mM stock solution, which was stored at -20°C. Gefitinib (ZD1839) was purchased from Selleckchem, dissolved in dimethyl sulfoxide (DMSO) to yield a stock concentration of 10 mM, and stored at -20°C. For the quantification of surface receptor expression, the fluorescent-conjugated antibody Alexa Fluor 488-α-EGFR (Biolegend, Cat#35298) was utilized.

Cell lines and culture

Breast cancer (BC) cell lines MCF-7 (#HTB-22) EGFR WT, Low expression of EGFR, MDA-MB231 (#HTB-26) EGFR WT, Overexpression of EGFR, and human lung cancer cell lines A549 (#CCL-185) EGFR WT, NCI-H1975 (#CRL-5908) EGFR mutation T790M were obtained from ATCC. Cells were cultured in Dulbecco's modified Eagle's medium (DMEM) (BC cell line), Ham's F-12K (Kaighn's) Medium (A549), and Roswell Park Memorial Institute (RPMI) 1640 Medium (NCI-H1975) supplemented with 10% fetal bovine serum

(FBS) and 1% penicillin/streptomycin. All cells were maintained in a humidified incubator at 37°C with 5% CO_2. The culture medium was renewed twice a week, while cells were trypsinized with 0.25% trypsin-EDTA and subcultured in the culture medium.

Cell viability assay (MTT Assay)

The cytotoxic effects of BE and gefitinib were determined using the MTT assay. Briefly, cells were seeded $1x10^4$ cells/well into 96-well plates and incubated for 24 h to allow for attachment. To assess the cytotoxicity of the individual agents, cells were treated with varying concentrations of gefitinib (0–60 μM) or BE (0–600 μM) for 24 and 48 h. Based on the cell viability data from these single treatments, sublethal concentrations yielding approximately 80%-70% cell viability were selected for the subsequent combination assays. After the respective treatment periods, MTT reagent was added to each well, and the plates were further incubated for 3 h. The culture medium containing the MTT reagent was then discarded, and the resulting formazan crystals were dissolved in DMSO. Finally, the absorbance was measured at 570 nm, with a reference wavelength of 690 nm, using a microplate spectrophotometer (BioTek Instruments, USA), and the half-maximal cytotoxic concentration (CC_{50}) was determined to evaluate the cytotoxicity of BE. Briefly, cells were treated with various concentrations of BE for 24 and 48 h, and the percentage of cell viability was plotted against the logarithmic concentrations of the treatment. The CC_{50} values were then calculated using non-linear regression analysis with GraphPad Prism version 8 software.

Flow cytometry analysis

To evaluate the effect of BE on the surface expression of EGFR, flow cytometry analysis was performed. Briefly, cells were seeded and subsequently treated with varying concentrations of BE (0–320 μM) or epidermal growth factor (EGF) 100 ng/ml for BC cell line and 30 ng/ml for the lung cancer cell line, serving as a positive control for EGFR internalization for 24 h. Following the 24 h. incubation, the cells were harvested using 0.25% Trypsin-EDTA. The trypsinization process was strictly controlled and kept as brief as possible to minimize surface receptor cleavage, washed twice with cold phosphate-buffered saline (PBS), and resuspended in a staining buffer consisting of 2% fetal bovine serum (FBS) in PBS. To specifically detect surface-localized EGFR, the cells were kept intact without permeabilization. The cell suspension was then incubated with Alexa Fluor 488-α-EGFR antibody for 30 min at 4°C in the dark, according to the manufacturer's protocol. Finally, the cells were washed to remove unbound antibodies, and the surface EGFR fluorescence intensity was quantified using a flow cytometer (Cytoflex S, Beckman Coulter Life Sciences, USA).

Statistical analysis

The mean and standard error of the mean (Mean ± SEM) from at least three independent experiments were calculated. PRISM GraphPad PRISM 8 was used to test the significant differences between the two groups using one-way ANOVA and post-test with Dunnett's test. p value < 0.05 was considered as the significant differences (* demonstrating $p < 0.05$, **demonstrating $p < 0.01$, ***demonstrating $p<0.001$ and ****demonstrating $p < 0.0001$).

Results

Cytotoxic effect of gefitinib on cancer cells

Baseline sensitivity was established by evaluating the cytotoxic effects of gefitinib on MCF-7, MDA-MB231, A549, and NCI-H1975 cancer cell lines over 24 and 48 h using the MTT assay. Fig. 1 illustrates that gefitinib treatment results in a reduction in cell viability that is both dose- and time-dependent, although the response profiles varied among the different cell lines. After 24 h of treatment (Fig. 1A), the inhibitory effect was modest across all cell lines. However, extending the treatment duration to 48 h (Fig. 1B) demonstrated varying degrees of drug sensitivity among the cell lines. Specifically, A 549cells exhibited a greater reduction in cell viability starting at a gefitinib concentration of 30μM ($p < 0.0001$). In contrast, MDA-MB 231and NCI-H 1975cells have less response to gefitinib after 48h of treatment. These findings confirmed the gefitinib resistance of the triple-negative breast cancer and the T790M mutation characteristic of TKI monotherapy

Cytotoxic effect of BE on BC and lung cancer cells

The cytotoxic potential of BE as a single treatment was further elucidated by assessing CC_{50} in relation to the drug-resistant cell lines, MDA-MB231 and NCI-H1975. Fig. 2 illustrates that BE treatment decreased cell viability in a manner dependent on concentration; nonetheless, the sensitivity exhibited differences between the two cell lines. In the context of TNBC (Fig. 2A), BE demonstrated comparatively low cytotoxicity. The determined CC_{50} values were 448.6 μM at 24 h and 452.0 μM at 48 h. In contrast, the EGFR-mutant lung cancer cell line NCI-H1975 (Fig. 2B) exhibited greater sensitivity to BE in comparison to MDA-

MB231. The CC_{50} values were established at 204.5 µM after 24 h, subsequently decreasing to 166.2 µM following 48 h of treatment. The observed reduction in CC_{50} signifies a time-dependent increase in cytotoxicity within lung cancer cells. The observed CC_{50} values in both cell lines suggest that BE exhibits moderate potency against these resistant phenotypes when administered as a standalone treatment. The results obtained, along with the restricted effectiveness of Gefitinib as a standalone treatment, underscore the justification for exploring the synergistic capabilities of co-treatment with BE and Gefitinib.

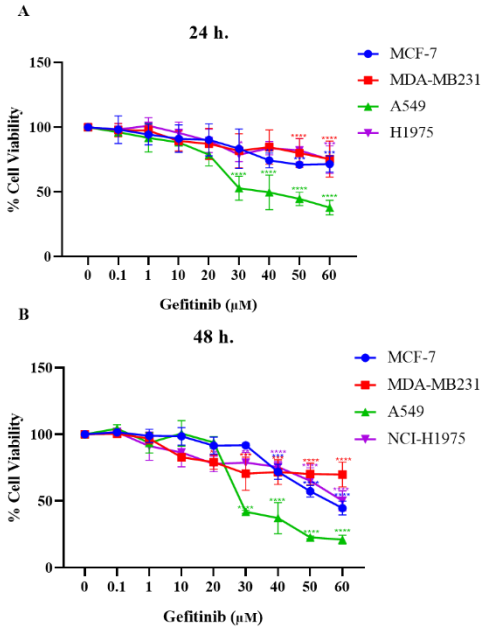

Fig. 1 The effect of gefitinib on the viability of BC and lung cells. Cells were treated with indicated concentrations of gefitinib for (A) 24 h and (B) 48 h. Cell viability was determined by MTT assay. *, **, *** and **** denote $p < 0.05$, $p < 0.01$, $p < 0.001$ and $p < 0.0001$, respectively Data are presented as Mean ± SEM from three independent experiments (n=3).

Effect of combination treatment with gefitinib and BE

To examine the potential of BE in sensitizing drug-resistant cancer cells to TKI therapy, a combination treatment strategy was assessed in both MDA-MB231 and NCI-H1975 (Fig. 3). Cells were subjected to a consistent sub-lethal concentration of gefitinib (30 µM) in conjunction with varying concentrations of BE at 160, 240, and 320 µM for MDA-MB231 cells (Fig. 3A), and at 80, 160, and 240 µM for NCI-H1975 cells (Fig. 3B) over periods of 24 and 48 h.

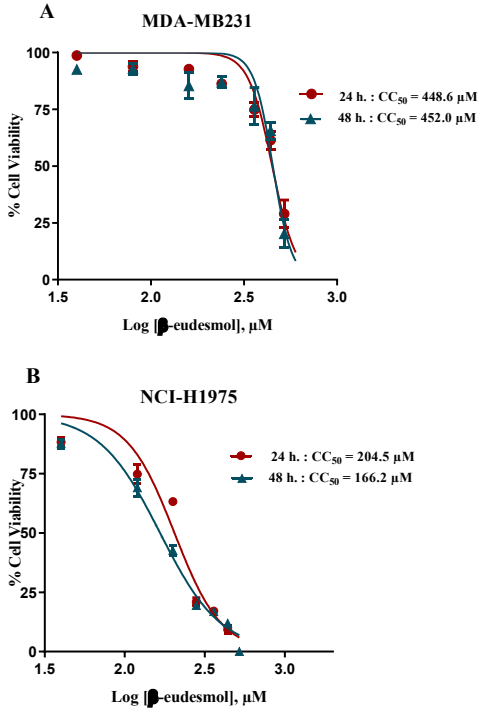

Fig. 2 The half-maximal cytotoxic concentration (CC_{50}) for (A) MDA-MB231 and (B) NCI-H1975. Cells were subjected to treatment with varying concentrations of BE ranging from 0 to 600 µM, and the effects were assessed at 24 and 48 h. from three independent experiments (n=3).

Gefitinib monotherapy at a concentration of 30 µM demonstrated a limited inhibitory effect in both cell lines. In MDA-MB231 cells, the viability was recorded at 91.2 ± 2.35 at 24 h. and 79.6 ± 3.14 at 48 h. Similarly, NCI-H1975 cells exhibited viabilities of 86.4 ± 8.5 at 24 h and 77.6 ± 7.68 at 48 h.

Upon combination with BE, cytotoxicity exhibited a significant enhancement, although the degree of enhancement varied. In the MDA-MB231 model, co-treatment with the highest concentration of BE (320 µM) led to a statistically significant reduction in cell viability when compared to gefitinib alone at both 24 and 48 h *($p < 0.05$)*, with viability decreasing to 73.1 ± 3.43 and 59.4 ± 2.48, respectively. In the NCI-H1975 model, inclusion of BE (up to 240 µM) exhibited a trend indicative of increased cytotoxicity, particularly resulting in a further decrease in cell viability at the 48-h time point.

Effect of BE on the surface expression of EGFR in MDA-MB231 cells

To assess the impact of BE on the surface localization of EGFR, MDA-MB231 cells were analyzed through flow cytometry. Fig. 4 illustrates the preliminary result that treatment with EGF at a concentration of 100 ng/ml, utilized as a positive control, led to a significant decrease in surface EGFR levels. This outcome confirms ligand-induced receptor internalization and validates the assay system. Following this validation, the evaluation of BE revealed that treatment with varying concentrations (0–320 µM) for 24 h did not substantially alter the mean fluorescence intensity (MFI) and the percent of positive cells of

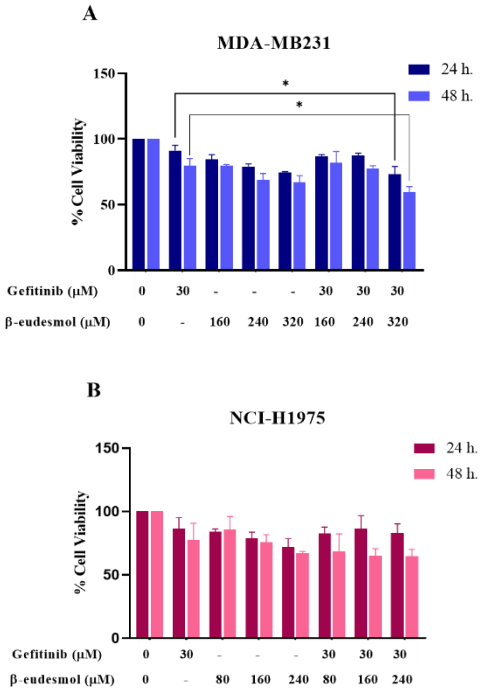

Fig. 3 The cytotoxic effects of the combination treatment of gefitinib and BE in drug-resistant cancer cells. Cells were subjected to treatment with a sub-lethal concentration of gefitinib (30 µM) alone and varying concentrations of BE for durations of 24 and 48 h. The assessment of cell viability was conducted utilizing the MTT assay, with results expressed as a percentage in relation to the untreated control group. Data are expressed as the Mean ± SEM derived from three independent experiments (n=3). Statistical significance is indicated by $*p < 0.05$, demonstrating a notable difference compared to the gefitinib-only group at the specified time points.

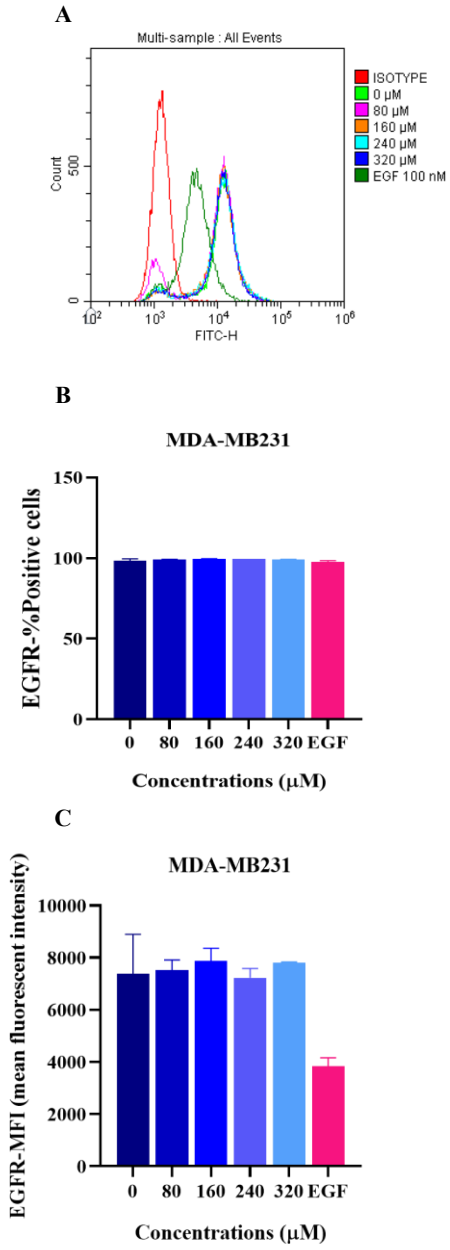

Fig. 4 Effect of BE on surface EGFR expression in MDA-MB231 cells. Cells were treated with the indicated concentrations of BE (0–320 µM) or EGF (100 ng/ml) (positive control) for 24 h. The levels of surface-localized EGFR were quantified via flow cytometry. (A) Representative flow cytometry histogram of EGFR expression (B), the percentage of EGFR-positive cells, and (C) MFI of surface EGFR. Data are presented as the Mean ± SEM from two independent experiments (n=2).

surface EGFR compared to the control: 95% ethanol (0 µM). The results suggest that BE neither down-regulates nor induces the internalization of surface EGFR in MDA-MB231 cells.

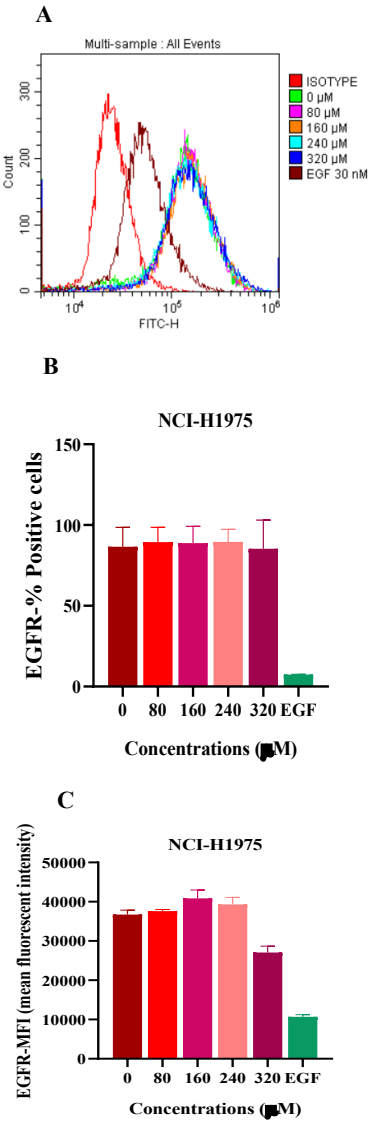

Fig. 5 Effect of BE on surface EGFR expression in NCI-H1975 cells. Cells were treated with the indicated concentrations of BE (0–320 µM) or EGF (30 ng/ml), a positive control, for 24 h. The surface expression of EGFR was analyzed via flow cytometry. The bar graphs illustrate (A) Representative flow cytometry histogram of EGFR expression, (B) The percentage of EGFR-positive cells, and (C) MFI of surface EGFR. Data are presented as the Mean ± SEM from two independent experiments (n=2).

Effect of BE on surface EGFR expression in NCI-H1975 cells

To further examine the effect of BE on surface EGFR expression in lung cancer, NCI-H1975 cells were assessed through flow cytometry. Fig. 5 demonstrates the preliminary results that treatment with EGF at 30 ng/ml, utilized as a positive control, showed a reduction trend in the percentage of MFI. Treatment with BE at concentrations from 0 to 320 µM did not influence the percentage of EGFR-positive cells, which remained consistently elevated across all groups. However, further confirmation is needed.

Discussion

The emergence of both intrinsic and acquired resistance to EGFR-TKIs, especially gefitinib, provides a significant challenge in the treatment of breast and lung cancers. We examined the chemo-sensitizing potential of BE to overcome this challenge. To elucidate the efficacy of BE in TKI resistance, we confirmed the cytotoxic effect of gefitinib in low and high EGFR expression in both breast and lung cancer cell lines. followed by the cytotoxic effect of BE on the overexpressed EGFR in MDA-MB231 and NCI-H1975 cells.

Our initial cell viability tests revealed that A549 and MCF7 were sensitive to gefitinib, while MDA-MB231 and NCI-H1975 demonstrated notable drug resistance. The EGFR-overexpressing WT model (MDA-MB231) and the mutation-driven acquired resistance in the T790M model (NCI-H1975) are highly consistent with previous findings (11,12). These two cell lines have distinct EGFR profiles, which is the primary reason gefitinib cannot completely eradicate them. This finding strongly supports previous research showing that TKI resistance is primarily caused by aberrant EGFR status, whether via WT overexpression in MDA-MB231 or the T790M secondary mutation in NCI-H1975 (2-4).

As a consequence, these two resistant cell lines were selected as in vitro models for our subsequent combination studies. Single-agent treatments exhibited limitations in eliminating MDA-MB231 cells; however, the therapeutic potential of BE as a chemosensitizer was effectively demonstrated in the combination regimen. The combination of administration of gefitinib with 320 µM BE significantly decreased cell viability in intrinsically resistant MDA-MB231 cells at both 24 and 48 h. compared to gefitinib alone (Fig. 3A). In T790M-mutated NCI-H1975 cells, combination therapy demonstrated a reduction trend in cell survival compared to single-agent gefitinib when cultured with BE for 48 h. This slight decrease in

NCI-H1975 indicates that a higher dose of the combination agents might be necessary to fully address the significance of the drug resistance imposed by the T790M mutation. The other mechanism of cell death induction may be involved in the combination treatment with BE.

To confirm the important role of EGFR expression and cell survival, we quantified surface EGFR expression utilizing flow cytometry. The cytometric analysis demonstrated that BE treatment slightly downregulated the mean fluorescent intensity of EGFR presented on the plasma membrane of NCI-H1975 cells (preliminary results) (Fig. 5C). Interestingly, the reduction of surface EGFR at higher concentrations appears to correspond with the decrease in cell viability observed in the BE-alone treatment. Moreover, it is well-documented that EGF binding provokes rapid receptor endocytosis and subsequent lysosomal degradation (13,14). Consistent with this, the decreasing trend of surface EGFR observed in our resistant lung cancer model suggests that BE might promote receptor internalization or modulation. However, whether this process explicitly involves protein degradation pathways warrants further investigation.

Furthermore, β-elemene, a sesquiterpene compound, has been extensively reported to robustly downregulate EGFR expression and attenuate its downstream signaling in various cancer models (8,15). This parallel indicates that BE likely has a similar modulatory effect, potentially by enhancing EGFR internalization or obstructing its transport to the cell surface. BE effectively reduces the functional reserve of EGFR at the membrane, dismantling the primary compensatory survival network and neutralizing the resistance associated with both WT overexpression and the T790M mutation. These results present a promising novel combination strategy to enhance clinical outcomes in patients with refractory EGFR-driven malignancies.

Conclusion

The emergence of resistance to tyrosine kinase inhibitors (TKIs) constitutes a significant challenge in oncological therapy. This study illustrates that BE, a bioactive sesquiterpenoid, exhibits essential anticancer properties and can enhance the effectiveness of Gefitinib. The findings demonstrate that the combination of BE and Gefitinib produces an increased cytotoxic effect than either agent individually, with the most significant sensitization noted in MDA-MB231 cells. However, the observed reduction in surface expression in NCI-H1975 is an important finding for further elucidating the relationship between EGFR localization, protein degradation, and the cell apoptosis pathway.

Acknowledgements

The authors gratefully acknowledge the financial and facility support provided by the Department of Anatomy, Faculty of Medical Science, Naresuan University.

References

1. Cho BC, Ahn MJ, Kang JH, Soo RA, Reungwetwattana T, Yang JC, et al. Lazertinib Versus Gefitinib as First-Line Treatment in Patients With EGFR-Mutated Advanced Non-Small-Cell Lung Cancer: Results From LASER301. J Clin Oncol. 2023;41(26):4208-17.
2. Cooper AJ, Sequist LV, Lin JJ. Third-generation EGFR and ALK inhibitors: mechanisms of resistance and management. Nat Rev Clin Oncol. 2022;19(8):499-514.
3. Kinnel B, Singh SK, Oprea-Ilies G, Singh R. Targeted Therapy and Mechanisms of Drug Resistance in Breast Cancer. Cancers (Basel). 2023;15(4).
4. Zhang Q, Wang R, Xu L. Clinical advances in EGFR-TKI combination therapy for EGFR-mutated NSCLC: a narrative review. Transl Cancer Res. 2023;12(12):3764-78.
5. Ben Sghaier M, Mousslim M, Pagano A, Ammari Y, Luis J, Kovacic H. beta-eudesmol, a sesquiterpene from Teucrium ramosissimum, inhibits superoxide production, proliferation, adhesion and migration of human tumor cell. Environ Toxicol Pharmacol. 2016;46:227-33.
6. Hang LH, Shao DH, Chen Z, Chen YF, Shu WW, Zhao ZG. Involvement of spinal CC chemokine ligand 5 in the development of bone cancer pain in rats. Basic Clin Pharmacol Toxicol. 2013;113(5):325-8.
7. Tachikawa E, Takahashi M, Kashimoto T. Effects of extract and ingredients isolated from Magnolia obovata thunberg on catecholamine secretion from bovine adrenal chromaffin cells. Biochem Pharmacol. 2000;60(3):433-40.
8. Mu L, Wang T, Chen Y, Tang X, Yuan Y, Zhao Y. beta-Elemene enhances the efficacy of gefitinib on glioblastoma multiforme cells through the inhibition of the EGFR signaling pathway. Int J Oncol. 2016;49(4):1427-36.
9. Narahara C, Saeheng T, Chaijaroenkul W, Dumre SP, Na-Bangchang K, Karbwang J. beta-Eudesmol induces the expression of apoptosis pathway proteins in cholangiocarcinoma cell lines. J Res Med Sci. 2020;25:7.

10. Acharya B, Chajaroenkul W, Na-Bangchang K. beta-Eudesmol Inhibits the Migration of Cholangiocarcinoma Cells by Suppressing Epithelial-Mesenchymal Transition via PI3K/AKT and p38MAPK Modulation. Asian Pac J Cancer Prev. 2022;23(8):2573-81.
11. Moon DO, Kim MO, Heo MS, Lee JD, Choi YH, Kim GY. Gefitinib induces apoptosis and decreases telomerase activity in MDA-MB-231 human breast cancer cells. Arch Pharm Res. 2009;32(10):1351-60.
12. Lee JY, Lee YM, Chang GC, Yu SL, Hsieh WY, Chen JJ, et al. Curcumin induces EGFR degradation in lung adenocarcinoma and modulates p38 activation in intestine: the versatile adjuvant for gefitinib therapy. PLoS One. 2011;6(8):e23756.
13. Wang H, Li S, Li H, Li C, Guan K, Luo G, et al. SGEF enhances EGFR stability through delayed EGFR trafficking from early to late endosomes. Carcinogenesis. 2013;34(9):1976-83.
14. Yao N, Wang CR, Liu MQ, Li YJ, Chen WM, Li ZQ, et al. Discovery of a novel EGFR ligand DPBA that degrades EGFR and suppresses EGFR-positive NSCLC growth. Signal Transduct Target Ther. 2020;5(1):214.
15. Wang J, Xu C, Chen Y, Shao L, Li T, Fan X, et al. beta-elemene enhances the antitumor activity of erlotinib by inducing apoptosis through AMPK and MAPK pathways in TKI-resistant H1975 lung cancer cells. J Cancer. 2021;12(8): 2285-94.

P-12

Effects of Melatonin on Autophagy-Related Pathways in Pancreatic Beta Cells in Streptozotocin-Induced Type 1 Diabetic Rats

Khunchanit Duangplee[1], Pariwat Wisetwongsa[2], Janyaruk Suriyut[2], Ratchadaporn Pramong[2*]
[1] Doctor of Medicine Program, Faculty of Medicine, Srinakharinwirot University, Bangkok, Thailand
[2] Department of Anatomy, Faculty of Medicine, Srinakharinwirot University, Bangkok, Thailand
*Corresponding author, e-mail: ratchadapornpr@g.swu.ac.th

Abstract

Type 1 diabetes is a chronic immune-mediated disorder characterized by the destruction of insulin-producing pancreatic beta cells due to autoimmune mechanisms. During disease progression, pancreatic beta cells are exposed to damaging factors, such as proinflammatory cytokines and hyperglycemia, which promote oxidative stress and cellular damage. Autophagy plays a critical role in maintaining beta cell homeostasis and survival under stress conditions. Melatonin exhibits potent antioxidant properties and has been widely studied for its therapeutic potential in metabolic disorders, with evidence suggesting that it may improve oxidative homeostasis by influencing autophagy-related pathways. Therefore, this study aimed to investigate the effects of melatonin on autophagy-associated alterations in pancreatic beta cells in a rat model of type 1 diabetes. Male Wistar rats were randomly divided into four groups: control, diabetic, diabetic treated with melatonin (10 mg/kg), and melatonin-only (10 mg/kg). Type 1 diabetes was induced by a single intraperitoneal injection of streptozotocin (60 mg/kg), and melatonin was administered intraperitoneally for eight weeks. Pancreatic tissues were collected at the end of the experimental period. Insulin expression and the autophagy-associated marker p62 in the islets of Langerhans were evaluated by double immunohistochemical staining, while pancreatic insulin levels were analyzed by Western blotting. The results demonstrated that diabetic rats exhibited a significant reduction in insulin expression, accompanied by a decreased number of p62-positive cells in the islets of Langerhans. In contrast, melatonin-treated diabetic rats showed a significant increase in insulin expression along with enhanced p62 immunoreactivity. These findings indicate that melatonin treatment partially restores insulin expression in pancreatic beta cells of type 1 diabetic rats and is associated with altered p62 immunoreactivity, suggesting a modulatory effect on autophagy-related pathways. Such modulation may contribute to improved beta cell survival and insulin production. Further studies incorporating additional markers of autophagic flux are warranted to elucidate the precise molecular mechanisms by which melatonin regulates autophagy in pancreatic beta cells.

Keywords *Melatonin, Type 1 diabetes, Pancreatic beta cell, Autophagy, P62*

P-13

Therapeutic Potential of Curcumin in Restoring Hepatic Autophagy in Streptozotocin‑Induced Type 1 Diabetic Rats

Napat Uesettasak[1], Pongsak Khanpetch[2], Cheng Nilbu-nga[2], Ratchadaporn Pramong[2*]
[1] Doctor of Medicine Program, Faculty of Medicine, Srinakharinwirot University, Bangkok, Thailand
[2] Department of Anatomy, Faculty of Medicine, Srinakharinwirot University, Bangkok, Thailand
*Corresponding author, e-mail: ratchadapornpr@g.swu.ac.th

Abstract

Autophagy is a cellular self-digestion pathway responsible for the degradation of damaged cellular components. Impaired autophagy, leading to the accumulation of damaged organelles, may contribute to the development of various pathological conditions. Decreased autophagy has been closely associated with the progression of several diseases, including hepatocellular carcinoma. Autophagy also plays an essential role in regulating the function of pancreatic beta cells and insulin target tissues and has been reported to be inhibited in various tissues, including the liver, in type 1 diabetes. Curcumin has been reported to induce autophagy and protect against liver injury caused by oxidative stress. In this study, the effects of curcumin on the autophagy pathway in the liver of a type 1 diabetic rat model were investigated. The expression levels of LC3B and Beclin-1, key markers of autophagosome formation, were determined using an enzyme-linked immunosorbent assay (ELISA), while the level of p62, a marker of autophagic clearance, was assessed by Western blot analysis. Diabetes was induced in male rats by a single intravenous injection of streptozotocin (60 mg/kg body weight). The rats (n = 6) were divided into three groups: control, diabetic group (DM), and diabetic supplemented with curcumin (200 mg/kg body weight; DMC group). Curcumin was administered by oral gavage for 12 weeks, after which liver tissues were collected for analysis. The levels of LC3B and Beclin-1 were markedly decreased in the DM group compared with the control group ($p < 0.01$), indicating impaired autophagy. In addition, hepatic p62 expression was significantly increased in the DM group ($p < 0.05$), suggesting defective autophagic clearance. In contrast, curcumin supplementation significantly increased LC3B and Beclin-1 expression while markedly reducing p62 expression in the DMC group ($p < 0.01$). These findings suggest that curcumin restores autophagic activity and enhances autophagic clearance, highlighting its therapeutic potential as an autophagy-related antioxidant for the prevention and treatment of diabetes-induced hepatic injury.

Keywords *Curcumin, Autophagy, p62, LC3B, Beclin-1*

P-14

Protective Effect of Melatonin against Inflammation in the Liver of Streptozotocin-Induced Type 1 Diabetic Rats

Chaiyavut Charoensrisan[1], Chittapon Jantararussamee[2], Pattanapong Boonprom[2], Ratchadaporn Pramong[2*]
[1] Doctor of Medicine Program, Faculty of Medicine, Srinakharinwirot University, Bangkok, Thailand
[2] Department of Anatomy, Faculty of Medicine, Srinakharinwirot University, Bangkok, Thailand
*Corresponding author, e-mail: ratchadapornpr@g.swu.ac.th

Abstract

Type 1 diabetes mellitus is a chronic inflammatory disorder characterized by insulin deficiency and persistent hyperglycemia, which can lead to structural and functional damage in multiple organs, including the liver. Hepatic injury in diabetes is largely attributed to oxidative stress and inflammation mediated by Kupffer cell activation. Melatonin, a pineal hormone with potent antioxidant and anti-inflammatory properties, has been reported to protect against diabetic complications; however, its effects on hepatic inflammation in type 1 diabetes remain unclear. This study aimed to investigate the effects of melatonin on hepatic inflammation by examining Kupffer cell infiltration in a rat model of streptozotocin-induced type 1 diabetes. Male Wistar rats were divided into four groups (n = 3 per group): control, diabetic, melatonin-treated diabetic, and melatonin-only. Type 1 diabetes was induced by a single intraperitoneal injection of streptozotocin (60 mg/kg). Melatonin (10 mg/kg) was administered intraperitoneally for eight weeks, with the dose selected based on previous studies demonstrating its anti-inflammatory and antioxidant efficacy in diabetic animal models. Liver tissues were collected and analyzed by immunohistochemical staining for ED1, a Kupffer cell marker, followed by semiquantitative densitometric analysis. The diabetic group showed a significant increase in ED1-positive Kupffer cells compared with the control group, indicating pronounced hepatic inflammation. In contrast, melatonin treatment significantly reduced the number of ED1-positive cells, suggesting suppression of Kupffer cell activation and infiltration. The melatonin-only group showed no significant difference compared with the control group. Overall, melatonin administration markedly attenuated diabetes-induced hepatic inflammation by reducing Kupffer cell activation and preserving liver architecture. These findings suggest that melatonin exerts hepatoprotective effects through its antioxidant and anti-inflammatory mechanisms and may represent a potential therapeutic agent for preventing liver injury in type 1 diabetes. Future studies that include standard drug-treated positive control groups will be important for direct comparison and confirmation of these effects.

Keywords *Melatonin, Type 1 diabetes, Liver injury, Inflammation, Kupffer cell*

P-15

From Canvas to Code: A Systematic Review of Artificial Intelligence Transforming Medical Illustration in Medical Education

Ujwala Bhanarkar[1]*, Yogesh Sontakke[2], Ashish Pundhir[3]
[1] Department of Anatomy, AIIMS Kalyani, West Bengal, India
[2] Department of Anatomy, JIPMER, Puducherry, India
[3] Department of CMFM, AIIMS Kalyani, West Bengal, India
*Corresponding author, e-mail: ujju.pretty15@gmail.com

Abstract
Background: Medical illustration has traditionally played a vital role in conveying complex anatomical concepts and facilitating effective clinical communication. With the emergence of artificial intelligence (AI), the field of medical visualization is undergoing transformation. AI-driven tools enable rapid generation, customization, and enhancement of anatomical visuals, offering new possibilities for teaching and learning. This systematic review explores the role of AI-generated medical illustrations and evaluates their influence on medical education. **Method**s: A systematic search was conducted in PubMed, Scopus, Web of Science, and IEEE Xplore for studies published between 2010 and 2025, following PRISMA guidelines. Only peer-reviewed articles were included; grey literature, abstracts, and editorials were excluded. Studies were included if they described the development, application, or evaluation of AI-generated medical illustrations in educational or clinical contexts. Data were extracted on publication trends, AI technologies, educational outcomes, and limitations. **Results**: From 739 records, 57 studies met the inclusion criteria. Quality was assessed using the Mixed Methods Appraisal Tool (MMAT 2018). Publications increased after 2018, peaking in 2023–2025. Deep learning models, especially CNNs, predominated, with generative adversarial networks (GANs) used for image synthesis and natural language processing (NLP) mainly for annotation tasks. Tools such as DALL·E, Midjourney, Stable Diffusion, and Adobe Firefly were reported. Most studies (72%) involved undergraduates, with fewer (28%) postgraduates. About 68% reported improved engagement and understanding, though 11.5% noted concerns about accuracy, reliability, and ethics. **Conclusion**: Artificial intelligence is reshaping medical illustration by enabling scalable, dynamic, and engaging resources. Despite its benefits, validation of anatomical accuracy and educational effectiveness remains essential. Future research should develop standardized evaluation frameworks and integrate AI-driven tools with evidence-based educational strategies. Further studies should examine long-term learning outcomes, interdisciplinary integration, and faculty training requirements. Emphasis on ethical governance, data transparency, and reproducibility will strengthen adoption and ensure responsible use across diverse educational settings globally in both resource-rich and resource-limited institutions worldwide.

Keywords *Artificial intelligence, Anatomical accuracy, Deep learning, Educational technology, Medical illustration, Medical education, Visual learning*

P-16

Sesamin-Mediated ROS Reduction in L929 Fibroblasts: Limited Impact on Cytotoxicity and Migration Under Oxidative Injury

Thita Suksakit[1], Suteera Narakornsak[1], Natnicha Kampan[1], Waleephan Treebupachatsakul[1], Rungusa Pantan[1*]
[1] Department of Anatomy, Faculty of Medicine, Chiang Mai University
*Corresponding author, e-mail: rungusa.p@cmu.ac.th

Abstract

Oxidative stress contributes to cellular injury and delays wound healing, particularly in fibroblasts, which are essential for tissue repair. Sesamin, a lignan compound derived from sesame seeds, has been reported to possess antioxidant and cytoprotective properties. This study aimed to investigate the protective effect of sesamin against hydrogen peroxide (H_2O_2)–induced oxidative stress in L929 mouse fibroblast cells as a wound healing model. Cells were pretreated with sesamin (30, 40, and 50 μM) for 24 h, followed by a 3-h H_2O_2 exposure. Cell viability was evaluated using the MTT assay. Cell migration was assessed by the wound scratch assay. In addition, reactive oxygen species (ROS) levels were evaluated using the DCFH-DA assay. Results showed that 50 μM sesamin pretreatment significantly enhanced basal L929 cell viability ($p < 0.05$) but unexpectedly reduced migration compared with the control. In addition, sesamin (30-50 μM) showed a trend toward attenuating H_2O_2-induced cytotoxicity and significantly decreased ROS levels. These results demonstrate sesamin's proliferative and antioxidative potential but reveal antimigratory effects and insufficient cytoprotection against H_2O_2-induced cytotoxicity, limiting its overall efficacy as a wound healing therapeutic in this fibroblast model.

Keywords *Sesamin, Oxidative stress, Wound healing, Fibroblast, Cell migration*

Background

Oxidative stress is a critical factor contributing to cellular damage and impaired tissue repair. It occurs when reactive oxygen species (ROS) production exceeds cellular antioxidant defenses, causing lipid peroxidation, protein modification, DNA damage, and mitochondrial dysfunction [1,2]. Hydrogen peroxide (H_2O_2), a common oxidative stress inducer, readily penetrates the cell membrane to generate secondary ROS. This reduces cell viability and impairs cellular function.

In wound healing, fibroblasts play an essential role in proliferation, migration to the injured site, and extracellular matrix synthesis. Oxidative stress has been shown to impair fibroblast proliferation and migration, thereby delaying wound closure and tissue repair [3,4]. Therefore, decreasing oxidative damage in fibroblasts is essential for accelerating wound healing processes.

Sesamin is a natural lignan compound isolated from sesame seeds (*Sesamum indicum*) and has been reported to possess antioxidant, anti-inflammatory, and cytoprotective properties. Previous studies have demonstrated that sesamin can reduce ROS, enhance endogenous antioxidant enzyme activity, and protect cells from oxidative stress–induced apoptosis [5-7]. However, the protective effects of sesamin against oxidative stress in fibroblasts remain unclear. Therefore, this study aimed to investigate the effects of sesamin on H_2O_2-induced cell death and migration in L929 mouse fibroblasts.

Materials and Methods

Cell Culture

L929 mouse fibroblast cells (NCTC clone 929) were cultured with Minimum Essential Medium (MEM) supplemented with 12% horse serum and 1% penicillin-streptomycin. L929 were maintained at 37°C in a humidified atmosphere of 95% air and 5% CO_2. The L929 cells were sub-cultured at 80% confluence. Sesamin was dissolved in dimethyl sulfoxide (DMSO) and diluted with cell culture medium (final DMSO concentration ≤ 0.1%).

Sesamin was isolated and purified by the Thailand Excellence Center for Tissue Engineering and Stem Cells, Department of Biochemistry, Faculty of Medicine, Chiang Mai University, Thailand. Ground sesame seeds were repeatedly extracted with hexane to obtain a lignan-rich crude extract. The extract was separated by column chromatography using a hexane–ethyl acetate gradient, and sesamin-containing fractions were further purified by repeated chromatography and ethanol recrystallization to yield highly pure sesamin crystals. Identity and purity were confirmed by NMR, MS, and HPLC against an authentic standard.

MTT assay

L929 cells were seeded into 96-well plates at a density of 1×10^4 cells/well and were cultured at 37°C and 5% of CO_2. Optimal proliferative dose-response of sesamin (10-60 μM, 24 h) and toxic dose-response of H_2O_2 (100-400 μM, 3 h) were determined prior to the prevention experiment. The cells were pretreated with sesamin (30, 40, and 50 μM) for 24 h before being exposed to H_2O_2 300 μM for 3 h. Then, the medium was replaced with 100 μL MTT solution (1 mg/mL in serum-free medium) and incubated for 4 h at 37°C. Formazan crystals were solubilized with 100 μl DMSO, and the absorbance was measured using a microplate reader (BioTek Synergy H1 Hybrid Microplate Reader, BioTek Instrument, Winooski, VT, USA) at a wavelength of 570 nm.

Wound Scratch assay

L929 cells were seeded into 24-well plates at a density of 1×10^5 cells/well and allowed to reach approximately 80% confluence. After that, cells were arrested for 24 h in a serum-free medium before a linear scratch wound was generated on the confluent cell monolayer using a sterile 200 μL pipette tip. The plates were washed with phosphate-buffered saline (PBS) to remove detached cells and then pretreated with 50 μM sesamin, which was selected based on the MTT dose-response results. Images of the scratch area were captured using an inverted light microscope at 0, 12, and 24 h after scratching. Wound closure was quantified using ImageJ software (NIH, USA).

DCFH-DA assay

2',7'-dichlorodihydrofluorescein diacetate cells. L929 cells were seeded in 96-well plates at a density of 5×10^5 cells/well, then pretreated with sesamin (30, 40, and 50 μM) for 24 h before exposure to H_2O_2 (300 μM) for 3 h. After that, the cells were washed with PBS and incubated with DCFH-DA (10 μM) in fresh medium at 37°C for 30 min. The fluorescence was measured at an excitation of 488 nm and an emission of 525 nm using a fluorescence microplate reader (BioTek Synergy H1 Hybrid Microplate Reader, BioTek Instruments, Winooski, VT, USA).

Statistical analysis

Data were plotted using GraphPad Prism 7.0 (GraphPad Software, Inc.). All values are presented as mean ± SEM. Statistical differences among more than two groups were analyzed by one-way analysis of variance (ANOVA), and pairwise comparisons were assessed using a paired t-test, as appropriate. When ANOVA indicated a significant effect, Bonferroni's post hoc test was used to identify differences between groups. A p-value of < 0.05 was considered statistically significant.

Results and Discussion

Cell viability

Concentrations of sesamin were selected based on preliminary dose-response experiments. Enhancement was observed at 50 μM ($p < 0.05$ vs. the control group, Fig. 1). Additionally, H_2O_2 at 300 μM was chosen as the toxic dose, reducing viability by ~50% ($p < 0.01$ vs. the control group, Fig. 2). showed a non-significant trend toward preserving cell viability following H_2O_2 exposure (Fig. 3).

In this study, 24 h pretreatment with sesamin failed to attenuate H_2O_2-induced loss of viability in L929 cells. In contrast, sesamin (1 μM) with 3 h pretreatment protected SH-SY5Y neuronal cells from H_2O_2-induced oxidative stress [8]. These findings highlight that both cell type and treatment time may affect the antioxidant efficiency of sesamin. Future investigations should evaluate strategies to enhance cytoprotection in fibroblast models relevant to wound healing.

Cell migration

The wound scratch assay was used to assess the effect of sesamin on L929 fibroblast migration. Incubation with 50 μM sesamin did not significantly affect wound closure, as indicated by wider wound widths at 12 h and 24 h compared with the control group (n=6, Fig. 4).

These findings contrast with the study in endothelial cell migration for angiogenesis [9] but align with its downregulation of MMP-1 and MMP-3, key mediators of cell migration, in synovial fibroblasts [10], suggesting a shared antimigratory mechanism across fibroblast lineages. However, the potential protective effect of sesamin against H_2O_2-inhibited migration requires further investigation,

particularly in other fibroblast models and under different dosing and exposure conditions.

DCFH-DA assay

ROS production in L929 cells was quantified using the DCFH-DA assay. Exposure to H_2O_2 significantly elevated ROS levels compared with the control ($p < 0.001$). However, pretreatment with sesamin (40 and 50 μM) significantly attenuated these elevated ROS levels when compared with the H_2O_2-treated group ($p < 0.05$, Fig. 5). These findings align with previous reports demonstrating the potent antioxidative properties of sesamin.

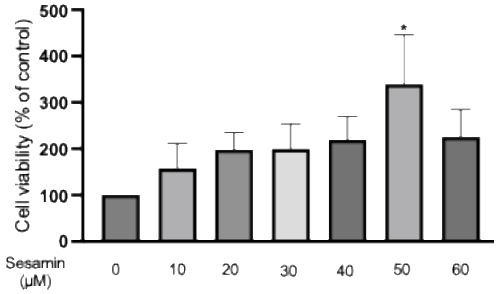

Fig. 1 Effects of sesamin on the viability of cells. L929 cells were pretreated with sesamin (10-60 μM) for 24 h before being evaluated by MTT assay. The data are presented as means±SEM (n=3). *$p < 0.05$ compared with the control group.

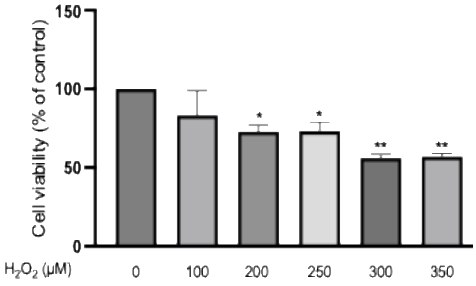

Fig. 2 Effect of H_2O_2 on cell viability. L929 cells were exposed to H_2O_2 (100-350 μM) for 3 h before being evaluated by MTT assay. The data are presented as means±SEM (n = 3). *$p < 0.05$ and **$p < 0.01$compared with the control group.

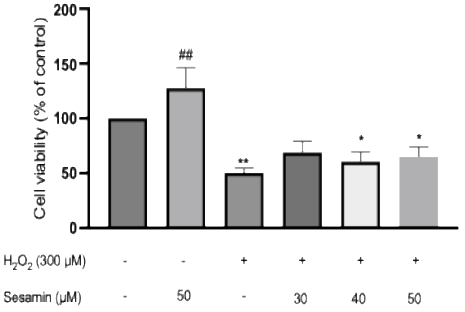

Fig. 3 Protective effect of sesamin against H_2O_2-induced cell death. L929 cells were pretreated with sesamin (30, 40, and 50 μM) for 24 h, followed by exposure to H_2O_2 for 3 h. Cell viability was evaluated using the MTT assay. The data are presented as means±SEM (n=6). **$p < 0.01$, *$p < 0.05$ compared with the control group and ##$p < 0.01$ compared with H_2O_2-treated group.

.

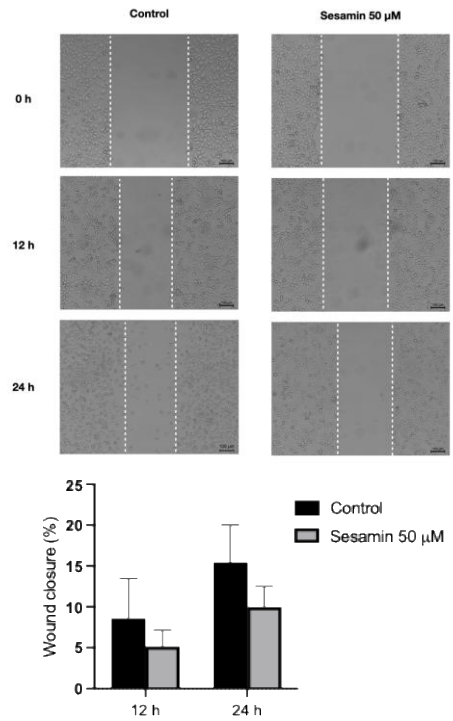

Fig. 4 Sesamin inhibits the migration of L929 cells. Representative images are recorded after 12 and 24 h of L929 treatment with sesamin 50 μM compared with non-treatment control in the wound scratch assay (scale bar = 100 μm). The graph is presented as means±SEM (n = 6).

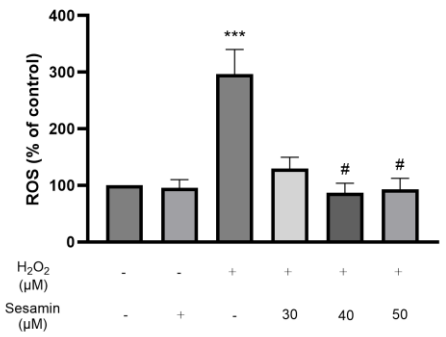

Fig. 5 Effect of sesamin on reactive oxygen species (ROS) production. The ROS levels were measured and expressed as a percentage of the control. Cells were pretreated with sesamin (50 μM), H_2O_2 (300 μM), and sesamin (30, 40, and 50 μM) followed by H_2O_2 (300 μM). Data are expressed as mean±SEM (n=6). ***p < 0.001 compared with control and #p < 0.05 compared with H_2O_2-treated group.

Conclusion

Sesamin significantly reduced H_2O_2-induced ROS in L929 fibroblasts. However, sesamin did not significantly rescue H_2O_2-induced cytotoxicity and did not affect migration under the tested conditions. These findings suggest selective protection from oxidative stress without improving overall wound healing. Moreover, this discrepancy suggests that sesamin may differentially affect specific phases of wound healing, particularly the inflammatory and proliferative phases.

Acknowledgements

This work was supported by Stem Cell and Molecular Research Unit, Department of Anatomy, Faculty of Medicine, Chiang Mai University and funded by Faculty of Medicine, Chiang Mai University.

References

1. Valko M, Leibfritz D, Moncol J, Cronin MT, Mazur M, Telser J. Free radicals and antioxidants in normal physiological functions and human disease. Int J Biochem Cell Biol. 2007;39:44-84.
2. Sies H. Oxidative stress: a concept in redox biology and medicine. Redox Biol. 2015;4:180-183.
3. Schafer M, Werner S. Oxidative stress in normal and impaired wound repair. Pharmacol Res. 2008;58:165-171.
4. Sen CK, Roy S. Redox signals in wound healing. Biochim Biophys Acta. 2008;1780:1348-1361.
5. Kang MH, Naito M, Tsujihara N, Osawa T. Sesamolin inhibits lipid peroxidation in rat liver and kidney. J Nutr. 1998;128:1018-1022.
6. Wu WH, Wang SH, Kuo YH, et al. Sesamin attenuates oxidative stress and inflammation in experimental models. J Agric Food Chem. 2011; 59:610-616.
7. Lee CC, Chen PR, Lin S, et al. Sesamin induces antioxidant defense through modulation of oxidative stress–related pathways. Mol Nutr Food Res. 2015;59:181-190.
8. Ruankham W, Suwanjang W, Wongchitrat P, Prachayasittikul V, Prachayasittikul S, Phopin K. Sesamin and sesamol attenuate H_2O_2-induced oxidative stress on human neuronal cells via the SIRT1-SIRT3-FOXO3a signaling pathway. Nutr Neurosci. 2021;24:90-101.
9. Sunzhi Y, Wei W, Xiaoyan C, Yingbin D, Sesamin promotes angiogenesis and accelerates wound healing in rats via alleviates TBHP-induced apoptosis in human umbilical vein endothelial cells. Biosci Biotechnol Biochem. 2020;84:887-897.
10. Khansai M, Phitak T, Klangjorhor J, Udomrak S, Fanhchaksai K, Pothacharoen P, Kongtawelert P. Effects of sesamin on primary human synovial fibroblasts and SW982 cell line induced by tumor necrosis factor-alpha as a synovitis-like model. BMC Complement Altern Med. 2017;17:1-13.

P-17

Microstructure Analysis and *In Vitro* Anti-Urolithiasis Activity of *Gracilaria fisheri* Sulfated Galactans Obtained by Different Extraction Methods

Tawut Rudtanatip[1*], Waraporn Sakaew[1], Somsuda Somintara[1], Choowadee Pariwatthanakun[2]
[1] Electron Microscopy Unit, Department of Anatomy, Faculty of Medicine, Khon Kaen University, Mittraphap Road, Khon Kaen, Thailand
[2] Division of Anatomy, Faculty of Medicine, Mahasarakham University, Nakhonsawan Road, Maha Sarakham, Thailand
*Corresponding author, e-mail: tawut@kku.ac.th

Abstract

Urolithiasis, characterized by the formation of calculi within the kidneys, is a painful urological disorder that may lead to progressive deterioration of renal function. Despite the availability of various therapeutic approaches, the prevention of stone recurrence and preservation of renal function remain significant clinical challenges. Sulfated galactans (SG), sulfated polysaccharides isolated from *Gracilaria fisheri*, exhibit various therapeutic properties, including antioxidant and anticancer activities. The determination of molecular structure is essential to ensure reproducibility and to enhance the biological activities of sulfated polysaccharides. In this study, we investigated the microstructural properties and anti-urolithiasis activity of SG from *G. fisheri*. SG were isolated using three extraction techniques: cold water, hot water, and autoclave-assisted extraction, yielding CWSG (10.18%), HWSG (39.56%), and AASG (20.15%), respectively. Following isolation and partial purification, the physicochemical and microstructural characteristics of the extracts were analyzed using gel filtration chromatography (GFC), high-performance liquid chromatography (HPLC), Fourier-transform infrared (FTIR) spectroscopy, and scanning electron microscopy coupled with energy-dispersive X-ray spectroscopy (SEM–EDX). The anti-urolithiasis activity was evaluated using calcium oxalate crystal nucleation and aggregation assays. GFC and HPLC analyses indicated that the molecular weights of CWSG, HWSG, and AASG ranged from 840 to 1670 kDa and that these extracts were primarily composed of xylose, fructose, and galactose. FTIR analysis confirmed that CWSG, HWSG, and AASG exhibited structural features characteristic of heterogeneous polysaccharides. Furthermore, SEM–EDX analysis revealed that the extracts possessed sheet-like structures with irregular shapes and contained carbon, oxygen, and sulfur elements. All extracts demonstrated anti-urolithiasis activity by inhibiting crystal nucleation and aggregation and by modifying crystal morphology and size. The nucleation inhibition rates of CWSG, HWSG, and AASG were 100.35%, 95.86%, and 110.89%, respectively, while the aggregation inhibition rates were 54.43%, 41.27%, and 99.02%, respectively. Notably, AASG exhibited the highest anti-urolithiasis activity. These findings highlight the potential application of AASG as a functional food component for the management of urolithiasis.

Keywords *Sulfated galactan, Different extractions, Microstructure analysis, Crystal morphology, Nucleation*

P-18

Effects of Cricket Protein Lysate on Mammary Gland Carcinoma: An *In Vitro* Study Using Human Cell Line

Sasipat Teerawongsuwan[1], Theepakorn Surapha[1], Samart Dorn-In[2], Ruttachuk Rungsiwiwut[1,3*]
[1] Department of Anatomy, Faculty of Medicine, Srinakharinwirot University, Sukhumvit 23, Bangkok, 10110, Thailand
[2] Unit of Food Hygiene and Technology, Centre for Food Science and Veterinary Public Health, University of Veterinary Medicine Vienna, Veterinaerplatz 1, Vienna, 1210, Austria
[3] Research unit in stem cell innovation and tissue engineering, Srinakharinwirot University, Sukhumvit 23, Bangkok, 10110, Thailand
*Corresponding author, e-mail: ruttachuk@g.swu.ac.th

Abstract

Edible insects, particularly crickets, are increasingly promoted as sustainable protein sources due to their high nutritional value and low environmental impact. In addition to essential nutrients, cricket proteins contain bioactive peptides that have cationic, hydrophobicity, and α-helix, which enhance cancer apoptosis. Despite the growing use of cricket-derived products in food and nutritional supplements, their biological effects on mammalian cells, including cancer cells, remain poorly understood. This study investigated the effects of cricket protein lysate (concentration range from 0.1-1000 µg/ml) on the human breast cancer cell line MCF7, focusing on cytotoxicity, lysosomal responses, mitochondrial integrity, and the expression of epithelial–mesenchymal transition (EMT)–related genes. MCF7 cells were exposed to increasing concentrations of cricket protein lysate. Cellular morphology and viability were evaluated to assess cytotoxicity. Lysosomal activity was examined using lysosomal staining to detect changes in lysosomal accumulation and organization. Mitochondrial integrity was assessed by measuring the expression of TOMM20, a mitochondrial outer membrane protein. Quantitative real-time PCR was performed to analyze the expression of EMT-associated genes, including E-cadherin, N-cadherin, vimentin, Snail, and Twist. Cricket protein lysate induced concentration-dependent morphological changes and significantly reduced cell viability, with pronounced cytotoxicity at higher concentrations. Lysosomal staining revealed increased lysosomal accumulation at intermediate doses, indicating cellular stress, whereas severe disruption of lysosomal organization was observed at the highest concentration. A concentration-dependent decrease in TOMM20 expression suggested mitochondrial dysfunction. Gene expression analysis demonstrated modulation of EMT-related markers, with reduced E-cadherin and increased expression of N-cadherin, vimentin, Snail, and Twist at sublethal concentrations. In contrast, the highest concentration resulted in broad suppression of gene expression, consistent with severe cytotoxic injury. Cricket protein lysate induces cellular stress and cytotoxicity in MCF7 cells and modulates EMT-associated gene expression, indicating that cricket-derived protein components may influence cancer cell physiology. Further studies are required to identify the active components and clarify their underlying mechanisms.

Keywords *Anticancer effect, Crickets, Breast cancer, Stem cells*

P-19

The Potential of Quercetin Co-treatment with Neurogenic Induction on Neuronal Differentiation of Human Stem Cells from Apical Papilla, An *In Vitro* Study

Tarinee Chodchavanchai[1], Supanat Lumbikananda[1], Peeratchai Seemuang[2], Amarin Thongsuk[1], Tatcha Balit[3], Nopporn Jongkamonwiwat[1], Charoensri Thonabulsombat[1], Anupong Thongklam Songsaad[4*]
[1] Department of Anatomy, Faculty of Science, Mahidol University, Bangkok, Thailand
[2] Department of Pharmacology, Faculty of Dentistry, Mahidol University, Bangkok, Thailand
[3] School of Medicine, Walailak University, Nakhon Si Thammarat, Thailand
[4] Department of Anatomy, Faculty of Dentistry, Mahidol University, Bangkok, Thailand
*Corresponding author, e-mail: anupong.son@mahidol.ac.th

Abstract

Neurodegenerative diseases represent a significant global health challenge, characterized by the progressive loss of neuronal cells. Moreover, adult neurogenesis in the central nervous system is restricted, resulting in limited regenerative capacity. Dental tissues derived from mesenchymal stem cells, specifically human stem cells from the apical papilla (hSCAPs), present a promising alternative candidate due to their ectomesenchyme origin and migratory neural crest stem cells derivative. Therefore, these cells could serve as a potential source for neuronal differentiation. Interestingly, Quercetin, which is a flavonoid compound that could activate *SIRT1,* which is a central modulator of neuronal differentiation. Therefore, this study aims to demonstrate the synergistic effect of Quercetin on neuronal differentiation. hSCAPs triggered neuronal differentiation by using Quercetin co-treatment with neuronal induction medium. hSCAPs were isolated from human third molars and characterized with mesenchymal stem cell properties. The cytotoxicity of Quercetin (0-80 μM) was assessed by using a colorimetric (MTT) assay. To evaluate neurogenic-enhancing potential, hSCAPs were induced by neurogenic induction with non-cytotoxic concentrations of Quercetin co-treatment, followed by qRT-PCR for neuronal-associated markers. These findings demonstrated that hSCAPs revealed self-renewal ability, expressed mesenchymal stem cell markers (CD73+, CD90+, CD105+, and CD34-), and presented multilineage differentiation abilities, indicating characteristics of mesenchymal stem cells. The cytotoxicity of Quercetin was not observed at 0-20 μM. These non-cytotoxic concentrations were performed in co-treatment with neurogenic induction. Firstly, the neurogenic induction can trigger the differentiation of hSCAPs into immature neuronal-like cells (increased *TUBB3*). Specifically, 1.25 μM of Quercetin co-treatment significantly promoted *TUBB3* expression when compared with neurogenic induction. Furthermore, the highest number of Cresyl violet positive cells, which presented neuronal-like morphologies, was observed at 1.25 μM of Quercetin, which indicated their neurogenic differentiation enhancing potential. Taken together, Quercetin could serve as a synergistic neuronal enhancer to mitigate the neuronal loss of neurodegenerative diseases.

Keywords *Quercetin, Human stem cell from apical papilla, Neuronal differentiation, Co-treatment*

Background

Neurodegenerative diseases represent a significant global health challenge, serving as a primary cause of permanent disability and mortality, affecting over three billion individuals worldwide (1). This heterogeneous group of disorders, including stroke, Alzheimer's disease, Parkinson's disease, and various cerebrovascular conditions, is characterized by the progressive loss of neuronal structure, function, and cell number within the brain and spinal cord. Despite advancements in medical science, current therapeutic modalities remain largely unsuccessful in arresting the neuro-degenerative process (2). Effective treatment is further complicated by the central nervous system's (CNS) inherently limited regenerative capacity and the physiological barrier presented by the blood-brain barrier (BBB), which prevents nearly 98% of small-molecule drugs and 100% of large-molecule

pharmacological agents from reaching target neural tissues (3).

Neurogenesis, the intricate process of generating functional neurons from neural stem cells (NSCs), is highly active during embryonic development but becomes severely restricted in the adult brain (4). While embryonic neurogenesis is marked by rapid and widespread expansion, adult neurogenesis is spatially confined to two specific anatomical niches: the subventricular zone (SVZ) of the lateral ventricles and the subgranular zone (SGZ) of the hippocampal dentate gyrus (5,6).

To overcome the limitations of adult neurogenesis and the ethical concerns surrounding stem cell sources, mesenchymal stem cells (MSCs) derived from dental tissues have emerged as a promising alternative. Among these, stem cells from the apical papilla (hSCAPs) isolated from the immature tissue at the tips of developing tooth roots represent an exceptionally early and potent stem cell population (7). hSCAPs exhibit superior proliferative rates and colonogenic capacities compared to other MSCs (8). Critically, hSCAPs originate from the migratory neural crest cells, which is reflected in their constitutive expression of neural markers including β-III tubulin, Nestin, and GFAP. This inherent neurogenic predisposition, combined with their ease of isolation from discarded third molars and significant immunomodulatory properties, positions hSCAPs as an ideal candidate for neuro-regenerative medicine (9).

In addition, the efficacy of stem cell-based therapies can be significantly enhanced through the use of bioactive compounds. Quercetin, a natural flavonoid found abundantly in various fruits and vegetables, has attracted substantial interest due to its potent antioxidant and neuroprotective properties. Notably, Quercetin possesses the ability to cross the BBB and has been shown to modulate the proliferation and differentiation of neural progenitor cells. At the molecular level, Quercetin acts as an *SIRT1* activator, a pathway previously implicated in promoting neuronal development (10).

Therefore, this study aims to investigate the potential of Quercetin to enhance the neuronal differentiation of human stem cells from apical papilla (hSCAPs). By utilizing the synergistic effects of Quercetin co-treatment with neuronal induction to enhance the neurogenic differentiation potential of hSCAPs.

Materials and Methods

Isolation and characterization of hSCAPs

Apical papilla tissues were extracted from human third molars (n=3, 18-21 years old), followed by a dual enzymatic disaggregation method. The ethical consideration and research protocol were approved by the Ethics Committee on Human Rights Related to Human Experimentation of Faculty of Dentistry/Faculty of Pharmacy, Mahidol University (COE. No. MU-MOU 2024/DT081).

These isolated cells were performed characterization of MSCs properties, including plastic adherent ability, cell morphology, colony-forming unit (CFU), cell surface markers analysis (CD34, CD73, CD90, and CD105) by flow cytometry, and multilineage differentiation abilities (osteogenic, adipogenic, and neurogenic differentiation). In addition, investigation of ecto-mesenchyme origin and migratory neural crest derivatives was performed by using immunocyto-chemistry (nestin and β-III tubulin).

Cell viability of Quercetin-treated hSCAPs

After characterization, the cytotoxicity of Quercetin-treated hSCAPs was assessed by colorimetric (MTT) assay. hSCAPs were seeded at a density of 10,000 cells/well in a 96-well plate. After 24 hours, the cells were incubated with various concentrations of Quercetin (0, 1.25, 2.5, 5, 10, 20, 40, and 80 μM), which dissolved with dimethyl sulfoxide (DMSO) for 30 hours. The vehicle group was used to determine the cytotoxicity of this solvent by adding DMSO equal to the amount of DMSO of the highest Quercetin concentration (0.4% v/v).

The neuronal-enhancing potential of Quercetin co-treatment

To demonstrate the neuronal differentiation ability, hSCAPs at a density of 100,000 cells/well in a 6-well plate were cultured with neurogenic induction, which served as a positive group, and compared with basal medium (negative group). Moreover, the non-cytotoxic concentrations of Quercetin were co-induced with neurogenic induction. The neuronal induction protocol was divided into 2 phases: phase I for 24 hours, and phase II for 6 hours (Table 1).

To evaluate the neuronal-enhancing potential of Quercetin co-treatment, the expression of neuronal-associated genes was performed by qRT-PCR, including *NES* and *TUBB3,* which are early-neural progenitor and immature neurons markers, respectively. The potential validated gene of the positive control was further investigated with Quercetin co-treatment.

Furthermore, the optimal concentration of Quercetin co-treatment was identified by the identification of Nissl bodies, which are the typical hallmark of neuronal-like cells, by Cresyl violet staining. The number of Cresyl violet positive cells

was compared among the negative, positive, and Quercetin co-treatment groups.

Statistical analysis

The individual experiment was performed in triplicate (n=3). The data were expressed as mean ± SEM. Statistical significance was determined using a One-Way ANOVA followed by post hoc Tukey's multiple comparison test for cell viability, *TUBB3* expression, and percentage of Cresyl violet positive cells. Comparison of gene expression between negative and positive groups was analyzed by an unpaired t-test. All statistical analyses with significance set at $*p < 0.05$ using GraphPad Prism software.

Table 1 Neuronal induction protocol

Design	Induction phase I (24 hours)	Induction phase II (6 hours)
Negative	- DMEM/F/12 - 10% FBS - 1% Antibiotic-antimycotic	- DMEM/F/12 - 1% Antibiotic-antimycotic
Positive	- DMEM/F/12 - 10% FBS - 1% Antibiotic-antimycotic - 1% β-mercaptoethanol - 0.5% bFGF	- DMEM/F-12 - 1% Antibiotic-antimycotic - 2% DMSO - 1% BHA
Quercetin co-treatment	- DMEM/F/12 - 10% FBS - 1% Antibiotic-antimycotic - 1% β-mercaptoethanol - 0.5% bFGF - Quercetin (non-toxic concentrations)	- DMEM/F-12 - 2% DMSO - 1% Antibiotic-antimycotic - 1% BHA - Quercetin (non-toxic concentrations)

Results

Characterization of hSCAPs

According to the International Society for Cell & Gene Therapy (ISCT) minimal criteria, the isolated cells from human apical papilla tissues need to be characterized with MSC properties (11). Firstly, the isolated cells from human apical papilla tissues presented plastic adherent ability and fibroblast-like morphology (Fig 1A). The cells reveal colony-forming units, indicating that cells have self-renewal ability (Fig 1B). The isolated cells showed positive expression of nestin (Fig 1C), and β-III tubulin (Fig 1D) indicated ectomesenchyme origin and migratory neural crest derivative. The cells were highly expressed as MSCs markers, more than 95% of CD73, CD90, and CD105, and negatively expressed CD34 (less than 2%) (Fig 1E). Multilineage differentiation properties were elucidated. The cells presented calcium nodules, lipid droplet accumulation, and Nissl substance, indicating osteogenic, adipogenic, and neurogenic differentiation, respectively (Fig. 1H-1F). Therefore, the isolated cells were characterized as MSCs, namely hSCAPs.

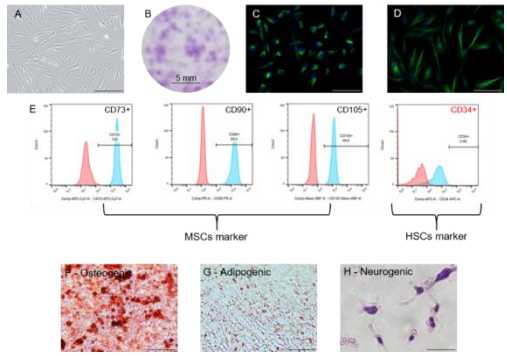

Fig. 1 The characterization of hSCAPs. (A) Bright field microscopic image. (B) Colony-forming unit. (C-D) Immunocytochemistry of nestin and β-III tubulin staining. (E) Cell surface antigen molecule by flow cytometry. (F) Osteogenic differentiation by Alizarin red staining. (G) Adipogenic differentiation by Oil Red O staining. (H) Neurogenic differentiation by Cresyl violet staining. Scale bar: (A), (C), (D) = 200 μm, (B) = 5 mm., (F), (G) = 100 μm, and (H) = 20 μm.

The cytotoxicity of Quercetin-treated hSCAPs

To investigate the cytotoxicity of Quercetin treatment, hSCAPs were incubated with Quercetin concentrations of 0-80 μM for 30 hours. After treatment, Quercetin at 0-20 μM showed non-cytotoxicity on hSCAPs, whereas 40 and 80 μM decreased their cell viability (Fig. 2). Therefore, the non-cytotoxic concentrations were further investigated in subsequent experiments.

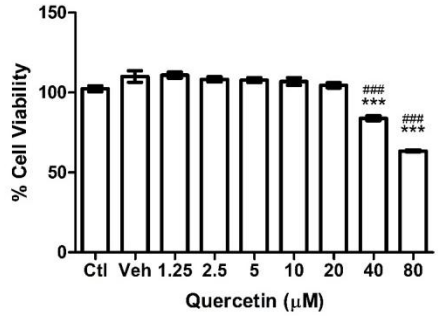

Fig. 2 The cell viability of Quercetin-treated hSCAPs for 30 hours .MTT assay was used to determine cell viability . Data were expressed as the mean ± SEM; n =3, $^{***}p < 0.001$, compared with the control group. $^{###}p < 0.001$, compared with the vehicle group.

The potential of Quercetin co-treatment on enhancing neuronal differentiation of hSCAPs

To investigate the enhancing effect of Quercetin on neuronal differentiation, hSCAPs were co-treated with neurogenic induction and non-cytotoxic concentrations of Quercetin (0-20 µM) for 30 hours. The significant difference of *NES* expression between negative and positive groups was not observed (Fig. 3A). Interestingly, the positive group showed significantly increased of *TUBB3* (Fig. 3B), indicating that the neurogenic induction induced differentiation of hSCAPs into immature neuronal-like cells.

Moreover, Quercetin co-treatment showed evidence of neuronal differentiation ability of hSCAPs. Quercetin co-treatment at 1.25 µM resulted in the highest expression of *TUBB3*. Whereas Quercetin co-treatment 20 µM showed a significant decrease of *TUBB3*, when compared with the positive group (Fig. 3C). Therefore, Quercetin co-treatment 1.25 µM could serve as an optimal concentration of Quercetin co-treatment.

Under Cresyl violet staining, the undifferentiated cells presented fibroblast-like morphology with dark spots of nucleoli and pale staining of nuclei in the negative group (Fig. 4A, black asterisks), whereas the positive (Fig. 4B, black arrows) and Quercetin co-treatment 1.25 µM groups (Fig. 4C, black arrows) revealed the differentiated cells, which exhibited neuronal-like morphologies with intensely purple-stained Nissl substance. To quantify the percentage of Cresyl violet-positive cells, the differentiated cells were counted to report the neuronal differentiation ability. The differentiated cells of the positive group were higher than those of the negative group. Interestingly, Quercetin co-treatment at 1.25 µM exhibited the highest percentage of Cresyl violet positive cells when compared with the positive and negative groups (Fig. 4D).

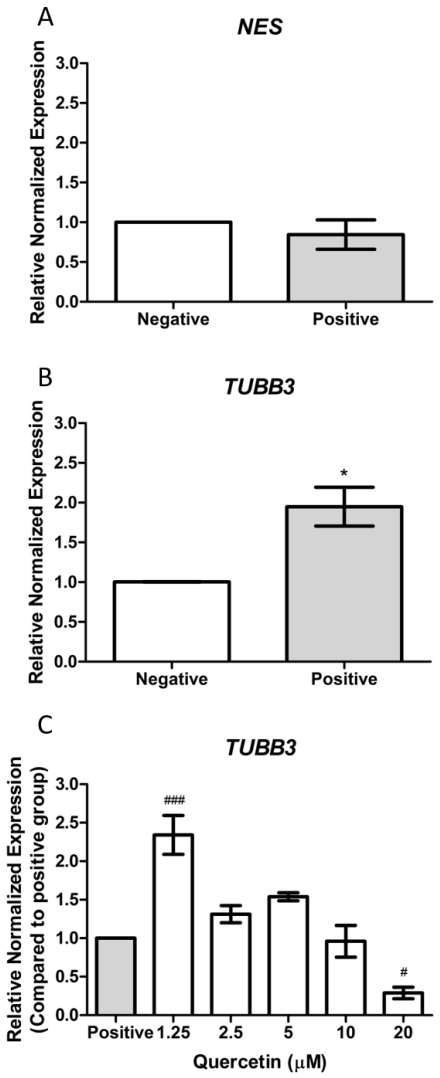

Fig. 3 Optimal concentration of co-treatment-Quercetin with neuronal induction for 30 hours . The positive group showed a decreasing trend of (**A**) *NES* and a significant increase of (**B**) *TUBB3*. (**C**) Quercetin at 1.25 µM showed the highest expression of *TUBB3*. Data were expressed as the mean ± SEM; n =3, *p<0. 05, compared with the negative group. $^{\#}p < 0.05$, $^{\#\#\#}p < 0.001$, compared with the positive group.

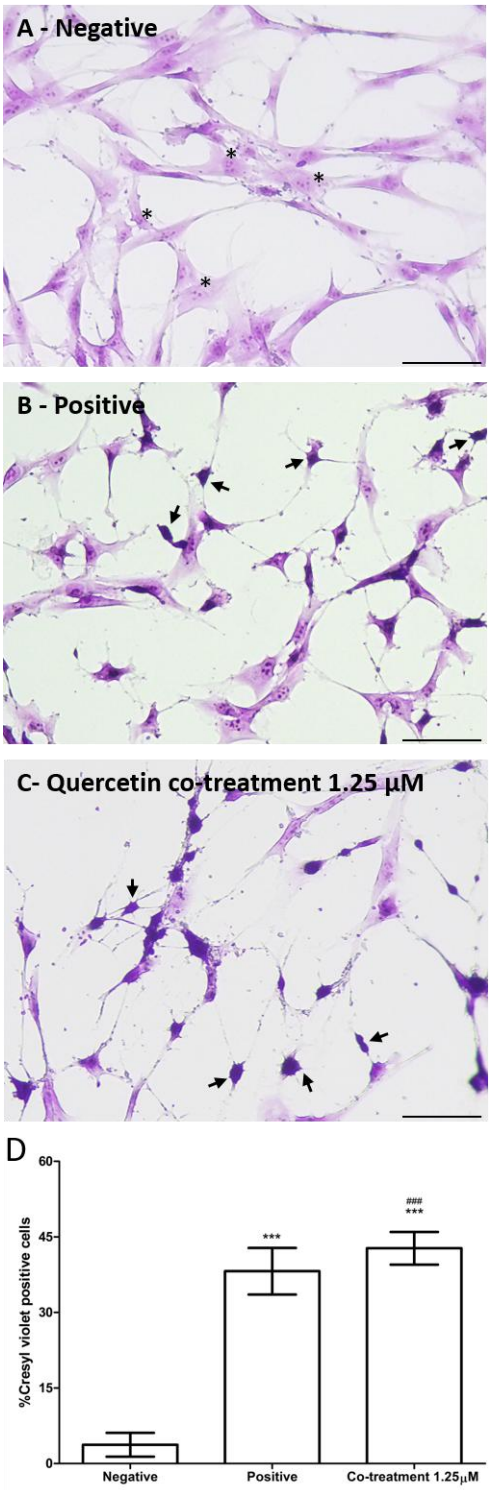

Fig. 4 Characterization of neuronal-like cells by using Cresyl violet staining among (A) negative, (B) positive, (C) Quercetin co-treatment 1.25 µM groups. (D) The typical neuronal hallmark, which presented with intense purple of Nissl body were quantify into the percentage of Cresyl violet positive cells. Scale bar: 100 µm. Data were expressed as the mean ± SEM; n =3, ***$p < 0.001$, compared with the negative group. $^{\#\#\#}p < 0.001$, compared with the positive group.

Discussion

hSCAPs showed MSCs' properties following the International Society for Cellular Therapy (ISCT) minimal criteria (11) including plastic adherent abilities and morphology of MSCs (Fig. 1A). The colony-forming units indicated that they have self-renewal ability (Fig. 1B). The isolated cells present positive expression of MSCs surface markers and Negative expression of hematopoietic markers (Fig. 1E). In addition, the apical papilla-isolated cells demonstrated osteogenic, adipogenic, and neurogenic differentiation to indicate multilineage differentiation properties. (Fig. 1F-1H). The apical papilla-isolated cells were show positively stained with nestin (Fig. 1C) and β-III tubulin (Fig. 1D), indicating their migratory neural crest derivative and ectomesenchyme origin (9). Altogether, this finding verified that human apical papilla-isolated cells were characterized as MSCs, namely hSCAPs.

The cell viability was observed to show cytotoxic effect at 40 and 80 µM, whereas it showed non-cytotoxicity in Quercetin 0-20 µM for 30 hours (Fig. 2). Furthermore, the vehicle group, which contained a DMSO concentration equivalent to that used in the highest Quercetin concentration (80 µM), demonstrated that the 0.4% DMSO (solvent) was non-toxic to the cells. These results confirm that the cytotoxicity observed at high concentrations was induced by Quercetin itself rather than the solvent. The cellular toxicity of Quercetin at 40-80 µM was described by the hormetic dose-response effect, leading to positive responses (associated with beneficial effects) at low concentrations and negative responses (associated with toxic effects) at high concentrations (12).

According to the results, a positive medium enhances neuronal-like cells derived from hSCAPs to a significant increase in *TUBB3* expression. On the other hand, *NES* expression was not significantly different. The results indicate that the positive group was not associated with enhancing neuronal differentiation in the early stage, but rather enhanced the cells' drive to neurons, resulting in the immature stage.

Moreover, Quercetin co-treatment at 1.25 µM triggered neuronal differentiation of hSCAPs, which

presented the highest expression of *TUBB3*, acting as immature neuronal-like cells. Quercetin concentration at 20 μM significantly decreased *TUBB3,* indicating that high concentrations of Quercetin may exert inhibitory effects on the TrkB signaling pathway, which is essential for driving neuronal differentiation (13). Furthermore, high concentrations of flavonoid compounds could induce irreversible cell-cycle arrest, acting as a molecular brake that counteracts the pro-neurogenic effects observed at lower doses. This two-phase response accounts for the down-regulation of *TUBB3* at high dosages, echoing findings from previous studies on human umbilical cord-derived MSCs differentiation (14). However, further study should be required to demonstrate the underlying mechanism of Quercetin treatment. In addition, the quantification results of the percentage of Cresyl violet positive cells revealed the highest number of neuronal-like cells in Quercetin co-treatment at 1.25 μM.

Previous studies have established that Quercetin possesses the capacity to permeate the BBB, a critical pharmacokinetic property for neurotherapeutic agents (10). Beyond its ability to facilitate neuronal differentiation, Quercetin demonstrates potent neuroprotective effects by mitigating neuronal damage and apoptosis (15). These effects are largely mediated through the activation of SIRT1, a central modulator of neurogenesis. Mechanistically, Quercetin promotes neuro-regeneration by enhancing neurite outgrowth, elevating intracellular cyclic adenosine mono-phosphate (cAMP) levels, and modulating key signaling cascades, including the PI3K/Akt and AMPK pathways (10,16).

However, to further confirm the underlying mechanism, the future study will observe the SIRT1 receptor in hSCAPs to confirm the binding mechanism of Quercetin. Furthermore, neuronal-like cells derived from Quercetin-treated hSCAPs will be further investigated in functional neuronal activities by using calcium imaging, impedance measurement, and patch clamp assays.

Conclusion

This finding suggests that Quercetin can serve as a neuronal enhancer of hSCAPs, which present alternative therapeutics for neurodegenerative diseases.

Acknowledgements

This work was supported by the Faculty of Science, Mahidol University, and Faculty of Dentistry, Mahidol University, Thailand.

References

1. World Federation of Neurology. WHO Report Finds Neurological Conditions Now Affect Over One-Third of the World's Population 2025 [Available from: https://wfneurology.org/activities/news-events/wfn-news/2025-10-17-wcn2025-who-report-1-in-3-neurological-conditions.
2. Gioia R, Biella F, Citterio G, Rizzo F, Abati E, Nizzardo M, et al. Neural Stem Cell Transplantation for Neurodegenerative Diseases. International Journal of Molecular Sciences. 2020;21:3103.
3. Sivandzade F, Cucullo L. In-vitro blood-brain barrier modeling: A review of modern and fast-advancing technologies. J Cereb Blood Flow Metab. 2018;38(10):1667-81.
4. Alsina FC, Silver DL. Chapter 28 - Posttranscriptional and translational control of neurogenesis: roles for RNA-binding proteins. In: Rubenstein J, Rakic P, Chen B, Kwan KY, editors. Patterning and Cell Type Specification in the Developing CNS and PNS (Second Edition): Academic Press; 2020. p.731-50.
5. Wooden JI, Thompson KR, Guerin SP, Nawarawong NN, Nixon K. Consequences of adolescent alcohol use on adult hippocampal neurogenesis and hippocampal integrity. Int Rev Neurobiol. 2021;160:281-304.
6. Zibara K, Ballout N, Mondello S, Karnib N, Ramadan N, Omais S, et al. Combination of drug and stem cells neurotherapy: Potential interventions in neurotrauma and traumatic brain injury. Neuropharmacology. 2019;145(Pt B):177-98.
7. Sonoyama W, Liu Y, Yamaza T, Tuan R, Wang S, Shi S, et al. Characterization of the Apical Papilla and Its Residing Stem Cells from Human Immature Permanent Teeth: A Pilot Study. Journal of Endodontics. 2008;34:166-71.
8. Kang J, Fan W, Deng Q, He H, Huang F. Stem Cells from the Apical Papilla: A Promising Source for Stem Cell-Based Therapy. BioMed Research International. 2019;2019(1):6104738.
9. Huang GT, Sonoyama W, Liu Y, Liu H, Wang S, Shi S. The hidden treasure in apical papilla: the potential role in pulp/dentin regeneration and bioroot engineering. J Endod. 2008;34(6):645-51.
10. Grewal AK, Singh TG, Sharma D, Sharma V, Singh M, Rahman MH, et al. Mechanistic insights and perspectives involved in neuroprotective action of quercetin. Biomed Pharmacother. 2021;140:111729.
11. Dominici M, Le Blanc K, Mueller I, Slaper-Cortenbach I, Marini F, Krause D, et al. Minimal

criteria for defining multipotent mesenchymal stromal cells. The International Society for Cellular Therapy position statement. Cytotherapy. 2006;8(4):315-7.
12. Calabrese EJ, Mattson MP, Calabrese V. Resveratrol commonly displays hormesis: Occurrence and biomedical significance. Human and Experimental Toxicology. 2010; 29(12):980-1015.
13. Wang X, Ma S, Meng N, Yao N, Zhang K, Li Q, et al. Resveratrol Exerts Dosage-Dependent Effects on the Self-Renewal and Neural Differentiation of hUC-MSCs. Molecules and Cells. 2016;39(5):418-25.
14. Ichwan M, Walker T, Nicola Z, Ludwig-Müller J, Böttcher C, Overall R, et al. Apple Peel and Flesh Contain Pro-neurogenic Compounds. Stem Cell Reports. 2021;16.
15. Li Y, Man M, Tian Y, Zhao G, Liu F, Zhao J, et al. Quercetin protects against neuronal toxicity by activating the PI3K/Akt/GSK-3β pathway in vivo models of MPTP-induced Parkinson's disease. Inflammopharmacology. 2025;33(7): 4063-76.
16. Chiang MC, Tsai TY, Wang CJ. The Potential Benefits of Quercetin for Brain Health: A Review of Anti-Inflammatory and Neuro-protective Mechanisms. Int J Mol Sci. 2023; 24(7).

P-20

Investigation of Individual Oligodendrocyte Characteristics in the Corpus Callosum of Aged Mice

Sasikarn Looprasertkul[1,2,3], Reiji Yamazaki[2], Yasuyuki Osanai[2], Nobuhiko Ohno[2,4*]
[1] Department of Anatomy, Faculty of Medicine, Chulalongkorn University, Pathumwan, Bangkok, Thailand
[2] Division of Histology and Cell Biology, Department of Anatomy, School of Medicine, Jichi Medical University, Tochigi, Japan
[3] Section of Electron Microscopy, Supportive Center for Brain Research, National Institute for Physiological Sciences, Aichi, Japan
[4] Division of Ultrastructural Research, National Institute for Physiological Sciences, Aichi, Japan
*Corresponding author, e-mail: nohno@nips.ac.jp

Abstract

Oligodendrocytes generate myelin sheaths around axons in the central nervous system, enabling rapid nerve conduction and maintaining efficient neuronal communication. Because myelin synthesis and maintenance are energetically demanding, oligodendrocytes require substantial metabolic support. Aging is associated with mitochondrial dysfunction and reduced energy production, which may impair myelin maintenance and myelination. However, how aging affects morphology, myelinating capacity, and metabolic features of individual oligodendrocytes remains poorly understood due to technical challenges in analyzing their detailed structure. In this study, we investigated the ultrastructural morphology of individual oligodendrocytes in the corpus callosum of an aged mouse (18-month-old). Serial block-face scanning electron microscopy was used to generate large-volume datasets for three-dimensional reconstruction of individual oligodendrocytes. Nuclei, myelinated axons, and mitochondria were automatically segmented using the deep-learning-based automated segmentation-UNIEM with subsequent proofreading, followed by manual segmentation of oligodendrocyte cell bodies and processes. Three-dimensional analysis of 19 oligodendrocytes in aged mice revealed that individual oligodendrocytes formed myelin sheaths around axons with diameters ranging from 359 to 1707 nm, with corresponding myelin thicknesses ranging from 102 to 1039 nm. Individual oligodendrocytes showed distinct preferences for axons within specific diameter ranges. Based on myelin thickness, oligodendrocytes could be broadly categorized into two groups: thin-myelin and thick-myelin oligodendrocytes. Cells forming thicker myelin sheaths exhibited larger cell body and nuclear volumes and a greater total mitochondrial volume compared with those forming thinner myelin sheaths, although the relative mitochondrial volume within cells was similar between groups. In addition, the number of myelin-forming branches per oligodendrocyte was significantly reduced in aged mouse (19 oligodendrocytes) compared with young mouse (11 oligodendrocytes) in Tanaka et al., 2021. Together, these findings demonstrate that aging alters the structural organization and myelinating capacity of individual oligodendrocytes and reveals heterogeneity in mitochondrial and morphological features associated with myelin thickness at the single-cell level.

Keyword *Oligodendrocyte, Aging, Serial block-face scanning electron microscopy, Central Nervous System, Corpus Callosum*

P-21

Effects of Probiotic Supplementation on Blood Chemical Parameter and Sucrose Preference Test in Chronic Unpredictable Mild Stress-Induced Rats

Suwapat Pakansit[1], Jariya Samo-on[1], Porntipha Vitheejongjaroen[2], Sutisa Nudmamud-Thanoi[1,3], Jureepon Roboon[1*]
[1] Department of Anatomy, Faculty of Medical Science, Naresuan University, Phitsanulok, Thailand
[2] CPF (Thailand) Public Company Limited, Ayutthaya, Thailand
[3] Centre of Excellence in Medical Biotechnology, Naresuan University, Phitsanulok, Thailand
*Corresponding author, e-mail: jureeponr@nu.ac.th

Abstract
Background: Chronic stress is a major risk factor for anxiety and depressive disorders, leading to behavioral and physiological alterations as well as disruptions in the gut–brain axis. The chronic unpredictable mild stress (CUMS) model is widely used to induce depressive-like behaviors in rodents, which can be assessed using the sucrose preference test as an indicator of anhedonia. Chronic stress has also been associated with alterations in platelet levels. Probiotics, such as *Lactiplantibacillus plantarum* 299V (299V), have been reported to exert antidepressant effects. Fluoxetine (Flu), a selective serotonin reuptake inhibitor widely used for stress-related disorders, served as a reference treatment. Furthermore, *Lacticaseibacillus rhamnosus* (CPF01) and *Limosilactobacillus fermentum* (CPF02) may modulate the gut–brain axis and alleviate stress-related disorders; however, their mechanisms remain unclear. **Objective:** This study aimed to evaluate the effects of *Lacticaseibacillus rhamnosus* and *Limosilactobacillus fermentum* on attenuating depressive-like behaviors and altering blood chemistry in rats subjected to CUMS. **Methods:** Eight-week-old male Sprague–Dawley rats were divided into eight groups: Control, CPF01, CPF02, CUMS, CUMS+CPF01, CUMS+CPF02, CUMS+299V, and the CUMS+Flu groups. Rats in control groups were not subjected to CUMS, while depressed rats were exposed to CUMS for 56 days. In the probiotic-supplemented group, rats were orally administered CPF01, CPF02, 299V, or Flu during the final 28 days of the experiment. Depressive-like behavior was assessed using the Sucrose Preference Test (SPT), and blood chemistry parameters were analyzed at the end of the study. **Results:** CUMS-induced depressive-like behavior, as indicated by reduced sucrose preference. Probiotic supplementation attenuated these behavioral changes. Treatment with probiotics did not significantly affect complete blood count (CBC), liver function, or kidney function parameters. However, CUMS reduced platelet volume, whereas probiotic treatment restored platelet volume toward normal levels. **Conclusion:** These findings suggest that supplementation of probiotics, *Lacticaseibacillus rhamnosus* (CPF01) and *Limosilactobacillus fermentum* (CPF02), alleviates CUMS-induced depressive-like behaviors, potentially through modulation of the gut-brain axis and restoration of platelet volume.

Keywords *Chronic unpredictable mild stress (CUMS), Lacticaseibacillus rhamnosus, Limosilactobacillus fermentum, Sucrose preference test, Blood chemistry*

P-22

Therapeutic Effects of Nano-Curcumin in A Dexamethasone-Induced Depression Model: Evidence from Histological and Proteomic Analyses

Ponthip Cheenkhwan[1,6], Suchiwa Pan-on[2], Waree Tiyaboonchai[3,6], Samur Thanoi[4], Sawanya Charoenlappanit[5], Sittiruk Roytrakul[5], Jureepon Roboon[1,6], Sutisa Nudmamud-Thanoi[1,6*]

[1] Department of Anatomy, Faculty of Medical Science, Naresuan University, Phitsanulok, Thailand

[2] Department of Cosmetic Science and Technology, Faculty of Pharmaceutical Sciences, Burapha University, Chonburi, Thailand

[3] Department of Pharmaceutical, Faculty of Pharmaceutical Sciences, Naresuan University, Phitsanulok, Thailand

[4] Department of Anatomy, School of Medical Sciences, University of Phayao, Phayao, Thailand

[5] National Centre for Genetic Engineering and Biotechnology, National Science and Technology Development Agency, Pathum Thani, Thailand

[6] Centre of excellence in Medical Biotechnology, Naresuan University, Phitsanulok, Thailand

*Corresponding author, e-mail: sutisat@nu.ac.th

Abstract

Major depressive disorder is associated with dysregulation of the hypothalamic–pituitary–adrenal axis and excessive glucocorticoid exposure, which can lead to neuronal damage and molecular alterations in brain regions involved in emotional and cognitive regulation. Curcumin, a bioactive polyphenolic compound obtained from Curcuma longa, has been widely recognized for its antidepressant, antioxidant, and neuroprotective activities. Despite these beneficial properties, its therapeutic application is limited due to poor aqueous solubility, restricted penetration across the blood–brain barrier, and rapid metabolic degradation. In our previous study, administration of nano-curcumin significantly alleviated depressive-like behaviors in rats. However, the underlying histological and molecular mechanisms remain unclear. Therefore, this study aimed to evaluate the therapeutic effects of nano-curcumin in a dexamethasone-induced depression model and to investigate its impact on neuronal histology and molecular pathways. An experimental depression model was established through dexamethasone administration (1.5 mg/kg). Nano-curcumin treatment (100 mg/kg) and fluoxetine (10 mg/kg) were subsequently applied to assess its potential neuroprotective effects. Histological analysis was performed to evaluate neuronal morphology in the hippocampus and entorhinal cortex. In addition, proteomic analysis was conducted to identify differentially expressed proteins associated with signaling pathways involved in neuronal function and stress responses. Histological findings showed that dexamethasone exposure neuronal damaged characterized by shrunken cell bodies, and pyknotic nuclei in both brain regions. Nano-curcumin attenuated these alterations, indicating a protective effect against glucocorticoid-induced neurotoxicity. Proteomic analysis revealed significant alterations in proteins associated with the mitogen-activated protein kinase (MAPK) signaling pathway, including proteins associated with cellular stress responses, apoptosis regulation, and neuronal plasticity. These findings suggest that nano-curcumin exerts antidepressant effects by regulating neuronal survival and stress responses via the MAPK pathway, highlighting its therapeutic potential for stress-related depressive disorders.

Keywords *Depression, Nano-curcumin, Neuroprotective effects, Mitogen-activated protein kinase (MAPK) signaling pathway, Proteomics*

P-23

Age-Related Differences in the Association Between Cognitive Performance and Middle Frontal Gyrus Cortical Thickness

Thunyarut Bannawongsil[1*], Tussaneeya Ngamvong[1], Napawan Taradolpisut[2], Athikhun Suwannakhan[2,3]
[1] Department of Anatomy, Faculty of Medicine, Bangkokthonburi University, Thawi Watthana, Bangkok, Thailand
[2] Department of Anatomy, Faculty of Science, Mahidol University, Bangkok 10400, Thailand
[3] Human Anatomy Unit, Department of Biomedical Sciences, College of Medicine and Health, University of Birmingham, Edgbaston B15 2TT, United Kingdom
*Corresponding author, e-mail: thunyarut.ban@bkkthon.ac.th

Abstract

Changes in cognitive abilities across the lifespan are a key focus of contemporary neuroscience. While crystallized intelligence is generally preserved with age, executive function and memory often decline. The left rostral middle frontal gyrus (LRMFG), a core region of the frontal cortex, plays an important role in executive processing and higher-order cognitive control. However, the relationship between age, cognitive performance, and structural variation in this region remains unclear. This study examined associations between LRMFG cortical thickness, age, and cognitive performance using data from the publicly available LEMON dataset, comprising 227 healthy participants, including a young (N= 153, 25.1 ± 3.1 years, range 20–35 years, 45 female) and an elderly group (N= 74, 67.6 ± 4.7 years, range 59–77 years, 37 female). High-resolution T1-weighted MP2RAGE MRI was analysed alongside cognitive assessments: the Trail Making Test (TMT) for visuomotor speed and executive function, the California Verbal Learning Test (CVLT) for verbal learning and memory, and the Wortschatztest (WST) for crystallized intelligence. Cortical thickness was measured using 3D Slicer. Measurements were performed independently by two observers and repeated twice, with averaged values used for analysis. Inter-observer reliability demonstrated moderate agreement (ICC = 0.59; F = 2.45). A modest negative association was observed between age and LRMFG thickness ($r \approx -0.20$, $p = 0.003$), indicating age-related thinning. Significant differences in thickness were observed across TMT categories (visuomotor speed: $H = 16.92$, $p < 0.001$; executive function: $H = 13.46$, $p = 0.004$), with lower thickness associated with poorer performance. LRMFG thickness also showed a modest positive association with verbal memory, based on a composite CVLT score ($r \approx 0.18–0.20$, $p < 0.05$). No significant association was observed with WST scores. These findings suggest that LRMFG cortical thickness is modestly associated with age, executive function, and memory, but not with crystallized intelligence.

Keywords *Cortical thickness, Ageing, Executive function, Verbal memory, Magnetic resonance imaging*

P-24

Tuna Blood Hydrolysate Attenuates Apoptosis in Dopaminergic Neurons in An *In Vitro* Model of Parkinson's Disease

Morakot Sroyraya[1], Panlekha Rungruang[2], Daraphan Rodthayoy[1], Patnaree Phopaijit[1], Sita Keeratikornpisut[1], Veerawat Sansri[3*]
[1] Department of Anatomy, Faculty of Science, Mahidol University, Bangkok, Thailand
[2] Regional Medical Sciences Center 5, Department of Medical Sciences, Ministry of Public Health, Samut Songkhram, Thailand
[3] Department of Basic Medical Science, Faculty of Medicine Vajira Hospital, Navamindradhiraj University, Bangkok, Thailand
*Corresponding author, e-mail: veerawat@nmu.ac.th

Abstract

Parkinson's disease (PD) is a neurological condition that becomes more severe over time and primarily impacts the elderly. Its pathogenesis encompasses genetic and environmental interactions that promote the excessive generation of reactive oxygen species (ROS) and free radicals, leading to oxidative stress. These processes disrupt cellular homeostasis and damage organelles, ultimately leading to neuronal apoptosis. There is currently no cure for Parkinson's disease, and although levodopa remains the most effective symptomatic treatment, its long-term use is often associated with motor complications such as dyskinesia and motor fluctuations. Fish protein hydrolysates contain bioactive compounds that reduce free radicals and cell death. This study sought to assess the neuroprotective efficacy of tuna blood hydrolysate (TBH) by investigating its capacity to mitigate apoptosis in a cellular model of Parkinson's disease. Differentiated SH-SY5Y cells displaying dopaminergic neuron-like characteristics were employed and exposed to MPP^+ to model Parkinsonian neurotoxicity. The results showed that TBH, especially the pepsin-digested formulation, greatly lowered the amount of ROS inside cells, as shown by the DCFDA fluorescence assay, which measures intracellular ROS generation. Moreover, Western blot analysis demonstrated that TBH influenced apoptosis-related signaling by decreasing pro-apoptotic proteins (BAX, cytochrome c, cleaved caspase-9, and cleaved caspase-3) and increasing the anti-apoptotic protein BCL-2 in comparison to the MPP^+-treated group. These findings suggest that TBH protects against MPP^+-induced neuronal damage by attenuating oxidative stress and modulating the mitochondrial apoptotic pathway. TBH may therefore be a promising natural neuroprotective candidate for further investigation in PD-related research.

Keywords *Parkinson's disease, Tuna blood hydrolysate, Neuroprotection, Oxidative stress, Apoptosis*

P-25

Nutrient Foramen Position in Upper Thoracic Vertebrae for Posterior Thoracic Pedicle Screw Placement in a Northeast Thai Population

Supatsapa Unsri[1], Chanasorn Poodendaen[2], Narawadee Chompoo[2], Poonikha Namwongsakool[2], Pruet Boonsing[2], Kitinat Rodthongdee[3], Suthat Duangchit[3], Kaemisa Srisen[2*]
[1] Graduate student, Department of Anatomy, Faculty of Medical Science, Naresuan University, Phitsanulok, Thailand
[2] Department of Anatomy, Faculty of Medical Science, Naresuan University, Phitsanulok, Thailand
[3] Department of Physiology, Faculty of Medical Science, Naresuan University, Phitsanulok, Thailand
*Corresponding author, e-mail: kaemisas@nu.ac.th

Abstract

Thoracic spinal disorders, such as scoliosis, often require surgical stabilization using pedicle screw fixation. Accurate identification of the pedicle screw entry point is essential to prevent injury to the spinal cord and surrounding critical structures. This study aimed to investigate the incidence and anatomical position of the nutrient foramen in the posterior elements of upper thoracic vertebrae and to evaluate its potential as an anatomical landmark for posterior pedicle screw placement in a northeastern Thai population. A total of 600 dry thoracic vertebrae from T1 to T6 (100 vertebrae at each level) were examined from 100 adult skeletons (50 males and 50 females) aged 20 years and older. The position of the nutrient foramen was measured using three anatomical reference points: the distance to the inferior border of the superior articular facet (OA), the lateral border of the lamina (OB), and the midline of the spinous process (OC). Statistical analysis was performed using SPSS. The highest incidence of the nutrient foramen was observed at T1 (84.5%), whereas the lowest incidence was found at T6 (41.0%). Significant sex-related differences ($P < 0.05$) were identified in all measured parameters at the T1 and T3 levels. Significant bilateral asymmetry was observed at T3 (LC vs. RC, $p=0.01$), while no significant asymmetry was found at the other vertebral levels. These findings provide morphometric data on the distribution of nutrient foramina in the upper thoracic vertebrae (T1–T6). When present, the nutrient foramen may serve as a useful anatomical landmark for posterior pedicle screw placement, potentially improving surgical accuracy and safety in the northeastern Thai population.

Keywords *Thoracic vertebrae, Spinal cord, Nutrient foramen, Pedicle screw, Surgical anatomy, Thai population*

Background

Thoracic spine disorders, including traumatic injuries, degenerative diseases, and congenital deformities, present substantial challenges in spinal surgery. Pedicle screw fixation is widely utilized for the surgical management of these conditions due to its superior biomechanical stability and ability to achieve three-dimensional deformity correction [1]. Nevertheless, the complex morphology of the thoracic vertebrae and their proximity to critical neurovascular structures render accurate screw placement technically demanding [2].

The reported rates of pedicle screw misplacement in thoracic vertebrae surgery range from 3% to 44.2%, with potentially devastating complications including spinal cord injury, nerve root damage, and vascular complications [3]. Traditional anatomical landmarks for pedicle screw insertion have relied heavily on the intersection of anatomical lines and surface features, which can vary across populations and are affected by pathological changes [4].

The nutrient foramen is a consistent anatomical feature of the vertebrae and has attracted attention as a potential surgical reference point. These foramina serve as entry points for nutrient vessels supplying the vertebral body and exhibit relatively consistent distribution patterns [5]. Previous studies have demonstrated population-specific variations in vertebral anatomy, highlighting the importance of region-specific anatomical data for surgical planning [6].

Although several investigations have examined thoracic vertebral morphometry in different populations [7], limited data are available regarding nutrient foramen patterns in Southeast Asian populations, particularly in Thailand. Most existing studies have focused on European and North American populations, which may limit their applicability to Thai patients [8].

Therefore, this study aims to determine the incidence and position of nutrient foramina in the posterior thoracic lamina of the northeastern Thai population. The findings are expected to provide population-specific anatomical data, supporting improved safety and accuracy in thoracic pedicle screw placement.

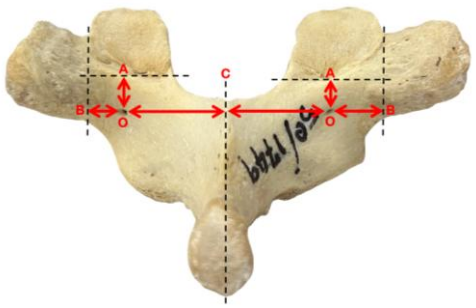

Fig. 1 Anatomical landmarks: distance from nutrient foramen to the inferior border of the superior articular facet (OA), distance from nutrient foramen to the lateral border of the laminae (OB), and distance from nutrient foramen to the midline of the spinous process (OC).

Materials and Methods

This anatomical study examined 600 dried upper thoracic vertebrae (T1-T6) obtained from 100 complete adult skeletons (50 males, 50 females) collected at the Unit of Human Bone Warehouse for Research (UHBWR), Department of Anatomy, Faculty of Medicine, Khon Kaen University. All specimens were from individuals aged 20 years or older at the time of death. Only well-preserved vertebrae without pathological deformities or damage were included in the study. The position of the nutrient foramen on the posterior lamina was measured bilaterally using a digital vernier caliper with an accuracy of 0.01 mm. All measurements were performed independently by two observers, and the mean value was used for analysis. When more than one nutrient foramen was present on a single lamina, all foramina were identified. The foramen selected for measurement was the one that showed the most symmetrical position relative to the corresponding foramen on the contralateral side, to allow consistent bilateral comparison. The mean value of the three measurements was used for analysis. The following parameters were measured relative to three anatomical landmarks, including distance from nutrient foramen to the inferior border of the superior articular facet (OA), distance from nutrient foramen to the lateral border of the laminae (OB), and distance from nutrient foramen to the midline of the spinous process (OC) (Fig. 1). Statistical analysis was performed using SPSS software. The following analyses were performed: descriptive statistics (mean, standard deviation, and range) for all measurements; an independent t-test for comparisons between male and female specimens; a paired t-test for bilateral comparisons between the left and right sides; and an ANOVA for assessment of inter-level variations (T1–T6). The level of statistical significance was set at $P < 0.05$.

Results

The analysis of 600 dry upper thoracic vertebrae (T1-T6) identified distinct patterns in nutrient foramen distribution by vertebral level and gender. The highest incidence was at T1 (84.5%), followed by T2 (72.0%) and T3 (53.5%), while the lowest was observed at T6 (41.0%). The data of gender-specific analysis showed a higher incidence of nutrient foramina in males across most vertebral

Table 1 Incidence and distribution of nutrient foramen on the posterior thoracic laminae (T1-T6): a gender-specific bilateral analysis

T level	Male (N=50)		Female (N=50)		Total (%)
	Left (%)	Right (%)	Left (%)	Right (%)	
T1	92.0 (46/50)	90.0 (45/50)	74.0 (37/50)	82.0 (41/50)	84.5 (169/200)
T2	84.0 (42/50)	78.0 (39/50)	58.0 (29/50)	68.0 (34/50)	72.0 (144/200)
T3	64.0 (32/50)	52.0 (26/50)	50.0 (25/50)	48.0 (24/50)	53.5 (107/200)
T4	48.0 (24/50)	48.0 (24/50)	44.0 (22/50)	40.0 (20/50)	45.0 (90/200)
T5	56.0 (28/50)	52.0 (26/50)	50.0 (25/50)	54.0 (27/50)	53.0 (106/200)
T6	38.0 (19/50)	56.0 (28/50)	32.0 (16/50)	38.0 (19/50)	41.0 (82/200)

levels, with the largest disparity at T1 (92.0% left, 90.0% right in males vs. 74.0% left, 82.0% right in females). A similar trend was observed at T2.

Furthermore, the bilateral distribution analysis revealed general symmetry in males, except at T6 (38.0% left, 56.0% right), while females showed symmetry at all upper thoracic vertebrae (T1-T6), as shown in Table 1.

These results suggest that the nutrient foramen may serve as a useful anatomical landmark for identifying the pedicle screw entry point when present. Nevertheless, at levels with a low incidence or absence of the nutrient foramen—findings that may normally occur among individuals—reliance on additional anatomical landmarks may be necessary for accurate determination of the thoracic pedicle screw entry point.

Statistical analysis revealed significant correlations and differences in upper thoracic vertebrae measurements, with varying degrees of bilateral symmetry across vertebral levels and gender. In males, T4 displayed the highest level of bilateral symmetry, with a correlation of $r = 0.76$ between the left (LA) and right (RA) sides. In contrast, T5 showed significant paired differences in the left (LB) and right (RB) sides, resulting in a correlation of $r = -0.04$. In females, different patterns were displayed. The strongest correlations were observed at T3 and T6, with values of $r=0.82$ and $r=0.77$, respectively. Similar to the males, T6 also exhibited notable paired differences in LB and RB, resulting in a correlation of $r = -0.16$. Overall, the upper thoracic vertebrae (T1-T6) demonstrated significant asymmetry at T3, with a left-right comparison yielding $p < 0.01$. T4 and T5 showed the strongest correlations, as detailed in Table 2.

The findings emphasize significant anatomical differences and bilateral correlations in the position of the nutrient foramen, which may have important implications for thoracic pedicle screw placement and planning of surgical techniques. The observed sex-specific and level-specific patterns provide valuable reference data for improving the accuracy and safety of thoracic pedicle screw placement in the northeastern Thai population.

Morphometric analysis demonstrated significant sex-related differences in nutrient foramen positions across the thoracic vertebrae, most prominently in the upper thoracic levels (T1–T4). For LA measurements, males exhibited significantly greater values, particularly at T1, T3, and T4 ($p < 0.01$). RA measurements also showed significant sex differences at T1 ($p < 0.01$), T3 ($p=0.01$), and T5 ($p = 0.01$). Similarly, LB values were consistently larger in males, with statistically significant differences observed at T1 and T2 ($p < 0.01$) and at T3 ($p=0.01$). RB measurements demonstrated significant differences at T1 ($p < 0.01$) and T3 ($p = 0.01$). RC measurements exhibited the greatest absolute values among all parameters and showed significant sex differences at T1 and T4 ($p < 0.01$), as shown in Table 3.

These results prove that a consistent pattern was observed across all parameters, demonstrating greater distances in males compared with females, with the most pronounced differences in the upper thoracic levels (T1–T4). All parameters showed statistically significant inter-level variation ($p < 0.01$) in both sexes, indicating region-specific distribution patterns of the nutrient foramen along the upper thoracic vertebrae.

Discussion

This study provides comprehensive morphometric data on nutrient foramen distribution in upper thoracic vertebrae of the Northeast Thai population. Our findings reveal the highest incidence of nutrient foramen at T1 (84.5%), consistent with previous Asian population studies [9,10].

Significant gender dimorphism was observed, particularly in the upper thoracic region (T1-T4). Male specimens showed consistently larger measurements, most notably at T1 (LA: 6.05±1.57 mm vs 5.00±1.26 mm, $p=0.001$) [11]. The precise mapping of nutrient foramen positions provides reliable landmarks for surgical navigation, with consistent bilateral symmetry observed in most levels except T6 [12].

Regional variations revealed unique characteristics in the Northeast Thai population compared to other Asian populations. Mean LA distances at T1 were smaller than those reported in Korean (male: 6.89±1.62 mm, female: 5.85±1.33 mm) and Chinese populations (male: 6.72±1.58 mm, female: 5.67±1.29 mm) [13,14]. These population-specific variations emphasize the importance of regional anatomical data for surgical planning [15].

Bilateral analysis showed asymmetrical patterns, particularly at T6 in males (left: 38.0%, right: 56.0%). Strong correlations were observed in the upper thoracic region, with the highest correlation at T4 between LA & RA ($r=0.761$) in males and T3 and T6 ($r=0.824$, $r=0.772$) in females [16].

In some vertebrae, more than one nutrient foramen may be present on the lamina. In the present study, when multiple foramina were identified, the foramen selected for measurement was the one that most closely corresponded in

position to the nutrient foramen on the contralateral side to allow symmetrical bilateral comparison. Nevertheless, smaller accessory foramina may also occur and should be recognized during anatomical evaluation or surgical procedures.

Clinical recommendations include utilizing consistent nutrient foramen patterns in T1-T4 as surgical landmarks and considering gender-specific approaches in surgical planning [17]. The comprehensive analysis contributes new insights into thoracic vertebral anatomy specific to the Thai population, supporting the trend toward precision spine surgery [18].

Conclusion

This study concludes that the nutrient foramen can serve as an anatomical landmark for determining the entry point in upper thoracic pedicle screw placement when the nutrient foramen is identifiable. However, its application should be considered in relation to the vertebral level, patient sex, and the possibility of absence of the nutrient foramen. In cases where the nutrient foramen cannot be identified, additional anatomical landmarks are required. In the present study, data from three anatomical reference points were collected to provide alternative guidance for determining the pedicle screw entry point.

The findings of this study provide fundamental anatomical data for surgeons and population-specific information regarding the position of the nutrient foramen in the Northeastern Thai population, which may contribute to improved accuracy and safety in thoracic pedicle screw placement in the future.

Acknowledgements

The authors would like to express their sincere gratitude to the Unit of Human Bone Warehouse for Research (UHBWR), Department of Anatomy, Faculty of Medicine, Khon Kaen University, for their support and for allowing the collection of skeletal data, which was essential to the success of this study.

Ethics Statement

Ethical approval for this study was granted by the Center for Ethics in Human Research, Khon Kaen University (Approval No. HE651220).

References

1. Suk SI, Lee CK, Kim WJ, Chung YJ, Park YB. Segmental pedicle screw fixation in the treatment of thoracic idiopathic scoliosis. Spine. 1995;20(12):1399-405.
2. Gelalis ID, Paschos NK, Pakos EE, Politis AN, Arnaoutoglou CM, Karageorgos AC, et al. Accuracy of pedicle screw placement: a systematic review of prospective in vivo studies comparing free hand, fluoroscopy guidance and navigation techniques. Eur Spine J. 2012;21(2): 247-55.
3. Kim YJ, Lenke LG, Kim J, Bridwell KH, Cho SK, Cheh G, et al. The morbidity of pedicle screw fixation in adolescent idiopathic scoliosis. Spine. 2007;32(12):1395-1400.
4. Vaccaro AR, Rizzolo SJ, Balderston RA, Allardyce TJ, Garfin SR, Dolinskas C, et al. Placement of pedicle screws in the thoracic spine. Part I: Morphometric analysis of the thoracic vertebrae. J Bone Joint Surg Am. 1995; 77(8):1193-1199.
5. Oshina M, Okuda S, Miyauchi A, Haku T, Yamashita T, Iwasaki M, Oda T. Nutrient foramina of the cervical and thoracic spine: Anatomical study as a guide for pedicle screw insertion. BMC Musculoskelet Disord. 2018; 19:312. doi:10.1186/s12891-018-2218-0.
6. Masharawi Y, Rothschild B, Dar G, Peleg S, Robinson D, Been E, et al. Facet orientation in the thoracolumbar spine: three-dimensional anatomic and biomechanical analysis. Spine. 2004;29(16):1755-63.
7. Scoles PV, Linton AE, Latimer B, Levy ME, Digiovanni BF. Vertebral body and posterior element morphology: the normal spine in middle life. Spine. 1988;13(10):1082-6.
8. Karabekir HS, Yildizhan A, Atar EK, Aydin ME. Morphometric analysis of the thoracic vertebrae: a cadaveric study. Eur Spine J. 2011; 20(6):948-53.
9. Murlimanju BV, Prabhu LV, Pai MM, Rai R, Dhananjaya KVN. Morphological and topographical anatomy of nutrient foramina in human thoracic vertebrae. Romanian Journal of Morphology and Embryology. 2011;52(3):859-862.
10. Gupta C, D'souza AS, Raythe B. A morphometric study of nutrient foramina in human thoracic vertebrae. Sultan Qaboos Univ Med J. 2013;13(1): e77-e82.
11. Bastir M, García-Martínez D, Torres-Tamayo N, Palancar CA, Pina M, Riesco-López A. Intraspecific variation and sexual dimorphism in the human thoracic vertebrae. Am J Phys Anthropol. 2014;155(4):513-521.
12. Oshina M, Okuda S, Miyauchi A, Haku T, Yamashita T, Iwasaki M, Oda T. Nutrient foramina of the cervical and thoracic spine: Anatomical study as a guide for pedicle screw

insertion. BMC Musculoskelet Disord. 2018; 19:312. doi:10.1186/s12891-018-2218-0
13. Choi JH, Kim JH, Kim SH, Lee WS. Morphometric analysis of thoracic pedicles in the Korean population. Asian Spine J. 2009; 3(1):1-6.
14. Liu Y, Zhu F, Xu L, Qiu Y. Thoracic pedicle morphometry in a Chinese population: A CT-based study. Eur Spine J. 2010;19(8):1391-1397.
15. Zhuang Z, Zhou Y, Xu H, Wang K, Liu J. Evaluation of thoracic pedicle morphometry in a Chinese population using three-dimensional computed tomography. Eur Spine J. 2012;21(1): 125-130. doi:10.1007/s00586-011-1931-0.
16. Parent S, Labelle H, Skalli W, de Guise JA. Morphometric analysis of anatomic landmarks for pedicle screw placement. Spine. 2004;29(6): E123-E128.
17. Hirano T, Hasegawa K, Takahashi HE, Uchiyama S, Hara T, Washio T, et al. Structural characteristics of thoracic pedicles in the Japanese population. Spine. 1997;22(6):650-655.
18. Hicks JM, Singla A, Shen FH, Arlet V. Complications of pedicle screw fixation in scoliosis surgery: A systematic review. Spine. 2010;35(11): E465-E470.

Table 2 Bilateral correlation analysis and paired differences of nutrient foramina measurements in upper thoracic vertebrae

	Male (N=50)				Female (N=50)				Overall (N=100)			
	Correlation (r)	Mean	SD	P-value	Correlation (r)	Mean	SD	P-value	Correlation (r)	Mean	SD	P-value
T1												
LA & RA	0.16	-0.16	2.09	0.62	0.53	0.13	1.21	0.53	0.39	-0.03	1.75	0.88
LB & RB	0.14	-0.09	1.96	0.77	0.55	0.25	1.21	0.22	0.47	0.06	1.67	0.73
LC & RC	0.44	0.11	1.68	0.66	0.35	-0.49	1.72	0.10	0.50	-0.15	1.72	0.43
T2												
LA & RA	0.37	-0.59	1.81	0.07	0.39	0.07	1.49	0.82	0.39	-0.30	1.69	0.18
LB & RB	0.41	0.14	1.42	0.59	0.66	-0.22	1.14	0.35	0.56	-0.02	1.31	0.91
LC & RC	0.55	-0.24	1.37	0.32	0.61	-0.04	1.43	0.88	0.62	-0.16	1.39	0.40
T3												
LA & RA	0.27	0.21	2.36	0.70	0.82	0.10	1.22	0.76	0.58	0.16	1.93	0.62
LB & RB	0.07	0.19	1.55	0.58	0.25	0.68	1.14	0.04	0.21	0.40	1.39	0.10
LC & RC	0.40	-0.61	1.45	0.07	0.54	-0.66	1.10	0.04	0.47	-0.63	1.29	0.01
T4												
LA & RA	0.76	-0.03	1.67	0.95	0.60	-0.59	2.25	0.38	0.68	-0.29	1.94	0.46
LB & RB	0.38	0.32	1.00	0.25	0.42	-0.20	1.22	0.58	0.36	0.08	1.12	0.72
LC & RC	0.67	-0.19	1.23	0.58	0.50	-0.17	2.01	0.78	0.62	-0.18	1.60	0.57
T5												
LA & RA	0.70	0.14	1.97	0.76	0.74	0.29	1.51	0.49	0.75	0.20	1.76	0.51
LB & RB	-0.04	-0.17	1.32	0.58	0.64	-0.33	0.74	0.12	0.29	-0.24	1.10	0.22
LC & RC	0.45	-0.14	1.73	0.73	0.82	-0.02	1.30	0.95	0.67	-0.09	1.54	0.74
T6												
LA & RA	0.56	1.27	3.08	0.18	0.77	-0.50	1.82	0.43	0.60	0.51	2.71	0.40
LB & RB	0.26	-0.34	1.34	0.40	-0.16	-0.70	1.84	0.29	0.18	-0.49	1.54	0.16
LC & RC	0.73	0.36	1.72	0.48	0.47	-0.46	1.48	0.38	0.66	0.01	1.63	0.98

r: Paired Sample Correlation, LA: Distance from nutrient foramen to the inferior border of the superior articular facet on the left side., RA: Distance from nutrient foramen to the inferior border of the superior articular facet on the right side., LB: Distance from nutrient foramen to the lateral border of the laminae on the left side., RB: Distance from nutrient foramen to the lateral border of the laminae on the right side., LC: Distance from nutrient foramen to the midline of the spinous process on the left side., RC: Distance from nutrient foramen to the midline of the spinous process on the right side.

Table 3 Comparative analysis of bilateral nutrient foramina measurements in male and female upper thoracic vertebrae: mean values and standard deviations

Parameter	T Level	Male		Female		P-value
		Mean	SD	Mean	SD	
LA	T1	6.05	1.57	5.00	1.26	0.00
	T2	7.93	1.60	7.29	1.21	0.08
	T3	9.00	2.09	7.41	1.87	0.00
	T4	10.41	1.67	8.47	2.12	0.00
	T5	10.70	2.28	9.77	1.84	0.11
	T6	11.16	2.74	9.39	2.35	0.05
	P-value	< 0.01*		< 0.01*		
LB	T1	5.81	1.55	4.37	1.11	0.00
	T2	4.12	1.30	3.01	1.30	0.00
	T3	3.54	1.14	2.84	0.86	0.01
	T4	3.32	1.05	2.87	0.86	0.11
	T5	3.02	0.95	2.57	0.94	0.08
	T6	3.98	2.48	2.49	0.91	0.03
	P-value	< 0.01*		< 0.01*		
LC	T1	16.34	1.68	14.64	1.40	0.00
	T2	14.29	1.45	13.51	1.52	0.03
	T3	12.78	1.44	11.98	1.25	0.03
	T4	12.96	1.13	11.77	1.47	0.00
	T5	12.90	1.52	12.41	1.70	0.27
	T6	12.83	2.37	11.98	1.49	0.22
	P-value	< 0.01*		< 0.01*		

Parameter	T Level	Male		Female		P-value
		Mean	SD	Mean	SD	
RA	T1	6.18	1.21	4.88	1.21	0.00
	T2	8.00	1.65	7.46	1.73	0.18
	T3	8.91	2.05	7.28	2.15	0.01
	T4	9.63	2.42	8.64	2.19	0.18
	T5	11.00	2.54	9.12	2.23	0.01
	T6	10.51	2.95	10.19	1.77	0.68
	P-value	< 0.01*		< 0.01*		
RB	T1	5.98	1.43	4.22	1.32	0.00
	T2	3.88	1.3	3.27	1.34	0.53
	T3	3.14	1.11	2.36	0.84	0.01
	T4	2.78	0.75	2.71	1.22	0.83
	T5	3.12	0.82	2.61	0.90	0.04
	T6	3.62	1.23	3.17	1.15	0.21
	P-value	< 0.01*		< 0.01*		
RC	T1	16.32	1.52	15.19	1.52	0.00
	T2	14.63	1.29	13.5	1.58	0.00
	T3	13.33	1.44	12.39	1.65	0.04
	T4	13.18	1.56	12.15	1.95	0.06
	T5	13.18	1.76	12.00	1.81	0.02
	T6	12.52	1.80	12.10	1.56	0.41
	P-value	< 0.01*		< 0.01*		

*significant differences between Thoracic level in each parameter (one-way ANOVA, $p < 0.05$)

P-26

Anatomical Study of the Nerve Supply of the Carotid Body in Thai Cadaver by Dissection

Ploypatcha Ngamasawadechakul[1], Benjaporn Pamornpol[1], Anuch Durongphan[1*]
[1] Department of Anatomy, Faculty of Medicine Siriraj Hospital, Mahidol University, Bangkok, 10700, Thailand
*Corresponding author, e-mail: anuch.dur@mahidol. ac.th

Abstract

The human carotid body is a small peripheral chemoreceptor located at the carotid bifurcation. It detects changes in arterial oxygen, carbon dioxide, and pH and relays this information to the central nervous system to help maintain homeostasis. This study investigated the gross anatomical nerve supply of the human carotid body in Thai cadavers. Fifty-four cadavers, including 42 embalmed cadavers and 12 soft cadavers, were examined by dissection. Nerve branches entering the carotid body were identified, traced proximally to their origins, and counted. The main nerve supply arose from the carotid sinus branches of the glossopharyngeal nerve and the superior laryngeal branches of the vagus nerve. The median number of carotid sinus branches was 3, with an interquartile range of 2 to 4. The median number of superior laryngeal branches, pharyngeal branches, and sympathetic branches was 2, with an interquartile range of 0 to 3. The carotid sinus branches and superior laryngeal branches each gave rise to as many as 6 branches, whereas the pharyngeal and sympathetic branches contributed as many as 5. Communicating branches to the carotid sinus branches were also identified from the superior laryngeal, pharyngeal, and sympathetic branches. No statistically significant side-to-side differences were observed. The human carotid body receives complex and variable neural innervation, with the carotid sinus and superior laryngeal branches as the principal contributors.

Keywords *Human carotid body, Carotid sinus branches, Superior laryngeal branches, Pharyngeal branches, Sympathetic branches*

Background

The human carotid body (CB) is a small structure located at the carotid bifurcation (1). It has a complex innervation that includes the carotid sinus branches (CSN) of the glossopharyngeal nerve (CN IX), the superior laryngeal (SLN) and pharyngeal (PN) branches of the vagus nerve (CN X), and sympathetic (Sym) fibers (1-3). The CB functions primarily as a peripheral chemoreceptor, maintaining arterial homeostasis by detecting changes in arterial oxygen (O_2), carbon dioxide (CO_2), and pH, thereby helping to prevent hypoxemia (4,5). These chemical signals are transmitted to the central nervous system through sensory nerve fibers, which in turn promote activation of the sympathetic nervous system (6).

Previous microdissection studies have shown that the neural connections of the CB are complex. Monfared et al. reported contributions from the SLN and the superior cervical ganglion (7). Schulz et al. described nerve branches associated with the CSN, including contributions from CN IX, CN X, Sym fibers, and the hypoglossal nerve (8). Tubbs et al. reported CSN contributions from the pharyngeal branches of CN IX and Sym fibers (9). Toorop et al. also identified branches of CN IX and Sym fibers as contributors to the CSN (3).

However, gross anatomical dissection studies examining the number of nerve branches supplying the CB remain scarce. Further anatomical investigation is therefore needed to clarify the number of nerves supplying the CB.

Materials and Methods

Cadaveric specimen

Fifty-four subjects (42 embalmed cadavers and 12 soft cadavers) were collected from the Department of Anatomy, Faculty of Medicine Siriraj Hospital, Mahidol University. These cadavers were recruited for this study with approval of the Committee of Siriraj Institutional Review Board, Faculty of Medicine Siriraj Hospital, Mahidol University (SIRB No 652/2567).

Sample collection

Inclusion criteria comprised Thai embalmed and soft cadavers obtained from the Faculty of Medicine Siriraj Hospital, Mahidol University, with an intact CB and preserved surrounding nerve endings. Cadavers were excluded if there was history or evidence of neck surgery, or any injury involving the CB, internal carotid artery, or external carotid artery that could compromise the integrity of the CB and its nerve endings.

The human cadaveric dissection

Cadavers were positioned supine with the neck extended. The CN IX, CN X, common carotid artery, internal carotid artery, external carotid artery, and CB were exposed by removing overlying connective tissue and fat. After the CB was identified, all nerve fibers terminating within the CB were identified and traced proximally to their parent nerves. Then record the number of nerve supply, nerve branches, and their communication on the case record form.

For this study, the CSN was operationally defined as the branch arising from CN IX that coursed to the carotid bifurcation and entered the CB. The CSN was followed proximally as it ascended along the medial aspect of the ICA to join the main trunk of CN IX inferior to the jugular foramen. The CN IX was defined as the main glossopharyngeal trunk receiving the CSN below the jugular foramen (Fig. 1).

The SLN was operationally defined as the branch arising from CN X at the level of the inferior vagal ganglion that coursed toward the carotid bifurcation and contributed fibers to the CB. The SLN fibers were traced proximally to their origin from the CN X at the lower portion of the inferior vagal ganglion.

The PN were defined as vagal branches arising from the upper portion of the inferior vagal ganglion and coursing to the pharynx, including any branches that provided communicating fibers to the CSN.

The Sym contributions were defined as nerve branches entering the CB from the posterior aspect of the carotid bifurcation and were traced proximally to the superior cervical ganglion, running deep to the CN X.

Statistical analysis

Normality was assessed using the Shapiro-Wilk test. The number of nerves supplying the human carotid body was summarized as the median with interquartile range (IQR). Comparisons between the right and left sides were performed using the Wilcoxon signed-rank test. A *p-value* < 0.05 was considered statistically significant. All analyses were conducted using IBM SPSS Statistics, version 30.

Results and Discussion

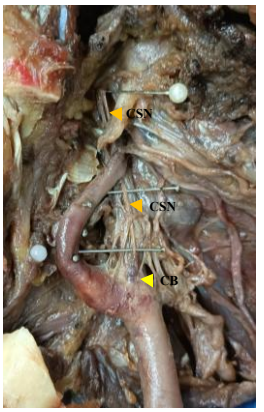

Fig. 1 The carotid sinus branch of the glossopharyngeal nerve supplies the carotid body. CB: Carotid body, CSN: Carotid sinus branches.

Baseline characteristics are presented in Table 1, with no statistically significant difference in gender between types of cadavers. The mean ± SD of age (years) was 71.50±12.99 and ranged from 51-91 in soft cadavers, while in embalmed cadavers it was 77.62±11.83 and ranged from 50-97, with no statistically significant difference between the two types of cadavers.

Table 1 Demographic characteristics of cadavers

Baseline	Soft cadavers (n=12)	Embalmed cadavers (n=42)	*p-value*
Gender, n (%)			0.73
Male	9 (75%)	27 (64.3%)	
Female	3 (25%)	15 (35.7%)	
Age (years), Mean ± SD (min-max)	71.50±12.99 (51-91)	77.62±11.83 (50-97)	0.16

The number of nerve supply of the human carotid body

The number of nerves supplying human CB is presented in Table 2. The IQR number of CSN branches was 3 (2-4), whereas that of the SLN, PN, and Sym branches was 2 (0-3).

Comparisons between cadaveric types are presented; the CSN and the IQR numbers were 3 (2–

4) on both types. For SLN, it was 2 (0.25–3) on soft cadavers and 2 (0-3) on embalmed cadavers. For PN, the values were 2 (0–2.75) on soft cadavers and 2 (0–3) on embalmed cadavers. For Sym, the values were 2 (0.25–2.75) on soft cadavers and 2 (0–3) on embalmed cadavers. No statistically significant differences between types were observed.

Side-to-side comparisons are presented in Table 3. For CSN, the IQR number was 3 (2–4) on both sides. For SLN, it was 2 (0–3) bilaterally. For PN, the values were 1.5 (0–2.25) on the right and 2 (0–3) on the left. For Sym, the values were 2(0–3) on the right and 1 (0–2) on the left. No statistically significant side-to-side differences were observed.

Table 2 The number of nerves supplied to the human carotid body

	Cadavers (n=54)			
Number of nerve supply	**Mean±SD**	**min, max**	**Median**	**Q1-Q3**
CSN	2.82±1.79	0-6	3.00	2.00-4.00
SLN	1.96±1.72	0-6	2.00	0.00-3.00
PN	1.58±1.44	0-5	2.00	0.00-3.00
Sym	1.57±1.45	0-5	2.00	0.00-3.00
CSN anast. PN	0.36±0.73	0-3	0.00	0.00-0.00
CSN anast. SLN	0.21±0.61	0-3	0.00	0.00-0.00
CSN anast. Sym	0.48±0.88	0-3	0.00	0.00-1.00

CSN: Carotid sinus branches, PN: Pharyngeal branches, SLN: Superior laryngeal branches, Sym: Sympathetic branches, anast.: anastomosis

Discussion

Previous studies have investigated the microdissection of the nerve supply to the CB, but the number of contributing nerve branches has not been reported. These studies suggest that the innervation of the CB is complex and may involve CN IX, CN X, Sym fibers, and the hypoglossal nerve (7,8). They also described contributions to the CB through nerve branches associated with the CSN, including the SLN and PN of CN X, as well as Sym fibers (3,9). In the present study, the principal nerve supply to the CB arose from the CSN and SLN, with median numbers of 3 and 2 branches, respectively, on both sides. The PN and Sym fibers provided additional contributions, with median numbers of 1.5 and 2 branches on the right. Consistent with previous reports, branches associated with the CSN, including the SLN and PN of CN X and Sym fibers, were observed to contribute to the CB. These findings may improve understanding of the functional relationship between the CB and its nerve supply. Additionally, this information may be relevant for surgical procedures involving the carotid bifurcation and help reduce the risk of nerve injury during surgery. Further studies with larger sample sizes are essential to confirm the reproducibility of these findings. Moreover, the use of different cadaver preservation methods may help clarify the influence of various factors on anatomical observations.

Conclusion

In conclusion, this study showed that the human CB receives a complex and variable nerve supply. The primary contributions arose from the CSN and SLN, whereas the PN and Sym fibers provided secondary input.

Acknowledgements

The authors would like to thank you for the invaluable support from the Department of Anatomy, Faculty of Medicine Siriraj Hospital, Mahidol University.

Table 3. A comparison of the number of nerves supplying the human carotid body between sides in cadaveric specimens

	Right				Left				
Number of nerve supply	**Mean±SD**	**min, max**	**Median**	**Q1-Q3**	**Mean±SD**	**min, max**	**Median**	**(Q1-Q3)**	***p*-value**
CSN	2.83±1.91	0-6	3.00	2.00-4.00	2.81±1.68	0-6	3.00	2.00-4.00	0.97
SLN	1.93±1.75	0-6	2.00	0.00-3.00	2.00±1.70	0-5	2.00	0.00-3.00	0.69
PN	1.56±1.53	0-5	1.50	0.00-2.25	1.61±1.37	0-4	2.00	0.00-3.00	0.75
Sym	1.72±1.50	0-5	2.00	0.00-3.00	1.43±1.41	0-5	1.00	0.00-2.00	0.30
CSN anast. PN	0.33±0.70	0-3	0.00	0.00-0.00	0.39±0.76	0-3	0.00	0.00-1.00	0.74
CSN anast. SLN	0.20±0.56	0-2	0.00	0.00-0.00	0.22±0.66	0-3	0.00	0.00-0.00	0.81
CSN anast. Sym	0.54±0.91	0-3	0.00	0.00-1.00	0.43±0.86	0-3	0.00	0.00-0.25	0.52

CSN: Carotid sinus branches, PN: Pharyngeal branches, SLN: Superior laryngeal branches, Sym: Sympathetic branches, anast.: anastomosis
$p < 0.05$ was considered statistically significant

References

1. Heath D, Smith P. Diseases of the human carotid body: Springer Science & Business Media; 2012.
2. Standring S. Gray's anatomy: the anatomical basis of clinical practice. 41st ed. Philadelphia: Elsevier Limited; 2016.
3. Toorop RJ, Scheltinga MR, Moll FL, Bleys RL. Anatomy of the carotid sinus nerve and surgical implications in carotid sinus syndrome. J Vasc Surg. 2009;50(1):177-82.
4. Iturriaga R, Alcayaga J, Chapleau MW, Somers VK. Carotid body chemoreceptors: physiology, pathology, and implications for health and disease. Physiol Rev. 2021;101(3):1177-235.
5. Badoer E. The Carotid Body a Common Denominator for Cardiovascular and Metabolic Dysfunction? Front Physiol. 2020;11:1069.
6. Gold OMS, Bardsley EN, Ponnampalam AP, Pauza AG, Paton JFR. Cellular basis of learning and memory in the carotid body. Front Synaptic Neurosci. 2022; 14: 902319.
7. Monfared A, Kim D, Jaikumar S, Gorti G, Kam A. Microsurgical anatomy of the superior and recurrent laryngeal nerves. Neurosurgery. 2001; 49(4): 925-32; discussion 32-3.
8. Schulz SA, Wöhler A, Beutner D, Angelov DN. Microsurgical anatomy of the human carotid body (glomus caroticum): Features of its detailed topography, syntopy and morphology. Ann Anat. 2016;204:106-13.
9. Tubbs RS, Rizk E, Loukas M, Barbaro N, Spinner R. Nerves and Nerve Injuries: Vol 1: History, Embryology, Anatomy, Imaging, and Diagnostics Hardcover – June 10.

P-27

Functional Surgical Space of the Renal Artery in Relation to Hilar Clamping Feasibility: A Preliminary Cadaveric Study

Chanoknan Pamorn[1], Tanathip Buadang[1], Pitcha Praprukdee[1], Pattarapon Suaygad[1], Panawich Jirachotthamrongkul[1], Supphawit Phanmekhakun[1], Sukrit Sangkhano[1,2*]
[1] Department of Occupational Health and Safety, School of Public Health, Walailak University, Thasala, Nakhon Si Thammarat, Thailand
[2] Pre-clinical Science Unit, School of Public Health, Walailak University, Thasala, Nakhon Si Thammarat, Thailand
*Corresponding author, e-mail: sukrit.sa@mail.wu.ac.th

Abstract
Background: Hilar clamping is a fundamental step in minimally invasive partial nephrectomy; however, the actual availability of clampable arterial space under operative conditions remains poorly characterized. **Objective:** This study introduces the concept of functional surgical space (FSS) to evaluate the anatomical feasibility of renal artery clamping. **Methods:** Twenty kidneys from ten cadavers were examined. The renal artery length was measured from the aortic origin to the first branching point. The functional surgical space of the renal artery (FSS-RA) was defined as the longest uninterrupted arterial segment visible from an anterior approach without venous retraction. Clamp feasibility was defined as FSS ≥15 mm. Kidneys were classified into three categories: Type I (main renal artery clampable), Type II (main artery not clampable but at least one segmental or accessory artery clampable), and Type III (no clampable arterial segment). **Results:** Type I anatomy was observed in 5 kidneys (25%). Type II configuration, indicating the potential for selective or accessory arterial clamping, was identified in 7 kidneys (35%). The remaining 8 kidneys (40%) demonstrated no clampable arterial segment under baseline exposure conditions (Type III). These findings suggest that although direct hilar clamping of the main renal artery is feasible in only a minority of kidneys, alternative selective clamping strategies may be anatomically possible in a substantial proportion of kidneys. **Conclusion:** FSS assessment provides a practical anatomical framework for evaluating the feasibility of renal artery clamping. This preliminary cadaveric study highlights the importance of considering spatial hilar anatomy when planning vascular control strategies.

Keywords *Renal artery, Functional surgical space, Hilar anatomy, Partial nephrectomy, Minimally invasive surgery*

P-28

Microvascular-Associated Histopathological Changes in the Parathyroid Gland of Streptozotocin-Induced Diabetic Rats

Sani Baimai[1*], Chanachai Lohasaptawee[2], Jirat Boonmameepool[3], Chutikan Kaensa[1], Onsri Boonraksornpitak[1]
[1] Department of Anatomy, Faculty of Medicine Siriraj Hospital, Mahidol University, Bangkok, Thailand
[2] Medical Student, Faculty of Medicine Siriraj Hospital, Mahidol University, Bangkok, Thailand
[3] Faculty of Allied Health Sciences, Burapha University, Chonburi, Thailand
*Corresponding author, e-mail: sanibaimai@gmail.com

Abstract
Background: Diabetes mellitus (DM) is associated with systemic microvascular dysfunction, leading to impaired tissue perfusion and progressive structural changes in multiple organs. The parathyroid gland, with its dense microvascular network, is particularly vulnerable to diabetic microangiopathy. Clinically, DM is linked to disturbances in calcium–phosphate metabolism and may alter parathyroid hormone (PTH) secretion, contributing to bone and mineral disorders. Pathophysiologically, microangiopathy may compromise parathyroid perfusion and cellular function; however, histopathological evidence supporting these changes remains limited. **Objective:** To qualitatively and semi-quantitatively evaluate microvascular-associated histopathological changes of the parathyroid gland in streptozotocin (STZ)-induced diabetic rats compared with non-diabetic controls. **Methods:** A comparative histopathological study was conducted using male Sprague–Dawley rats (n =24) divided into control and diabetic groups. DM was induced by intraperitoneal injection of STZ (60 mg/kg). Rats were sacrificed at 4 weeks (short-term) and 24 weeks (long-term) after induction. Parathyroid tissues were perfused with normal saline, fixed in Bouin's solution, embedded in paraffin, sectioned, and stained with hematoxylin and eosin. Slides were coded and examined under light microscopy. Five non-overlapping high-power fields per gland were evaluated using a semi-quantitative morphological scoring system (graded 0–3) assessing (1) capillary lumen integrity, (2) vascular wall thickness and distortion, and (3) extent of perivascular and stromal alterations. Scores from each parameter were summed up to generate a total histopathological score. All evaluations were performed independently by two blind anatomists. Statistical analysis was performed using non-parametric tests. Differences between groups were analyzed using the Mann–Whitney U test ($p < 0.05$). **Results:** The controls exhibited preserved cord-like architecture, uniformly patent capillaries, thin vascular walls, and compact stroma. Chief cells showed uniform cytoplasm and nuclei. In contrast, diabetic rats exhibited irregular, narrowed capillary lumens, thickened, distorted vascular walls, and perivascular stromal expansion. Stromal pallor and separation of parenchymal cords were frequently observed. Parenchymal cells exhibited cytoplasmic vacuolation, increased nuclear variability, and architectural disorganization. These alterations were more pronounced in long-term DM, as reflected in higher semi-quantitative morphological scores. No evidence of vascular thrombosis or necrosis was detected. **Conclusion:** DM induces duration-dependent microvascular-associated histopathological alterations in the parathyroid gland, accompanied by progressive parenchymal and stromal changes. These findings support the role of microvascular disruption in structural remodeling during diabetes.

Keywords *Diabetic angiopathies, Parathyroid glands, Microcirculation, Histopathology, Streptozotocin*

P-29

Histopathological Remodeling of the Upper Esophageal Epithelium and Skeletal Muscle in Long-Term Diabetic Rats: Implications for Dysphagia

Thidarat Bandhitjeen[1], Sani Baimai[1]*, Chutikan Kaensa[1], Siriyakorn Pramchai[1]
[1] Department of Anatomy, Faculty of Medicine Siriraj Hospital, Mahidol University, Bangkok, Thailand
*Corresponding author, e-mail: sanibaimai@gmail.com

Abstract

Diabetes mellitus (DM) is associated with gastrointestinal complications, including esophageal dysmotility and dysphagia. While most studies focus on distal esophageal abnormalities and reflux-related pathology, structural changes in the upper esophagus—predominantly composed of skeletal muscle and essential for swallowing initiation—remain poorly characterized. Chronic hyperglycemia may induce microvascular injury, inflammation, and neuromuscular remodeling, impairing esophageal function. This study aimed to investigate histopathological remodeling of the epithelial, inflammatory, and muscular components of the upper esophagus in a long-term streptozotocin (STZ)-induced DM rat model and its relevance to dysphagia. Twelve male rats were divided into DM and control groups (n = 6 each). After 24 weeks, upper esophageal specimens were paraffin-embedded, sectioned (5 serial sections, 6 μm), and stained with hematoxylin and eosin. Structural changes were evaluated using a semi-quantitative scoring system for epithelial (A1–A3), inflammatory (B1), and muscular (C1–C2) remodeling (score 0–3). Five non-overlapping representative fields per section were analyzed under light microscopy at ×100 (overall architecture) and ×400 (cellular detail), and mean scores were calculated. Trained anatomists independently assessed all slides in a blinded manner. DM rats demonstrated pronounced upper esophageal remodeling. Compared to controls, the epithelium showed severe architectural distortion with hyperkeratinization and focal disruption (A1, score 3), along with basal cell hyperplasia and uneven thickening (A2–A3, score 2). Moderate mononuclear inflammatory infiltration with stromal fibrosis was observed in the lamina propria and submucosa (B1, score 2). The muscular layer exhibited fiber size variability, moderate hypertrophy, increased inter-fiber spacing, and early disorganization (C1–C2, score 2). In conclusion, long-term DM induces epithelial, inflammatory, and neuromuscular remodeling in the upper esophagus, providing morphological evidence of impaired neuromuscular integrity and supporting a mechanistic basis for DM-related dysphagia.

Keywords *Diabetes mellitus, Esophagus, Dysphagia, Histology, Rats*

P-30

Early Jejunal Epithelial, Stromal, and Microvascular Remodeling with Goblet Cell Mucin Depletion in Short-Term Streptozotocin-Induced Diabetic Rats

Onsri Boonraksornpitak[1], Sani Baimai[1]*, Chutikan Kaensa[1], Passara Lanlua[1], Ratchanok Kraiwong[2], Jirat Boonmameepool[3], Thanapat Pochanasomboon[1]
[1] Department of Anatomy, Faculty of Medicine Siriraj Hospital, Mahidol University, Bangkok, Thailand
[2] Faculty of Physical Therapy, Mahidol University, Bangkok, Thailand
[3] Faculty of Allied Health Sciences, Burapha University, Chonburi, Thailand
*Corresponding author, e-mail: sanibaimai@gmail.com

Abstract

Diabetes mellitus (DM) is a chronic metabolic disorder associated with multiple systemic complications; however, gastrointestinal involvement, particularly diabetic enteropathy, remains insufficiently characterized. The jejunum is a key site of nutrient absorption and mucosal defense and is especially vulnerable to diabetic injury. This study aimed to quantitatively evaluate epithelial, stromal, and microvascular alterations in the jejunal mucosa of streptozotocin-induced diabetic rats. Twenty-four male Sprague-Dawley rats were divided into control and DM groups, and jejunal tissues were examined after 4 weeks using hematoxylin and eosin (H&E), periodic acid–Schiff (PAS), Masson's trichrome, and toluidine blue staining. Morphometric analyses revealed that DM rats exhibited distorted villi, epithelial disruption, mild inflammatory infiltration, and increased intraluminal cellular debris, accompanied by significant increases in total wall thickness, mucosal thickness, villus height, and crypt depth. PAS staining demonstrated a marked reduction in goblet cell mucin area fraction, indicating impaired mucosal protection and increased epithelial cell loss. Toluidine blue staining revealed abnormal Paneth cell morphology with increased accumulation of secretory granules, suggesting altered secretory activity and functional differentiation. In addition, Masson's trichrome staining showed increased collagen accumulation in the lamina propria and narrowing of mucosal capillary lumens, reflecting early microangiopathic and fibrotic remodeling under diabetic conditions. Collectively, these findings demonstrate that short-term diabetes induces significant structural and cellular alterations in the jejunum, leading to disrupted epithelial homeostasis, compromised mucosal barrier integrity, and progressive stromal remodeling, which may contribute to the development of diabetic enteropathy.

Keywords *Diabetes mellitus, Streptozotocin, Jejunum, Goblet cell, Histopathology*

Background

Diabetes mellitus (DM) is a chronic metabolic disorder characterized by persistent hyperglycemia resulting from either insulin deficiency or insulin resistance (1) .Globally, approximately 589 million adults aged 20-70 years were affected by DM in 2024, and this number is projected to rise to 853 million by 2050 (2) .While the vascular, renal, and neural complications of diabetes have been extensively investigated, gastrointestinal (GI) involvement, particularly diabetic enteropathy (DE), has received comparatively less attention, despite being a common and devasting conditions (1, 3-5). The jejunum, a primary site of nutrient absorption, is particularly vulnerable to diabetic injury. Jejunal damage contributes to bacterial overgrowth, mucosal inflammation, and impaired absorption, leading to maldigestion and malnutrition, which together reduce patients' quality of life (6-9). The epithelial lining primarily consists of enterocytes, goblet cells, Paneth cells, and enteroendocrine cells, each performing specialized yet interdependent roles in enzymatic digestion, mucosal protection, innate defense, and hormonal regulation, respectively (10-12). The lamina propria of the jejunum contains fibroblasts, fenestrated capillaries, central lacteals, and diverse immune cells that support nutrient absorption and mucosal defense (12).

Despite increasing recognition of diabetic enteropathy, the quantitative relationships between jejunal histopathological changes, epithelial secretory dysfunction, and lamina propria remodeling remain poorly defined. Previous studies have demonstrated that diabetes induces significant jejunal morphophysiological alterations, including increased villus height and crypt depth, which reflect a compensatory response to chronic hyperglycemia (14). Evidence suggests that diabetes triggers the up-regulation of advanced glycation end-products (AGEs) and their receptors (RAGE) throughout the small intestine, leading to structural remodeling and tissue injury (9). Moreover, integrated quantitative evidence linking epithelial secretory dysfunction with stromal and microvascular remodeling in early-stage diabetes remains limited. Therefore, this study aimed to provide a comprehensive histopathological and morphometric analysis of these alterations in the jejunum of short-term streptozotocin-induced diabetic rats, with an integrated analysis of epithelial and structural changes. The findings provide insight into the histopathology of diabetic enteropathy and may inform strategies to prevent gastrointestinal complications in diabetes patients.

Materials and Methods

Twenty-four male Sprague-Dawley rats aged 5–8 weeks (weighing 200-270 g) were randomly assigned to the control (n=12) and diabetes (DM; n=12) groups using a computer-generated randomization sequence and maintained for 4 weeks. Diabetes was induced by a single intraperitoneal injection of streptozotocin (60 mg/kg) dissolved in 0.1 Molar of citrate buffer, while control rats received the same concentration and volume of citrate buffer alone. Rats with fasting blood glucose levels exceeding 300 mg/dL at 72 hours post-injection were confirmed as diabetic. All animals were sacrificed 4 weeks after induction.

At the end of the experimental period, animals were deeply anesthetized by halothane inhalation and perfused with 0.9% sodium chloride (NaCl), followed by 0.1 M phosphate buffer solution (PBS). Jejunal tissues were then fixed in Bouin's solution for routine histological and morphometric analyses. Selected samples were fixed in 2.5% glutaraldehyde for high-resolution cellular evaluation. The small intestine was subsequently excised and measured. The jejunum was defined as the segment beginning distal to the first 12 cm from the pylorus, corresponding to the duodenojejunal flexure. A 15-cm mid-jejunal portion was initially identified, from which a 0.5-cm segment was collected at the same anatomical level (exactly 15 cm distal to the gastroduodenal junction) in all rats to ensure consistency. For histological analysis, three representative sections were selected from each tissue sample with a section interval of 30 µm to ensure that distinct villi and crypts were measured. This standardized section interval was employed as a reproducible technique to minimize measurement bias and support the validity of the morphometric data. Tissue samples approximately 0.5 cm in length were fixed in fixatives for at least 24 hours before histological and morphometric processing.

Paraffin-embedded tissue sections were stained with Hematoxylin and Eosin (H&E) for general histological evaluation, Periodic Acid–Schiff (PAS) stain to identify mucin granules in goblet cells, Masson's trichrome stain to visualize collagen fibers within the mucosal layer, and toluidine blue to assess Paneth cell secretory granules. Digital images were acquired using a light microscope equipped with a digital imaging system (Olympus Optical Co., Ltd., Tokyo, Japan). Quantitative measurements were performed using ImageJ software (National Institutes of Health, USA).

Measurements were conducted on multiple non-overlapping fields per section, with at least three sections analyzed per animal. Morphometric parameters included total wall thickness (measured from the villus tip to the outer border of the serosa), mucosal thickness (measured from the villus tip to the muscularis mucosae), villus height (measured from the villus tip to the villus-crypt junction), and crypt depth (measured from the villus-crypt junction to the crypt floor). Only well-oriented, longitudinal-sectioned villi and crypts were included in villus height and crypt depth measurement. Capillary profiles were considered circular when the ratio of maximum to minimum luminal diameter was less than 1.5, and the mean minimal luminal diameter was calculated for both groups.

Goblet cell mucin content was quantified as a percentage area fraction on PAS-stained sections. Paneth cell secretory granules were quantified at the crypt base on toluidine blue-stained sections, while collagen deposition was quantified as the lamina propria area fraction on Masson's trichrome-stained sections using gland-based delineation. All parameters were analyzed using region-of-interest (ROI)-based area fraction analysis with identical threshold settings across all samples. All measurements were performed blindly to minimize assessment bias.

Quantitative data were expressed as mean ± standard deviation (SD). The sample size was determined based on previous studies (4, 8) demonstrating sufficient power in morphometric

analyses in diabetic rat models with similar experimental designs. Data normality was assessed using the Shapiro-Wilk test. Statistical comparisons between control and DM groups were performed using a two-tailed independent *t*-test with SPSS software version 20.0 (SPSS Inc., Chicago, IL, USA). Bonferroni correction was applied to control the family-wise error rate. Differences were considered statistically significant when $p < 0.05$. All experimental procedures were approved by the Siriraj Institutional Animal Care and Use Committee, Faculty of Medicine Siriraj Hospital, Mahidol University, Bangkok, Thailand, and conducted in accordance with international guidelines for the care and use of laboratory animals.

Results and Discussion

All STZ-injected rats (n=12) maintained fasting blood glucose levels above 300 mg/dL throughout the 4-week experimental period, confirming the persistent state of severe diabetes.

Histopathological examination revealed a preserved four-layered jejunal structure in both groups. The mucosa consisted of columnar epithelium with well-defined villi and crypts. Control rats displayed tall, slender villi and regularly arranged tubular glands (Fig. 1A), whereas DM rats exhibited distorted villi, focal epithelial detachment from the basement membrane, villous hyperplasia, mild inflammatory infiltration of the lamina propria, and intraluminal cellular debris (Fig. 1B). To quantify these alterations, total wall thickness, mucosal thickness, villus height, and crypt depth were measured. Both villus height, crypt depth, total wall thickness, and mucosal thickness were significantly increased in the diabetic group (Table 1), consistent with previous studies reporting that diabetes mellitus is associated with enhanced intestinal epithelial proliferation, leading to villus elongation and crypt hyperplasia (13-15). Interestingly, the observed increases in villus height, crypt depth, mucosal thickness, and total wall thickness in STZ-induced diabetic rats do not signify improved intestinal health but rather represent compensatory hyperplasia and structural remodeling. This intestinal growth adaptation is likely driven by hyperphagia, a hallmark of diabetes where increased food intake triggers the expansion of the absorptive surface area to satisfy energy demands and the elevated levels of glucagon-like peptide 2 (GLP-2), which stimulates epithelial cell proliferation during the early stages of the disease (18,19). Consequently, while the structures appear larger, they reflect a pathological response to metabolic stress and nutrient malabsorption. Such morphological alterations have been reported to involve activation of the canonical Wnt/β-catenin signaling pathway (13, 16-17). In addition, insulin deficiency–induced hyperphagia increases nutrient exposure in the intestine and elevates circulating glucagon-like peptide-2 (GLP-2), a potent intestinotrophic hormone that further promotes crypt epithelial proliferation (18-19). Together, these mechanisms contribute to increased villus height, crypt depth, and mucosal hyperplasia observed under diabetic conditions.

Goblet cells scattered among enterocytes were identified by PAS staining. In control rats, goblet cells exhibited a typical wine-glass morphology with basally located round-to-oval nuclei and abundant mucin granules (Fig. 2A). In contrast, DM rats showed pale staining, indicating reduced mucin content, together with disrupted surface epithelium and cellular debris within the lumen (Fig. 2B). Quantitative analysis demonstrated a significant reduction in goblet cell mucin area fraction in the jejunum of DM rats (Table 2). This finding is consistent with previous reports showing decreased expression of trefoil factor 3 (TFF3) in diabetes, suggesting a reduction in goblet cell population (20). Moreover, several studies have reported a significant decrease in goblet cell numbers in diabetic conditions (21,22). This reduction may be partly attributed to increased epithelial cell loss mediated by inflammatory cytokines (23,24). Among these, tumor necrosis factor-α (TNF-α) plays a key role by activating death receptor signaling and caspase-8, while mitochondrial stress further contributes to apoptosis through the activation of caspase-9 and caspase-3 (25). Together, these pathways may accelerate epithelial cell loss and contribute to goblet cell depletion and impaired mucosal barrier integrity under diabetic conditions.

Toluidine blue staining revealed typical Paneth cell morphology in control rats, characterized by pyramidal-shaped cells with basally located round nuclei and densely stained apical secretory granules (Fig. 3A). In contrast, DM rats exhibited swollen Paneth cells with irregular nuclei and heterogeneous, pale-stained apical secretory granules (Fig. 3B). These morphological alterations were further confirmed by H&E staining in the insets of Figure 3A and 3B; while control rats exhibited dense eosinophilic granules, diabetic rats showed a noticeable reduction in granule density. The demonstration of Paneth cell degranulation and secretory dysfunction suggests a significant impairment in the synthesis and secretion of antimicrobial proteins.

Quantitative analysis showed a tendency toward increased accumulation of Paneth cell secretory granules in DM rats (Table 2), although this difference did not reach statistical significance. This morphological alteration is consistent with previous reports suggesting suppression of the Notch/Hes1 signaling pathway under diabetic conditions, which biases intestinal stem cell differentiation toward secretory lineages, including Paneth cells (20,27). Nevertheless, reduced expression of antimicrobial peptides derived from Paneth cells indicates impaired functional differentiation (26). Collectively, these findings suggest that DM disrupts epithelial lineage balance, resulting in the accumulation of morphologically altered but potentially functionally impaired Paneth cells, which may compromise intestinal barrier integrity.

Persistent hyperglycemia has been suggested to activate convergent mechanisms that damage the intestinal mucosa, particularly through excessive production of reactive oxygen species (ROS). Increased ROS generation induces oxidative stress, which has been associated with reduced antioxidant enzyme activity and elevated oxidative stress markers in the diabetic small intestine (28,29). Elevated ROS levels impair mitochondrial function, disrupt the electron transport chain, and reduce ATP synthesis, thereby further amplifying ROS production (28). In addition, oxidative stress may interfere with endoplasmic reticulum (ER) homeostasis, leading to cellular dysfunction and epithelial injury under diabetic conditions (30). Highly secretory epithelial cells, particularly goblet and Paneth cells, are especially vulnerable to ER stress (31). Dysregulated inositol-requiring enzyme 1 alpha (IRE1α) signaling has been reported to impair mucin and antimicrobial protein synthesis and promote epithelial apoptosis, ultimately compromising mucosal barrier integrity and predisposing to intestinal inflammation and bacterial overgrowth in diabetes (8,20,26,29).

In addition, Masson's trichrome staining was used to evaluate collagen accumulation and capillary diameter in the jejunum. In control rats, the lamina propria consisted of loose connective tissue with sparse collagen fibers (Fig. 4A) and minimal collagen deposition around capillaries (Fig. 5A). In contrast, diabetic rats exhibited mild collagen accumulation within the lamina propria (Fig. 4B) and increased perivascular collagen deposition (Fig. 5B). Quantitative analysis confirmed a significant increase in collagen accumulation in lamina propria collagen area fraction in the DM group, accompanied by significant narrowing of mucosal capillary lumens (Table 3). Previous studies have shown that DM promotes excessive formation of advanced glycation end products (AGEs) binding to the receptor for advanced glycation end products (RAGE), thereby inducing oxidative stress and chronic inflammation, primarily via nuclear factor-kappa B signaling (32). These processes contribute to endothelial dysfunction and microangiopathic remodeling, characterized by basement membrane thickening and increased collagen deposition in the lamina propria (33,34). Moreover, DM promotes a profibrotic intestinal environment through increased transforming growth factor-β expression and extracellular matrix deposition, including fibronectin and type IV collagen, leading to progressive intestinal fibrosis and structural remodeling (21). These structural damages impair absorptive function and compromise the mucosal barrier against pathogens, collectively contributing to the development and progression of diabetic enteropathy

This study has several limitations. The relatively short duration of diabetes induction (4 weeks) may not fully represent chronic intestinal remodeling. In addition, functional assessments of intestinal absorption and barrier integrity were not performed. Future studies incorporating longer follow-up periods, functional permeability assays, and molecular analyses are warranted to further elucidate the pathogenesis of diabetic enteropathy.

Conclusion

Short-term diabetes mellitus induces significant histopathological alterations in the jejunum, including epithelial hyperplasia, goblet cell mucin depletion, Paneth cell morphological dysfunction, and progressive stromal remodeling. These changes reflect early disruption of epithelial homeostasis, impaired mucosal defense mechanisms, and progressive microvascular and fibrotic alterations. Collectively, such pathological remodeling may contribute to intestinal barrier dysfunction and the development of diabetic enteropathy. These findings highlight the vulnerability of the jejunal mucosa to early diabetic injury and emphasize the importance of early gastrointestinal monitoring and preventive strategies in the clinical management of diabetic patients.

Acknowledgements

This research was supported by Chalermprakiat Grants, Faculty of Medicine Siriraj Hospital, Mahidol University, Thailand. This study was supported by the Chalermphrakiat Grant, Faculty of Medicine Siriraj Hospital, Mahidol University, Bangkok, Thailand, and a travel grant

from the Anatomy Association of Thailand (AAT) for the 48th International Conference of the Anatomy Association of Thailand (AAT 48).

References

1. Antar SA, Ashour NA, Sharaky M, Khattab M, Ashour NA, Zaid RT, et al. Diabetes mellitus: classification, mediators, and complications; a gate to identify potential targets for the development of new effective treatments. *Biomed Pharmacother.* 2023;168:115734.
2. International Diabetes Federation. *IDF Diabetes Atlas.* 11th ed. Brussels: International Diabetes Federation; 2025. ISBN: 978-2-930229-96-6.
3. Roy S, Kim D. Retinal capillary basement membrane thickening: role in the pathogenesis of diabetic retinopathy. *Prog Retin Eye Res.* 2021;82:100903.
4. Baimai S, Sricharoenvej S, Lanlua P, Choompoo N. Altered chief cell morphology in the gastric gland of streptozotocin-diabetic rats. Int J Morphol. 2023;41(4):1043–1052.
5. Mogensen CE, Steffes MW, Deckert T, Christiansen JS. Functional and morphological renal manifestations in diabetes mellitus. *Diabetologia.* 1981;21(2):89–93.
6. Asgharnezhad M, Joukar F, Fathalipour M, Khosousi M, Hassanipour S, Pourshams A, et al. Gastrointestinal symptoms in patients with diabetes mellitus and non-diabetic: a cross-sectional study in north of Iran. *Diabetes Metab Syndr.* 2019;13(3):2236–40.
7. Zhao M, Liao D, Zhao J. Diabetes-induced mechanophysiological changes in the small intestine and colon. *World J Diabetes.* 2017; 8(6):249–69.
8. Zhong HJ, Yuan Y, Xie WR, Chen MH, He XX. Type 2 diabetes mellitus is associated with more serious small intestinal mucosal injuries. *PLoS One.* 2016;11(9):e0162354.
9. Chen P, Zhao J, Gregersen H. Up-regulated expression of advanced glycation end-products and their receptor in the small intestine and colon of diabetic rats. *Dig Dis Sci.* 2012;57(1):48–57.
10. Ovalle WK, Nahirney PC. *Netter's Essential Histology.* 2nd ed. Philadelphia, PA: Saunders Elsevier; 2013.
11. Young B, O'Dowd G, Woodford P. *Wheater's Functional Histology: a text and colour atlas.* 6th ed. Philadelphia, PA: Elsevier; 2013.
12. Ross MH, Pawlina W. *Histology: a text and atlas with correlated cell and molecular biology.* 6th ed. Philadelphia, PA: Wolters Kluwer; 2020.
13. Lerkdumnernkit N, Sricharoenvej S, Lanlua P, Niyomchan A, Baimai S, Chookliang A, et al. The effects of early diabetes on duodenal alterations in rats. *Int J Morphol.* 2022;40(2): 389–95.
14. da Rosa CVD, Azevedo SCSF, Bazotte RB, Peralta RM, Buttow NC, Pedrosa MMD, et al. Supplementation with L-glutamine and L-alanyl-L-glutamine changes biochemical parameters and jejunum morphophysiology in type 1 diabetic Wistar rats. *PLoS One.* 2015; 10(12):e0143005.
15. El-Moneam Samar A, Hussein H, El-Fark M, Mohammed Ali M, Kamel E. Role of bone marrow-derived mononuclear stem cells versus Nigella sativa oil on jejunal alterations in diabetic adult male albino rats [dissertation]. Zagazig (Egypt): Zagazig University; 2022.
16. Dorfman T, Pollak Y, Sohotnik R, Coran AG, Bejar J, Sukhotnik I. Enhanced intestinal epithelial cell proliferation in diabetic rats correlates with β-catenin accumulation. *J Endocrinol.* 2015;226(3):135–43.
17. Perochon J, Carroll LR, Cordero JB. Wnt signalling in intestinal stem cells: Lessons from mice and flies. *Genes (Basel).* 2018;9(7):326.
18. Fischer KD, Dhanvantari S, Drucker DJ, Brubaker PL. Intestinal growth is associated with elevated levels of glucagon-like peptide 2 in diabetic rats. *Endocrinology.* 1997;138(1): 149–58.
19. Thulesen J, Hartmann B, Nielsen C, Holst JJ, Poulsen SS. Diabetic intestinal growth adaptation and glucagon-like peptide 2 in the rat: effects of dietary fibre. *Gut.* 1999;44(6): 826–31.
20. Min XH, Yu T, Qing Q, Yuan YH, Zhong W, Chen GC, et al. Abnormal differentiation of intestinal epithelium and barrier dysfunction in diabetic mice associated with depressed Notch/NICD transduction. *Cell Biol Int.* 2014; 38(10):1194–204.
21. Barman S, Srinivasan K. Ameliorative effect of zinc supplementation on compromised small intestinal health in streptozotocin-induced diabetic rats. *Chem Biol Interact.* 2019;307:37–50.
22. Ettarh RR, Carr KE. A morphological study of the enteric mucosal epithelium in the streptozotocin-diabetic mouse. *Life Sci.* 1997; 61(18):1851–58.
23. Kuo WT, Shen L, Zuo L, Shashikanth N, Ong MLDM, Wu L, et al. Inflammation-induced occludin downregulation limits epithelial apoptosis by suppressing caspase-3 expression. *Gastroenterology.* 2019;157(5):1323–37.e2.

24. Lau KS, Cortez-Retamozo V, Philips SR, Pittet MJ, Lauffenburger DA, Haigis KM. Multi-scale in vivo systems analysis reveals the influence of immune cells on TNF-α-induced apoptosis in the intestinal epithelium. *PLoS Biol.* 2012;10(9): e1001383.
25. Ramachandran A, Madesh M, Balasubramanian KA. Apoptosis in the intestinal epithelium: its relevance in normal and pathophysiological conditions. *J Gastroenterol Hepatol.* 2000; 15(2):109–20.
26. Yu T, Yang HS, Lu XJ, Xia ZS, Ouyang H, Shan TD, et al. Association of bactericidal dysfunction of Paneth cells in streptozocin-induced diabetic mice with insulin deficiency. *Med Sci Monit.* 2016;22:3062–72.
27. Noah TK, Shroyer NF. Notch in the intestine: regulation of homeostasis and pathogenesis. *Annu Rev Physiol.* 2013;75:263–88.
28. Yuan T, Yang T, Chen H, Fu D, Hu Y, Wang J, et al. New insights into oxidative stress and inflammation during diabetes mellitus-accelerated atherosclerosis. *Redox Biol.* 2019; 20:247–60.
29. Malik A, Morya RK, Bhadada SK, Rana S. Type 1 diabetes mellitus: complex interplay of oxidative stress, cytokines, gastrointestinal motility and small intestinal bacterial overgrowth. *Eur J Clin Invest.* 2018;48(11): e13030.
30. Cao SS, Kaufman RJ. Endoplasmic reticulum stress and oxidative stress in cell fate decisions and human disease. *Antioxid Redox Signal.* 2014;21(3):396–413.
31. Chong WC, Shastri MD, Eri R. Endoplasmic reticulum stress and oxidative stress: a vicious nexus implicated in bowel disease pathophysiology. *Int J Mol Sci.* 2017;18(9): 2005.
32. Figueroa-Romero C, Sadidi M, Feldman EL. Mechanisms of disease: the oxidative stress theory of diabetic neuropathy. *Rev Endocr Metab Disord.* 2008;9(3):301–14.
33. Las Casas LE, Finley JL. Diabetic micro-angiopathy in the small bowel. *Histopathology.* 1999;35(3):267–70.
34. Byun K, Yoo YC, Son M, Lee J, Jeong GB, Park YM, et al. Advanced glycation end-products produced systemically and by macrophages: a common contributor to inflammation and degenerative diseases. *Pharmacol Ther.* 2017; 177:44–55.

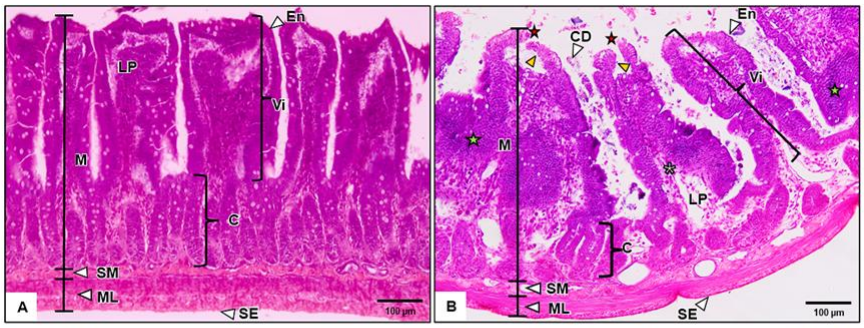

Fig. 1 Light micrograph showing the four layers of the jejunal wall, villus height, and crypt depth in the short-term control (A) and diabetic (B) groups with H&E staining. M: Mucosa; SM: submucosa; ML: Muscular layer; SE: Serosa; Vi: Villi; C: Crypt; CD: Cell debris; Red stars: Disrupted surface epithelium; Green stars: Hyperplasia; Yellow arrowheads: Epithelial detachment from the basement membrane; White asterisks: Mild inflammatory cell infiltration. (10X)

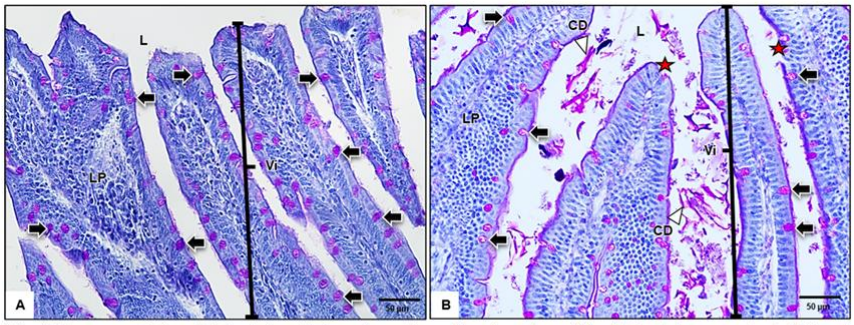

Fig. 2 Representative PAS-stained jejunal sections showing the villi of short-term control (A) and diabetic (B) groups. Thick black arrows indicate goblet cells; Vi: villi; L: jejunal lumen; red star: disrupted surface epithelium; CD: cell debris. Diabetic rats exhibit reduced goblet cell mucin content compared with controls. (20X)

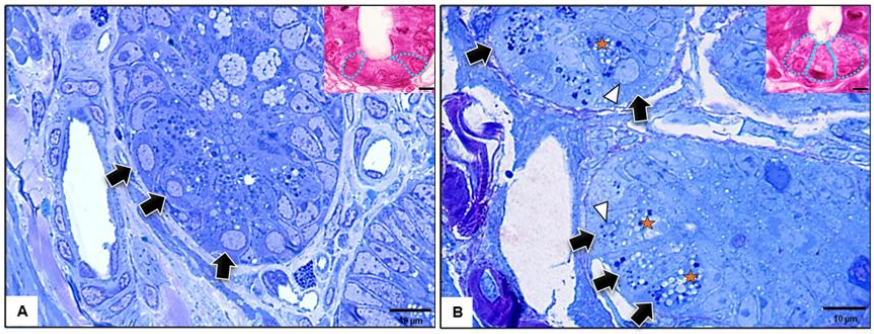

Fig. 3 Light micrographs showing cross-section of the jejunal mucosa crypt of the short-term control (A) and diabetic (B) groups with toluidine blue staining. Thick black arrows: Paneth cells; White arrowheads: Paneth cells swelling with irregular nuclei; Orange stars: Heterogeneous secretory granules in Paneth cells. (100X). Insets (A, B) show high-magnification views of Paneth cells (Blue dotted lines) using H&E staining, clearly demonstrating the eosinophilic secretory granules at the crypt base. (20X)

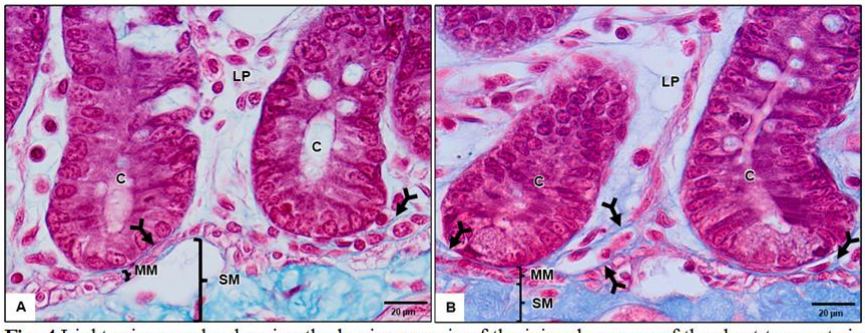

Fig. 4 Light micrographs showing the lamina propria of the jejunal mucosa of the short-term rats in control (A) and diabetic (B) groups with Masson's Trichrome staining. LP: Lamina propria; MM: Muscularis mucosae; C: Crypts; SM: Submucosa; Black arrow with tails: Collagen fiber. (60X)

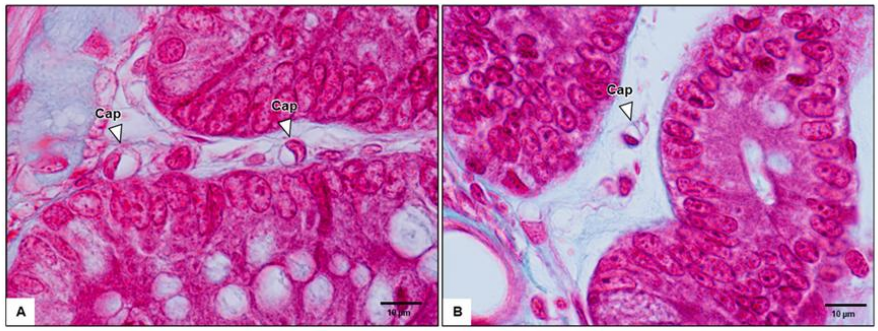

Fig. 5 Light micrographs showing the fenestrated capillaries in the lamina propria of the jejunal mucosa in control (A) and diabetic (B) groups with Masson's Trichrome staining. Cap: Capillaries in the lamina propria of the jejunum. (100X)

Table 1 The Quantitative analysis of total wall thickness, mucosal thickness, villi height and crypt depth (µm)

Parameters	*Control* ($n = 90$)	*DM* ($n = 90$)
Total wall thickness	599.99 ± 70.42	642.43 ± 103.73*
Mucosal thickness	516.80 ± 66.50	551.11 ± 83.81*
Villi height	357.02 ± 54.36	402.10 ± 54.66*
Crypt depth	130.86 ± 18.72	141.04 ± 21.76*

Results expressed as Mean±SD
*$p < 0.05$, compared to age-matched control rats in the same duration.

Table 2 The Quantitative analysis of the percentage area of goblet cells and secretory granules of Paneth cells

Parameters	*Control* ($n = 90$)	*DM* ($n = 90$)
% area of goblet cells	4.90 ± 1.87	3.50 ± 1.81*
% area of secretory granules of Paneth cells	1.88 ± 1.19	2.63 ± 1.43

*$p < 0.05$, compared to age-matched control rats in the same duration

Table 3 The Quantitative analysis of capillary diameter in lamina propria (µm) and of the percentage area of collagen accumulation in lamina propria

Parameters	*Control* ($n = 90$)	*DM* ($n = 90$)
Capillary diameter	5.05 ± 0.80	4.50 ± 0.77*
% area of collagen accumulation	2.70 ± 1.49	6.60 ± 2.63*

Results expressed as Mean±SD
*$p < 0.05$, compared to age-matched control rats in the same duration

P-31

A Novel and Applicable Method for Sex Estimation Based on 2D Auricular Surface Images of the Hip Bone: Morphometric Image Analysis in a Thai Population

Nattida Srinak[1], Pittayarat Intasuwan[2], Apichat Sinthubua[2], Patison Palee[3] and Pasuk Mahakkanukrauh[2,4*]
[1] Program in Forensic Osteology and Odontology, Faculty of Medicine, Chiang Mai University, Suthep Road, Chiang Mai, Thailand
[2] Department of Anatomy, Faculty of Medicine and Research Cluster in Osteology Research and Training Center (ORTC), Chiang Mai University, Suthep Road, Chiang Mai, Thailand
[3] College of Arts, Media and Technology, Chiang Mai University, Suthep Road, Chiang Mai, Thailand
[4] Excellence Center in Osteology Research and Training Center (ORTC), Chiang Mai University, Suthep Road, Chiang Mai, Thailand
*Corresponding author, e-mail: pasuk034@gmail.com

Abstract

Sex estimation of skeletal remains is a critical component of forensic identification. Although the hip bone provides high accuracy for morphological assessment, this approach requires substantial expertise and may be limited by subjectivity. Morphometric approaches offer greater objectivity and require less technical expertise. In recent years, these measurements have increasingly been applied to digital images, allowing skeletal structures to be quantified without direct handling of physical specimens. Three-dimensional imaging techniques are increasingly used in forensic anthropology; however, they often require specialized equipment and technical expertise. In contrast, two-dimensional imaging approaches are more accessible and practical for many forensic applications, although they may not fully capture the complexity of three-dimensional anatomical structures. This study investigates the auricular surface of the hip bone as an alternative region for sex estimation using morphometric image analysis and evaluates the level of accuracy achievable from two-dimensional (2D) images. A total of 140 dry hip bones from 70 Thai adults (35 males and 35 females), including both left and right sides, from the Osteology Research and Training Center, Chiang Mai University, were photographed in anatomical position from a superior view. The auricular surface area was measured using image analysis software (MATLAB). Descriptive statistics and discriminant function analysis were applied to assess sex differences and classification accuracy. The results demonstrated that males exhibited significantly larger auricular surface areas than females (10.95 ± 1.61 mm² in males and 9.19 ± 1.64 mm² in females, $p < 0.05$). Discriminant function analysis yielded an overall classification accuracy of 74.3%, with accuracies of 71.4% and 77.1% for males and females, respectively. The measurement of auricular surface area may therefore serve as a complementary tool for sex estimation in forensic contexts within the Thai population. Further studies with larger sample sizes are needed to improve classification accuracy and validate this approach.

Keywords *2D image, Auricular surface, Image analysis, Morphometric, Sex estimation*

P-32

An Alternative Metric for Sex and Stature Estimation: Femoral Intertrochanteric Length on 3DCT

Phannavich Malawan[1,2,3*], Apichat Sinthubua[3,4], Pasuk Mahakkanukrauh[3,4]
[1] Department of Radiological Technology, Faculty of Associated Medical Science, Chiang Mai University, Chiang Mai, Thailand
[2] Ph.D. Program in Forensic Osteology and Odontology, Faculty of Medicine, Chiang Mai University, Thailand
[3] Forensic Osteology and Odontology, Faculty of Medicine, Chiang Mai University, Thailand
[4] Department of Anatomy, Faculty of Medicine, Chiang Mai University, Thailand
*Corresponding author, e-mail: Phannavich.M@cmu.ac.th

Abstract
Background: Estimation of sex and stature from skeletal remains is one of the fundamental pillars of forensic anthropology. The femur is a highly reliable bone for such assessments. However, conventional methods typically rely on key variables such as maximum femoral length and femoral head diameter. In many forensic scenarios, these landmarks are frequently damaged due to severe fractures, trauma, or burning. Therefore, identifying novel alternative localized markers that remain preserved in fragmented remains is essential. **Methods:** This study utilized three-dimensional computed tomography (3DCT) to generate reconstructed models of 200 dry femora. Morphometric analysis of the intertrochanteric length (INTL) was performed, defined as the linear distance from the superior part of the greater trochanter (from the inferior margin of the impression for gluteus medius insertion) to the lowest point of the tip of the lesser trochanter. Sex estimation was conducted using discriminant function analysis, and stature estimation was calculated through linear regression equations derived from the correlation between INTL and maximum femoral length (MFL) using SPSS statistical software. **Results:** Statistical analysis demonstrated that INTL is a significant indicator of sexual dimorphism, achieving a classification accuracy of 83%. For stature estimation, a strong positive correlation was observed between INTL and MFL ($r = 0.68$). The regression equation predicting femoral length from INTL yielded a standard error of estimation (SEE) of 1.90 cm, indicating a reliable level of precision for stature reconstruction. **Conclusion:** The findings demonstrate that INTL is a valuable and reliable metric for estimating both sex and stature. With high classification accuracy and a significant correlation with total femoral length, INTL provides a practical alternative for forensic practitioners when conventional landmarks are compromised by trauma or fragmentation.

Keywords *Forensic anthropology, Computed tomography, Femur, Sex estimation, Stature estimation, 3DCT*

P-33

Sex Determination Based on Cranial Base Osteometry in A Thai Population

Nuttanicha Thumpunya[1], Pagorn Navic[1], Patison Palee[2], Sukon Prasitwattanaseree[3], Apichat Sinthubua[1], Pasuk Mahakkanukrauh[1,4*]
[1] Department of Anatomy, Faculty of Medicine, Chiang Mai University, Chiang Mai, Thailand
[2] College of Arts, Media and Technology, Chiang Mai University, Chiang Mai, Thailand
[3] Department of Statistics, Faculty of Science, Chiang Mai University, Chiang Mai, Thailand
[4] Excellence in Osteology Research and Training Center, Chiang Mai University, Chiang Mai, Thailand
*Corresponding author, e-mail: pasuk034@gmail.com

Abstract

Biological identification is a fundamental task in archaeology, anthropology, and forensic science. Sex determination is typically the first step when a skeleton is discovered, as it provides the basis for subsequent estimation of other biological characteristics, such as age, stature, and ancestry. The cranium, particularly the cranial base, is frequently recovered at forensic scenes due to its dense composition of compact bone and protection by surrounding soft tissues. This inherent robustness makes the cranial base especially valuable in cases involving severe fragmentation or thermal damage. This study aimed to determine sex using osteometric parameters derived from the cranial base in a Thai population. A total of 100 adult Thai dry crania (50 males and 50 females), obtained from the Osteology Research and Training Center (ORTC), Faculty of Medicine, Chiang Mai University, were examined. Four cranial base triangular perimeters, derived from ten linear measurements obtained using a digital vernier caliper, were analyzed using discriminant function analysis to develop sex determination equations. The results demonstrated cross-validated classification accuracies ranging from 73% to 90%. These findings indicate that osteometric analysis of the cranial base can provide reliable accuracy for sex determination and may be particularly useful in cases where only the cranial base is preserved. Nevertheless, further studies incorporating larger sample sizes are recommended to improve the robustness and generalizability of the derived equations.

Keywords *Biological identification, Cranial base, Forensic science, Osteometric, Sex determination*

P-34

Sex-Related Differences in Histomorphology Using An AI-Based Approach

Kewalee Pichetpan[1], Phruksachat Singsuwan[1], Apichat Sinthubua[1], Patison Palee[3], Sukon Prasitwattanaseree[4], Pasuk Mahakkanukrauh1[1,2*]
[1] Department of Anatomy, Faculty of Medicine, Chiang Mai University, Chiang Mai, Thailand
[2] Excellence Center in Osteology Research and Training Center (ORTC), Chiang Mai University, Chiang Mai, Thailand
[3] College of Arts, Media and Technology, Chiang Mai University, Chiang Mai, Thailand
[4] Department of Statistics, Faculty of Science, Chiang Mai University, Chiang Mai, Thailand
*Corresponding author, e-mail: beekp1427@gmail.com

Abstract

Sex determination is essential for fragmented remains. While the medial clavicle is a robust indicator, manual histomorphological analysis is time-consuming and subjective. To overcome these limitations, artificial intelligence is integrated into the analytical process. This study investigated histomorphological techniques for identifying sex-related differences through the analysis of histological images. The research utilized medial clavicle samples of documented sex, age, and cause of death from 17 Thai cadavers, comprising 12 males and 5 females, with ages ranging from 41 to 92 years. Cortical bone sections were subjected to decalcification in nitric acid solutions for a duration of 14 to 16 days, followed by standard histological processing and staining with hematoxylin and eosin. High-resolution digitized images were captured using an Olympus BX63 motorized microscope integrated with cellSens imaging software. Damaged tissue sections were excluded, and all viable images were preserved in Tagged Image File Format. These histological images were employed to train computational models within the MATLAB environment to identify sex-specific characteristics. The training dataset included 68 standardized images, and model performance was evaluated based on classification accuracy. Results indicated that transfer learning facilitated superior performance. This study applied pre-trained deep learning architectures to discern sex-related variations in medial clavicle morphology. The most effective model derived from the AlexNet architecture achieved accuracy rates of 75.00%, 80.00%, and 73.17% across three separate validation trials. Furthermore, the top-performing model based on the VGG-16 architecture demonstrated enhanced accuracy rates of 80.00%, 85.00%, and 73.17%, respectively. These histological findings underscore the forensic potential of intelligent computing systems for sex determination. This research establishes a foundational framework for future advancements in forensic identification using microscopic imaging and deep learning techniques. Importantly, AI-identified sex-specific features focused on the size and shape of secondary osteons, reflecting distinct micro-anatomical patterns and bone remodeling variations between sexes.

Keywords *Sex determination, Medial clavicle, Histomorphology, Artificial intelligence, Deep learning*

P-35

Cutaneous Histopathological Changes in the Plantar Skin of STZ-Induced Diabetic Rats

Chutikan Kaensa[1], Sani Baimai[1]*
[1] Department of Anatomy, Faculty of Medicine, Siriraj Hospital, Mahidol University, Bangkok, Thailand
*Corresponding author, e-mail: sani.bai@mahidol.ac.th

Abstract

Diabetes mellitus is associated with progressive microvascular and neuropathic complications affecting peripheral tissues, including the skin; however, duration-dependent histopathological alterations in plantar skin remain incompletely characterized. This study evaluated such changes in the plantar skin of male Sprague-Dawley rats with Streptozotocin (STZ)-induced diabetes and compared short- and long-term effects with time-matched controls. Male Sprague-Dawley rats (approximately 200-250 g) were divided into four groups: short-term control and diabetic groups (4 weeks, n = 6 each), and long-term control and diabetic groups (24 weeks, n = 6 each). All animal procedures received ethical approval, obtained from the Institutional Review Board, Faculty of Medicine Siriraj Hospital, Mahidol University (COA No. 009/2565). After STZ administration (STZ 60 mg/kg, single intraperitoneal dose), hyperglycemia was confirmed by fasting blood glucose ≥ 250 mg/dL. At 4 or 24 weeks, plantar paw skin was harvested, fixed, embedded, sectioned, and stained with hematoxylin and eosin. Histological evaluation focused on epidermal morphology (keratinocyte density, stratum structure); dermal microvasculature (arterioles and capillaries). Both short- and long-term control groups exhibited preserved epidermal stratification, well-interdigitated rete ridges, a compact stratum corneum, and densely organized dermal collagen bundles. Vascular structures appeared structurally intact, with no duration-related changes observed in non-diabetic animals. The short-term diabetic group demonstrated early architectural disruption, including mild irregular epidermal thickness, reduced collagen compactness, and subtle vascular wall prominence. In contrast, the long-term diabetic group exhibited more pronounced changes, including distorted epidermal architecture with flattened rete ridges, uneven keratinization, and marked dermal collagen disorganization, along with vascular wall thickening and luminal narrowing. These changes corresponded with increased semi-quantitative morphological scores in diabetic groups. These findings provide histopathological evidence of progressive structural changes in the plantar skin of STZ-induced diabetic rats, supporting the impact of chronic hyperglycemia on peripheral cutaneous tissues.

Keywords *Diabetes mellitus, Streptozotocin, Plantar skin, Cutaneous histopathology, Sprague-Dawley Rats*

P-36

Right-Sided Duplicated Ureter: A Case Report

Kewithinwangbo Newme[1]
[1] Department of General Surgery, AIIMS Guwahati
*Corresponding author, e-mail: adinewme@gmail.com

Abstract
Background: Ureteral duplication is a rare anomaly of the urinary tract, with an incidence of 0.5% to 3%. Bilateral double ureters are even rarer, occurring in 1 of 500 individuals. **Case scenario:** A 45-year-old lady presented to the outpatient department with complaints of lower abdominal pain and intermittent heavy menstruation. Clinical examination revealed mild tenderness in the right iliac fossa (RIF) and a vague, ill-defined swelling in the same region. **Result:** The ultrasound (USG) and contrast-enhanced computed tomography (CECT) of the abdomen revealed a right adnexal mass suggestive of carcinoma of the ovary. Findings in other organs were within normal limits. Intraoperative findings revealed a carcinomatous lesion of the right ovary adherent to the uterus and the ileocecal region. A hysterectomy with bilateral salpingo-oophorectomy was performed. During the dissection of the right ovarian tumor, the incomplete right -sided duplicated ureters were identified incidentally. The left side ureter was single. The imaging study did not comment on any ureteral anomalies. **Discussion:** Ureteric duplication is associated with the ectopic ureterocele, vesicoureteral reflux, and urinary infection. Imaging studies might also miss the abnormality until the pathology is evident. The imaging diagnosis of complete ureteral duplication can be easily missed and is difficult to identify by routine CT examination. Iatrogenic ureteral injuries appear to be more prevalent in gynecological and general surgical procedures, with the majority of gynecological injuries occurring during abdominal hysterectomy and salpingo-oophorectomy. **Conclusion:** Therefore, the surgeons should be more careful while performing hysterectomy and any pelvic operations, to avoid iatrogenic injury of the ureter, as it adds to morbidity. Moreover, surgeons should be meticulous in dissection and confirm identification of the ureter, as the higher incidence of renal-ureteral abnormalities in women, and sometimes it may be confused with the round ligament.

Keywords *Right-sided ureteral duplication, Ureteral abnormality, Vesicoreflux*

P-37

Unilateral Innominate Foramen in Parietal Bone Near Mastoid Angle: A Rare Osteological Variant

Balkund Kailash[1*], Maheshwari TP[1], Das RS[1]
[1] AIIMS, Raebareli, India
*Corresponding author, email: drkailashbalkund@gmail.com

Abstract
Background: Parietal foramina are paired openings located near the sagittal suture at the posterior aspect of the parietal bones. These foramina normally transmit emissary veins that connect extracranial veins to the superior sagittal sinus. The mastoid foramen, present in the mastoid part of the temporal bone, transmits an emissary vein connecting extracranial veins with the sigmoid sinus. The present case report describes a unilateral innominate foramen in the left parietal bone at the mastoid angle, observed in a dry adult human female skull during routine osteological examination in the department of Anatomy at AIIMS Raebareli, India. The foramen was oval in shape, located near the mastoid angle of the parietal bone, and exhibited smooth, well-defined margins. It measured approximately 3.1 mm in the transverse diameter and 2.4 mm in the vertical diameter, as determined using a digital vernier calliper. **Objective:** To identify and document the presence of a unilateral innominate foramen in the parietal bone and its clinical significance. **Results:** The surrounding skull structures appeared normal, with a sulcus extending from the mastoid foramen to the innominate foramen. The unusual location of this foramen in the parietal bone is clinically significant due to its potential association with vascular variations and increased vulnerability to injury during surgical procedures. Furthermore, Neurosurgical approaches to the posterior cranial fossa through the asterion require awareness of such rare foraminal variants in order to avoid procedural complications. Management of Dural arteriovenous fistulas often involves access through emissary veins, particularly those associated with the transverse and sigmoid sinuses. Therefore, endovascular surgeons should consider the possibility of anatomical variations such as that observed in this case. When a probe was passed through the innominate foramen, it reached the intracranial junction of the transverse and sigmoid sulci. The unusual location of the foramen represents a persistent aberrant embryonic vascular channel during intramembranous ossification, which normally regresses as cranial bone development progresses. **Conclusion:** This case highlights the importance of recognizing rare anatomical variations and contributes to the existing literature by providing detailed morphological observation. Awareness of this anomaly is essential for anatomists, radiologists, and neurosurgeons in order to prevent potential surgical and diagnostic complications.

Keywords *Parietal foramen, Mastoid foramen, Emissary vein, Asterion, Dural arteriovenous fistula*

P-38

Unilateral Duplication of Foramen Spinosum with Unusual Bilateral Variation of Hypoglossal Canals in A Dry Human Skull-Their Clinical Implications

Maheshwari TP[1]*, Das RS[1]
[1] Department of Anatomy, All India Institute of Medical Sciences, Raebareli, India
*Corresponding author, email: id-tpm1984@gmail.com

Abstract
Background: Foramen spinosum is one of the foramina of the skull that lies bilaterally close to the spine of the sphenoid in the middle cranial fossa. Recurrent meningeal branch of the mandibular nerve, middle meningeal artery and vein usually pass through it. Hypoglossal canal is a paired bony canal lying deep to the occipital condyles, directed anterolaterally through which the hypoglossal nerve, meningeal branch of ascending pharyngeal artery, and emissary veins of the basilar plexus pass. Duplication of the foramen spinosum, along with duplication and triplication of the hypoglossal canal in the same skull, is a rare osteological variant that may lead to variation in the course of contents. The presence of duplication and triplication of these structures becomes clinically significant for surgeons approaching the middle and posterior cranial fossae. **Objective**: To study clinical implications of variation in the foramen spinosum and hypoglossal canal. **Result:** We report a case with duplication of the left foramen spinosum, having a maximum diameter of 3.3 mm and 2.7 mm located just medial to the spine of the sphenoid. The same skull showed duplication of the left hypoglossal canal with a maximum extracranial diameter of 6.5mm and triplication of the right hypoglossal canal with a maximum diameter of 7.6 mm located lateral to the occipital condyles. **Conclusion:** Coexistence of variation in two types of foramina would certainly make it much more clinically significant during skull base surgery to approach the middle meningeal artery and hypoglossal nerve in the middle and posterior cranial fossa, respectively. Surgeons should be cognizant of these variants while doing surgical procedures involving the middle meningeal artery and transcondylar approach for the hypoglossal nerve to avoid further complications.

Keywords *Foramen spinosum, Hypoglossal canal, Duplication, Triplication*

P-39

Prostatic Calcification as a Potential Imaging Biomarker for Predicting Prostatic Disease Severity in Thai Men

Boottoh Nambunruang[1], Laphatrada Yurasakpong[2], Athikhun Suwannakhan[2,3], Pathompong Limsila[2], Taweesak Tangrodchanapong[4*]

[1] Department of Medical Education, Institute of Medicine, Suranaree University of Technology, Nakhon Ratchasima, Thailand
[2] Department of Anatomy, Faculty of Science, Mahidol University, Rama VI Road, Ratchathewi, Bangkok, Thailand
[3] Human Anatomy Unit, Department of Biomedical Sciences, College of Medicine and Health, University of Birmingham, Edgbaston, Birmingham, United Kingdom
[4] Radiological Technology School, Faculty of Health Science Technology Chulabhorn Royal Academy, Bangkok Thailand
*Corresponding author, e-mail: taweesak.tan@cra.ac.th

Abstract

Prostate calcifications are frequently detected on imaging, yet their volumetric characteristics and clinical associations remain insufficiently quantified. This study aimed to determine the prevalence and volumetric characteristics of prostate calcifications using three-dimensional (3D) image segmentation. Specifically, this study aimed to quantify the volume and number of prostatic calcifications on CT imaging and evaluate their association with prostate cancer and benign prostatic hyperplasia (BPH) in Thai men. A retrospective analysis of CT imaging from 277 patients was performed. Among these, 167 patients (60.3%) showed unremarkable findings, 61 (22.0%) had prostatic enlargement, 4 (1.4%) had prostate cancer, and 21 (7.6%) demonstrated isolated calcifications, with several patients presenting combined findings. Overall, calcifications were identified in 28 patients (10.1%), including 18 patients with isolated calcifications (6.5%), 8 with calcifications associated with prostatic enlargement (2.9%), 1 with calcifications associated with prostate cancer (0.4%), and 1 with calcifications associated with both enlargement and cancer (0.4%). Three-dimensional segmentation was performed using 3D Slicer, where DICOM images were imported, and calcifications were segmented. Volumetric measurements were calculated using the Segment Statistics module. Calcification volumes demonstrated wide variability among patients. Correlation analysis showed no significant association between patient age and calcification volume (Spearman's ρ-0.21 to 0.07, $p > 0.05$). In contrast, the number of calcification sites showed a strong positive correlation with total calcification volume ($\rho = 0.763$, $p < 0.00001$). The overall mean calcification volume was 341.5 ± 428.9 mm³, with progressively larger volumes observed as the number of calcification sites increased; patients with four sites demonstrated the highest mean volume (1498.9 ± 1124.1 mm³). In conclusion, a higher number of calcification sites is strongly associated with greater total volume, suggesting that multi-site calcifications may reflect increased pathological severity. The ongoing research is evaluating whether these volumetric patterns can predict disease severity by integrating imaging data with broader clinical and laboratory parameters.

Keywords *Prostatic calcification, Prostate cancer, Benign prostatic hyperplasia, Computerized tomography*

P-40

Effects of Standardized Extract of *Centella asiatica* (ECa 233) on Male Reproductive Function in High-fat Diet-fed Rats

Chanapa Runthasot[1,2], Natthapong Khamaiam[1,2], Siriporn Kreungnium[1,2], Aubonwan Sitthikhankaeo[1,2], Kanyakorn Aitsarangkun Na Ayutthaya[1,2], Apichaya Niyomchan[3], Piyanee Sriya[4], Mayuree H. Tantisira[5], Hiroki Nakata[6,7], Peter J Mark[8], Wai Chen[9], Kroekkiat Chinda[2,10,11], Kannika Adthapanyawanich[1,2,11], Yutthapong Tongpob[1,2,11*]

[1] Department of Anatomy, Faculty of Medical Science, Naresuan University, Phitsanulok, Thailand, 65000
[2] Integrative Cardiovascular Research Unit, Faculty of Medical Science, Naresuan University, Phitsanulok, Thailand, 65000
[3] Department of Anatomy, Faculty of Medicine Siriraj Hospital, Mahidol University, Bangkok, Thailand, 10700
[4] Department of Anatomy, Phramongkutklao College of Medicine, Rajavithi Road, Rajadevi, Bangkok, 10400
[5] Faculty of Pharmaceutical Sciences, Burapha University, Chonburi, Thailand, 20131
[6] Department of Clinical Engineering, Faculty of Health Sciences, Komatsu University, Komatsu, Japan, 923-0961
[7] Department of Integrative Cancer Therapy and Urology, Kanazawa University Graduate School of Medical Science, Kanazawa, Japan, 920-8641
[8] School of Human Sciences, The University of Western Australia, Crawley, Western Australia, Australia, 6009
[9] Curtin Medical School, and Curtin Enable Institute, Curtin University, Perth, Western Australia, Australia, 6102
[10] Department of Physiology, Faculty of Medical Science, Naresuan University, Phitsanulok, Thailand, 65000
[11] Centre of Excellence in Medical Biotechnology, and AI CARE Research Cluster, Naresuan University, Phitsanulok, Thailand, 65000
*Corresponding author, e-mail: yutthapongt@nu.ac.th

Abstract

Background: High-fat diet (HFD)-induced dyslipidemia is strongly associated with oxidative stress and chronic inflammation, which contribute to impaired spermatogenesis and reduced sperm quality. These pathophysiological changes involve increased lipid peroxidation, disruption of the blood–testis barrier and altered testicular microenvironment. Standardized extract of *Centella asiatica* (ECa 233) contains bioactive triterpenoids with well-documented antioxidant and anti-inflammatory properties that may mitigate these mechanisms. However, its protective effects on male reproductive function under metabolic stress remain unclear. **Objective:** To investigate the effects of ECa 233 on reproductive outcomes (including testicular weight, histopathology, sperm concentration, and sperm viability) in HFD-fed rats. **Methods**: Male Wistar rats were divided into five groups (n=4-6/group): normal diet, HFD, HFD+ECa 233 (10 mg/kg/day), HFD+ECa 233 (30 mg/kg/day), and HFD+simvastatin (40 mg/kg/day), administered orally for 12 weeks. Serum lipid profiles, body weight gain, and relative testicular weight were measured. Sperm concentration and viability were assessed from cauda epididymis samples, and testicular histopathology was evaluated using hematoxylin and eosin staining. **Results**: HFD rats exhibited marked dyslipidemia, with significantly increased body weight gain (p<0.05), alongside decreased relative testicular weight (p<0.05), sperm concentration and viability (p<0.05), and testicular histopathology abnormalities (p<0.01) compared with ND. ECa 233 at 30 mg/kg/day significantly reduced triglycerides, total cholesterol, and low-density lipoprotein cholesterol (p<0.05), with efficacy comparable to simvastatin; however, it did not significantly improve male reproductive parameters or testicular morphology. **Conclusion**: ECa 233 effectively ameliorated HFD-induced dyslipidemia but did not significantly improve male reproductive function under the present experimental conditions. This dissociation suggests that metabolic improvement alone may be insufficient to reverse reproductive damage, which may require longer treatment duration, earlier intervention, or direct modulation of testicular oxidative and inflammatory pathways. Further studies with larger sample sizes and mechanistic investigations are warranted.

Keywords *Centella asiatica, ECa 233, High-fat diet, Dyslipidemia, Oxidative stress, Male reproductive function*

P-41

Osteological Investigation of Anatomical Variations of the Clivus

Athikhun Suwannakhan[1,2*], Luisa Leiss[1], Iosif Alhendi[1], David Kirson[1], Arada Chaiyamoon[3]
[1] Human Anatomy Unit, Department of Biomedical Sciences, College of Medicine and Health, University of Birmingham, Edgbaston, Birmingham B15 2TT, UK
[2] Department of Anatomy, Faculty of Science, Mahidol University, Ratchathewi, Bangkok 10400, Thailand
[3] Department of Anatomy, Faculty of Medicine, Khon Kaen University. Khon Kaen 40002, Thailand
*Corresponding author, e-mail: a.suwannakhan@bham.ac.uk

Abstract

The clivus is a sloping portion of the cranial base extending from the dorsum sellae to the anterior margin of the foramen magnum. Numerous osteological and radiological investigations have described anatomical variations of the clivus and adjacent cranial base structures, including the fossa navicularis magna, condylus tertius, and basilar processes. Nevertheless, certain variations remain insufficiently characterized. In particular, the median basilar canal (MBC) has received limited attention, with only a single previous osteological investigation reported. Furthermore, the basilar tubercles of the clivus (BTC), a morphological feature recently described by our group, have not previously been investigated in osteological specimens and currently lack prevalence data in the literature. Accordingly, the present study aimed to investigate variations of the clivus, with particular emphasis on the MBC and BTC, through osteological examination supplemented by radiological confirmation. A total of 161 dry skulls of unknown sex and age from the osteological collection of the College of Medicine and Health, University of Birmingham, were examined. Each specimen was systematically inspected for anatomical variations of the clivus and surrounding cranial base structures. The MBC was the most frequently observed variation, identified in 24 specimens (14.9%). The BTC were identified in 13 specimens (8.1%). Additional variations included fossa navicularis magna in 8 specimens (5.0%), basilar processes in 3 specimens (1.9%) (unilateral, n=2; bilateral, n=1), tubercle at the anterior margin of the foramen magnum in 2 specimens (1.2%), and condylus tertius in 2 specimens (1.2%). This study provides further osteological and radiological evidence of anatomical variations in the clivus and confirms the presence of the median basilar canal on CT imaging. Moreover, it presents the first prevalence data for the basilar tubercles of the clivus, supporting their recognition as a distinct anatomical variant of the cranial base.

Keywords *Clivus, Skull base, Anatomical variation, Computed tomography*

P-42

Hyperostosis Frontalis Interna Predominantly Confined to the Frontal Bone: A Case Report

Min Woo Seo[1], Soo-Bin Kim[2], Hyun Jin Park[1*]
[1] Department of Anatomy, School of Medicine, Konkuk University, Chungju, South Korea
[2] Department of Oral Anatomy, Institute of Biomaterial Implant, College of Dentistry, Wonkwang University, Iksan, South Korea
*Corresponding author, e-mail: hjpark321@kku.ac.kr

Abstract
Background: Hyperostosis frontalis interna (HFI) is characterized by irregular thickening of the endocranial surface of the frontal bone and is most commonly seen in elderly women. It is usually asymptomatic and often goes unrecognized clinically because it occurs on the internal surface of the skull. HFI has been linked to aging, female sex, postmenopausal hormonal changes, obesity, and endocrine imbalance. Although generally benign, marked thickening may affect neurosurgical planning, radiologic interpretation, and forensic identification. While it is often detected incidentally on imaging, it is less frequently reported in anatomical dissection studies. **Objective:** The present case describes an extensive form of HFI identified during routine cadaveric dissection. **Method:** During gross anatomical dissection of a 75-year-old female donor who died of heart failure, marked thickening of the inner table of the frontal bone was observed following removal of the calvaria. **Result:** The endocranial surface demonstrated irregular, nodular, and uneven bony overgrowth predominantly confined to the frontal bone. The lesion did not cross the midline and showed no destructive or lytic features. Mild extension into the anterior parietal bone was noted; however, the principal distribution remained within the frontal region. The temporal and occipital bones were not involved. The outer table appeared grossly unremarkable. Based on its morphology and distribution pattern, the findings were consistent with hyperostosis frontalis interna. **Conclusion:** This case highlights the importance of recognizing HFI during anatomical dissection and underscores its relevance in anatomical education and clinical awareness. Accumulation of further cadaveric reports may contribute to a better understanding of its pathogenesis and epidemiologic characteristics.

Keywords *Hyperostosis frontalis interna, Calvarial hyperostosis, Anatomical variation*

P-43

Sex Estimation Using Atlas Vertebra Measurements in A Central Thai Sample

Chayanit Manoonpol[1], Sani Baimai[1]*, Chanya Chotchungchutchaval[1], Chaithud Kerdtubtim[1], Apidta Thanawibulchai[1], Chutikan Kaensa[1]
[1] Department of Anatomy, Faculty of Medicine Siriraj Hospital, Mahidol University, Bangkok, Thailand
*Corresponding author, e-mail: sanibaimai@gmail.com, baimaisani@gmail.com

Abstract

Sex estimation is a fundamental aspect of forensic anthropology, aiding in the identification of unknown individuals. While molecular techniques such as proteomics and genomics provide high accuracy, they can be costly and sensitive to environmental conditions. Osteological methods remain essential, particularly when well-preserved skeletal remains, such as the pelvis and skull, are unavailable. This study investigates the potential of the atlas (C1) vertebra for sex estimation in a Central Thai sample. A total of 130 first cervical vertebrae (65 males, 65 females) were analyzed using digital calipers. Twelve osteometric measurements were obtained and assessed through univariate and multivariate statistical analyses. The same observer took all measurements three times, and intra-observer reliability was confirmed using the intraclass correlation coefficient (ICC), which ranged from 0.912 to 0.980. Statistical assumptions for multivariate analysis were tested and met. Significant differences ($p < 0.05$) were found in nearly all measurements, except for the width of the superior articular facets. Male atlas measurements were consistently larger than those of females. The univariate discriminant function using the width of the left inferior articular facet showed the highest classification accuracy of 76.9%. A stepwise discriminant function including the width of the fovea and the width of the left inferior articular facet achieved 76.2% accuracy. The direct multivariate function incorporating all twelve variables provided the highest accuracy of 77.7%, with comparable sensitivity and specificity. Compared with previous studies in different populations, the findings emphasize the necessity of developing population-specific discriminant functions. Atlas-based osteometric analysis provides a useful alternative with moderate accuracy for sex estimation when primary indicators are unavailable. Further research with larger sample sizes and additional anatomical variables is recommended to refine the accuracy of these models. These findings contribute to forensic anthropology, physical anthropology, and bioarchaeology, offering valuable population-specific data for sex determination in Thai individuals.

Keywords *Atlas morphometrics, Sex estimation, Thai sample, Physical anthropology, Osteometric analysis*

Background

Sex determination is one of the most important aspects of forensic anthropological studies (1–9). Several studies have compared molecular methods, such as proteomic and genomic methods, with osteological methods (10). Although molecular studies have high accuracy and sensitivity, there are many limitations (11-12). Genomics-based methods require a sufficient amount of uncontaminated DNA and are relatively expensive. In addition, environmental factors such as sunlight, high temperature, and humidity can degrade DNA more easily than skeletal structures. Therefore, osteological methods remain widely used (10–12).

The seven cervical vertebrae play important roles in head positioning (13). The atlas (C1) is an atypical cervical vertebra. The atlas has neither a vertebral body nor a spinous process. It consists of two lateral masses, each composed of a transverse process, a superior articular facet, and a tubercle for the transverse ligament (13). Between the transverse process and the superior facet is the foramen transversarium, through which the vertebral artery passes to supply blood to the brain. The right and left lateral masses are connected by the anterior and posterior arches. The superior articular facet of C1 is connected to the occipital condyles of the skull, which then form a joint called the craniovertebral joint. In contrast, its inferior facet is connected to the superior facet of the axis (C2). Furthermore, the

atlas has another articular facet at the midline of its anterior arch that receives the anterior articular facet of the dens of the axis (13-14).

Previous studies have unanimously concluded that the pelvic bone is the best indicator for determining sex (5-6, 8-9, 15-16). However, the long bones, skull, and pelvic girdle have larger surface areas than the cervical vertebrae and contain more destructible chemical substances in their cortex, making them less likely to remain intact (8,17). Among the seven cervical vertebrae, previous research has preferentially focused on C1 (atlas), C2 (axis), and C7 because of their distinct morphologies (8,13-14). Therefore, the atlas was selected as the focus of this study. Krishan et al. (18) described two main approaches for sex determination in forensic anthropology. Morphological methods rely on visual assessment of skeletal features and are useful for rapid preliminary evaluation; however, their accuracy depends on the preservation of the remains. In contrast, metric methods quantify size differences between males and females using imaging techniques such as CT, MRI, or radiography. These data can then be analyzed using statistical approaches, such as discriminant analysis, to develop predictive models for sex estimation (2,18). Metric methods rely on measurable size differences between sexes. These measurements can be obtained from CT scans, MRI, or radiography and analyzed using discriminant analysis to develop predictive models for sex estimation. The accuracy of this approach depends on which statistical method is used (2,18). For these reasons, the osteometric method is most commonly used for sex determination (2). Previously, the assessment of the cervical vertebrae for sexual dimorphism involved measuring three parameters: maximum body height, the anterior-posterior of the vertebral foramen, and the transverse diameter of the vertebral foramen (2,8,19). However, the C1 vertebra has no vertebral body; it is not possible to measure the vertebral body height of the C1 vertebra (8,13-14). Previous studies have reported that the most dimorphic parameter is the maximum cervical vertebral body height, followed by the cervical transverse diameter and cervical anterior-posterior diameter (2,8,19). In morphological sex determination studies, the accuracy differs across different populations (1-2, 4-5, 16, 18-20) reported that the same discriminant function shows different accuracy when used in two populations (5). Thus, the functions derived from previous sex estimation studies are population-specific and cannot be applied to other population groups.

This study aimed to generate a discriminant function by using twelve measurements of the atlas from people living in the central region of Thailand and to investigate the sexual dimorphism of the atlas among the Thai population.

Materials and Methods

Osteometric data were collected from 130 human first cervical vertebrae (atlas vertebrae) obtained from a recognized osteological collection at the Department of Anatomy, Faculty of Medicine, Siriraj Hospital, Mahidol University, Bangkok, Thailand. This collection comprises skeletal remains of individuals with known sex, age, and origin. Ethical approval was granted by the Siriraj Institutional Review Board (SIRB) under protocol No. 763/2554 (Exempt). The sample included 65 male and 65 female atlas vertebrae. All individuals in the study were confirmed adults, with ages at death ranging from 20 to 69 years. Only specimens without pathological deformities or postmortem damage were selected to ensure anatomical normality. All measurements were taken directly from the vertebrae using a digital sliding caliper with a precision of 0.01 mm and recorded to the nearest millimeter (Fig. 1A-1C). All measurements were performed three times by a single primary observer to ensure consistency. Inter-observer reliability was additionally assessed among trained anatomists. The intraclass correlation coefficient (ICC) was calculated to assess intra-observer reliability. The results showed excellent reliability, with ICC values ranging from 0.912 to 0.98 across all variables. Inter-observer reliability among anatomists trained in the measurement protocol used in this study ranged from 0.91 to 0.96. Post hoc power analysis was conducted using G*Power 3.1.9.7 (21). The analysis, based on an effect size of $f^2(V) = 0.67$, $\alpha = 0.05$, two groups, and 12 response variables, yielded a statistical power of 0.99 for a sample size of 100. Our study included 130 participants, further strengthening the statistical power beyond the calculated requirements. All statistical analyses were performed using IBM SPSS Statistics version 30.0. Before discriminant function analysis, assumptions including normality, homogeneity of variance-covariance matrices, independence, linearity, multicollinearity, and absence of outliers were tested and confirmed to be met. These preliminary checks confirmed that the data were appropriate for the use of multivariate discriminant analysis.

Results and Discussion

Descriptive statistics for all measured dimensions of the first cervical vertebra (atlas), including means, SDs, and ranges for males and females, are summarized in Table 1. For example,

the width of the superior articular facet ranged from 18.2–24.5 mm in males (mean±SD: 21.3±1.5 mm) and 16.1–22.0 mm in females (mean±SD: 19.0±1.3 mm), demonstrating clear sexual dimorphism. All measurements were significantly larger in males than in females, with mean differences reaching statistical significance at the $p < 0.01$ level. This consistent pattern of sexual dimorphism indicates that the atlas exhibits measurable morphological differences between sexes in the studied population.

Each of the twelve linear measurements was subjected to discriminant function analysis using univariate, stepwise, and direct multivariate approaches to evaluate their effectiveness in sex estimation. Univariate discriminant function analysis revealed that all variables contributed to sex discrimination, although with varying levels of accuracy (Table 2). Among the individual measurements, the width of the left inferior articular facet (M7) demonstrated the highest average classification accuracy of 76.90%.

Each dimension was multiplied by its co-efficient and added to the corresponding constant. For example, the discriminant function score(y) for the width of the left inferior articular facet was calculated as follows:

$$Y = 0.906\ (M7) - 13.80$$

The discriminant function derived from this parameter showed satisfactory performance, with a sensitivity of 78.69% (95% CI: 67.60-89.60%) and a specificity of 75.36% (95% CI: 64.62–86.18%), respectively, suggesting that inferior articular facet dimensions may be informative indicators of sex-related differences in atlas morphology. These findings likely reflect functional and biomechanical differences related to load transmission and articulation with the axis, which tend to be more pronounced in males.

The stepwise discriminant functional analysis, incorporating all twelve variables, selected only two measurements, the width of the fovea (M3) and the width of the left inferior articular facet (M7), as the most discriminative predictors (Table 3). The resulting function achieved an average accuracy of 76.20%, with a sensitivity of 75.76% (95% CI: 66.20-85.80%) and a specificity of 76.56% (95% CI: 66.30-86.70%), respectively.

$$Y = 0.255(M3) + 0.843(M7) - 15.088.$$

The retention of only two variables in the optimal model suggests that specific articular foraminal dimensions capture the majority of sex-related variation in the cervical vertebra, while additional measurements contribute limited independent discriminatory power. This parsimonious model may be advantageous in forensic contexts where incomplete or fragmented remains restrict the number of measurable parameters.

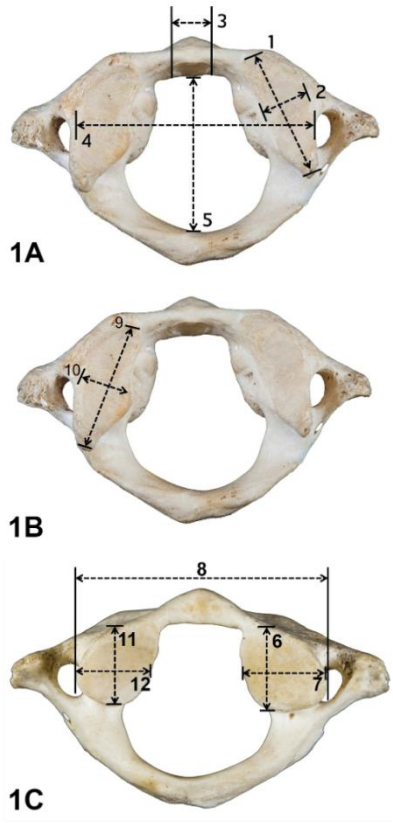

Fig. 1 shows the locations of measurements. All primary measurements were performed by a single investigator to minimize variability. Inter-observer reliability was additionally assessed in order to eliminate inter-observer partiality.1: Length of right superior articular facet (M1), 2: Width of right superior articular facet (M2), 3: Width of fovea (M3), 4: Distance between the lateral edges of the superior facet (M4), 5: Length of the vertebral foramen (M5), 6: Length of left inferior articular facet (M6), 7: Width of left inferior articular facet (M7), 8: Distance between the lateral edges of the inferior facet (M8), 9: Length of left superior articular facet (M9), 10: Width of left superior articular facet (M10), 11: Length of right inferior articular facet (M11), 12: Width of right inferior articular facet (M12).

percentages of all functions. The primary discriminant function- including all twelve atlas measurements- achieved the highest average accuracy of 77.70%; however, this level of accuracy is considered moderate in forensic contexts. Functions based on subsets of measurements demonstrated lower accuracy, with inferior facet variables (75.40%) outperforming the fourth function, which includes the distance between the lateral edges of the facet and the length of the vertebral foramen (70%), and the second function- the superior facet dimensions (66.20%). The best discriminant function obtained by the direct method was as follows:

$$Y = 0.007\,(M1) + 0.017(M2) + 0.264(M3) - 0.072\,(M4) + 0.075(M5) + 0.183(M6) + 0.292(M7) + 0.089(M8) + 0.087(M9) + 0.104(M10) - 0.050(M11) + 0.299(M12) - 19.585$$

The sensitivity and specificity of the function from the direct discriminant function analysis were 77.27% (95% CI: 67.1–87.5%) and 78.13% (95% CI: 68.1–88.1%), respectively. These results reinforce the importance of inferior facet morphology as a discriminator of sex, whether using single-measure or stepwise approaches.

The classification accuracies obtained in this study are comparable to those reported in previous research, although variations across studies highlight the population-specific nature of atlas-based sex estimation. Rozendaal (8) reported accuracy rates ranging from approximately 66.9%–74% accuracy for males and 70.2%–79.5% accuracy for females using measurements from multiple cervical vertebrae in European populations, with multivariate approaches exceeding 80% accuracy when several vertebral levels were included (8). Similarly, studies in Brazilian and Turkish populations using computed tomography or logistic regression models have reported higher accuracies (approximated 81-89%), particularly when vertebrae beyond the atlas were analyzed (2,7). The somewhat lower accuracy observed in the present study may be attributed to the exclusive focus on the first cervical vertebra, differences in measurement techniques, and population-specific skeletal characteristics.

Further support for population specificity is provided by studies demonstrating substantial variation in atlas dimensions across ancestry groups. Marino (22) reported the accuracy rates of the functions were 77–85% and 75–85%, respectively. The researcher further validated those equations by using the first collection and the other two collections of samples. The accuracy rate over a total of 234 samples ranged from 60% to 85%. Moreover, Marino (22) generated additional, race-specific equations that achieved 68%–92% accuracy among 200 samples, which emphasizes that sex estimation equations should be population-specific to be more accurate (22).

One of the factors associated with atlas morphology is head posture because it influences the cervical vertebral column and craniofacial morphology (23). Other factors might include anatomically adjacent bony landmarks such as the second cervical vertebra (5), the occipital condyle (15), and the foramen magnum (24), which are significantly different between males and females.

The discriminant functions from this study cannot be used for sex determination in children; however, Johnson et al (25) reported that the spinal canal diameter does not significantly increase after the fourth year of age, whereas the height of the first cervical vertebra continues to increase until 14 years of age in girls and 18 years of age in boys (25).

Population-specific characteristics are crucial in estimating the sex of an unidentified vertebra using measurements of the first cervical vertebra. Therefore, discriminant functions should be applied appropriately, ensuring that the functions used for classification are derived from vertebrae of the same population as the unknown specimen (26,27).

In summary, the present study demonstrated that measurements of the first cervical vertebra can be used for sex estimation with moderate accuracy in a central Thai population. Among the evaluated approaches, direct multivariate discriminant analysis produced the highest overall accuracy, while the width of the left inferior articular facet emerged as the most informative single measurement. These results reinforce the importance of developing and applying population-specific discriminant functions and support the forensic utility of the atlas when more sexually dimorphic skeletal elements are unavailable. In forensic applications, classification accuracy in the range of 75–80% is generally considered moderate and should be interpreted with caution.

Conclusion

Until now, no study has generated any equation using the dimensions of an atlas from the Thai population in the central area of Thailand for sex determination. This research conducted 12 univariate equations, a multivariate discriminant function from the enter method, and another function from the stepwise method. This study concluded that the discriminant function from the enter method using all 12 measurements provided 77.7% accuracy. The discriminant function from the

stepwise method using the width of the fovea and the width of the left inferior articular facet reached an accuracy rate of 76.2%. When more reliable indicators, such as the pelvis or skull, are unavailable, these equations may serve as supportive tools for sex estimation in the Thai population for physical anthropology, forensic anthropology, and bioarchaeology instead. Future research could apply these sex-determining functions to larger sample sizes of the Thai population.

Acknowledgments

This research was supported by the Chalermphrakiat Grant, Faculty of Medicine Siriraj Hospital, Mahidol University, Thailand.

References

1. Chovalopoulou ME, Bertsatos A. Estimating sex of modern Greeks based on the foramen magnum region. J Anthropol. 2017.
2. Ekizoglu O, Hocaoglu E, Inci E, Karaman G, Garcia-Donas J, Kranioti E, et al. Virtual morphometric method using seven cervical vertebrae for sex estimation on the Turkish population. Int J Legal Med. 2021;135(5):1953–64.
3. Kim DI, Kwak DS, Han SH. Sex determination using discriminant analysis of the medial and lateral condyles of the femur in Koreans. Forensic Sci Int. 2013;233(1–3):121–5.
4. Lee UY, Han SH, Park DK, Kim YS, Kim DI, Chung IH, et al. Sex determination from the talus of Koreans by discriminant function analysis. J Forensic Sci. 2012;57(1):166–71.
5. Marlow EJ, Pastor RF. Sex determination using the second cervical vertebra—A test of the method. J Forensic Sci. 2011;56(1):165–9.
6. Mello-Gentil T, Souza-Mello V. Contributions of anatomy to forensic sex estimation: Focus on head and neck bones. Forensic Sci Res. 2022;7: 11–23.
7. Padovan L, Ulbricht V, Groppo FC, Neto JP, Andrade VM, Júnior LF. Sexual dimorphism through the study of atlas vertebra in the Brazilian population. J Forensic Dent Sci. 2019;11(3):158–62.
8. Rozendaal AS, Scott S, Peckmann TR, Meek S. Estimating sex from the seven cervical vertebrae: An analysis of two European skeletal populations. Forensic Sci Int. 2020;306.
9. Spradley MK, Jantz RL. Sex estimation in forensic anthropology: Skull versus postcranial elements. J Forensic Sci. 2011;56(2):289–96.
10. Buonasera T, Eerkens J, de Flamingh A, Engbring L, Yip J, Li H, et al. A comparison of proteomic, genomic, and osteological methods of archaeological sex estimation. Sci Rep. 2020; 10(1).
11. Bidmos MA, Gibbon VE, Strkalj G. Recent advances in sex identification of human skeletal remains in South Africa. S Afr J Sci. 2010; 106(11–12).
12. Easteal PW, Easteal S. The forensic use of DNA profiling. Canberra: Australian Institute of Criminology; 1990.
13. Moore K, Agur A, Dalley A. Clinically Oriented Anatomy. 7th ed. Baltimore: Lippincott Williams & Wilkins; 2014. p. 982–4.
14. Netter F. Netter Atlas of Human Anatomy: Classic Regional Anatomy Approach. 8th ed. Philadelphia: Elsevier; 2022. p. 25–196.
15. Gapert R, Black S, Last J. Sex determination from the occipital condyle: Discriminant function analysis in an eighteenth and nineteenth century British sample. Am J Phys Anthropol. 2009;138(4):384–94.
16. Rai H, Keluskar V, Patil S, Bagewadi A. Accuracy of measurements of foramen magnum and occipital condyle as an indicator for sex determination using computed tomography. Indian J Health Sci Biomed Res. 2017;10(1):80–3.
17. Işcan MY. Global forensic anthropology in the 21st century. Forensic Sci Int. 2001;117(1–2):1–6.
18. Krishan K, Chatterjee PM, Kanchan T, Kaur S, Baryah N, Singh RK. A review of sex estimation techniques during examination of skeletal remains in forensic anthropology casework. Forensic Sci Int. 2016;261:165.e1–8.
19. Kaeswaren Y, Hackman L. Sexual dimorphism in the cervical vertebrae and its potential for sex estimation of human skeletal remains in a white Scottish population. Forensic Sci Int Rep. 2019; 1:100023.
20. Torimitsu S, Makino Y, Saitoh H, Sakuma A, Ishii N, Yajima D, et al. Sexual determination based on multidetector computed tomographic measurements of the second cervical vertebra in a contemporary Japanese population. Forensic Sci Int. 2016;266:588.e1–6.
21. Faul F, Erdfelder E, Lang AG, Buchner A. G*Power 3: a flexible statistical power analysis program for the social, behavioral, and biomedical sciences. Behav Res Methods. 2007;39(2):175–91.
22. Marino EA. Sex estimation using the first cervical vertebra. Am J Phys Anthropol. 1995.
23. Kylamarkula S, Huggare J. Head posture and the morphology of the first cervical vertebra. Eur J Orthod. 1985;7(3):151–6.

24. Uthman AT, Al-Rawi NH, Al-Timimi JF. Evaluation of foramen magnum in gender determination using helical CT scanning. Dentomaxillofac Radiol. 2012;41(3):197–202.
25. Johnson KT, Al-Holou WN, Anderson RCE, Wilson TJ, Karnati T, Ibrahim M, et al. Morphometric analysis of the developing pediatric cervical spine. J Neurosurg Pediatr. 2016;18(3):377–89.
26. Hora M, Sládek V. Population specificity of sex estimation from vertebrae. Forensic Sci Int. 2018;291:279.e1.
27. Rohmani A, Shafie MS, Nor FM. Sex estimation using the human vertebra: A systematic review. Egypt J Forensic Sci. 2021;11:1–5.

Table 1 Basic statistics of all measurements (in mm.) and *p*-value for differences in means between males and females with each variable

	Male				Female				p-value
Measurement	**Mean**	**Min**	**Max**	**S.D.**	**Mean**	**Min**	**Max**	**S.D.**	
M1	21.94	17.54	26.29	2.04	20.55	15.28	25.56	2.49	0.001
M2	10.98	8.99	14.41	1.17	10.81	8.66	14.10	1.10	0.392
M3	9.13	5.74	13.52	1.53	8.52	6.19	11.06	1.12	0.011
M4	46.75	39.80	51.86	2.41	45.65	40.70	51.90	2.70	0.015
M5	29.79	25.51	35.39	2.08	28.27	21.94	37.31	2.44	0.000
M6	16.85	13.42	19.24	1.26	16.23	13.72	18.36	1.04	0.003
M7	15.87	12.66	18.95	1.15	14.60	12.81	17.62	1.05	0.000
M8	44.49	37.00	50.63	2.48	42.16	38.11	48.21	2.23	0.000
M9	21.95	17.15	27.61	2.22	20.48	14.46	26.97	2.57	0.001
M10	11.01	9.37	13.20	1.00	10.71	9.06	12.68	0.91	0.073
M11	16.85	13.39	20.07	1.25	16.35	13.33	18.11	1.01	0.013
M12	15.89	13.39	17.86	1.04	14.74	12.37	17.19	1.04	0.000

Table 2 Univariate discriminant function analysis from both sexes

Measurement	Unstandardized coefficient	Constant	Centroid	Sectioning point	Accuracy (%)
M1	0.439	-9.334	M = 0.306 F = -0.306	0.000	60.0
M2	0.880	-9.591	M = 0.075 F = -0.075	0.000	51.5
M3	0.747	-6.588	M = 0.225 F = -0.225	0.000	59.2
M4	0.391	-18.068	M = 0.215 F = -0.215	0.000	61.5
M5	0.441	-12.796	M = 0.334 F = -0.334	0.000	65.4
M6	0.865	-14.307	M = 0.269 F = -0.269	0.000	60.8
M7	0.906	-13.800	M = 0.575 F = -0.575	0.000	76.9
M8	0.424	-18.389	M = 0.495 F = -0.495	0.000	70.8
M9	0.416	-8.823	M = 0.305 F = -0.305	0.000	61.5
M10	1.051	-11.407	M = 0.158 F = -0.158	0.000	54.6
M11	0.881	-14.630	M = 0.222 F = -0.222	0.000	56.9
M12	0.962	-14.742	M = 0.553 F = -0.553	0.000	74.6

Table 3 Stepwise discriminant function analysis from both sexes

Function variables	Unstandardized coefficient	Standardized coefficient	Constant	Centroids	Sectioning point	Average accuracy (%)
M7	0.843	0.930	-15.088	M = 0.611	0.000	76.20
M3	0.255	0.342		F = -0.611		

Table 4 Direct discriminant function analysis from both sexes

Functions and Variables	Unstandardized coefficient	Standardized coefficient	Constant	Centroids	Sectioning point	Average accuracy (%)
Function 1						
(All twelve variables)			-19.585	M = 0.688	0.00	77.70
M1	0.007	0.016		F = -0.688		
M2	0.017	0.019				
M3	0.264	0.354				
M4	-0.072	-0.183				
M5	0.075	0.170				
M6	0.183	0.211				
M7	0.292	0.322				
M8	0.089	0.210				
M9	0.087	0.208				
M10	0.104	0.099				
M11	-0.050	-0.057				
M12	0.299	0.311				
Function 2						
(Superior facet variables)			-14.888	M = 0.375	0.00	66.20
M1	0.166	0.378		F = -0.375		
M9	0.257	0.618				
M2	0.165	0.187				
M10	0.379	0.361				
Function 3						
(Inferior facet variables)			-17.306	M = 0.622	0.00	75.40
M11	-0.044	-0.050		F = -0.622		
M6	0.235	0.272				
M12	0.465	0.483				
M7	0.462	0.510				
Function 4						
(Distance between the lateral edges of the facet and length of vertebral foramen variables)			-16.669	M = 0.530	0.00	70.00
M8	0.418	0.984		F = -0.530		
M4	-0.121	-0.310				
M5	0.144	0.327				

P-44

Cross-Platform Offline AI Framework and Applications for Real-time Personalized Posture and Gait Analysis

Atthaboon Watthammawut[1]*, Jitchon Polprayoon[1], Raksawan Poonkham[1], Monsicha Somrit[2]*
[1] Department of Anatomy, Faculty of Medicine, Srinakharinwirot University
[2] Department of Anatomy, Faculty of Science, Mahidol University
*Corresponding authors, e-mail: atthaboon@g.swu.ac.th, monsicha.som@mahidol.edu

Abstract
Background: Traditional posture and gait analysis systems have historically relied on expensive, laboratory-grade hardware such as motion capture or high-latency cloud-based processing. These limitations have restricted clinical-grade assessment to specialized institutions and facilities, creating barriers to accessibility, patient privacy, and real-time biofeedback in community health settings. Furthermore, the traditional systems have also required extensive training and education in the associated fields to use and, hence, restrict their usage to the wider populace. Therefore, for a basic postural and gait analytical system, we have developed a reactive application that was able to conduct and examine squat kinematics, ergonomic sitting posture, and shoulder symmetry with posture and gait analyses, and ultimately provide assessment results in real-time with a high level of confidence. **Objective:** To develop and deploy a high-fidelity, offline posture analyzer capable of providing real-time musculoskeletal feedback across multiple platforms without the need for specialized sensors or active internet connectivity. **Methods:** The application was engineered using a localized WebAssembly (WASM) architecture, utilizing a computer vision engine for skeletal tracking. The system was optimized for cross-platform deployment, including PC, web-based interfaces, and offline-capable mobile applications for Android and iOS. The framework in the prototype stage was specifically adapted for the Faculty of Medicine Health Promotion event at Srinakharinwirot University (January 8, 2026), focusing on three primary clinical assessments: squat kinematics, ergonomic sitting posture, and shoulder symmetry (Scapular Dyskinesis screening). The participants that were analysed and tracked was 151, all anonymously without retention of any unique identifying data. **Results:** The localized AI approach achieved near-zero latency on consumer-grade hardware while maintaining high-fidelity joint-angle accuracy (average of 85.3 % confidence for all joint assessments), while scores provided to the participants were based on measurements that were over 80% confidence, and had provided postural assessment feedback scoring that visibly corresponded to the human assessors' observations. During the University health event, the system provided immediate, actionable biofeedback to participants, successfully identifying postural deviations associated with injury risk in all 151 participants. **Conclusion:** This development represents a new frontier in personalized health analysis by transitioning AI from cloud-dependent, inaccessible systems to local, user-centric devices. By offering a high-utility, cross-platform solution, this framework increases accessibility to clinical-grade posture monitoring, facilitating early intervention and preventative care in public health.

Keywords *Artificial intelligence, Computer vision, Musculoskeletal system, Patient teaching and feedback, Postural and gait assessment, Real-time feedback*

P-45

Designing A Virtual Classroom in Embryology: A Prototype

Nutmethee Kruepunga[1*]
[1] Department of Anatomy, Faculty of Medicine, Kasetsart University
*Corresponding author, e-mail: nutmethee.kr@ku.th

Abstract

Embryology is the study of developmental dynamics in the human body. Its difficulty is the lack of realistic images demonstrating how structures change. Moreover, human embryos and fetuses are rarely available. Previously, alternative models such as chick and pig embryos were used by serial sectioning and whole mounting. Their development has partially been translated into human embryonic development, but 3D changes have been visualized inadequately. Recently, computer-aided 3D reconstruction has solved the problem. 3D models used in the prototype were reconstructed by the Department of Anatomy, Faculty of Medicine, Kasetsart University, Thailand, and the Department of Anatomy & Embryology, Faculty of Health, Medicine and Life Sciences, Maastricht University, the Netherlands. Although 3D PDFs are easily accessible, they can provide only a stage-by-stage 3D model. The developmental dynamics are limited for visualization. Therefore, the goal is to provide 3D models of human development simultaneously. As virtual experience is popular currently, it is selected as a prototype for embryology classrooms due to its potential. Our prototype of a virtual classroom in embryology is still developing. More comments on user experience are required.

Keywords *Embryology, Virtual reality, Design thinking*

P-46

Students' Preferences Towards Problem-Based Learning (PBL) and Didactic Lectures: A Cross-Sectional Questionnaire-Based Study

Anup Pandeya[1*], Navindra Phuyal[1], Ananda Kumar Mishra[1]
[1] Department of Anatomy, Rapti Academy of Health Sciences, Ghorahi Dang, Nepal
*Corresponding author, e-mail: anup.bpkihs@gmail.com

Abstract

Among various methods of delivering medical education, the didactic teaching method has been the most common approach in the past. However, with the advancement in the medical curriculum, additional teaching methods like Problem-Based Learning (PBL) were introduced, which are aimed at improving students' learning and critical thinking in real-world applications. This study aimed to investigate medical students' perspectives towards the PBL method and didactic lectures for better academic performance and long-term retention of knowledge. The study was conducted among 100 medical undergraduate students exposed to PBL and didactic teaching in a health science academy of Nepal with the help of a structured questionnaire. The results suggest that 78% of students prefer both the didactic lectures and the PBL methods for learning medical subjects. However, only 8% of students choose the PBL method while 14% of students believe the didactic lectures are better. Further, we ask for more effective teaching methods for the students in the basic medical science and clinical science subjects. The results recommend 70% of students prefer the didactic lectures, which they assume are appropriate for gaining in-depth knowledge, while 10% choose the PBL method, and 30% wish both the PBL and didactic lectures as considered effective for the basic science subjects. In contrast, 96% of students choose PBL in the clinical subjects while only 4% choose both the PBL and the didactic lecture method. None of the students prefer the didactic teaching method in the clinical subjects. To conclude, the combined method of teaching, comprising didactic lectures and PBL, is preferred in basic science subjects, while PBL is the most common choice among students in clinical subjects.

Keywords *Students' preferences, Lecture methods, Medical students*

P-47

Reimagining Basic Anatomy Assessment: A 7-Year Longitudinal Study on Fairness, Joyful Learning, and Evidence-Based Reform

Worawit Suphamungmee*
Department of Anatomy, Faculty of Science, Mahidol University
272 Rama VI Road, Ratchathewi, Bangkok 10400, Thailand
*Corresponding author, e-mail: worawit.sup@mahidol.ac.th

Abstract

Anatomy education is undergoing global reassessment as institutions seek fairer evaluation systems and more meaningful laboratory experiences. This study examined whether anatomy assessments are equitable across examination modalities, whether cadaveric laboratory teaching produces measurable learning gains, and what longitudinal evidence supports the adoption of a reformed scoring scheme. A retrospective analysis (2019-2025) was conducted using individual student score records from 2,597 undergraduate health sciences students enrolled in Thai (n = 2,315) and English-medium (n = 282) programmes at Mahidol University, Faculty of Science. Scores were equilibrated to a 50:50 lecture-to-laboratory weighting for cross-year comparability. Statistical analyses included independent t-tests, Pearson correlation, and scenario modelling. Across both programmes, lecture examination scores (Thai 64.1%; international 59.7%) were consistently 12-13 percentage points lower than laboratory scores, identifying a structural bottleneck confirmed by a 29:1 asymmetry in lecture-only versus laboratory-only failure rates. Onsite examinations produced significantly lower scores than online formats (62.5% vs 66.1%, $p < 0.001$, Cohen's $d = 0.26$), reflecting modality-driven rather than knowledge-driven score differences. Laboratory performance improved steadily each semester under cadaver-based instruction (mean +3.77%, $p < 0.001$), confirming cumulative skill acquisition as the mechanism. Modelling of an alternative 80:0:20 scheme (lecture examination: laboratory examination: laboratory performance) projected improved pass rates in 2024-2025 without compromising academic standards, with 2025 Thai programme scores converging to within 0.2 points. These findings provide longitudinal evidence that anatomy assessment reform is both justified and data-ready. A lecture-weighted framework enhances fairness, while reconceptualizing the cadaveric laboratory as a joyful, performance-based learning scaffold offers a sustainable direction for contemporary health sciences anatomy education.

Keywords *Anatomy education, Assessment fairness, Cadaveric laboratory, Examination reform, Undergraduate health sciences*

Background

Anatomy has long been taught through two pillars: the lecture theatre and the cadaveric laboratory. Both are under contemporary scrutiny. Online assessment during the COVID-19 pandemic disrupted the comparability of anatomy scores across cohorts. Growing recognition of laboratory examination anxiety raises questions of fairness. Resource constraints additionally prompt faculty to question whether cadaveric teaching remains educationally justified [1,2,3].

Rather than designing an intervention, this study exploits seven years of natural variation across 2,597 individual records to answer three evidence-based questions: (1) Did examination modality create inequitable cohort advantages? (2) Does cadaveric laboratory teaching produce quantifiable learning gains? (3) Is a reformed 80:0:20 scoring scheme safe and fair to implement?

Materials and Methods

Participants

Retrospective cohort study using complete individual student score records (2019-2025) from two parallel second-year anatomy courses at the same Department of Anatomy, Faculty of Science, Mahidol University: the Thai-medium programme (n = 2,315; Medical Technology, Radiologic

Technology, Public Health; 7 cohort-years) and the English-medium international programme (n = 282; identical content; 7 cohort-years). Total: n = 2,597 records. Ethical declaration: this study involved secondary analysis of anonymized student assessment data collected as part of routine educational practice. No identifiable personal information was accessed. According to MU-CIRB self-assessment guidelines, the project did not meet the definition of human subject research; therefore, institutional ethical approval was not required.

Assessment structure

The assessment structure changed across three distinct periods, as summarized in Table 1. From 2019 to 2022, the lecture examination and laboratory examination each carried 40 points (40%), with laboratory performance accounting for 20 points (20%); examination delivery shifted from online to onsite, and cadaveric specimens were progressively introduced. In 2023–2024, the lecture examination weight increased to 50 points (50%), the laboratory examination remained at 40 points (40%), and laboratory performance was reduced to 10 points (10%). By 2025, the lecture examination had risen further to 60 points (60%), and the laboratory examination had been reduced to 30 points (30%), reflecting the trajectory towards a lecture-weighted framework.

Table 1 Assessment structure by period. Each examination split two equal parts of midterm and final scores (e.g., 30 pts Exam = 15 pts of midterm scores + 15 pts of final scores; 40 pts Exam = 20 pts of midterm scores + 20 pts of final scores; 50 pts Exam = 25 pts of midterm scores + 25 pts of final scores; 60 pts Exam = 30 pts of midterm scores + 30 pts of final scores).

Period	Lec Exam	Lab Exam	Lab Performance	Mode	Cadaver
2019-2022	40 pts (40%)	40 pts (40%)	20 pts (20%)	Online to Onsite	No to Yes
2023-2024	50 pts (50%)	40 pts (40%)	10 pts (10%)	Onsite	Yes
2025	60 pts (60%)	30 pts (30%)	10 pts (10%)	Onsite	Yes

Statistical analysis

All components were converted to a percentage of maximum points for each respective assessment period (2019–2022: 40/40/20; 2023–2024: 50/40/10; 2025: 60/30/10), enabling direct cross-year comparison. An equilibrated total (Equilibrated total= 0.5 × Lecture % + 0.5 × Lab %) was applied to all cross-year comparisons, standardizing the lecture-to-laboratory ratio to 1:1 and removing the cross-year weighting confound. Reform scenario modelling was conducted by applying the formula: 80:0:20 score = Lecture% × 0.80 + Lab Performance % × 0.20 to each student record. Pass rates and grade-band distributions were then computed for each cohort year and programme under both the actual and modelled schemes, enabling direct comparison. No assumptions regarding student behavior change under the reformed scheme were made; the modelling is purely arithmetic. All analyses were performed using Python (version 3.12) with pandas and scipy.stats libraries. Statistics: independent t-tests, Pearson r, one-sample t-tests ($\alpha = 0.05$) [13].

Results

Participant summary

Descriptive statistics for both programmes are summarized in Table 2. The Thai programme enrolled 2,315 students and the international programme 282 students, giving a combined total of 2,597 records across 14 cohort-years. Mean lecture examination scores were 64.1% (SD 14.2) for the Thai programme and 59.7% (SD 14.1) for the international programme, compared with laboratory examination scores of 77.1% (SD 14.7) and 72.5% (SD 15.3), respectively. Laboratory performance scores were markedly higher in both programmes (Thai 93.2%; international 99.2%), reflecting the near-ceiling nature of this component. The lecture–laboratory gap was virtually identical across both programmes (-13.0% and -12.8%), and overall pass rates exceeded 92% in both groups.

Table 2 Descriptive statistics by programme

	Thai	Inter-national	Combined
n (students)	2,315	282	2,597
Lecture score (mean ± SD)	64.1 ± 14.2%	59.7 ± 14.1%	63.5%
Lab exam score (mean ± SD)	77.1 ± 14.7%	72.5 ± 15.3%	76.5%
Lab performance (mean ± SD)	93.2 ± 7.1%	99.2 ± 3.1%	94.0%
Lecture-lab gap	-13.0%	-12.8%	-13.0%
Overall pass rate	95.4%	92.6%	95.0%

Assessment fairness: examination modality

Onsite examination produced significantly lower lecture scores than online (62.5% vs 66.1%; $t = 6.07$, $p < 0.001$, Cohen's $d = 0.26$) and dramatically lower laboratory performance scores (89.8% vs 97.9%; $d = 1.41$, very large effect) [4,5,6]. These differences reflect structural modality advantages rather than genuine knowledge differences. The international programme showed no significant lecture difference ($p = 0.83$; n.s.) (Fig. 1).

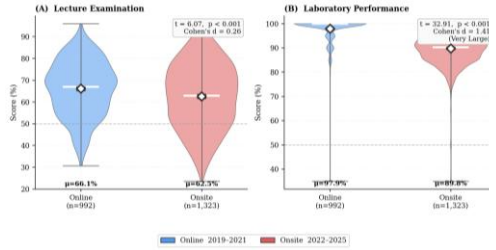

Fig. 1 Online vs onsite examination effect (Thai programme, n=2,315). (A) Lecture scores (d=0.26). (B) Laboratory performance (d=1.41). Diamonds = mean ± 95% CI.

The lecture bottleneck and failure asymmetry

Lecture and laboratory scores were strongly correlated (Thai $r = 0.776$; international $r = 0.808$; $p < 0.001$), confirming that both assessments evaluate the same underlying anatomical knowledge construct. Despite this construct equivalence, 11.6% of Thai students and 16.3% of international students failed the lecture examination while passing the laboratory examination, whereas only 0.4% showed the reverse pattern — a 29:1 asymmetry. To clarify directionality: for every one student who passes the lecture but fails the laboratory, approximately 29 students pass the laboratory but fail the lecture. This asymmetry demonstrates that laboratory examination failure is rare among students who demonstrate anatomy knowledge through written assessment; the bottleneck operates overwhelmingly in the lecture direction. Students who pass the laboratory but fail the lecture demonstrably possess anatomy knowledge, as confirmed by their laboratory performance scores (mean 91–99%) reflecting consistent semester-long engagement and competence. The higher lecture failure rate reflects the elevated written examination difficulty relative to specimen-identification tasks in this cohort, combined with the anxiety-suppressing effect of the cadaveric examination setting acting as construct-irrelevant variance (Fig. 2) [7,8].

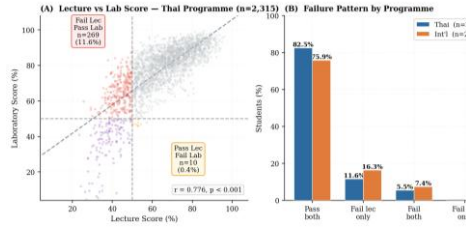

Fig. 2 The lecture-laboratory failure asymmetry. (A) Lecture vs laboratory score scatter (n=2,315, r=0.776). (B) Failure-pattern proportions by programme: 29:1 lecture: lab asymmetry.

Cadaveric laboratory as a learning scaffold

Laboratory examination scores improved consistently from midterm to final assessment across all 7 years (mean +3.77%; $t = 15.21$, $p < 0.001$). Lecture examination scores showed no consistent within-semester progression (mean −0.46%; $p = 0.056$, n.s.), and the laboratory improvement was significantly greater than the lecture improvement ($p < 0.001$). This specificity of improvement to the laboratory component is consistent with a cumulative cadaveric scaffold mechanism. In this curriculum, laboratory sessions progress through the body systems in anatomical structured sequence — from musculoskeletal to neurovascular, and later the internal organ systems in the semester — so that each laboratory session builds directly upon spatial understanding established in previous sessions. The three-dimensional tactile encounter with prosected cadaveric material integrates the knowledge introduced in lectures into a cohesive, embodied anatomical understanding that matures as the semester advances. Lecture examination scores do not show the same within-semester progression because written examination content and difficulty are calibrated independently for each sitting, and written recall of anatomy does not benefit from the same progressive spatial consolidation that repeated cadaveric exposure provides. The absence of lecture score improvement, therefore, reflects the nature of written examination calibration rather than a failure of lecture teaching (Fig. 3) [9,10,11].

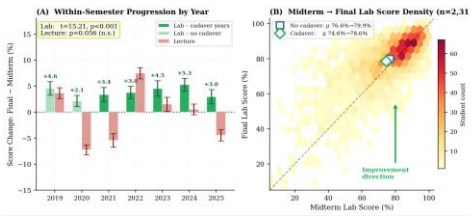

Fig. 3 Cadaveric laboratory teaching within semester score progression. (A) Within-semester lab and lecture score progression by year. (B) Midterm → final lab progression density (n=2,315): systematic upward shift.

The 80:0:20 reform scheme

Modelling the 80:0:20 scheme (80 pts lecture: 0 pts lab exam: 20 pts lab performance) showed pass rate improvements in 2024 and 2025 for both programmes. In 2025 (67% lecture weight), the Thai programme means scores converged to within 0.2 points under both schemes (71.5 vs 71.3), and the pass rate was higher under 80:0:20 (94.6% vs 91.4%). International programme 2025 pass rate improved from 73.9% to 82.6% (+8.7 percentage points). Score reductions in 2019-2023 reflect the removal of generous lab examination credit, not a structural flaw in the reform (Fig. 4).

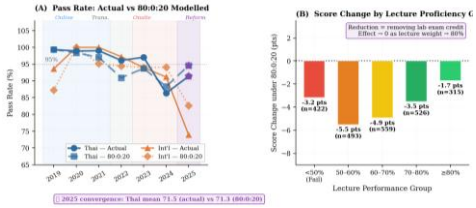

Fig. 4 Modelled 80:0:20 scoring scheme vs actual pass rates. (A) Actual vs 80:0:20 pass rates 2019-2025. (B) Mean score changes by lecture proficiency group: effect converges to zero as lecture weight increases.

Cross-programme structural consistency

The lecture-laboratory gap averaged -13.0% in the Thai programme and -12.8% in the international programme across all 7 years, both modalities, and both languages. This virtually identical gap confirms the structural origin of performance asymmetry: it is intrinsic to anatomy assessment design, not to cohort ability, language of instruction, or cultural context (Fig. 5) [12].

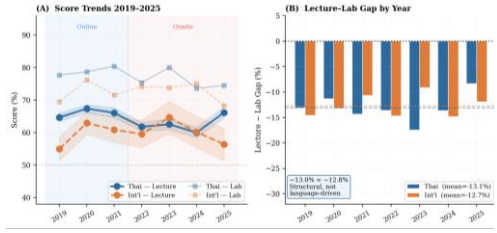

Fig. 5 Thai vs international programme: score trends and structural gap. (A) Lecture and laboratory score trends 2019-2025. (B) Lecture-lab gap per year: near-identical across both programmes (-13.0% vs -12.8%).

Discussion

Assessment Fairness

Two structural inequities emerge. First, online cohorts (2019-2021) benefited from a modality advantage (-13-16 percentile points for lab performance; $d = 1.41$) unrelated to anatomy knowledge. Second, the 29:1 failure asymmetry means laboratory examination systematically disadvantages students with strong conceptual knowledge but performance anxiety. Both inequities are corrected by the 80:0:20 scheme [4,5].

Joyful learning in the anatomy laboratory

The consistent within-semester laboratory improvement (+3.77%, every cohort year of the international programme) demonstrates the educational value of cadaveric laboratory teaching: tactile, three-dimensional encounter with prosected material consolidates spatial knowledge initiated by lectures and produces measurable, repeated learning gains. In this context, "joyful learning" refers to a cluster of empirically supported pedagogical conditions — reduced evaluative threat, intrinsic motivation, collaborative inquiry, and active engagement with authentic material — that the educational psychology literature associates with deeper processing and sustained knowledge retention [9,10]. The problem is not the laboratory examination format per se, but its current deployment as a high-stakes summative event in a setting that generates disproportionate anxiety relative to the lecture context, as evidenced by the very large modality effect ($d = 1.41$) on laboratory performance scores and the near-ceiling continuous performance scores (93–99%) that confirm students are competent and engaged outside the summative examination context. Reconceptualising the 20-point laboratory component through a structured formative rubric — pre-session preparation, in-session identification and clinical correlation, post-

session reflection — preserves the educational scaffold while removing the summative threat that suppresses performance, transforming the cadaveric laboratory from a feared examination venue into a site of joyful, evidence-based enquiry.

Evidence-based reform pathway

The 2025 convergence data confirm implementation safety. Three steps are proposed for 2026: (1) increase lecture examination to 80 points and remove the summative laboratory identification examination; (2) implement a structured 20-point laboratory performance rubric capturing preparation, identification, clinical relations, and reflection; (3) standardize examination difficulty across years using item banking and standard-setting protocols, as current between-year variance ($F = 12.9$, $p < 0.001$) undermines fair cohort comparisons [13].

Conclusion

Several limitations of this study warrant acknowledgement. First, this is a retrospective observational study; no experimental manipulation of assessment schemes was conducted, and the 80:0:20 modelling is arithmetic rather than prospective. Second, the COVID-19 pandemic (2019–2021) introduced online examination as a confounding variable that cannot be fully disentangled from secular trends in cohort ability or examination difficulty. Third, no direct measure of student anxiety was collected; the anxiety mechanism is inferred from the pattern of score differences across modalities and semesters rather than from validated psychological instruments. Future prospective studies incorporating anxiety inventories and a controlled implementation of the reformed scheme would strengthen the causal interpretation. Fourth, all data derive from a single institution and two parallel programmes; generalizability to other curricula and cultural contexts requires validation. This 7-year longitudinal analysis of 2,597 individual student records provides convergent evidence supporting anatomy assessment reform. The cadaveric laboratory is educationally essential and should be reimagined as a structured, joyful learning scaffold rather than a summative examination venue. Current assessment is structurally unfair: lecture examination weight should drive the grade. The 80:0:20 scheme is safe, fair, and data-ready for implementation in 2026.

Acknowledgements

The author thanks faculty colleagues and administrative staff of the Department of Anatomy, Faculty of Science, Mahidol University, for their support in maintaining accurate course records across seven academic years.

References

1. Drake RL, McBride JM, Lachman N, Pawlina W. Medical education in the anatomical sciences: the winds of change continue to blow. Anat Sci Educ 2009;2(6):253-9.
2. Sugand K, Abrahams P, Khurana A. The anatomy of anatomy: a review for its modernization. Anat Sci Educ 2010;3(2):83-93.
3. Pabst R. Anatomy curriculum for medical students: what can be learned for future curricula from evaluations and questionnaires completed by students, anatomists and clinicians in different countries? Ann Anat 2009;191(6):541-6.
4. Woldeab D, Brothen T. 21st century assessment: online proctoring, test anxiety, and student performance. Int J E-Learn Distance Educ 2019; 34(1):1-18.
5. Holt EA, High KA, Young TS, Durham Brooks T. A systematic review of online versus in-person exams: is cheating more prevalent in online settings? J Food Sci Educ 2022;21(2):63-75.
6. Hussein MJ, Yusuf J, Dingga ASN, Butt NS, Alqasmi I. Medical students' use and perception of online education tools during COVID-19 pandemic. Adv Med Educ Pract 2020;11:947-52.
7. Kerby J, Shukur ZN, Shalhoub J. The relationships between learning outcomes and methods of teaching anatomy as perceived by medical students. Clin Anat 2011;24(4):489-97.
8. Pawlina W, Drake RL. The role of anatomy in the medical curriculum: reflections on the status of the discipline. Anat Sci Educ 2008;1(1):1-2.
9. Aversi-Ferreira TA, Aversi-Ferreira RAGMF, Nishijo H. Effects of cadaveric dissection on undergraduate student performance and wellbeing. Anat Sci Educ 2023;16(3):462-73.
10. Böckers A, Jerg-Bretzke L, Lamp C, Brinkmann A, Traue HC, Böckers TM. The gross anatomy course: an analysis of its importance. Anat Sci Educ 2010;3(1):3-11.
11. Lufler RS, Zumwalt AC, Romney CA, Hoagland TM. Effect of visual-spatial ability on medical students' performance in a gross anatomy course. Anat Sci Educ 2012;5(1):3-9.
12. Bergman EM, Prince KJAH, Drukker J, van der Vleuten CPM, Scherpbier AJJA. How much anatomy is enough? Anat Sci Educ 2008;1(4): 184-8.

13. Cohen J. Statistical Power Analysis for the Behavioral Sciences. 2nd ed. Hillsdale, NJ: Lawrence Erlbaum; 1988.

P-48

A Variation-Based Translational Anatomy Education Model Using Pancreaticoduodenal Arterial Networks to Support Clinical Reasoning

Sani Baimai[1]*, Papon Cholvisudhi[2], Chutikan Kaensa[1], Ratchanon Puangket[1],
Lue.kasamakamin Bhumithadadech[2]
[1] Department of Anatomy, Faculty of Medicine Siriraj Hospital, Mahidol University, Bangkok, Thailand
[2] Medical student of Faculty of Medicine Siriraj Hospital, Mahidol University, Bangkok, Thailand
*Corresponding author, e-mail: sanibaimai@gmail.com

Abstract

Anatomy education is often focused on factual knowledge, with limited integration into clinical reasoning. This study proposes a variation-based translational anatomy education model using pancreaticoduodenal arterial networks to bridge this gap. This study aimed to evaluate a variation-based translational anatomy education model integrated with cadaveric dissection and digital learning to improve conceptual understanding and explore its potential to support clinical reasoning among second-year medical students. A cadaveric study of 32 specimens was conducted to classify pancreaticoduodenal arterial variations, which were translated into structured learning objectives and an assessment blueprint linking anatomical variation to clinical reasoning tasks. Ninety-one second-year medical students participated in a multimodal instructional intervention incorporating dissection, three-dimensional visualization, video modules, and scenario-based assessment. Student performance was analyzed using item analysis and internal consistency reliability (Cronbach's alpha = 0.78). Predominant arterial variations were identified and used to support instructional design. Students demonstrated high accuracy in identifying collateral circulation pathways (95%), while moderate performance in recognizing splenic artery branching (68%) indicated conceptual gaps. Recall-based classification accuracy reached 84%. Scenario-based questions assessing clinical application showed moderate accuracy (74–79%) but demonstrated greater discriminatory capacity than recall-based items, suggesting differentiation in levels of understanding. Most students reported positive perceptions of instructional usefulness (84%), improved understanding (78%), preference for multimodal learning (74%), and clearer visualization of future clinical roles (72%). A variation-based anatomy education model integrating dissection and digital learning may support the development of clinical reasoning through assessment-aligned instruction. This approach suggests a shift from memorization toward more clinically integrated understanding while maintaining assessment quality.

Keywords *Anatomical variation, Dissection, Digital learning, Clinical reasoning, Educational assessment*

P-49

Toward a National Framework for the Governance of Human Tissue in Thailand: The Need for Comprehensive Legislation

Athikhun Suwannakhan[1,2*]
[1] Department of Anatomy, Faculty of Science, Mahidol University, Ratchathewi, Bangkok 10400, Thailand
[2] Human Anatomy Unit, Department of Biomedical Sciences, College of Medicine and Health, University of Birmingham, Edgbaston, Birmingham B15 2TT, UK
*Corresponding author, e-mail: a.suwannakhan@bham.ac.uk

Abstract

The ethical use of human tissues in medical education, research, and public engagement requires clear regulatory frameworks to ensure respect for donors and public trust. In Thailand, however, the governance of human tissue remains largely decentralised, with individual universities and medical institutions developing their own internal regulations. While these institutional policies guide practices such as body donation, cadaveric dissection, and specimen handling, significant inconsistencies exist across institutions. More importantly, several emerging issues remain insufficiently addressed, including the use of human tissues for photography, digital dissemination, and potential commercial applications. In contrast, countries such as the United Kingdom have established comprehensive national legislation, notably the Human Tissue Act 2004, which provides standardised guidance on consent, storage, use, and public display of human tissues. The absence of an equivalent legislative framework in Thailand creates uncertainty for educators, researchers, and institutions, and may expose them to ethical and legal risks. This perspective argues that the current challenges cannot be fully resolved through institutional policies alone and require national-level legal oversight. A unified legislative framework would provide consistent standards for consent, handling, documentation, imaging, and permissible uses of human tissues across the country. The Anatomy Association of Thailand (AAT), as the principal professional body representing anatomical sciences in Thailand, is well-positioned to initiate dialogue among academic institutions, policymakers, and legal authorities. As a first step, AAT could convene expert panels, conduct nationwide consultations, and develop policy recommendations to support the drafting of future legislation. Establishing a comprehensive legal framework would strengthen ethical governance, ensure respect for donors, and align Thailand with international standards in anatomical science and medical education.

Keywords *Human tissue, Legislation, Ethics, Body donation*

P-50

Lowering the Barrier to 3D Anatomical Modeling: A Free macOS Photogrammetry Application

Athikhun Suwannakhan[1,2*], Luisa Leiss[1], James White[1], Nicole Smith[1], Iosif Alhendi[1], Tracey Wilkinson[1]
[1] Human Anatomy Unit, Department of Biomedical Sciences, College of Medicine and Health, University of Birmingham, Edgbaston, Birmingham B15 2TT, UK
[2] Department of Anatomy, Faculty of Science, Mahidol University, Ratchathewi, Bangkok 10400, Thailand
*Corresponding author, e-mail: a.suwannakhan@bham.ac.uk

Abstract

Three-dimensional (3D) anatomical models are increasingly incorporated into medical education, surgical training, and anatomical research. Despite their growing importance, the production of high-quality 3D models from physical specimens often requires costly commercial software or technically complex workflows, which limit accessibility, particularly in resource-constrained settings. This project describes the development of a macOS-based photogrammetry application designed to simplify and democratize anatomical 3D reconstruction. The application leverages Apple's RealityKit *PhotogrammetrySession* framework to generate 3D models from standard digital photographs. Through a streamlined graphical interface, users select an image set, choose a reconstruction detail level, and export a USDZ model without requiring command-line operations or proprietary platforms. Preliminary testing on osteological and cadaveric specimens demonstrated that accurate and visually detailed 3D reconstructions can be achieved using conventional photographic setups. By reducing technical barriers and simplifying the reconstruction process, this tool has the potential to expand access to 3D anatomical modeling in teaching laboratories, research, and digital archiving. Although the application is currently under active development, it is intended for future open-source release to encourage broader adoption within the anatomical community.

Keywords *Photogrammetry, 3D reconstruction, Digital anatomy, Education*

Author Index

Acknowledgments

We would like to acknowledge the following organizations and individuals for their support of the 48th International Conference of the Anatomical Association of Thailand (AAT48)
May 13th - 15th, 2026
Tsix5 Phenomenal Hotel, Pattaya, Chon Buri, Thailand

UPRIGHT SIMULATION CO., LTD.

WICER ENTERPRISE CO., LTD.

THE SCIENCE AND EDUCATIONAL CO., LTD.

PRIME MEDICAL CO., LTD.

OFFICIAL EQUIPMENT MANUFACTURING CO., LTD.

EMPIRE SCIENTIFIQUE CO., LTD.

WOLTERS KLUWER

SCION ASSOCIATED LIMITED PARTNERSHIP

COAX GROUP CORPORATION CO., LTD.

HUAYI SCIENCE AND EDUCATION CO., LTD.

MEGA LIFE SCIENCES PTY., LTD.

HOLLYWOOD INTERNATIONAL CO., LTD.

PATHOLOGY WARE INTERNATIONAL CO., LTD.

ELSEVIER (NEW KNOLEDGE INFORMATION CO., LTD.)

THANES SCIENCE CO., LTD.

CENGAGE LEARNING (THAILAND)

ABSOTEC CO., LTD.


UPRIGHT
SIMULATION
COMPANY LIMITED


WICER ENTERPRISE
บริษัท ไวเซอร์ เอ็นเตอร์ไพรส์ จำกัด


SCI·ED
THE SCIENCE AND EDUCATIONAL


Prime Medical
Company Limited


FLEXLAB
Advanced Laboratory Solution


EMPIRE
Scientifique


Wolters
Kluwer
Ovid


ASCION
SOCIATED
ห้างหุ้นส่วนจำกัดซายน์ออนแอสโซซิเอท


COAX


HUAYI


Wellness
We care
By
MEGA
We care


HTT
HOLLYWOOD
INTERNATIONAL


บริษัท พยาธิภัณฑ์อินเตอร์เนชั่นแนล จำกัด
PW
Pathology Ware International Co.,Ltd.

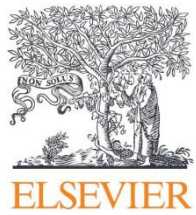
ELSEVIER


THANESCIENCE
บริษัท เทนส์ไซส์ จำกัด


Cengage


ABSOTEC
www.absotec.info
WWW.ABSOTECTHAILAND.COM
Specialize in Scanning Electron Microscope – Service Laboratory

AAT48

Organized by

The Anatomy Association of Thailand cooperated with
Department of Anatomy, Faculty of Medicine
Srinakharinwirot University